Alexandrov RESEARCH INSTITUTE OF TECHNOLOGY
NITI

PHASE DIAGRAMS FOR MULTICOMPONENT SYSTEMS CONTAINING CORIUM AND PRODUCTS OF ITS INTERACTION WITH NPP MATERIALS

(CORPHAD)

Phase #2

STUDY OF TERNARY OXIDIC SYSTEMS: SYSTEM U–Zr-O

PROGRESS REPORT

01/05/06 – 30/11/06

Project title	Phase diagrams for multicomponent systems containing corium and products of its interaction with NPP materials (CORPHAD, #1950.2)
Customer	ISTC
File specification	CORPHAD/RCP-0603
Place of project implementation	Alexandrov Research Institute of Technology (NITI) of the Russian Federal Agency for Atomic Energy
	Russia 188540, Sosnovy Bor of Leningrad Oblast, NITI

Project manager	Name	Yu. N. Aniskevich
	Signature	
	Date	November , 2006

Authors

Prof. V.B. Khabensky

Prof. S.V. Bechta

Dr. V.S. Granovsky
Prof. V.V. Gusarov

V.I. Almjashev
S.A. Vitol

E.V. Krushinov

Prof. Yu.B. Petrov

Dr. S.Yu. Kotova

Dr. A.A. Sulatskiy

Dr. I.V. Kulagin

Dr. D.B. Lopukh

Dr. A.V. Merzliakov

Dr. L.P. Mezentseva
V.G. Blizniuk
V.R. Bulighin

E.M. Beliaeva

E.K. Kaliago

N.E. Kamensky

R.A. Kosarevsky
A.V. Lisenko

A.P. Martynov

V.V. Martynov

E.V. Shevchenko

Contents

INTRODUCTION

The current work is carried out within the ISTC CORPHAD Project in order to specify phase diagrams of corium-based systems and products of its interaction with NPP materials. The availability of credible information about phase equilibria in such systems is very important for adequate forecasting of physicochemical phenomena taking place in a nuclear reactor during the core heatup and melting, molten pool formation and evolution, also in case of the melt interaction with materials of structures containing or contacting it. The analysis of information on phase diagrams, which are important for severe accident studies /1/, has shown that there are many systems, which need experimental data for a reliable phase diagram construction.

U–Zr–O is one of the basic systems essential for the reliable determination of the in-vessel corium phase equilibrium; of particular importance are its concentration regions, which correspond to oxygen concentration and cation composition representing reactor conditions. The investigation of such systems in the closest-to-equilibrium condition is possible only in the inert atmosphere or in the atmosphere with controlled oxygen partial pressure, when a special technology is applied. This is explained by an extremely high chemical activity of melts in the relevant concentration domain. Another peculiarity of the mentioned system is its easy stratification /2/. These U–Zr–O properties require advanced and complex methodologies of melt preparation, handling and investigation. For this reason the available experimental data are quite limited and often controversial; this particularly applies to the data on miscibility domain, (e.g. publications /2/ and /3/).

The current work is aimed at the experimental evaluation of liquidus and solidus temperatures for the compositions recommended by the CORPHAD project collaborators, and at the determination of coexisting liquids' composition in the miscibility gap. Beside that, melt crystallization at different cooling rates has been studied in detail.

As mentioned above, basic features of the studied system restrict the applicability of conventional methods of thermal analysis. Much attention and effort has been dedicated to the development of subject-oriented methodologies and corresponding experimental facilities. New original methodologies /4, 5/ have been developed by NITI and ISCh RAS. The report presents these methodologies and describes the experimental facilities. A limited inventory of compositions and properties have been measured using conventional methods and facilities, the produced results confirm the efficiency of newly-developed methods.

The appropriate thermodynamic calculations using GEMINI-2 code and NUCLEA-05 database have been made for the preliminary evaluation of equilibrium composition of the studied systems and comparison of these results with experimental data.

1. State of the art review

The U-Zr-O system has been studied by many authors. Unfortunately, the currently available data on it are still controversial. There are publications on several quasibinary phase diagrams, which belong to different sections of this ternary system.

Some of them deal with the studies of a rather narrow domain located close to sections UO_2 – $ZrO_{0.43}$ (Fig. 1.1.) /6/, UO_2 – $ZrO_{0.54}$ (Fig. 1.2) /7/ and UO_2 – $ZrO_{0.51}$ (Fig. 1.3) /8/.

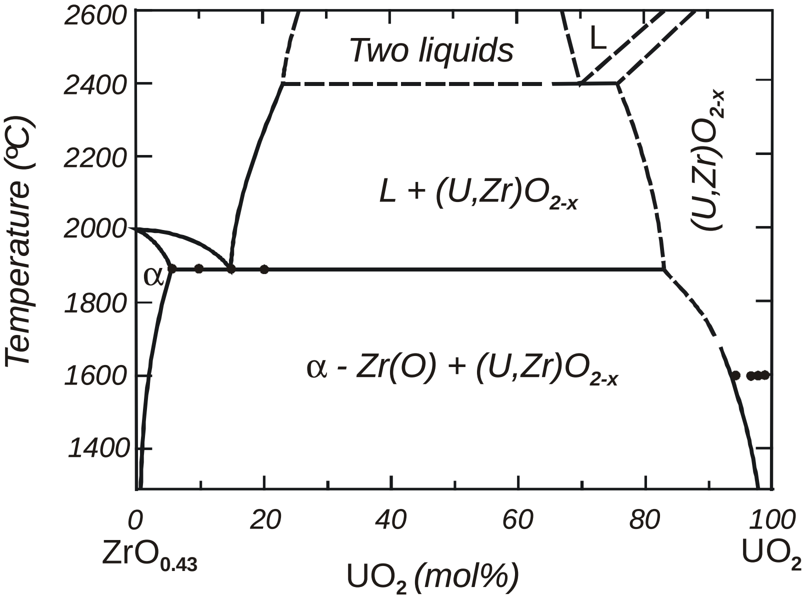

Fig. 1.1. Phase diagram of the $ZrO_{0.43}$ - UO_2 system /6/

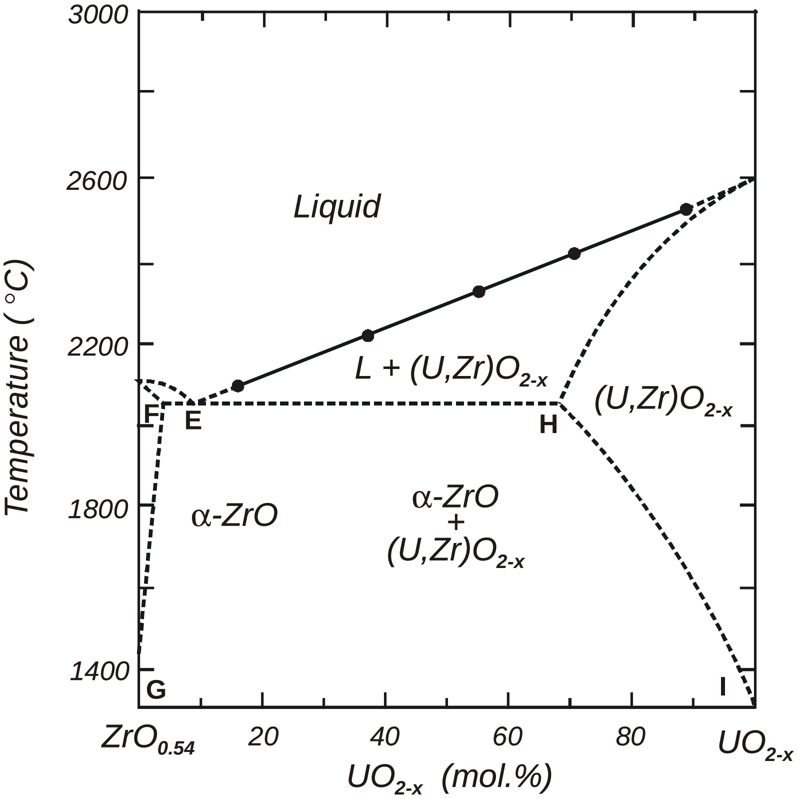

Fig. 1.2. Phase diagram of $ZrO_{0.54}$ - UO_2 /7/

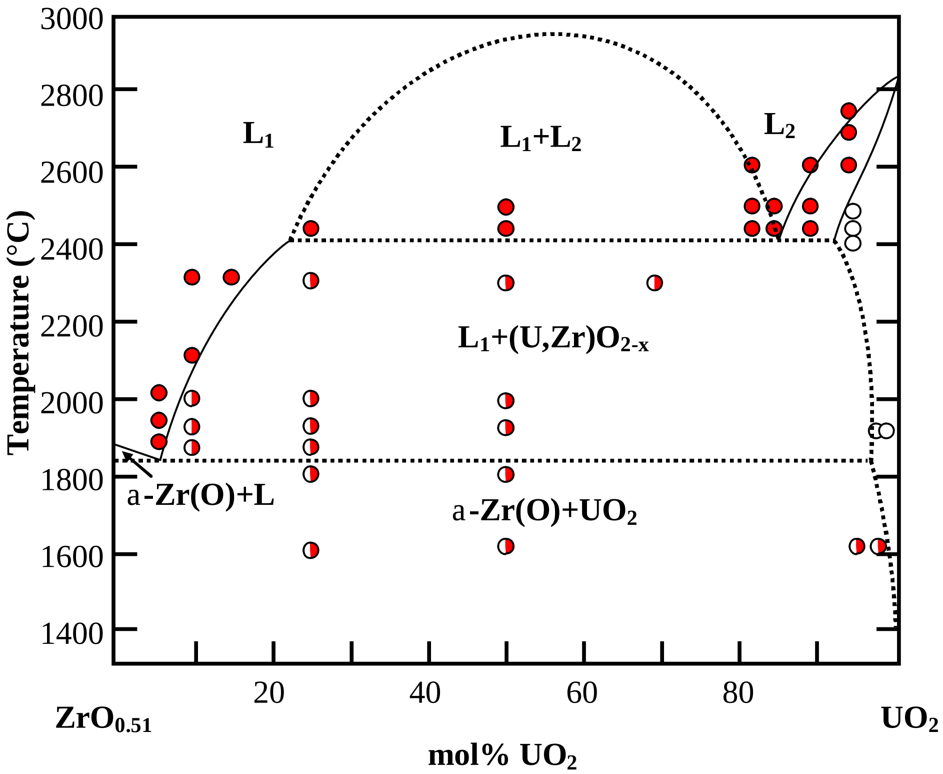

Fig. 1.3. Phase diagram $ZrO_{0.51}$ - UO_2 /8/

There is a publication presenting the study of Zr-UO_2 section /9/, in which the presence of a miscibility gap in the concentration interval 19 - 80 mol % of urania is shown (Fig. 1.4).

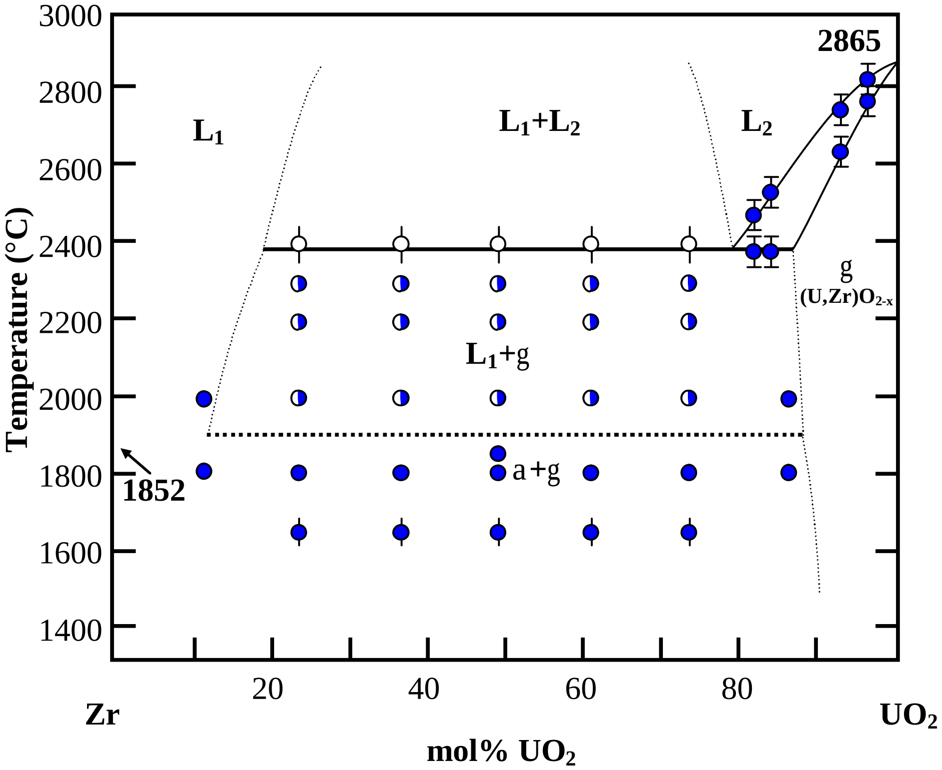

Fig. 1.4. Phase diagram of a pseudobinary Zr–UO_2 section /9/

There is an evident controversy in the current understanding of the liquid immiscibility in the molten suboxidized corium. On one hand, in a number of pseudobinary diagrams it is presumed that there is a miscibility gap with a monotectics temperature about 2400°C between UO_2 and α-Zr(O) with different Zr oxidation degree (Fig. 1.1.); on the other, the liquid phase immiscibility has not been found in the studies of uranium oxide dissolution kinetics in the oxidized zirconium /6/ (Fig. 1.2.). It should be noted that in an earlier work /8/ Politis suspected stratification in the domain close to the one considered in /6/. This apparent controversy of the data can be explained by the fact that in case of a miscibility gap with sharp boundaries even a minor shift from the section confining the gap can result in a departure from the immiscibility domain (for explanations see Fig. 1.5).

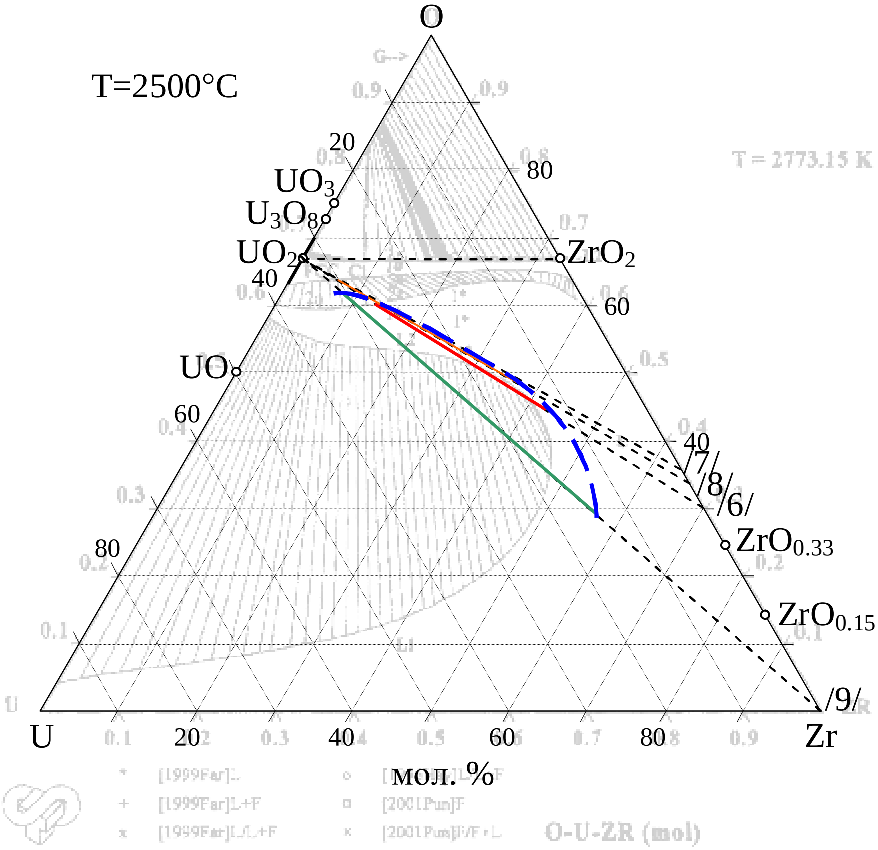

Fig. 1.5. Explanation to the experimental data of /6-9/

Until recently the majority of publications have considered the binary system of UO_2-ZrO_2 (Fig.1.6-1.12) /10-17/, which in terms of zirconium oxidation degree corresponds to the oxidized molten corium. The continuous reciprocal solubility between uranium and zirconium oxides was established. Due to the importance of this section for the analysis of phase equilibrium in the ternary system of U-Zr-O, different versions of phase diagrams and comments to them are presented below.

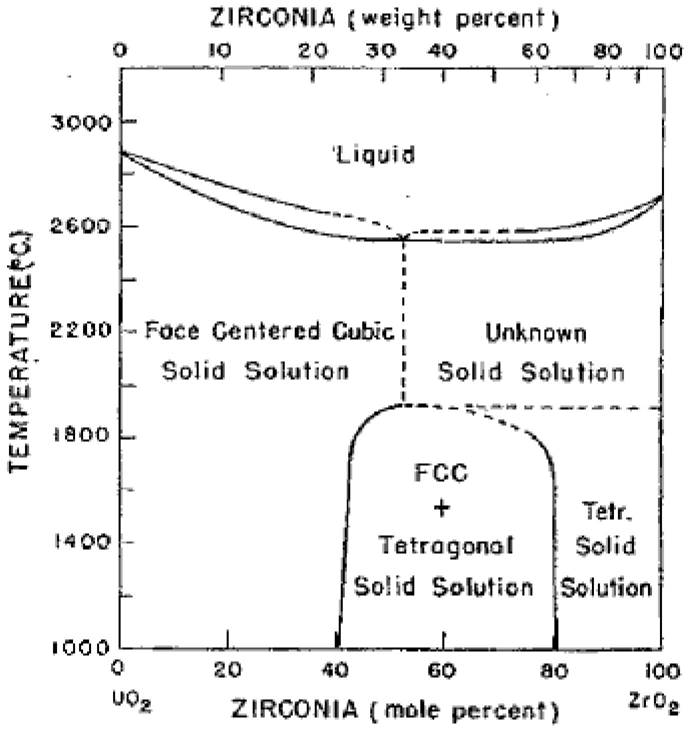

Fig. 1.6. Phase diagram of the UO_2-ZrO_2 system/10/

The first version of the UO_2-ZrO_2 phase diagram was put forward by Lambertson and Mueller /10/ (Fig. 1.6). UO_2 of > 99.9% purity and high-purity ZrO_2 were used as initial components. The compacted oxidic mixtures were sintered in the temperature range of 1600-1750°C in the electric furnace having H_2 atmosphere. Some mixtures were subjected to milling, compacting and heating, which was repeated up to three times. XRF and chemical analysis were used in the study. New compounds were not found, but extended regions of solid solution were detected in the UO_2-ZrO_2 system. It was determined that UO_2-based cubical solid solution extends up to 53 mol. % ZrO_2. The lattice parameters of this solid solution range from 5.46 to 5.32 Å, depending on the ZrO_2 content increase. Authors believe that boundaries of the ZrO_2-based tetragonal solid solution lie within 53 - 100 mol. % ZrO_2. In the work an assumption was made that at temperatures higher than 1900°C ZrO_2 has a polymorphic crystal structure, different from the monoclinic or tetragonal.

An attempt to specify the high-temperature part of the sub-solidus domain was made in /11/. The mixture of UO_2 and ZrO_2 was compacted into high-density pellets and heated in argon at 2300°C in Zr crucibles, quenching to the ambient temperature was conducted. XRF was used as the basic method of the study (Seiger high-temperature diffractometer).The author believes that the continuous solid solution above 1950°C and the presence of a boundary between tetragonal and monoclinic phases (Fig. 1.7) are the principally new features of the diagram in comparison with /10/. The author found a homogeneous phase in the UO_2-ZrO_2 system at 2300°C, which extended from 0 to 100 mol. % ZrO_2. The crystallized cubic structure of the pure UO_2 changes continuously to the tetragonal structure of ZrO_2. In case of specimens having 53-54 mol. % of ZrO_2 at temperatures above 2300°C the structure remains cubic, but it is tetragonal in cases with a higher ZrO_2 content.

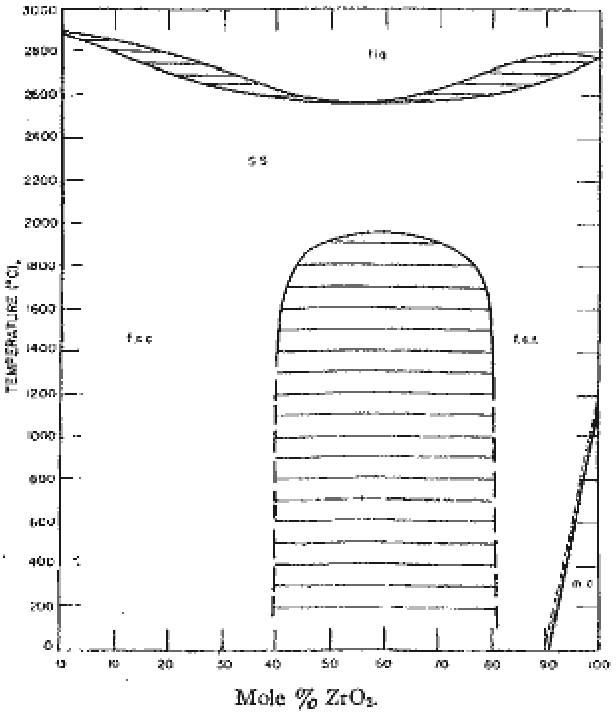

Fig. 1.7. Phase diagram of the UO$_2$-ZrO$_2$ system/11/

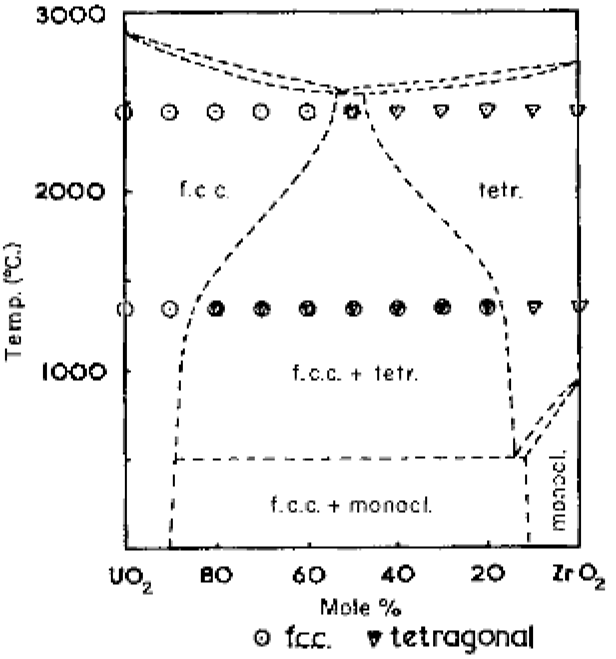

Fig. 1.8. Phase diagram of the UO2-ZrO$_2$ system/12/

A systematic study of subsolidus domain was made by Evans in /12/. The author used some data of publication /10/ and his own experimental data for constructing a phase diagram of the UO$_2$-ZrO$_2$ system. High-purity UO$_2$ and non-stabilized monoclinic form of ZrO$_2$ (lime-free) were used as initial components. Mixtures of these oxides were compacted into pellets and melted in the helium atmosphere in the solar furnace, after that the prepared specimens were conditioned in furnaces having helium atmosphere during 250 hours at 1350°C. Following this the furnace with specimens was cooled from 1350°C to 1100°C within 15 min, from 1100°C to 900°C within 29 min, and from 900°C to 700°C within 62 min. The specimens were removed from the furnace after 18 hours from the cooling start and subjected to the XRF analysis using Norelco diffractometer with Cu_{K_α}-

radiation. In the UO_2-ZrO_2 system the presence of extended solid solution domains based on each of the oxides was confirmed; a very narrow two-phase domain was found in a high-temperature domain near the eutectic point (Fig. 1.8). Solid solutions were identified as face-centered cubical and face-centered tetragonal on sides of UO_2 and ZrO_2, respectively. At temperatures below the eutectics (2550°C) about 45 mol. % of ZrO_2 is dissolved in UO_2 and vice versa. At 1350°C the solubility decreases, and it was found to be less than 15 mol. %. The tetragonal form of ZrO_2 cannot be stabilized by the UO_2 addition; the transition from tetragonal to the monoclinic phase in the ZrO_2-enriched solid solution takes place in the range from 940°C to the room temperature.

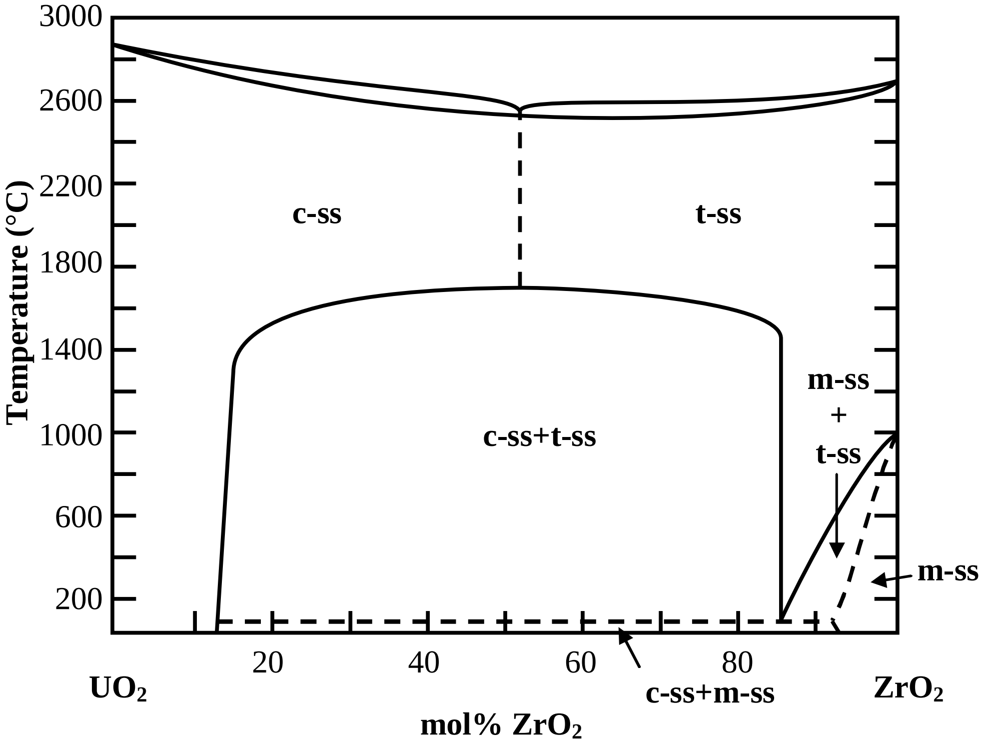

Fig. 1.9. Phase diagram of the UO_2-ZrO_2 system/13, 14/

Authors of publications /13, 14/ have proposed a UO_2-ZrO_2 phase diagram, which was different from versions /10/ and /11/ by the extended two-phase region (Fig. 1.9). The system was studied using the specimens, which were prepared by melting compacted mixtures of oxidic powders in the electric arc furnace in the atmosphere of chemically pure argon. The molten specimens were annealed in the furnace with a tungsten heater and quenched by ejecting from the heating zone onto the water-cooled tray of the furnace. Most useful for the phase diagram clarification was the microstructural analysis, which complemented the data of XRF, especially in the ZrO_2-rich domain. The studies show that the region of coexisting tetragonal and cubical solid solutions extends from 13.5 to 86 mol. % ZrO_2; and up to 1400-1500°C, it almost does not depend on temperature. The method of dilatometry was used to evaluate the temperatures of polymorphic transformation of ZrO_2-based solid solutions, which was caused by the ZrO_2 transition from the monoclinic to tetragonal modification and back. Added UO_2 brought the temperature of ZrO_2 polymorph transformation down from 1040°C (for pure ZrO_2) to 140°C (for a specimen containing 14 mol. % UO_2). The solid solution boundaries have been specified. It has been confirmed that UO_2 and ZrO_2 form a continuous series of solid solutions having cubical structure of UO_2 in the concentration interval from 0 to 51.3 mol. % ZrO_2 and having tetragonal structure of ZrO_2 in the concentration interval from 51.3 to 100 mol. % ZrO_2. Below 1675°C, at room temperature, the solid solution decomposes into two solutions – one, rich in UO_2, containing 13.5 mol. % ZrO_2, another, rich in ZrO_2 and containing 86 mol. % of ZrO_2. UO_2 added to ZrO_2 reduces the temperature of ZrO_2 polymorphic transformation, but it is practically impossible to stabilize the tetragonal modification of ZrO_2 with uranium dioxide, because at T=1000°C the tetragonal solid solution decomposes to monoclinic ZrO_2.

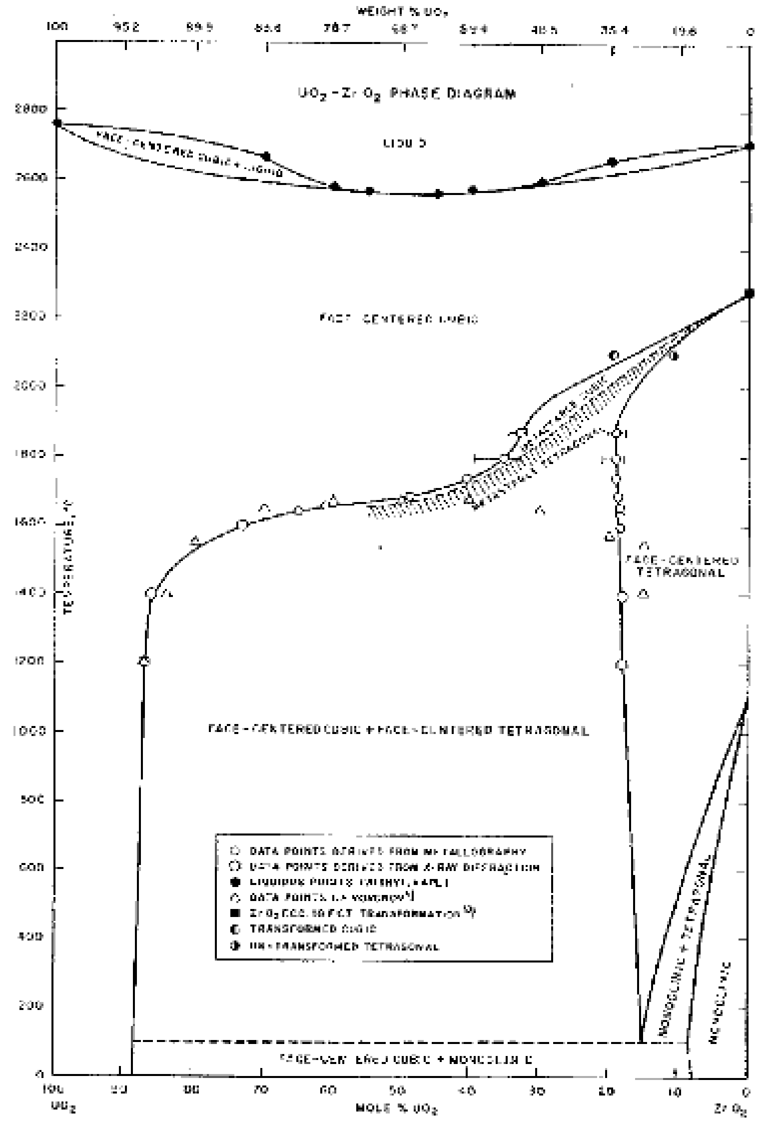

Fig. 1.10. Phase diagram of the UO_2-ZrO_2 system**/15/**

In /15/ a version of the UO_2-ZrO_2 phase diagram is proposed, for which the authors used their own data, i.e. those published in /11/ and /14/ for the solid phase region below 1200°C and liquidus points from unpublished data of Wisnyi L.G. (Knolls Atomic Power Laboratory). UO_2 produced by reduction of UO_3 and HfO_2-free ZrO_2 were used as initial components. The compacted mixtures were annealed at 1725°C in hydrogen until solid solutions of UO_2-ZrO_2 were formed. Then the specimens were crushed, compacted into pellets and exposed at 1725-1750°C in hydrogen during 72-110 h. The microstructural and X-ray studies of the specimens treated at lower temperatures (1875-1600°C) and quenched enabled to identify a two-phase domain, which contains two coexisting tetragonal phases with different lattice parameters. One of the phases, UO_2 – rich, has a textured structure, another – an equiaxial and non-textured one. These data on the specimen structure contradict the data of other authors, which assert that at high temperature the UO_2-ZrO_2 system has a continuous transition from the cubic structure of UO_2 to the tetragonal structure of ZrO_2 (Fig. 1.10).

In accordance with authors of /15/ phase diagram of the UO_2-ZrO_2 system has the following specific features:

1. There is a third polymorphous modification of ZrO_2 having a cubic face-centered structure; in the UO_2-ZrO_2 system at T > 2300°C continuous solid solution is formed, which has a cubic structure from UO_2 to ZrO_2.
2. Below 2300°C in the domain adjacent to ZrO_2 a two-phase region exists, in which a cubic face-centered UO_2-rich solid solution and tetragonal face-centered ZrO_2-based solid solution stay in equilibrium; at 1690°C this region extends from 50 to 19 mol. % UO_2, it narrows as the temperature increases. The equilibrium cubic phase is not fixed by quenching, at cooling it turns into a metastable tetragonal phase.
3. Below 1660°C the two-phase domain widens sharply, especially in the UO_2-adjacent region; at 1200°C the solubility of ZrO_2 in cubic UO_2 is only 13-14 mol. %, and UO_2 solubility in tetragonal ZrO_2 is 14-17 mol. %. The tetragonal solid solution undergoes monoclinic transformations at 140-1040°C, and cubic UO_2-based solid solution exists up to the room temperature level.

Paper /16/ examined the solubility of UO_2-ZrO_2 solid solutions in the fluoride melt Li_2BeF_4 in nickel vessels at 500-700°C in the helium atmosphere. In accordance with /17/ solid solutions are thermodynamically stable in the UO_2-ZrO_2 system at 500-700°C. Experimental results show that equilibrium oxidic phases crystallize from the melt not as solid solutions, but as nearly pure cubic UO_2 (ruby-red) and monoclinic ZrO_2 (colorless). X-ray diffractometry has confirmed the presence of exclusively pure UO_2 and ZrO_2 (Fig. 1.11).

The high-temperature domain of the UO_2-ZrO_2 system was specified by Bottomley and Cooquerelle (ITU), who applied the method of laser pulse heating and measured characteristic temperatures by the high-speed mono- and polychromatic pyrometry (solidus at heating, liquidus – at cooling) /17/ (Fig. 1.12).

As it is evident from the presented diagrams, there is a considerable difference in the interpretation /10-17/ of phase equilibrium in the subsolidus domain, and also in the close-to-eutectic region (in accordance with some authors) or azeotrope point (in accordance with others). The shape of liquidus curve implies the presence of a domain of solid solution immiscibility under the solidus line; the domain must be quite close to the solidus of the system (e.g. in /12/). Therefore, it can be concluded that at present there are principle differences in understanding even the most intensively studied section of the U-Zr-O system; each of those differences can influence the prognosis of phase equilibria in the direction of metallic components.

A great number of publications deal with the U-O system (see the reference list on pp. 292-294 in /18/). Many authors share the opinion that chemistry of the uranium-oxygen system is very complex due to the formation of oxides with variable compositions and non-stoichiometric oxides. There are also assumptions about the existence of homologous series of uranium oxides U_nO_{2n+2}, where n=2…4.

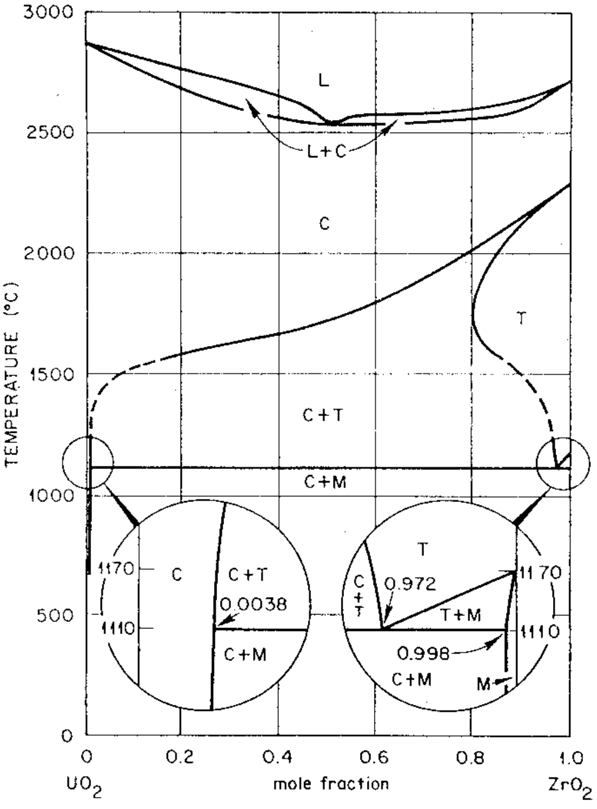

Fig. 1.11. Phase diagram of the UO_2-ZrO_2 system/16/

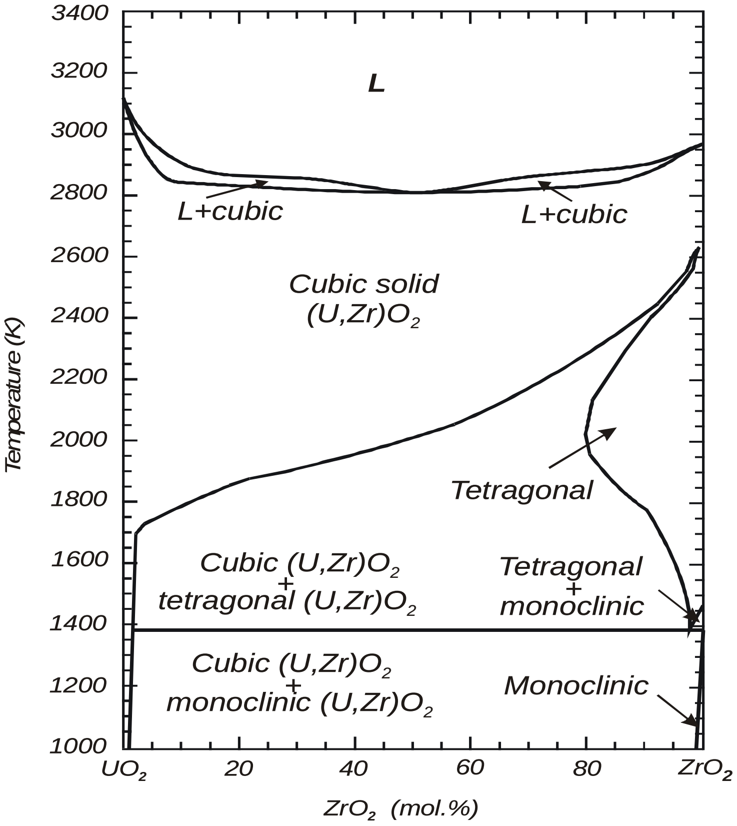

Fig. 1.12. Phase diagram of the UO_2-ZrO_2 system/17/

The most complete presentation of the subsolidus domain of the phase diagram is given in the overview /19/ (Fig. 1.13). Later the data were specified and updated, but the changes have not been principal.

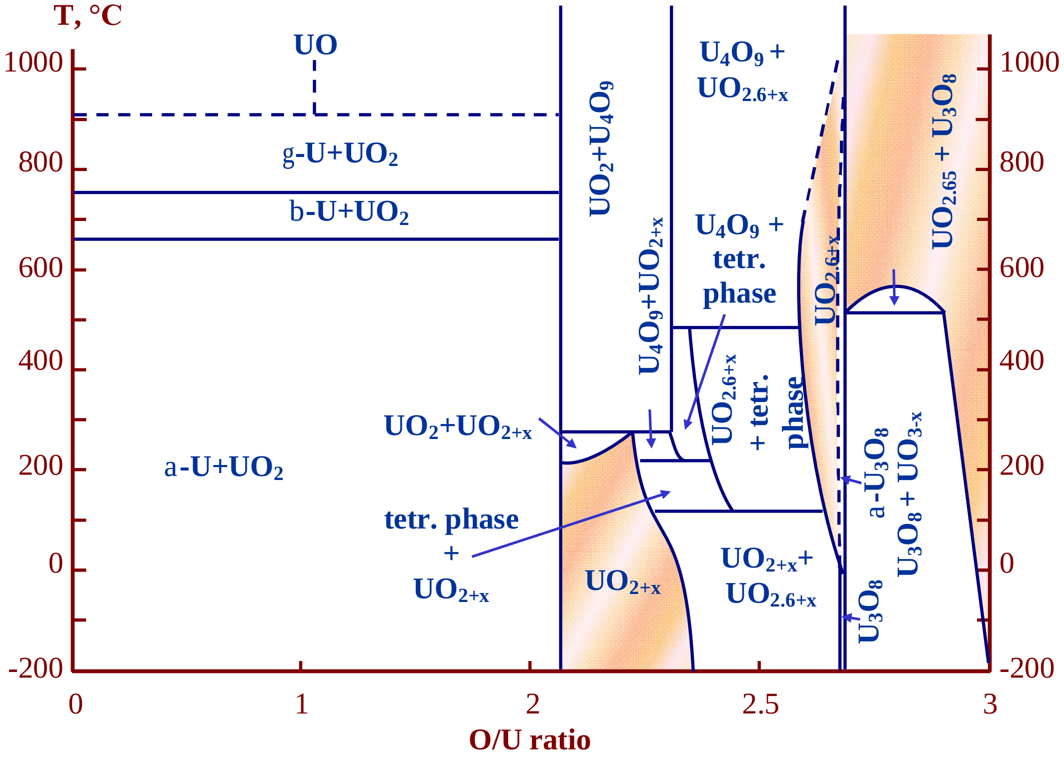

Fig. 1.13. Phase diagram of the U-O system /19/

The high-temperature part of the system also attracted the attention of many researchers.

Fig. 1.14 shows the phase diagram of the U-UO_2 system, which was constructed by Edwards and Martin /20, 21/.

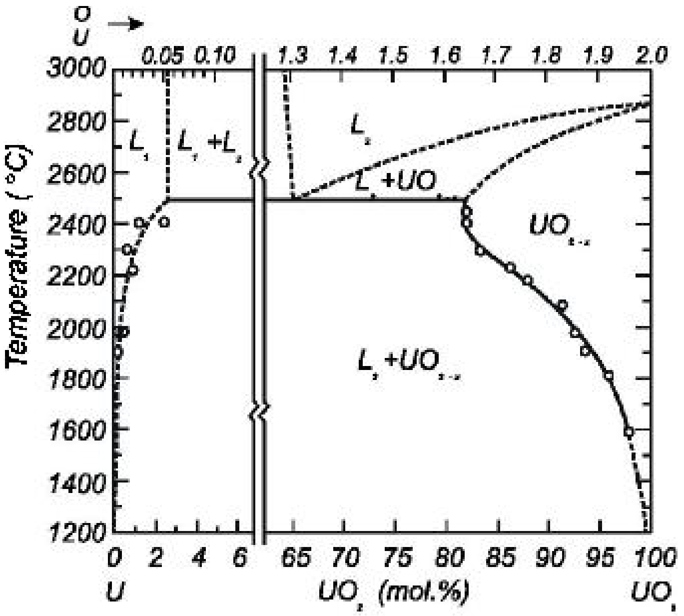

Fig. 1.14. Phase diagram of the U-UO_2 system /20, 21/

A peculiarity of this version of the diagram is a widening of the under-stoichiometric UO_2 region at the temperature growth and presence of the miscibility gap in the liquid state. Also noteworthy is an extremely low solubility of oxygen in liquid uranium, e.g. at the 2500 °C it is about 2.6 at.% O (see the top scale).

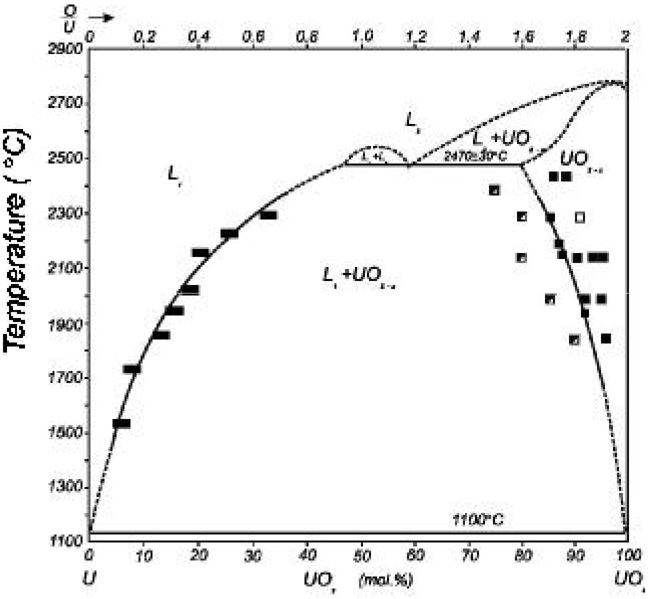

Fig. 1.15. Phase diagram of the U-UO_2 system /22/

Phase diagram of the U-UO_2 system (Fig. 1.15) constructed using the data of Guinet practically coincides with the one considered above in the domain of under-stoichiometric UO_2, but differs by substantial solubility of O in liquid U, which composes up to 30 at. % O (see the top scale) at 2300 °C /22/.

In the diagram of Edwards and Martin an extensive miscibility gap of L_1 and L_2 liquids lies within the interval of 2.5 - 65 mol.% UO_2 and has the height over 500K (Fig. 1.14). In the diagram of Guinet et al. the length of immiscibility domain is only 12 mol.% UO_2, and its height is assumed to be only about 100K (Fig. 1.15). Substantial deviations of experimental data on the degree of oxygen solubility in molten uranium in the U-UO_2 phase diagram are reflected as different widths of the miscibility gap.

Nevertheless, a later publication confirms the presence of a wider immiscibility domain /2/ (Fig. 1.16).

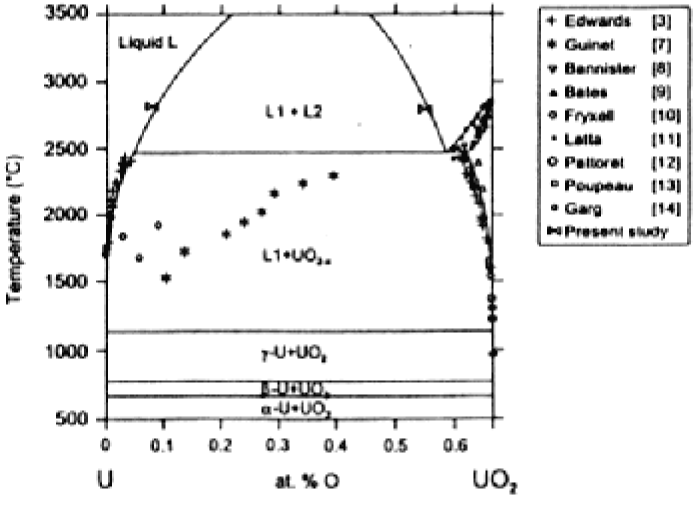

Fig. 1.16. Phase diagram of the U-UO_2 system/2/

A binary diagram of the Zr-O system has also been studied by many authors (see the reference list on pp. 187-189 in /18/). Most-studied in the system are ZrO_2 phases in the monoclinic (baddeleyite), tetragonal and cubic modifications. There are publications reporting solid solution Zr in ZrO_2, solid solutions of oxygen in α-Zr and in β-Zr, phases Zr_6O and Zr_3O. The data on existence of ZrO, Zr_2O, Zr_2O_3 phases are doubtful.

Fig. 1.17 shows two earlier versions of the Zr-O phase diagrams, which are based on publications /23/ and /24/, their main difference is the final solubility of oxygen in zirconium. In /25/ the emphasis is made on the study of the oxygen part of the diagram (Fig. 1.18).

In late 1970s the diagram was specified (point of eutectics, solubility limits of oxygen in zirconium) and new data in the high-temperature region (from the ZrO_2 side) have been provided /26/ (Fig. 1.19).

More detailed studies of high-temperature region and the domain of oxygen solid solutions in α-Zr were carried out by the authors of /27/ (Fig. 1.20).

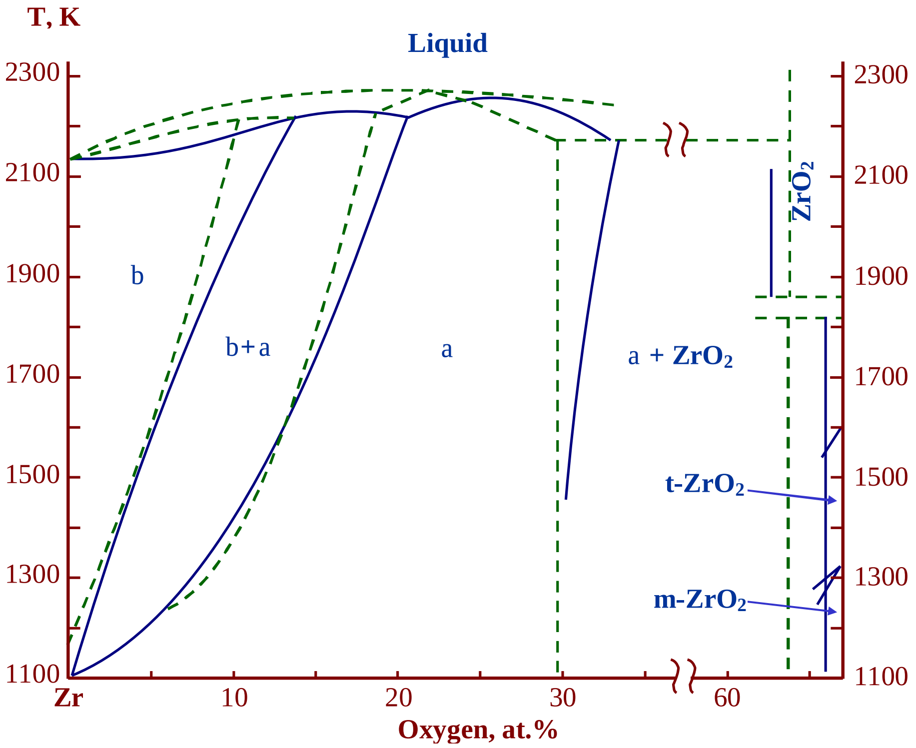

Fig. 1.17. Phase diagram of the Zr-O system: /23/ and /24/

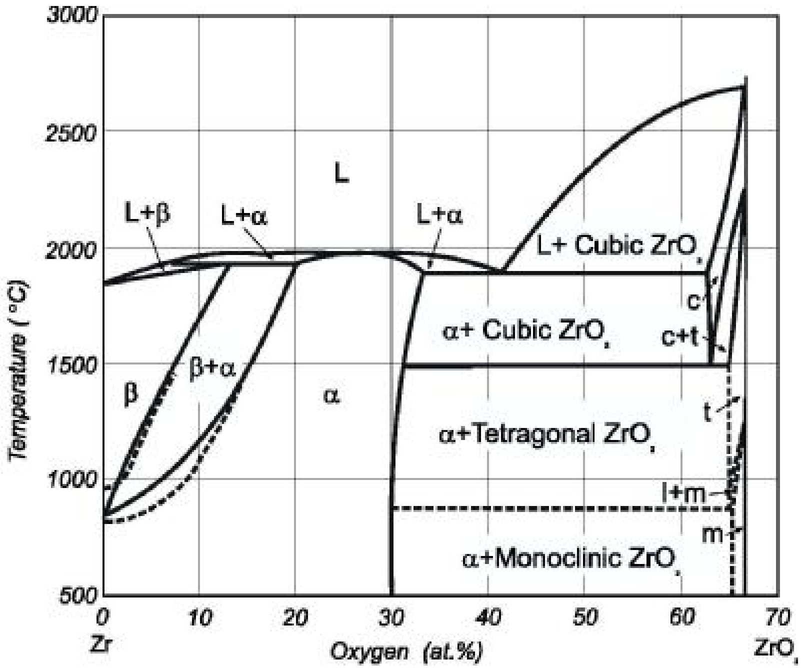

Fig. 1.18. Phase diagram of the Zr-O system /25/

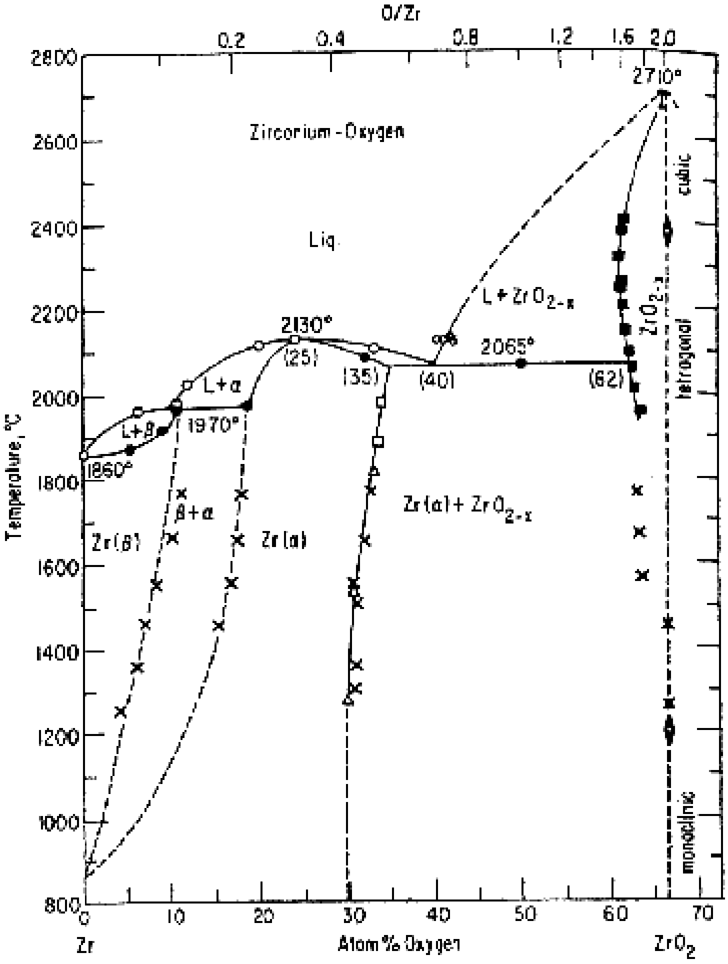

Fig. 1.19. Phase diagram of the Zr-O system /26/

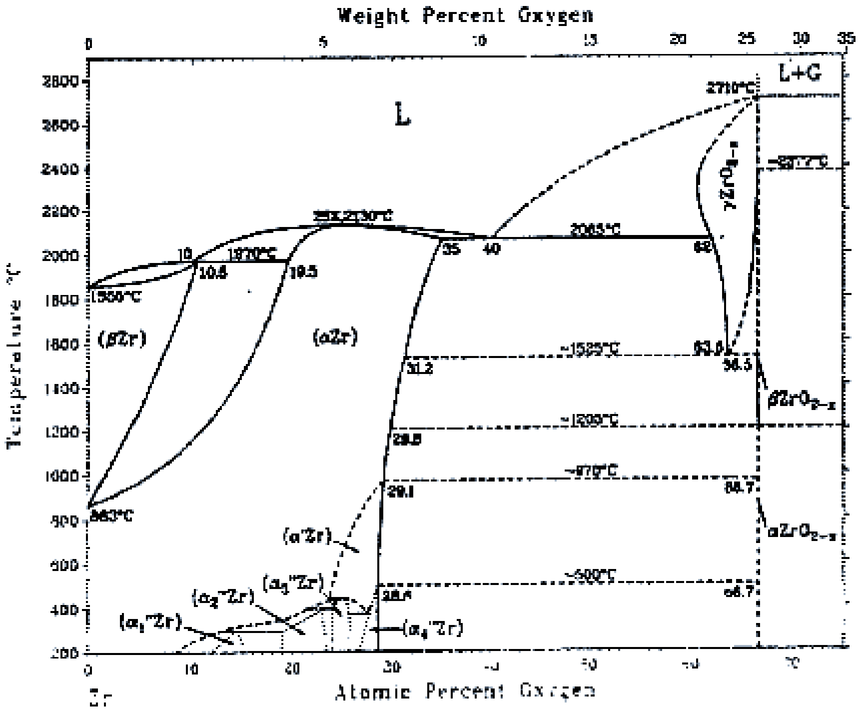

Fig. 1.20. Phase diagram of the Zr-O system /27/

Another interesting work is /28/. Its authors conducted the thermodynamic modeling of phase equilibria in the Zr-O system (Fig. 1.21). Of special importance is the prediction of temperature limits for the Zr_6O and Zr_3O existence and the final solubility of α-Zr-based solid solution in these compounds.

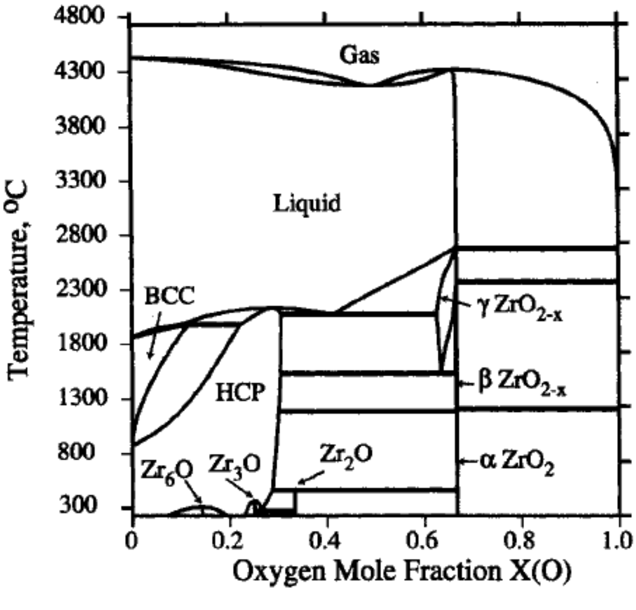

Fig. 1.21. Phase diagram of the Zr-O system /28/

Like in the case of UO_2-ZrO_2 and U-O systems, in spite of numerous studies, there still are unanswered questions about the limits of the phases existing in the system and even about new phases not plotted in any of the versions of this diagram

The binary system of U-Zr has also been a subject of many studies. A detailed overview of phase equilibria in this system is given on pp. 418-421 in /29/. Phase diagram of this system was constructed in /30/ and in /32/ (Fig. 1.23). A good agreement of the diagram versions should be noted.

A miscibility gap in this system has not been found. But we should take into account the immiscibility domain of solid solutions in the U-Zr system, which potentially, if a third component is added, can cross the liquidus line (Fig. 1.22 and Fig. 1.23). Another significant factor is the existence of a single compound in the system – δ phase having a wide homogeneity area. But at a rather high concentration of admixtures (oxygen or nitrogen) the homogeneity domain harrows sharply until δ phase disappears /33/.

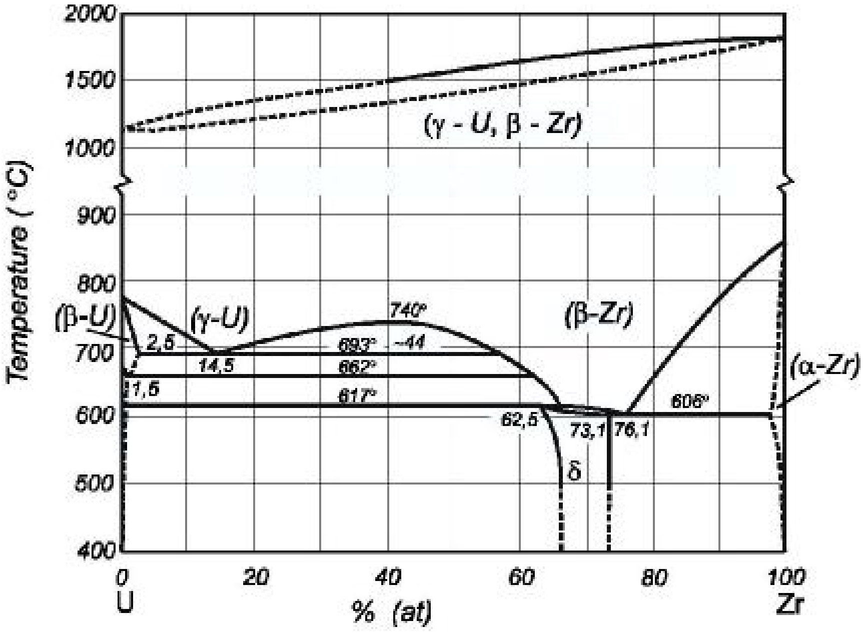

Fig. 1.22. Phase diagram of the U-Zr system /30/

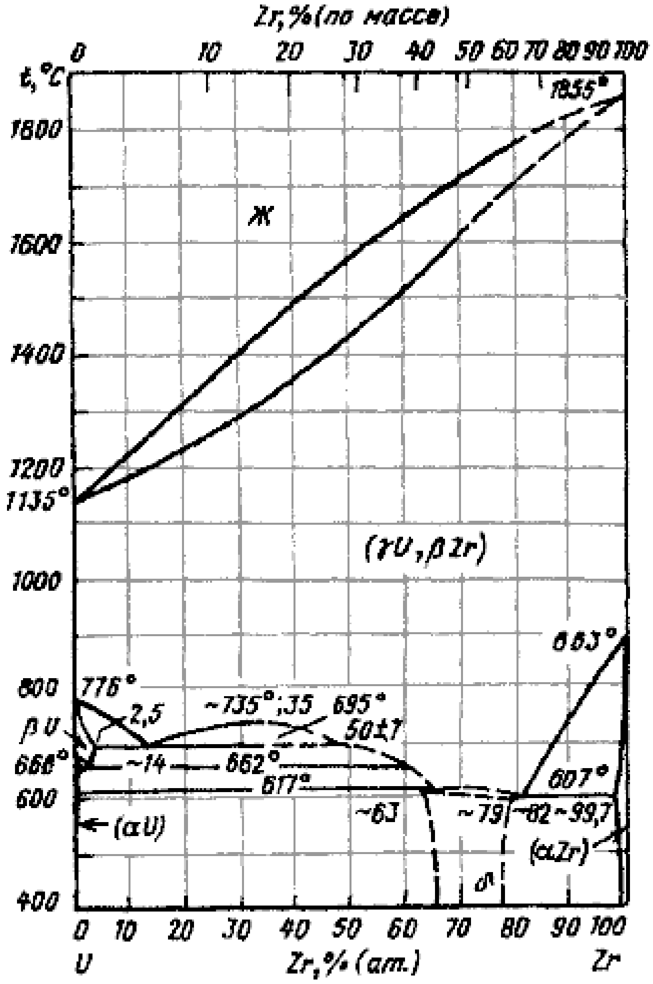

Fig. 1.23. Phase diagram of the U-Zr system /32/

For the analysis of experimental results and prediction of phase equilibria in the U-Zr-O system the GEMINI-2 code and NUCLEA database/34/ are used. Fig. 1.24 shows the calculated isothermal section of the considered ternary system, in which the experimental points are taken from publications. The analysis of data indicates the necessity to specify both phase boundaries and the boundaries of the miscibility gap, the existence of which has been confirmed in publications /2, 6, 8, 9, 20-22/.

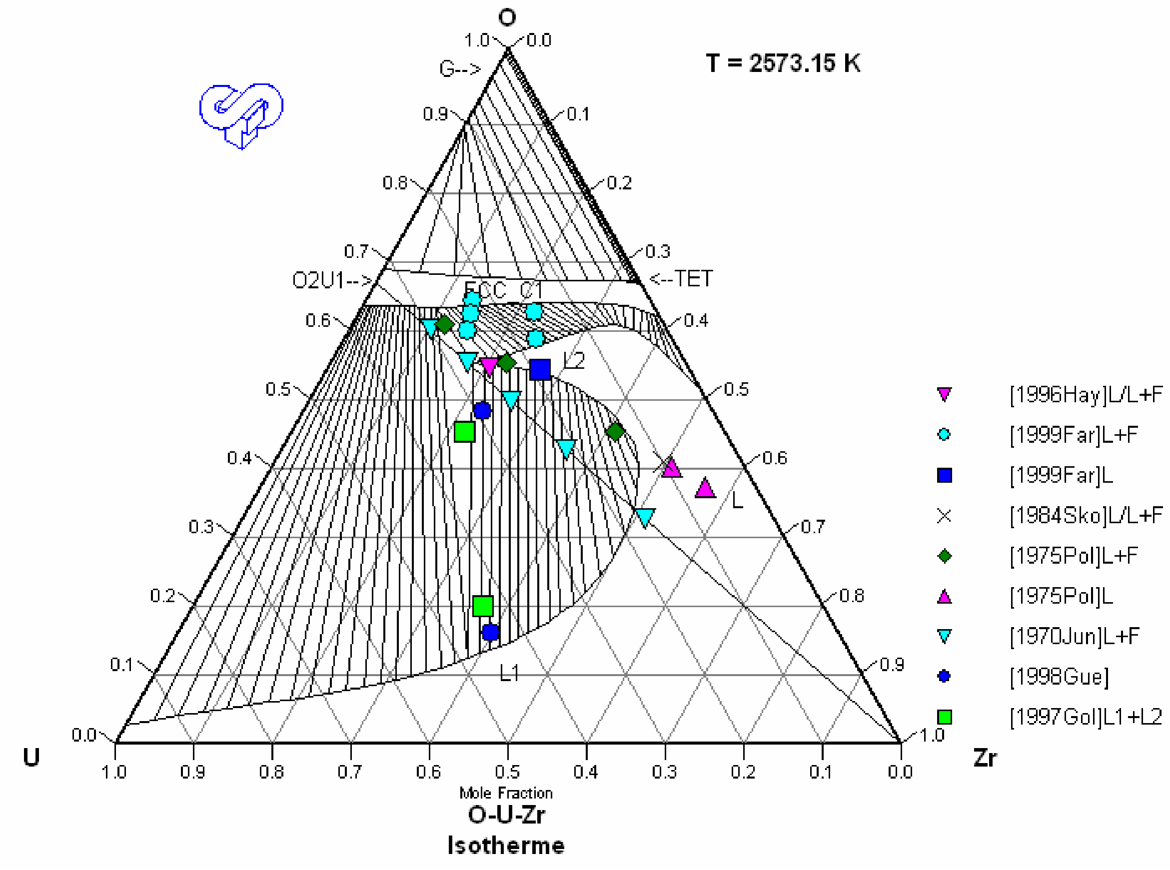

Fig. 1.24. U-Zr-O diagram isothermal section at 2573.15 K

The analytical overview of the published data on phase equilibria in the U-Zr-O system in comparison with the authors' own data is presented in /35/. It is shown that the miscibility gap in the considered isothermal section is considerably smaller than the predicted one (see Fig. 1.24) and a conclusion is made on the single liquid for compositions having the Zr oxidation index higher than 30 %, which are typical for the VVER/PWR severe accident conditions.

2. Experimental methodologies and facilities

The metal-oxidic systems are studied using the original methodologies, because the conventional methods cannot be applied for the whole range of compositions, especially in the high-temperature region. But some data, e.g. solidus temperatures, can be provided by the classical thermoanalysis methods. The application of an integrated complex of methods increases the reliability and accuracy of results.

2.1. Visual polithermal analysis in a cold crucible

During studies of the binary oxidic systems the liquidus temperature was determined using the original VPA IMCC methodology. Rasplav-3 tests facility with high-frequency induction heating was developed and built for experiments with metal-oxidic melts. Pretest experiments proved the efficiency of the methodology.

Specific features of the methodology for determining liquidus temperature of metal-oxidic systems are as follows:

- Molten pool is established on a thin water-cooled bottom
- The melt is homogenized and maintained in the superheated state
- Molten pool depth and bottom crust thickness are measured
- Local surface cooling of the superheated molten pool is performed by moving the pool vertically up in the inductor, at which the surface temperature and top view are registered. When the pool surface is beyond the inductor, its local cooling results in a solid phase formation on the surface
- Posttest frame-by-frame analysis of the video recording and determination of the minimum temperature of melt coexisting with solid phase is made
- Posttest physicochemical analysis of melt samples and determination of their composition is made (if required)

Fig. 2.1 shows an example of experimentally measured thermogram with images of molten pool surface. Fig. 2.2 shows the furnace schematics.

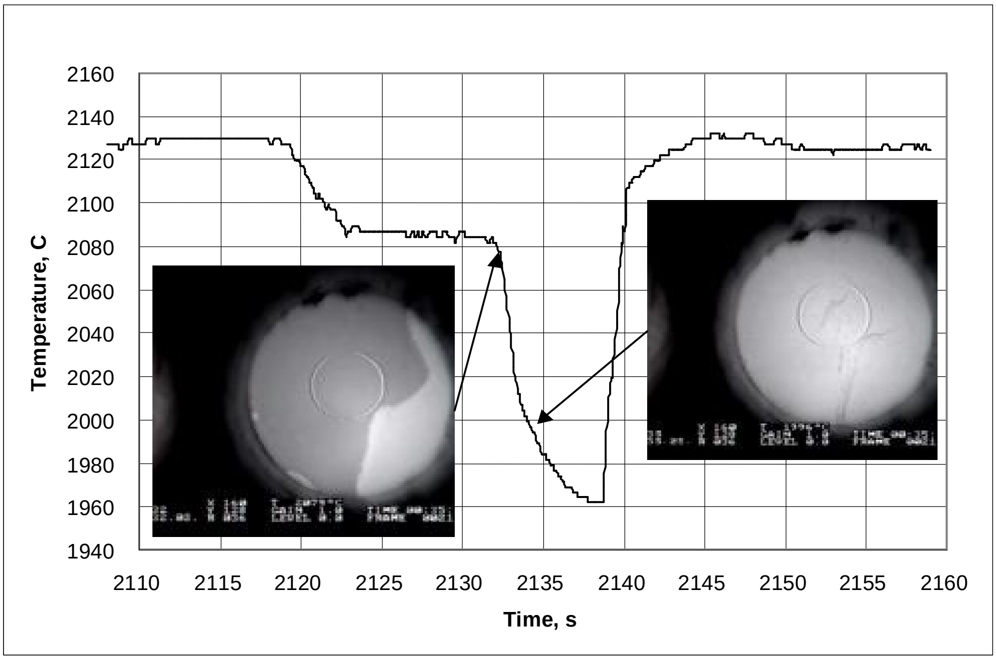

Fig. 2.1. An example of thermogram with images of the molten pool surface

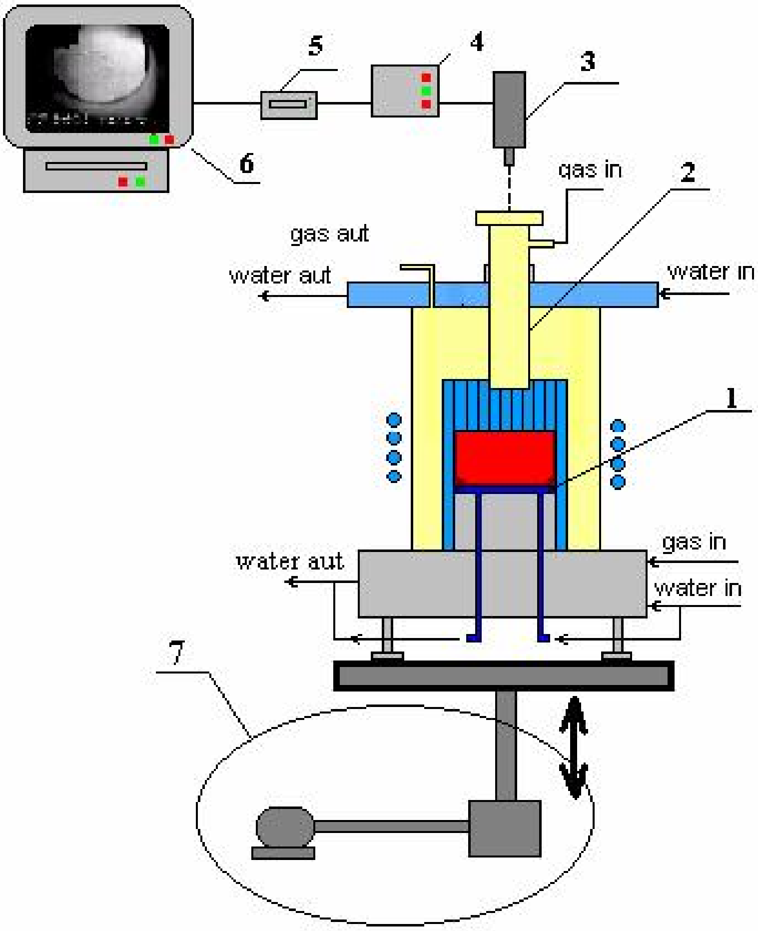

Fig. 2.2. Furnace schematics

1 – Water-cooled calorimeter; 2 – Water-cooled pyrometer shaft; 3 – Pyrometer combined with video camera; 4 – Data acquisition system; 5 –Video insert; 6 –Monitor/video recorder; 7 – Drive for vertical movement of the crucible.

The molten pool surface was monitored using the video camera combined with pyrometer (3). Device (5) enabled to insert measured temperatures, time and position of the pyrometer sighting spot into each video frame with a 50 Hz frequency; the recording was performed using video recorder (6). Temperature of the melt surface was measured by the spectral ratio pyrometer RAYTEK MR1-SC. Video camera was focused on the surface of molten pool through the pyrometer shaft, camera sighting spot was 22 mm in diameter. The pyrometer sighting spot was about 6 mm in diameter. The inner diameter of the cold crucible was 38 mm. The unrecorded annular zone along the crucible wall was 8 mm wide.

2.2. Differential method of liquidus and solidus temperature measurements in the hot crucible

Experimental facility “Tigel” of Kurchatov Institute was used in the experiments (Fig. 2.3).

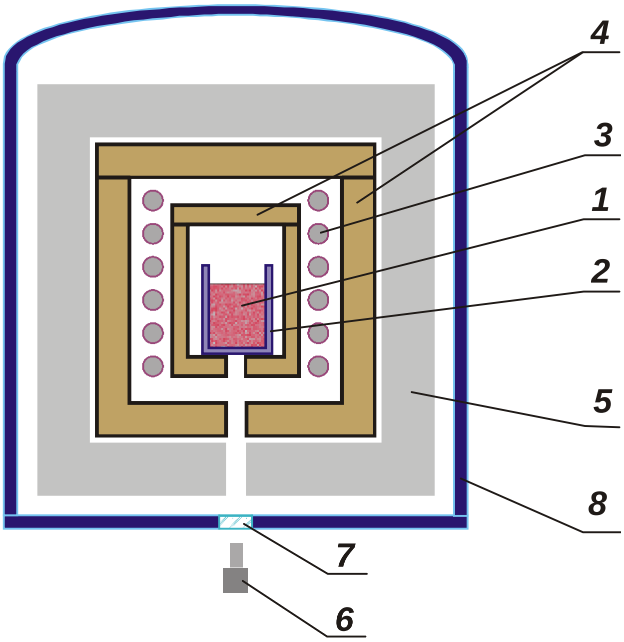

Fig. 2.3. “TIGEL” Experimental facility

1-Corium; 2-Crucible; 3-Heater; 4-Thermostats; 5-Thermal insulation; 6-Pyrometer; 7-Window; 8-Vessel

The methodology for measuring liquidus and solidus temperatures is as follows:

- A molten pool of specified composition is produced, superheated and homogenized in a refractory crucible;
- After the pool homogenization the heating is disconnected, temperature of the melt is measured by a pyrometer;
- Posttest analysis of the thermogram includes temperature differentiation, which enables to register thermal phenomena.

A graphite ohmic heater (3) was used during the experiments, its generator had the power of 4.5 kW and 50 Hz frequency. The temperature was measured by the pyrometer developed in the Institute of High Temperatures of the Russian Academy of Sciences. The pyrometer can register radiation in the wavelength range of 0.9 ÷ 1.1 μm. The error of temperature measurements is ~ 50°C. The main contribution into it is the pyrometer calibration accuracy.

Sintered corium pellets were used as the charge. In some experiments metallic zirconium and fine zirconium powder were added. Crucibles were fabricated from tungsten by the gas reduction technology (for CD1, 2 experiments). For CD3-5 tests we used crucibles made from graphite, the inner surface of it was coated with zirconium carbide ZrC. After charge installation the crucible was covered with a tungsten, tantalum or graphite lid.

In these experiments a serious problem is posed by the crucible material, which should not actively interact with the studied corium composition at high temperatures. Tungsten has proved its applicability for experiments with coria having a high content of oxygen (>58 at.%). When oxygen concentration decreases, the metallic component of corium starts to interact actively with tungsten, for this reason tungsten crucibles are not suitable for these experiments.

It is known that graphite crucibles were used for Zr melting in the early days of metallurgy. A carbide layer formed on the boundary between graphite and molten zirconium reduces the rate of carbon penetration into the melt bulk. Tests of crucibles manufactured from different brands of carbides were performed. Their results can be summarized in a following way:

- If the graphite density is below 1.6 g/cm^3, zirconium penetrates through the graphite wall of the crucible completely.

- If the graphite density is above 1.7 g/cm^3, a rather dense layer of zirconium carbide is formed on the inner surface of the crucible, which enables accident-free experiments.

Liquidus or solidus temperature is taken as the start of the thermal process registred from the curve of temperature reduction rate versus temperature. Fig. 2.4 shows an example of the curve.

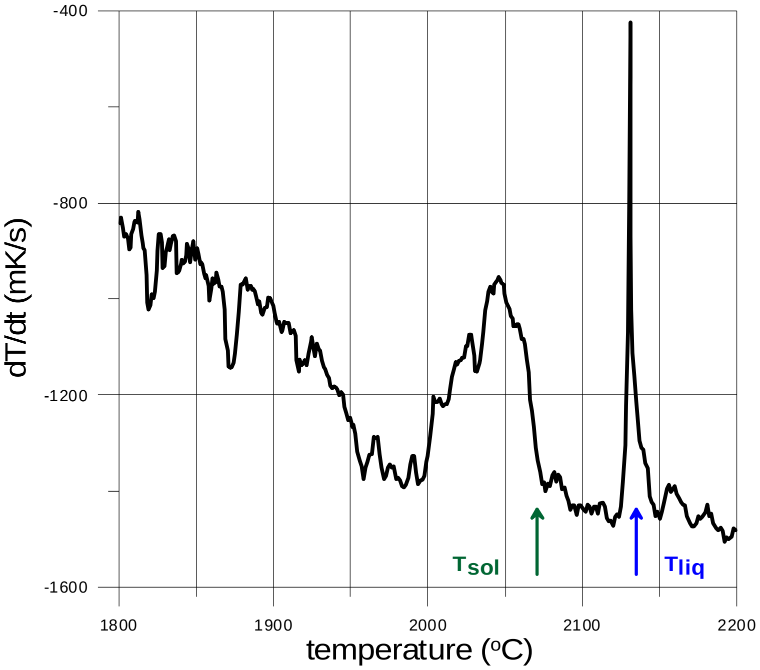

Fig 2.4 Melt cooling rate versus temperature in CD-3 test

2.3. Visual polithermal analysis in the Galakhov microfurnace

Solidus temperature was also determined using the method of visual polithermal analysis in the Galakhov microfurnace /36/.

The microfurnace schematics and experimental methodology are described in detail in /37/. Because of the interaction between samples and their holder (molybdenum, tungsten, iridium) the liquidus temperature measurements of the metal-oxidic systems were not feasible. A layer of ZrC was added on molybdenum holders by the magnetron sputtering, after that the holders were heated at 2000°C during 1 min. This measure did not provide an effective improvement. We should note that for some samples even solidus temperature measurements were not completely correct, because their interaction with holder was registered during heating.

3. Experiments and results

3.1. Analysis of initial charge materials

Before the experiments all charge components were analyzed for the content of the main component, and thermogravimetry was used to determine oxygen/uranium ratio in the UO_2 powder, it was 2.0 /38, 39/.

Table 3.1 gives the charge composition.

Table 3.1. Charge composition

Components	Concentration of the main component, %	Admixtures, mass. %	Note
UO_2 powder, dispersivity <200 µm	UO_2>98.9	Zr<0.79; Fe<0.30; As<0.0003; CuO<0.01; phosphates<0.002; chlorides<0.003.	Certificate data, thermogravimetry, XRF
ZrO_2 powder, dispersivity <100 µm	(ZrO_2+HfO_2) >99.4	Al_2O_3<0.03; Fe_2O_3<0.05; CaO<0.03; MgO<0.02; SiO_2<0.2; TiO_2<0.1; P_2O_5<0.15; (Na_2O+K_2O)<0.02.	Certificate data
Metallic Zr (alloy Nb-1)	Zr >99.0	Nb<1.0	XRF
Metallic U	U>97.3,incl. U^{238} – 99.72 U^{234} – 0.002; U^{235} – 0.28	Zr<2.7	XRF and gamma-spectrometry

3.2. Experimental matrixes

Tables 3.2 and 3.3 present experimental matrixes of CORD and CD series; their methodologies are explained in sections 2.1 and 2.2.

Table 3.2. CORD experimental matrix

Experiment	Charge composition, at.%			Mass, g	Objective
	U	Zr	O		
CORD28-I	8	52	40	300.0	T_{liq} measurement
CORD28-II	13	43	44	423.9	
CORD29	20	17	63	400.0	
CORD34	22	33	45	446.1	
CORD37	33	27	40	505.2	$T_{liq,}$ tie-line measurement
CORD42	40	25	35	534.9	
CORD41	60	-	40	533.3	

Table 3.3. Experimental matrix of the CD series

Experiment	Charge composition, at.%			U/Zr	Objective
	U	Zr	O		
CD1	22.9	19.1	58.0	1.20	T_{liq} measurement
CD2	25.7	15.8	58.5	1.63	
CD3	13.0	43.0	44.0	0.30	
CD4	8.0	52.0	40.0	0.15	
CD5	16.0	36.0	48.0	0.44	

It is clear from Table 3.3 and Fig 3.1 that CD experiments were made for compositions close to the section corresponding to the quasi-binary diagram UO_2-$ZrO_{0.43}$. Compositions of the CORD series cover a wide range of concentrations; they are located close to the assumed miscibility gap boundary in accordance with /1/. For the sake of experimental data cross-verification the compositions of two CORD experiments (28-I and 28-II) are the same as CD 4 and 3.

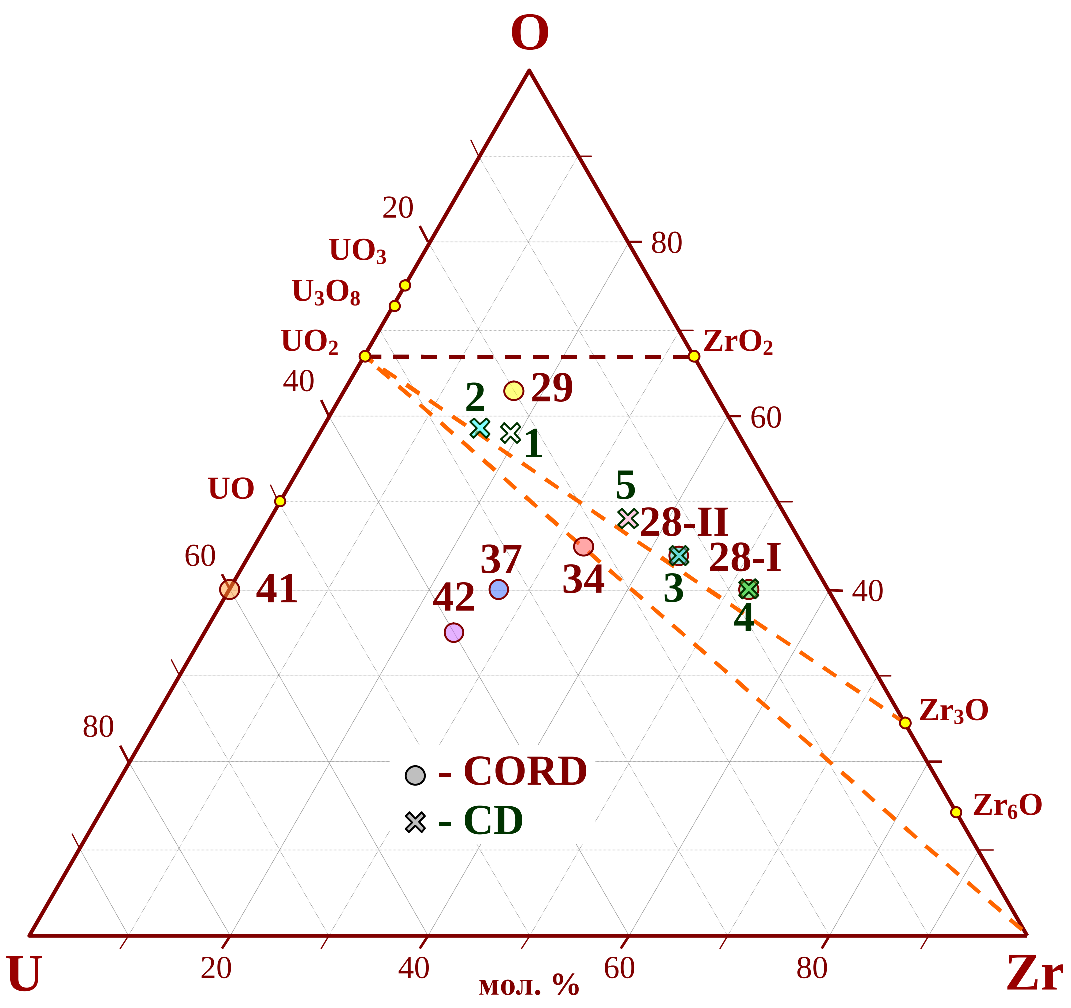

Fig. 3.1. Charge compositions of the CORD and CD series

3.3. Experimental procedures

Practically all experimental procedures of the CORD series aimed at measuring liquidus temperatures were identical, they included:

- Preparation of charge materials and their thorough mixing in argon.
- Furnace charging with a specified composition and its sparging with argon.
- Molten pool production and its superheating above the liquidus temperature.
- Measurement of the molten pool depth and bottom crust thickness.
- Melt sampling.
- Upward shift of the crucible with melt vs. inductor for the local cooling of the superheated melt surface – video recorded. Return of the crucible to the initial position. Control of the reproducibility of the measured temperature and heat flux into the crucible walls and bottom in comparison to those registered before the crucible shift. Repeated several times.
- Heating disconnection, video recording of the surface.
- Retrieval of ingot from the crucible for the analysis.

Note that in the first experiments CORD 28, 29 slightly different technique was used: the melt surface was cooled using the mobile electromagnetic screen; described in /37/.

Similar to CORD experiments CD tests had a standard procedure, which included:

- Preparation of corium charges and their loading into the crucible.
- Molten pool production and its homogenization.
- Heating disconnection, recording of the melt cooling thermogram.
- Posttest processing of the thermogram.

Brief comments to the CORD experiments are given below.

CORD28-I, II

The test studied two melt compositions. The initial charge composition in the crucible corresponded to CORD28-I. After the molten pool production and homogenization melt samples were taken and liquidus temperature was measured. The composition corresponding to CORD28-II was adjusted by introducing appropriate components into the molten pool. After the additions were molten and the melt homogenized, melt samples were taken and liquidus temperature was measured. Fig. 3.2 shows electrical characteristics of the HF generator throughout the test, as well as the melt surface temperature dynamics.

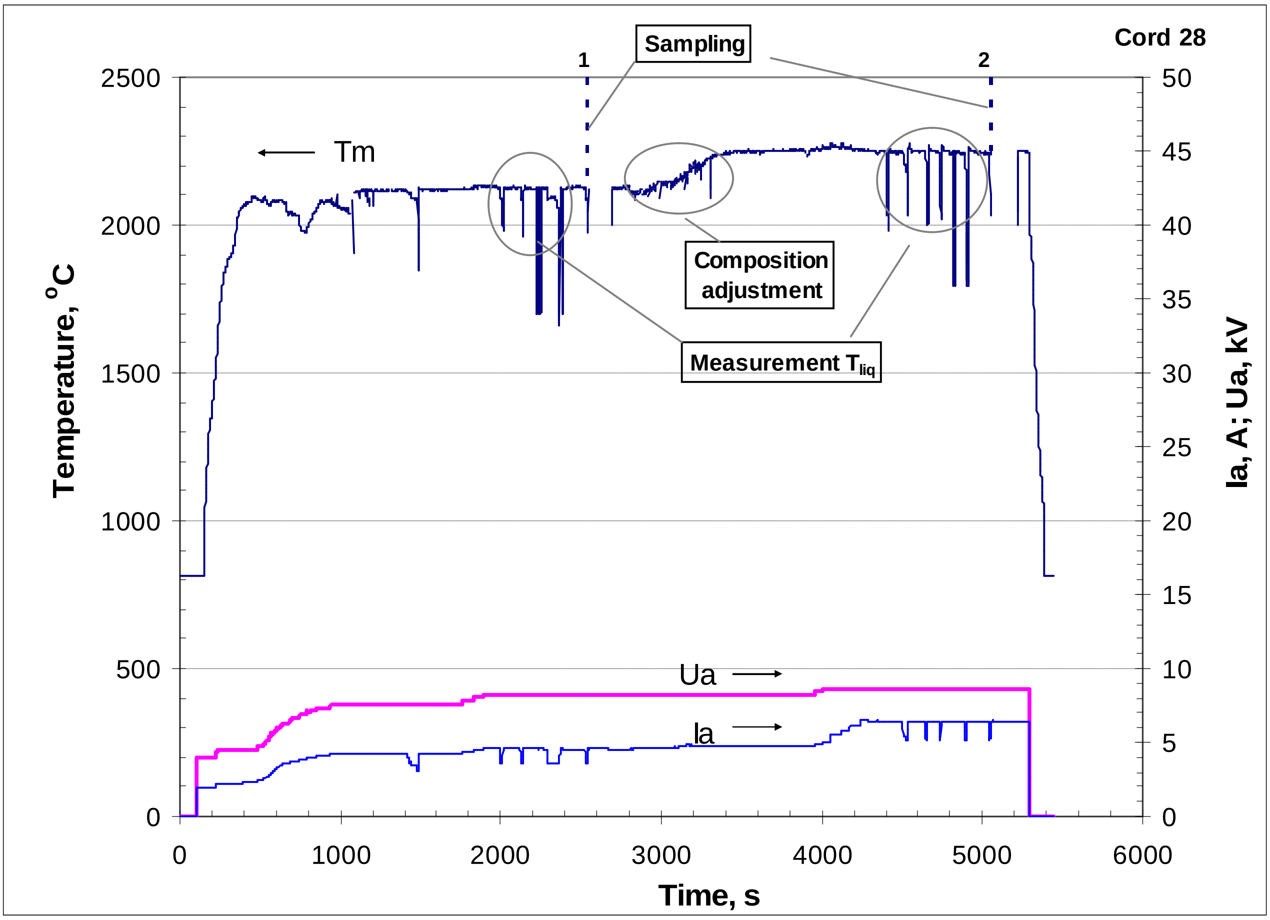

Fig. 3.2. Anode current (Ia), voltage (Ua) and pyrometer readings (Tm) vs. time in CORD28

CORD29

After the molten pool was produced and homogenized a melt sample was taken and liquidus temperature measured. Electrical characteristics of the HF generator throughout the test, as well as the temperature dynamics on the melt surface, are shown in Fig. 3.3.

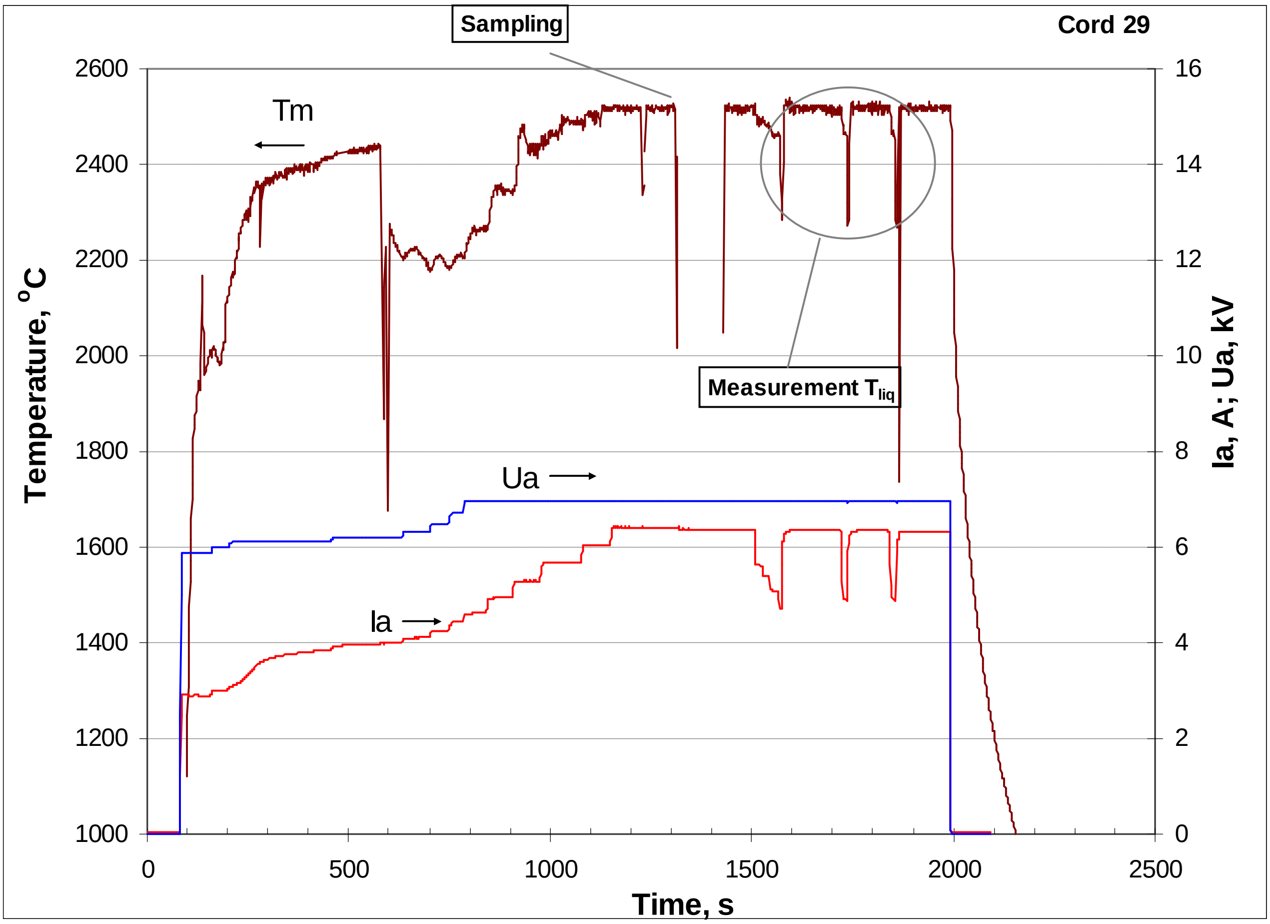

Fig. 3.3. CORD29 anode current (Ia), voltage (Ua) and pyrometer readings (Tm) vs. time

CORD34

Experiment CORD34 was used as a benchmark for the cross-verification of presented results and experimental data of ITU /47of the EC COLLOS project, in which the method of laser pulse heating was used /48/; also for the determination of a possible melt stratification, which was predicted for this composition by the thermodynamical calculations using the GEMINI-2 program.

5 samples were taken by dipping sampling rod into the melt; liquidus temperature was measured three times. Electrical characteristics of the HF generator in the test, as well as the temperature dynamics on the melt surface, are shown in Fig. 3.4. Melt crystallization was started from 2340ºC. Axial section of the ingot is shown in Fig. 3.8 (see Section 3.4.3).

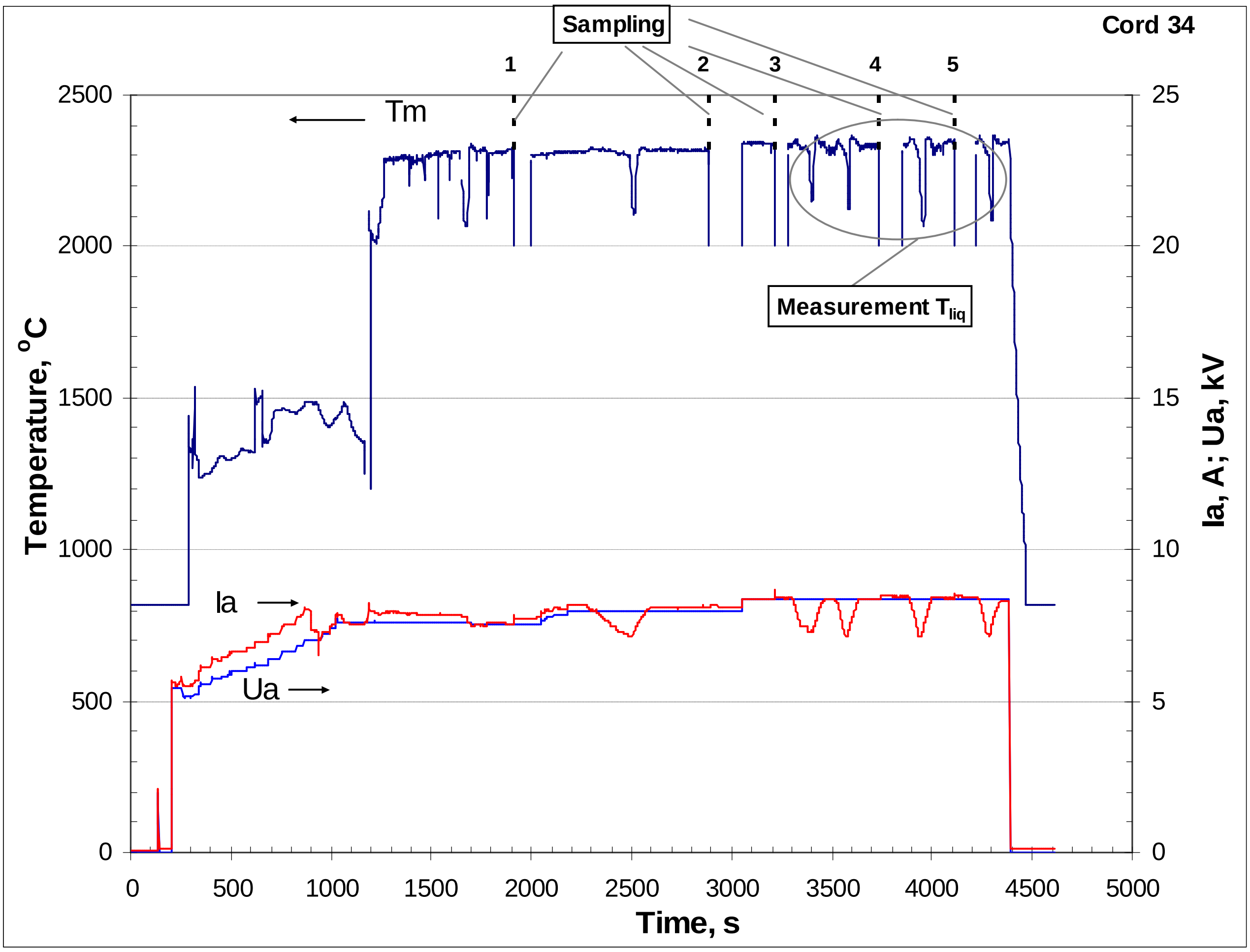

Fig. 3.4. Anode current (Ia), voltage (Ua) and pyrometer readings (Tm) vs. time in CORD34

CORD37

In accordance with thermodynamical calculations the specified melt composition can stratify. After the molten pool was produced and homogenized, a convective pattern, typical for oxidic pools, was observed on its surface. During the experiment two rod samples were taken; liquidus temperature was measured two times. Electrical characteristics of the HF generator in the test, as well as the temperature dynamics on the melt surface, are shown in Fig. 3.5. Melt crystallization was started from 2370°C. Examination of the ingot confirmed melt liquid immiscibilty: ingot separated into two parts; oxidic part had the mass of 198.8 g, and metallic -253.7g. Axial sections of the both parts are presented in Fig. 3.9 (see Section 3.4.3).

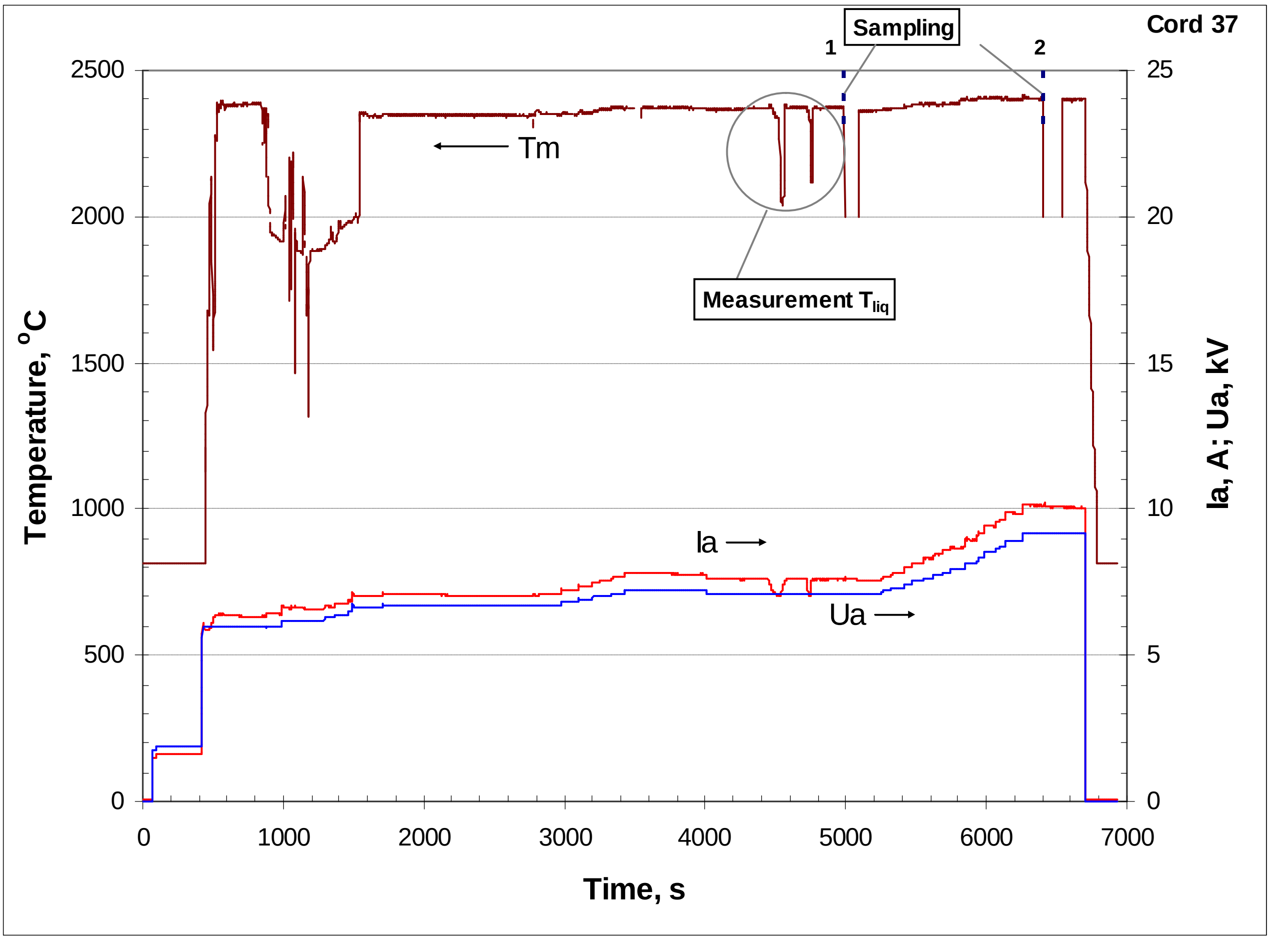

Fig. 3.5. CORD37 anode current (Ia), voltage (Ua) and pyrometer readings (Tm) vs. time

CORD41

The analysis of CORD37 ingot showed that molten pool stratified into two layers. The top one was oxidized, and the bottom - metallized.

For a better insight into the melt stratification peculiarities in the IMCC conditions and in order to refine the methodology of the tie-line construction in the miscibility gap a reference test in the better studied U-O system was conducted. Electrical characteristics of the HF generator throughout the test, as well as the temperature dynamics on the melt surface, are shown in Fig. 3.6. Molten pool was quenched from 2675°C temperature level. Fig 3.10 shows the ingot axial section (see Section 3.4.3); it confirms stratification of the melt having this composition.

CORD42

Differently from CORD37 this experiment had the composition having a lower content of oxygen, which assumably is typical for the miscibility gap. The experimental procedure was also changed in order to minimize studies and reduce the experiment duration. Melt samples were not taken. Electrical characteristics of the HF generator throughout the test, as well as the temperature dynamics on the melt surface, are shown in Fig. 3.7. Melt was quenched from 2480ºC. Fig 3.11 shows the ingot axial section; it confirms stratification of the melt having this composition (see Section 3.4.3).

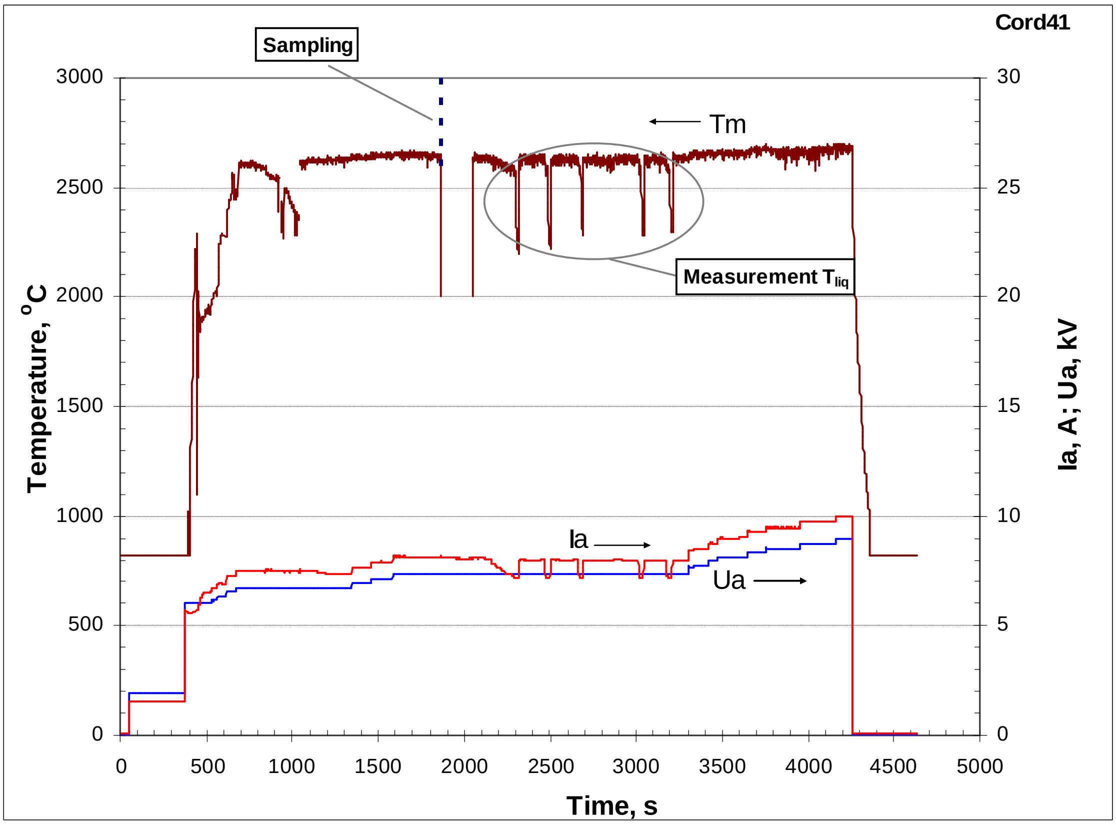

Fig. 3.6. CORD41 anode current (Ia), voltage (Ua) and pyrometer readings (Tm) vs. time

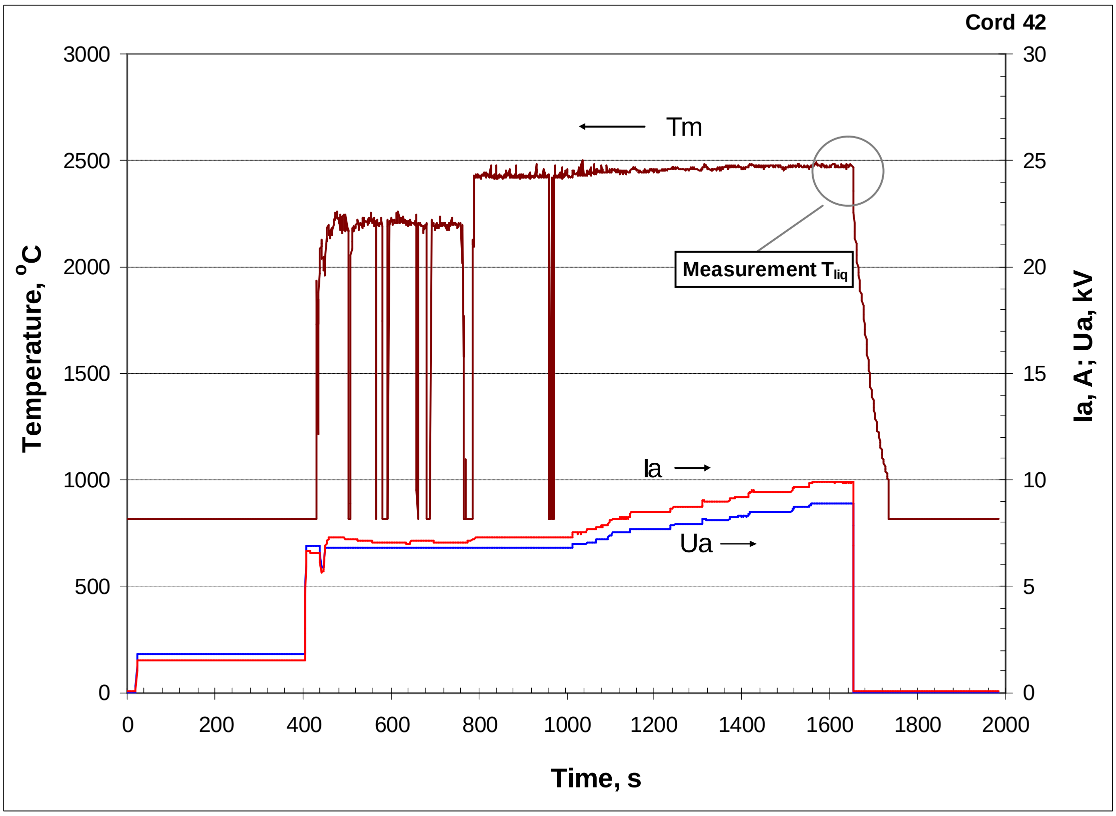

Fig. 3.7. CORD42 anode current (Ia), voltage (Ua) and pyrometer readings (Tm) vs. time

3.4. Posttest analysis

A detailed physicochemical analysis of melt samples and ingots was conducted in order to determine the composition of liquids coexisting in the melt and to study their crystallization pattern.

3.4.1. Material balance of experiments

In order to make the material balance of experiments the initial charge components and molten products were weighed with accuracy up to 0.1 g.

Table 3.3 shows the material balances of experiments CORD28, 29, 34, 37, 41, 42.

Table 3.3. Material balance of experiments CORD-28, 29, 34, 37, 41, 42

CORD	Introduced into the melt, g		Collected, g	
28	**UO_2**	192.7	**Ingot**	352.3
	ZrO_2	60.9	**Rod samples**	31.9
	Zr	170.3	**Probe samples**	24.8
			Spillages	11.9
	Σ	**423.9**	**Σ**	**420.9**
	Imbalance	**3.0**		
29	**UO_2**	296.4	**Ingot** 1)	350.0
	ZrO_2	78.0	**Rod samples**	12.1
	Zr	25.6	**Probe samples**	5.1
			Spillages	31.5
	Σ	**400.0**	**Σ**	**398.7**
	Imbalance	**1.3**		
34	**UO_2**	296.2	**Ingot**	321.1
	Zr	149.9	**Skull**	4.2
			Probe sample	26.9
			Spillages	6.5
			Samples	87.3
	Σ	**446.1**	**Σ**	**446.0**
	Imbalance	**0.1**		
37	**UO_2**	250.7	**Probe sample**	17.2
	Zr	116.4	**Ingot**	452.5
	U	138.1	**Rod samples**	24.0
			Spillages	11.0
	Σ	**505.2**	**Σ**	**504.7**
	Imbalance	**0.5**		
41	**U**	323.3	**Ingot**	507.9
	UO_2	210.0	**Rod sample**	8.4
			Probe sample	6.8
			Aerosols	2.3
			Spillages	7.3
	Σ	**533.3**	**Σ**	**532.7**
	Imbalance	**0.6**		

42	**U**	412.0	**Ingot1)**	524.5
	Zr	29.6	**Probe sample**	0.5
	ZrO_2	93.3	**Spillages**	9.0
	Σ	**534.9**	**Σ**	**534**
	Imbalance	**0.9**		

1) - Ingot was weighed with skull

Insignificant imbalance of experiments testifies to the credibility of conducted studies; small unmanageable losses of material and complete melting of the crucible charge confirm that the average melt composition corresponded to the specified charge composition minus spillages, composition of which was known.

3.4.2. Density of oxidic and metallic parts of the ingot

For calculating the mass of oxidic and metallic parts of ingots in CORD41, 42 experiments , their bottle densities were measured to be used for elemental mass balance, and their volume was calculated from their cross section area in the axisymmetrical formulation. Formula 3.1 was used for calculations.

$$m = V \cdot r \tag{3.1}$$

where m – mass of oxidic and metallic parts, g;

V – volume of oxidic and metallic parts, cm^3;

r - bottle density of oxidic and metallic parts, g/cm^3.

Density of metallic and oxidic parts was determined using methodology /31/. Sampling locations are shown in Figs. 3.10-3.11. High-purity ethyl alcohol was used as the picnometric liquid. Table 3.4 shows the measured bottle densities of oxidic and metallic parts of ingots from these experiments, also their calculated volumes.

Table 3.4. Measured bottle densities of oxidic and metallic ingot parts from experiments CORD41, 42 and their volumes

CORD	**Oxidic part**		**Metallic part**	
	Density, g/cm^3	**Volume, cm^3**	**Density, g/cm^3**	**Volume, cm^3**
41	11.9	26.3	15.4	12.7
42	9.8	18.6	11.4	30.0

Error of the bottle density measurements was ±2%.

3.4.3. Chemical analysis

Samples of the melt, rod and ingot samples of experiments CORD28, 29, 34, 37, 41, 42 were analyzed for the content of U_{total} and Zr_{total}.

Figs. 3.8-3.11 show sampling locations of CORD34, 37, 41, 42 for XRF, chemical analysis and spark mass-spectrometry.

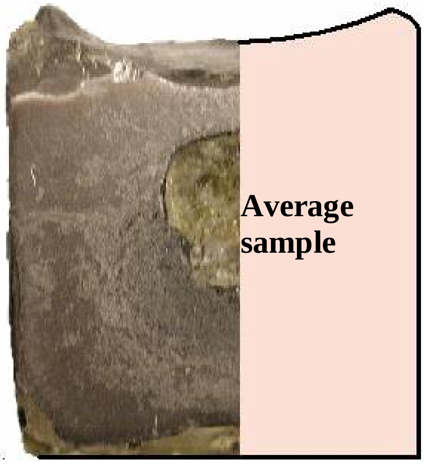

Fig. 3.8. Axial section and sampling of CORD34 ingot

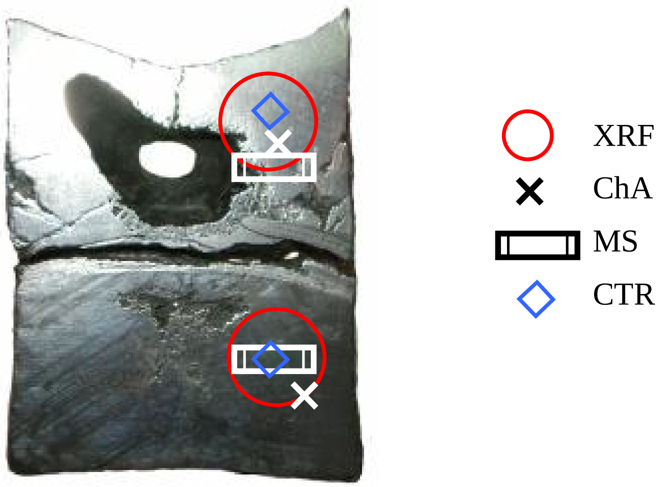

Fig. 3.9. Axial section and sampling of CORD37 ingot

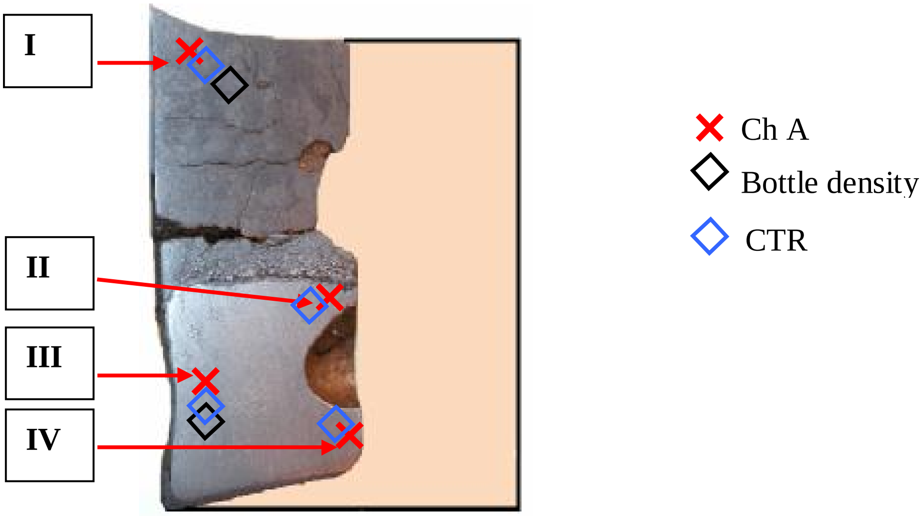

Fig. 3.10. Axial section and sampling of CORD41 ingot

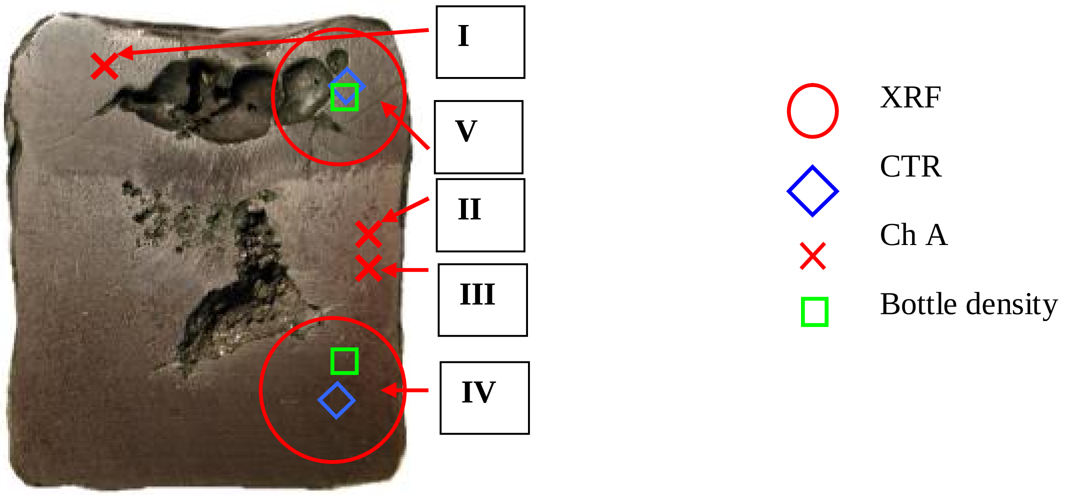

Fig. 3.11 Axial section and sampling of CORD42 ingot

Samples taken from the melt for experiments CORD28, 29, 34, 37; cutted from the ingot for experiment CORD29 and half of the CORD34 ingot (Fig. 3.8), also samplers having the mass up to 100 mg taken from ingots CORD37, 41, 42 (Fig. 3.9-3.11) were crushed to particle size 100 µm, quartered, after which they were crushed to particle size not more than 50 µm, after that they were analyzed for the content of U_{total} and $Zr_{total.}$ Samples for analysis were prepared in the argon atmosphere.

CORD28, 29, 34 samples were analyzed in accordance with the following methodology: corium sample having the mass of 0.1g was dissolved in the mixture of orthophosphoric and sulphuric acids (1:2) in the argon flow; after that total Zr as Zr^{4+} were determined by the photometry from the solution with the xylenol orange indicator, and U_{total} – also by photometry with arsenazo III.

Method for determining total zirconium is based on the formation of colored complex Zr (IV) compound with xylenol orange in the solution of sulfuric acid having the molar concentration equivalent 0,3 – 0,4 mol./dm^3 /40, 41, 42/. Zr detection is neither influenced by large quantities of Mo, W, U, Zn and Ti, not by admixtures of Fe (up to 50 µg), Pb, Ni, Cu, Th and Ta (>100 µg) /41, 42/.

Methodology for determining U_{total} using arsenazo III is applied for measuring uranium in micro-quantities in samples without uranium separation. It has the sensitivity of 0.04 µg/ml /44, 45/.

Samples from CORD37, 41, 42 were prepared using a new methodology of sample preparation. Ingot samples having the mass of 0.1-0.5g were fused with (3.0±0.5) g of potassium pirosulphate at (900±25)ºC until a transparent fusion cake was produced, which was dissolved at heating in 200-250 ml 1M solution of sulphuric acid; after that total Zr as Zr^{4+} was determined by photometry with xylenol orange indicator /40, 41, 42/ and U_{total} - with arsenazo III /43, 44/.

Table 3.5 shows the results of chemical analysis of samples from experiments CORD28, 29, 34, 37, 41, 42.

Table 3.5. Chemical analysis of samples from CORD28-I, 28-II, 29, 34, 37, 41, 42

CORD	Sample	Content, mass.%			Content, at.%		
		U	Zr	O[1]	U	Zr	O
28	Melt sample #1 (28-I)	22.5	69.2	8.3	6.9	55.3	37.8
	Melt sample #2 (28-II)	39.2	52.1	8.7	12.9	44.6	42.5
29	Melt sample	64.8	20.0	15.2	18.9	15.2	65.9
	Ingot average sample	65.0	20.3	14.7	19.3	15.7	65.0
34[2]	Ingot average sample	58.7	35.7	5.6	25.0	39.6	35.4
	Rod sample #1	56.3	38.0	5.7	23.4	41.3	35.3
	Rod sample #2	59.1	Undet.	-	-	-	-
	Rod sample#4	59.7	Undet.	-	-	-	-
	Rod sample#5	58.1	Undet.	-	-	-	-
37	Melt sample #1	66.3	25.6	8.1	26.1	26.3	47.5
	Melt sample #1 (*adjustment for oxygen)*	66.0	25.5	8.48[6]	25.5	25.7	48.8
	Melt sample #2	67.2	24.7	8.1	26.7	25.6	47.8
	Melt sample #2 (*adjustment for oxygen)*	66.9	24.6	8.48[6]	26.0	25.0	49.0
	Ingot (top)	66.2	25.4	8.4	25.7	25.7	48.5
	Ingot (top) (*adjustment for oxygen)*	66.2	25.4	8.38[6]	25.7	25.8	48.5
	Ingot (bottom)	73.6	24.2	2.2	43.4	37.3	19.3
	Ingot (bottom) (*adjustment for oxygen)*	73.0	23.7	3.30[6]	39.7	33.6	26.7
	Ingot (bottom) oxidized sample[5]	U^{+4}=22.3 U^{+6}=40.1	19.7	17.9	16.4	13.5	70.1
	Ingot (bottom) oxidized sample[5] (*adjustment for oxygen)*	73.5	23.2	3.3	40.1	33.1	26.8
41[3]	Zone I	91.2	1.1	7.7	43.7	1.4	54.9
	Zone II	97.8	1.3	0.9	85.4	3.0	11.6
	Zone IV	98.3	1.0	0.7	88.3	2.3	9.4
	Zone III	98.5	1.2	0.3	92.8	3.0	4.2

CORD	**Sample**	**Content, mass.%**			**Content, at.%**		
		U	**Zr**	**O1)**	**U**	**Zr**	**O**
	Average value of zones II, IV, III	98.2	1.17	0.63	88.8	2.7	8.5
42 4)	Zone I	70.8	20.9	8.3	28.5	21.9	49.6
	Zone II	81.8	16.1	2.1	52.8	27.1	20.1
	Zone IV (Fig.3.11) oxidized5)	U^{+4}=25.8 U^{+6}=43.0	14.1	17.1	19.1	10.2	70.7
	Zone IV (Fig.3.11) oxidized5) (*adjustment for oxygen)*	80.9	17.3	1.8 6)	52.9	29.5	17.5

1)- O determined from residue;

2) – Rod sample #3 (CORD34) got oxidized when taken from the crucible, for this reason the sample was not analyzed;

3)- Sampling locations, see Fig. 3.10;

4)- Sampling locations, see Fig. 3.11;

5)- Oxidized metallic part;

6)- Oxygen value was taken from CTR data, see Table 3.50 and recalculated data for main elements.

In CORD34 five melt samples were taken. Chemical analysis (total uranium determination) showed that their composition was close to the average ingot composition.

As explained later (Section 3.4.4), the cation composition of samples was determined by the method of XRF fundamental parameters. In order to specify its results samples from the metallic (bottom) part of the CORD37 ingot (see Fig. 3.9), and Zone IV from CORD42 (see Fig. 3.11) were oxidized. Subsequent chemical analysis was conducted to determine uranium stoichiometry after oxidation. Oxygen content in the metal, which was calculated from the sample weight gain at oxidation and data chemical analysis, coincides with CTR of these samples.

Updated oxygen data (Table 3.5) for CORD37 were used for making elemental balance presented in Table 3.6. Note that specified data for oxidized metal were used for the metallic part. For the elemental material balance the composition of melt samples was taken as equal to the composition of sample #1.

Table 3.6. Elemental material balance CORD37 in accordance with chemical analysis.

Element	**Introduced, g1)**	**Mass of oxidic part, g**	**Mass of metallic part, g**	**Collected, g**				**D, g**
				Samples2)	**Oxidic part, g**	**Metallic part, g**	**Sum, g**	
U	345.2	198.80	253.70	27.33	131.63	186.46	345.43	+0.25
Zr	119.8			10.38	50.51	58.87	119.75	-0.07
O	28.7			3.49	16.66	8.37	28.53	-0.18

1) – Introduced into the melt minus spillages (m=11.0g) and imbalance (m=0.5g);

2) – Mass of samples #1-9.8g, samples #2-14.2g, samples from the probe- 17.2 g.

Table 3.6. shows that for the main elements the imbalance does not exceed 0.5g.

Table 3.7. gives the elemental material balance of experiment CORD42. Composition of the metallic part was determined from Zone IV(oxidized metal) adjusted for oxygen using the CTR data, oxidic part was not adjusted in terms of oxygen, because oxygen content determined by the CTR in this part was 8.3 mass.%, which coincided with the chemical analysis data.

Table 3.7. Element specific mass balance of CORD42 in accordance with chemical analysis

Element	Introduced, g(1)	Mass of oxidic part,(2) g/ Density, g/cm^3	Mass of metallic part,(2) g/ Density, g/cm^3	Collected, g			D, g
				Oxidic part, g	Metallic part, g	Sum, g	
U	400.9	182.0/9.81	343.0/11.42	128.86	279.54	408.39	+7.49
Zr	102.5			38.04	57.29	95.33	-7.17
O	21.7			15.11	6.17	21.28	-0.42

(1) – Introduced into the melt minus spillages (m=9.0g)and imbalance (m=0.9g);

(2) – Masses of oxidic and metallic parts were calculated from their densities and volumes (Table3.4).

Imbalance of the main elements is approximately 7.5 g (Table 3.7). This can be explained by the presence of non-symmetrical pores in the ingot and, as a consequence, a larger error in determining the volumes of both ingot parts.

Table 3.8. gives the elemental material balance of CORD41. Composition of metallic and oxidic parts was determined by averaging compositions of zones II-IV and zone I combined with adjustment for oxygen (Table3.5). Samples of the melt and probe samples were assumed to belong to the oxidic part. Oxygen content in the oxidic part was adjusted using the CTR data.

Table 3.8. Element specific mass balance of CORD41 in accordance with chemical analysis

Element	Introduced, g(1)	Mass of oxidic part,(2) g/ Density, g/cm^3	Mass of metallic part,(2) g/ Density, g/cm^3	Collected, g			D, g
				Oxidic part, g	Metallic part, g	Sum, g	
U	488.8	327.9/26.3	195.2/12.7	299.60	192.14	491.73	2.90
Zr	10.3			3.61	2.28	5.90	4.40
O	24.0			24.69	0.78	25.47	1.50

(1) – Introduced into the melt minus spillages (m=7.3g), imbalance (m=0.6g) and aerosols (m=2.3g);

(2) – Masses of oxidic and metallic parts were calculated from their densities and volumes (Table3.4).

Imbalance of the main elements does not exceed 4.4 g (Table 3.8), which is also explained by the pore presence and, as a consequence, error in the volume determination.

Resulting imbalances (Tables 3.6-3.8) are less than 1% of the total charge mass, which testifies to the credibility of chemical data presented in Table 3.5.

3.4.4. X-ray fluorescence analysis (XRF)

X-ray fluorescence method was applied for the elemental analysis of samples using SPECTROSCAN MAX-GV spectrometer /45/.

For that the powders from CORD 28, 34, 37 melt samples and CORD29, 34 ingots samples were prepared by crushing to the particle size < 50 µm. Resulting powders were compacted into tablets and subjected to analysis.

In CORD 37 and 42 samples were cut from the tops (oxidized) and bottom (metallized) ingot parts; the slab-shaped samples had the size of ~ 10×15 mm^2.

All the samples were prepared in the argon atmosphere.

The method of fundamental parameters (MFP) was used for the quantitative analysis of prepared samples, it was chosen because of the unavailability of standard (reference) samples having low oxygen content. The method uses theoretical correlations describing physical processes exciting the X-ray fluorescence and its registration by spectrometer. This method enables to calculate concentrations of practically any inventory of determined elements in a studied specimen without reference specimens. The value of oxygen unidentifiable by spectrometer was taken from the CTR data, and in further calculations the sum of elements was taken as 100%.

The validity of MFP results for samples taken from CORD37 and 42 ingots was checked by XRF. Samples were oxidized during 4 hours by heating to 1100ºC in air, after that they were crushed on the vibrating mill to the <50 µm particle size. Tablets were made from compacted powders, which were analyzed by the SPECTROSCAN MAX-GV spectrometer after its calibration using oxidic reference specimens.

Comparison of results produced by the analyses of oxidic parts (oxidized and without oxidation) showed their identity within the measurement error. For metallic ingot parts same comparison showed a considerable divergence up to 30% relative. Such divergence can be explained by the absence of data, e.g. on the influence of atom location in the lattice of the U-Zr solid solution on theoretical correlations used in MFP. As the method of reference XRF is more accurate, the data on oxidized samples, more reliable, were used for compiling the material balance.

Table 3.9 shows the analysis results of corium sample from experiments CORD28, 29, 34, 37, 42

Table 3.9. XRF results of CORD 28, 29, 34, 37,42 samples

CORD	Samples	Content, mass.%			Content, at.%		
		U	Zr	O$^{1)}$	U	Zr	O$^{1)}$
28	Melt sample #1 (28-I)	25.0	66.6	8.4	7.7	53.7	38.6

CORD	Samples	Content, mass.%			Content, at.%		
		U	Zr	O1)	U	Zr	O1)
	Melt sample #2 (28-II)	39.6	51.5	8.9	12.9	43.9	43.2
29	Average ingot sample	64.7	21.5	13.8	19.8	17.2	63.0
342)	Average ingot sample	57.0	35.2	7.8	21.5	34.7	43.8
	Rod sample #1	55.1	37.0	7.9	20.5	35.9	43.7
	Rod sample #2	54.6	37.5	7.9	20.2	36.2	43.5
	Rod sample #4	56.5	35.5	8.0	21.1	34.5	44.4
	Rod sample #5	56.6	35.6	7.8	21.3	35.0	43.7
37	Melt sample #1	67.7	23.8	8.48	26.4	24.3	49.3
	Melt sample #2	69.6	22.0	8.48	27.5	22.7	49.8
	Ingot (top)	62.5	29.1	8.4	23.7	28.8	47.4
	Ingot (top) oxidized5)	58.7	25.2	16.1	16.1	18.1	65.8
	Ingot (top) oxidized (*adjustment for oxygen)*	64.1	27.5	8.38	24.6	27.5	47.9
	Ingot (bottom)	65.0	31.7	3.3	33.0	42.0	24.9
	Ingot (bottom) oxidized4)	64.8	18.7	16.5	18.0	13.6	68.4
	Ingot (bottom) oxidized (*adjustment for oxygen)*	75.0	21.7	3.3	41.5	31.3	27.2
423)	Zone IV	72.9	25.3	1.8	44.0	39.8	16.2
	Zone IV oxidized 4)	69.3	14.4	16.3	19.8	10.8	69.4
	Zone IV oxidized (*adjustment for oxygen)*	81.3	16.9	1.8	53.4	29.0	17.6
	Zone V	67.9	23.8	8.3	26.8	24.5	48.7
	Zone V oxidized	62.1	20.4	17.5	16.5	14.2	69.3
	Zone V oxidized (*adjustment for oxygen)*	69.0	22.7	8.3	27.4	23.5	49.0

1) – Oxygen value was taken from CTR (Table 3.50);

2) – Sample taken by rod #3 (CORD34) got oxidized when taken from the crucible, so it was not analyzed;

3)- See sampling locations in Fig. 3.11;

4)- Oxidized metallic part;

5)- Oxidized oxidic part.

Compositions of ingots and samples taken during CORD28, 29 and 34 experiments (Table 3.9.) are close to the planned, which is also confirmed by the material balance of experiments (masses of unmolten products are less than 1% from the total charge mass).

Table 3.10 shows the elemental material balance in accordance with XRF for CORD37. Compositions of oxidic and metallic parts were calculated using the data on oxidized sample with adjustment for oxygen. Probe sample was treated as Sample #1.

Table 3.10 CORD37 element specific mass balance in accordance with XRF

Element	Introduced, g[1]	Mass of oxidic part,[2] g/ Density, g/cm^3	Mass of metallic part,[2] g/ Density, g/cm^3	Collected, g				D, g
				Samples[2]	Oxidic part, g	Metallic part, g	Sum, g	
U	345.2	198.80	253.70	28.16	127.43	190.39	345.98	+0.80
Zr	119.8			9.55	54.71	54.94	119.20	-0.63
O	28.7			3.49	16.66	8.37	28.53	-0.17

[1] – Introduced into the melt minus spillages (m=11.0g) and imbalance (m=0.5g);

[2] – Mass of samples #1-9.8 g, samples #2-14.2 g, samples from probe - 17.2g.

Table 3.11 shows the elemental material balance determined by XRF for CORD42. Oxidic and metallic parts were calculated using the data on oxidized samples, zones V and IV (Table 3.9), respectively, with adjustment for oxygen.

Table 3.11. CORD42 element specific mass balance in accordance with XRF

Element	Introduced, g[1]	Mass of oxidic part,[2] g/ Density, g/cm^3	Mass of metallic part,[2] g/ Density, g/cm^3	Collected, g			D, g
				Oxidic part, g	Metallic part, g	Sum, g	
U	400.9	182.0/9.81	343.0/11.42	125.6	278.9	404.5	+3.6
Zr	102.5			41.3	57.9	99.2	-3.2
O	21.7			15.1	6.2	21.3	-0.4

[1] – Introduced into the melt minus spillages (m=9.0g) and imbalance (m=0.9g);

[2] – Masses of oxidic and metallic parts were calculated using their densities and volumes (Table3.4).

For main elements the imbalance does nor exceed 3.6 g (Table 3.11).

Resulting imbalances (Table 3.10-3.11) are less than 1% from the total charge mass.

3.4.5. Spark mass-spectrometry

Samples cut from CORD34 and 37 ingots were used for determining oxygen and other elements by the method of spark mass-spectrometry.

Samples were cut as rectangular prisms with dimensions approx. 2×2×(10÷15) mm^3 (two prisms for each zone).

The analysis was made by the spark mass-spectrometer IMS JEOL (Japan) equipped with double focusing and electric registration of mass-spectra.

For most elements the detectability limit was 0.5 µkg/g.

Table 3.12 shows the analyses results.

Table 3.12 Elemental composition of CORD34, 37 ingot determined by spark mass-spectrometry

CORD		U	Zr	O	Admixtures
		mass.%			
34		64.05	32.93	2.88	0.14
37	**(top)**	68.00	20.57	2.32	9.11
	(bottom)	79.76	17.71	2.44	0.09

Divergence of the data with results of chemical and XRF analyses is likely to be explained by the microquantities of samples used for the mass-spectrometry. These results were not used in further studies.

3.4.6. SEM/EDX analysis

3.4.6.1. SEM/EDX of CORD samples

The microstructure and elemental composition of samples were determined by the scanning electron microscopy (SEM) and energy dispersion X-ray (EDX).

For the SEM studies of samples the scanning electron microscope CamScan MV2300 was used. The elemental analysis of chosen specimen parts was carried out using the Oxford Link Pentafet microprobe.

Each specimen's spectral characteristics were identified, they were used for determining both the total composition and the composition of separate phases. The quantitative analysis was performed by comparing the intensities of the reference specimen (extra-pure specially prepared substances) and studied sample. Along with reference samples of U, Zr, UO_2, ZrO_2 from the Link kit, own reference samples were used for checking the adequacy of registered data.

The limit of the reliable detection of an element depends on its number in the Periodic table of elements; and it varies between 0.3 mass.% - 0.5 mass.%. The detection of elements in smaller amounts is not reliable.

The quantitative evaluation of oxygen by the EDX method in the systems with heavy cations (U and Zr) is not reliable due to the considerable difference (by several orders) in the intensities of spectral lines, and also due to the unavailability of reference samples, which would be close to the studied compositions in the Me/O ratio.

A complex methodology was developed for specifying oxygen content in metal-oxidic compositions; it uses the following data:

- volume fractions of coexisting phases; resulting from SEM analysis (in the approximation of microstructure isotropy);

- cation ratio in phases; resulting from EDX analysis;

- assumption that phase density is close to the stoichiometric phase density (the values of component density borrowed from the Pauling File project /46/ were: for UO_2(cubic)=10970 kg/m^3, for ZrO_2(cubic)=6270 kg/m^3, Zr_3O=6910 kg/m^3; U(cub)=19040 kg/m^3; Zr(cub)=6450 kg/m^3);

- assumption that the density of solid solutions follows the law of constituent components' density additivity;

- available data on phase equilibria in the binary sections of the studied system;

- assumption on the insignificant divergence between the assigned and actual compositions of the system (on the basis of conducted material balance).

It should be mentioned that in case of an unknown density of a component, and if its content in the phase was small, special methodologies were used for evaluating its mass. E.g. for evaluating U dissolved in α-Zr(O) an assumption about insignificant changes of the molar phase was taken; in this case the mass was calculated from the molecular mass of $Zr_{3-x}U_xO$ solid solution and known density of Zr_3O.

It should be noted that evaluation of volume fractions of coexisting phases using SEM images has a number of considerable limitations, which influence the accuracy of this method. It is necessary to accumulate images having the magnification enabling to see phase boundaries. For this reason only strongly-magnified SEM images having distinct inter-phase boundaries were selected for the analysis. This limitation can produce a strong influence on the adequacy of calculated composition because of the small area; and it excludes strongly anisotropic structures from analysis.

Ingots produced in experiments CORD34, 37, 41, 42 and CD3, 5 were cut along the axis, their halves and quarters were used in preparing specimens (polished sections) for the analysis of microstructure and identification of coexisting phases.

Figs. 3.12-3.69 show the microstructure of CORD samples, the average sample composition is given in Tables 3.13-3.47.

Experiment CORD28

CORD-28-I, 28-II melt samples taken during the measurement of liquidus temperature of two melt compositions were used for preparing templates for analysis. Both samples had the fine-grain structure typical for a fast specimen quenching. In the crystallized melt the main phases are α-Zr(O) and $(U,Zr)O_{2-x}$.-based. The primary precipitation phase is a $(U,Zr)O_{2-x}$-based solid solution (Fig. 3.12, 3.13 and Tables 3.13, 3.14). Pores having a typical size of 5 μm are evenly distributed across the whole surface of the polished section. The pores concentrate near the phase based on the α-Zr(O) solid solution. This observation and rounded shapes of pores imply that they originated from the release of excess oxygen during the α-Zr(O) crystallization. It is also possible to estimate the final solubility of uranium in the α-Zr(O)-based solid solution, coexisting with a solid solution of $U_{0.5}Zr_{0.5}O_2$ at the temperature, from which quenching started, – $Zr_{2.84}U_{0.16}O_{1+x}$.

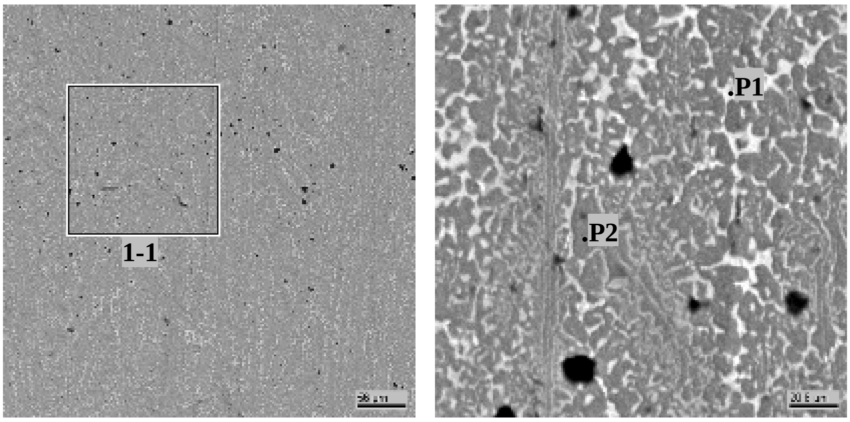

1(SQ1) 1-1

(a)

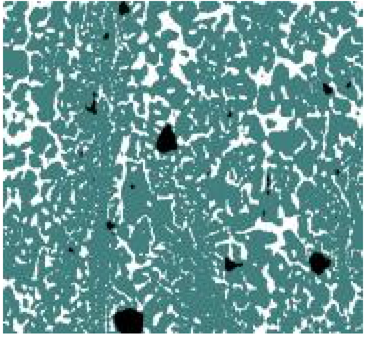

(b)

Fig. 3.12. Microphotographs (a) and microstructure image of 1-1 (b) zone, Sample #1 of CORD28-I

Table 3.13. EDX-analysis data and calculations of the average composition of Sample #1, CORD-28-I specimen

#		U	Zr	O
SQ1	mass.%	28.29	63.63	8.08
	mol.%	8.99	52.78	38.23
	mol.% MeO_x	14.56	85.44	
$SQ1^{calc}$	mass.%	25.9	66.13	7.97
	mol.%	8.17	54.42	37.41
	mol.% MeO_x	13.05	86.95	
P1	mass.%	62.34	20.77	16.89
	mol.%	16.95	14.74	68.31
	mol.% MeO_x	53.5	46.5	
P2	mass.%	11.84	79.22	8.95
	mol.%	3.37	58.78	37.85
	mol.% MeO_x	5.42	94.58	
$P1^{calc}$	mass.%	64.61	21.53	13.86
	mol.%	19.76	17.18	63.06
$P2^{calc}$	mass.%	12.11	80.96	6.93
	mol.%	3.71	64.7	31.59

The volume fractions of coexisting phases were determined by processing the SEM image of Zone 1-1 (Fig. 3.12b), they were: pore space – 1.67 vol. %, α-Zr(O)-based phase (dark-colored) – 76.93 vol. %, (U, Zr)O_{2-x} -based phase (light colored)– 21.4 vol. %.

In the evaluation of average compositions of resulting materials the following compounds were chosen as the crystallizing phases: solid solution (U, Zr)O_2 with cation/oxygen ratio of 1:2 and compound Zr_3O, because they represent oxygen content in the resulting solid solution $Zr_{3-x}U_xO$ in the best way. Uranium dissolved in it was evaluated using the EDX data (Table 3.13, P2). The final solubility of uranium in the $Zr_{3-x}U_xO$ phase coexisting with solid solution $U_{0.62}Zr_{0.38}O_2$ related to the temperature, at which the quenching was started, can be evaluated from the EDX data as $Zr_{2.85}U_{0.15}O_{1+x}$.

Known densities and volume fractions of coexisting phases enabled to get their molar ratio: 35.96 mol. % $U_{0.53}Zr_{0.47}O_2$ and 64.04 mol. % $Zr_{2.85}U_{0.15}O_{1+x}$ (15.77 mol. % $U_{0.53}Zr_{0.47}O_2$ and 84.23 mol. % $Zr_{0.95}U_{0.05}O_{0.33+x}$).

The calculated average compositions are given in Table 3.13 ($SQ1^{calc}$).

Using available data on phase equilibria and cation ratio in the identified phases we can determine the tie-line position at the possible minimum oxygen content in $U_xZr_{1-x}O_{2-y}$ solid solution. E.g. for CORD28-I the stoichiometry of $U_{0.53}Zr_{0.47}O_{1.71}$ was chosen using the data on the maximum oxygen solubility in U (63.8 mol. %) /20-22/ and in Zr (61 mol. %) /26-27/ at temperature, from which quenching started. It is assumed that oxygen solubility in the solid solution follows the linear law. In this case the $U_{0.53}Zr_{0.47}O_{1.71}$ solid solution will be contrasted to $Zr_{2.84}U_{0.16}O_{1\pm x}$ solid solution , having the oxygen content of 31.59 mol.% (calculated molar ratio – 26.73 mol.% $U_{0.53}Zr_{0.47}O_{1.71}$ and 73.27 mol.% $Zr_{0.95}U_{0.05}O_{0.46}$; the composition is given in Table 3.13, points $P1^{calc}$ and $P2^{calc}$). Fig. 3.13 shows the principle of the tie-line construction.

We should note a good agreement of results of the EDX, SEM/density and chemical analysis (compare Table 3.13 SQ1 and $SQ1^{calc}$ with Table 3.5, Sample #1 CORD28-I) and a minor deviation of the sample composition from the initial composition (Table 3.2, CORD28-I).

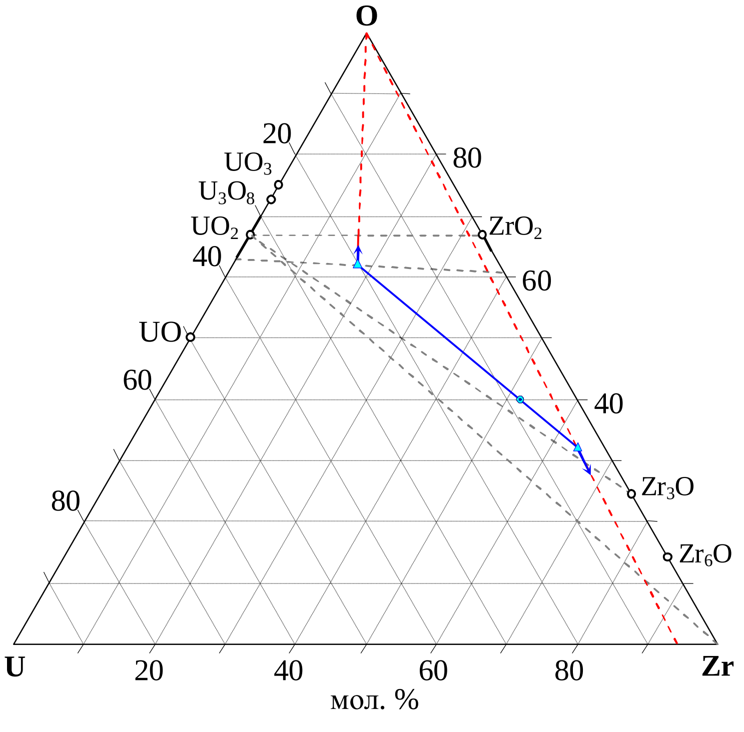

Fig. 3.13. Principle of the tie-line construction and oxygen content evaluation in the metallic phase; arrows show the error direction in the oxygen content evaluation in the coexisting phases using CORD28-I as an example

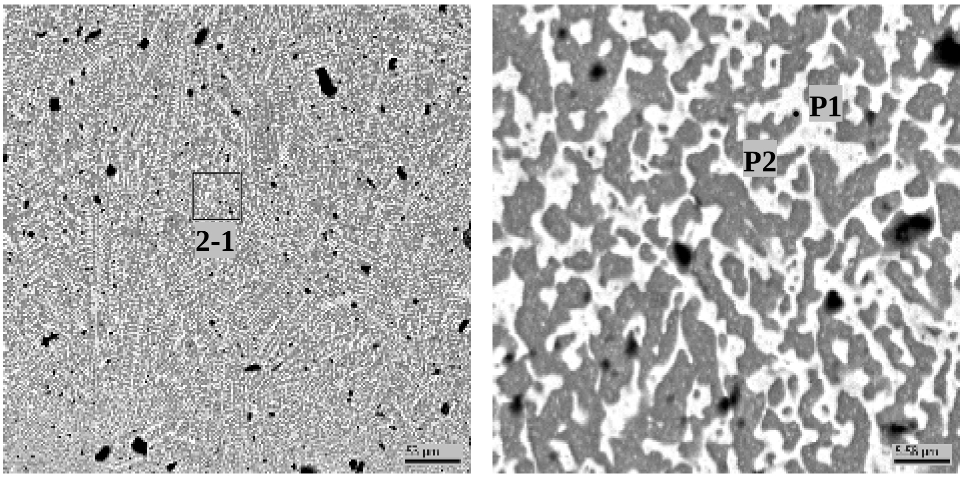

2(SQ1) 2-1

(a)

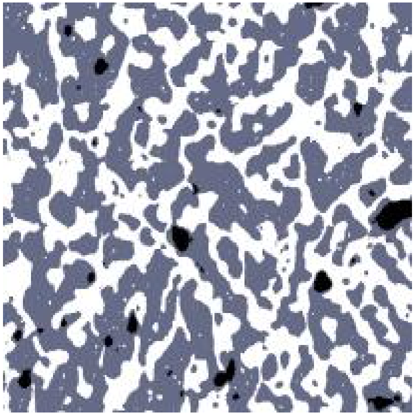

(b)

Fig. 3.14. Microphotographs (a) and microstructure of zone 2-1 (b), Sample #2 of CORD-28-II specimen. The structures are colored differently for better presentation

Table 3.14. EDX-analysis data and calculations of average composition of sample #2, specimen CORD-28-II

#		U	Zr	O
SQ1	mass.%	40.85	48.23	10.92
	mol.%	12.41	38.23	49.36
	mol.% MeO_x	24.50	75.50	
$SQ1^{calc}$	mass.%	39.82	50.13	10.05
	mol.%	12.44	40.86	46.70
	mol.% MeO_x	23.34	76.66	
P1	mass.%	67.71	16.23	16.06
	mol.%	19.40	12.13	68.46
	mol.% MeO_x	61.52	38.48	
P2	mass.%	11.19	83.46	5.34
	mol.%	3.63	70.60	25.77
	mol.% MeO_x	4.89	95.11	
$P1^{calc}$	mass.%	70.26	16.84	12.90
	mol.%	22.95	14.35	62.70
$P2^{calc}$	mass.%	11.18	83.33	5.49
	mol.%	3.60	70.06	26.34

Processing of the SEM image of zone 2-1 (Fig. 3.14b) provided the volume fractions of coexisting phases: pore space – 1.85 vol. %, α-Zr(O)-based phase – 56.71 vol. %, (U, Zr)O_{2-x} -based phase – 41.44 vol. %.

Table 3.14 ($SQ1^{calc}$) gives the calculated average composition.

Table 3.14 also gives calculated values for samples CORD28-I. Calculated fraction of oxidized phase $U_{0.62}Zr_{0.38}O_{1.83}$ (Table 3.14, point P1) is 51.3 mol.%, and of metallic phase $Zr_{0.95}U_{0.05}O_{0.28}$ (Table 3.14, point P2) – 48.7 mol.%, respectively.

Fig. 3.15 shows the diagram of the U-Zr-O system with plotted measured compositions and liquidus temperature (measured by VPA IMCC) of experiments CORD-28-I and 28-II. A good agreement of data on compositions can be noted. A deviation of CORD-28-II composition determined by SEM/EDX and SEM/density in the direction of a higher content of oxygen in comparison to the initial composition can be explained by the unrepresentativeness of analyzed zone (in this zone a (U,Zr)O_2-based solid solution was replaced by a more fusible phase based on the α-Zr(O)solid solution).

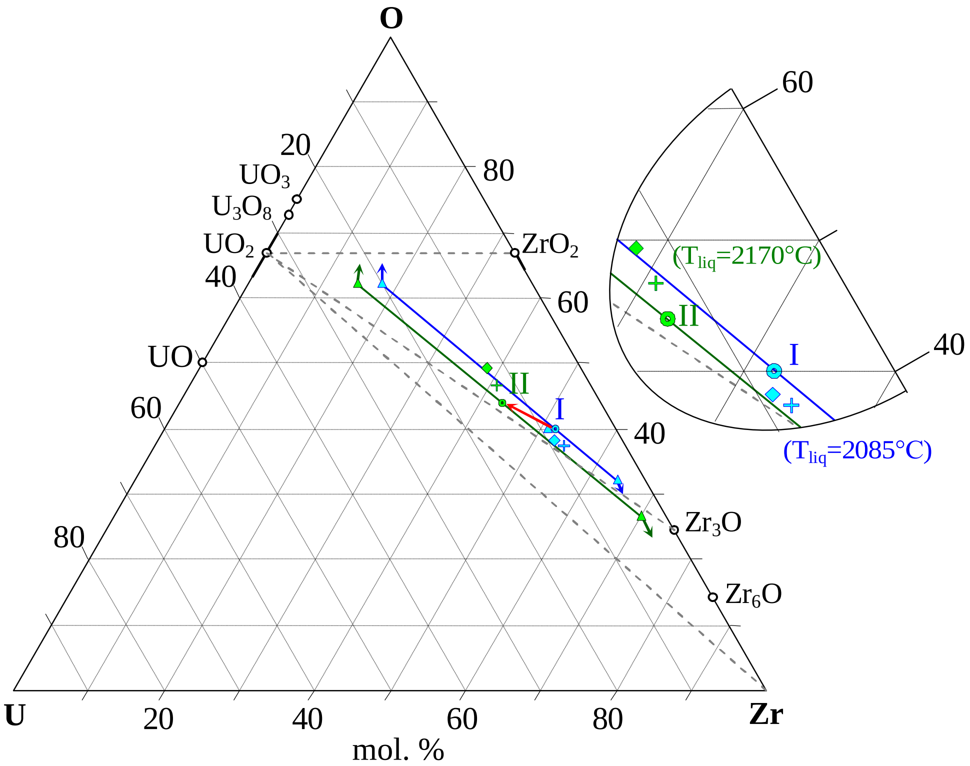

Fig. 3.15. Experimental results of CORD28-I, 28-II:◎ - initial composition, ◇ - SEM/EDX, + - SEM/density; △ - ends of tie-lines determined using data of SEM/EDX, charge composition and oxygen solubility in U and Zr

Experiment CORD29

A template was prepared from the CORD-29 melt sample and subjected to analysis.

The main phase is based on $(U, Zr)O_{2-x}$ solid solution having different cation ratios (Fig. 3.16, Table 3.15, P1-P3). Rounded α-Zr(O)-based inclusions are observed in the matrix of the main phase (Table 3.15, P4). The studied specimen had insignificant porosity.

In accordance with EDX data the final solubility of uranium in the α-Zr(O) solid solution-based phase coexisting with a solid solution of transient composition $U_xZr_{1-x}O_2$, at temperature of quenching start can be evaluated as $Zr_{2.86}U_{0.14}O_{1+x}$.

SEM image from Zone 1 presented in four contrasting colors (Fig. 3.16b) enabled to determine volume fractions of coexisting phases: pore space – 1.29 vol. %, α-Zr(O)-based phase – 6.17 vol. %, $(U, Zr)O_{2-x}$ solid solution-based phase containing big amount of zirconium – 73.65 vol. %, $(U, Zr)O_{2-x}$ solid solution-based phase containing smaller amount of zirconium – 18.9 vol. %.

Table 3.15 ($SQ1^{calc}$) gives the calculations of average composition ($SQ1^{calc}$).

Fig. 3.17 shows a diagram of the U-Zr-O system with plotted measurements of compositions and liquidus temperature (VPA IMCC) in CORD-29. A difference in cation ratios determined by the SEM/EDX and SEM/density can be explained by two reasons. First, EDX gives a lower than actual uranium content in the phase, because of its too small characteristic size; second, the composition of $(U_yZr_{1-y}O_{2-x})$ –based phase undergoes a gradual change; due to this the presentation of SEM image in two contrasting levels for the matrix phase has a large uncertainty. Along with that the oxygen content determined by the method of SEM/density agrees very well with the chemical and EDX analyses. In general, all data have a good convergence.

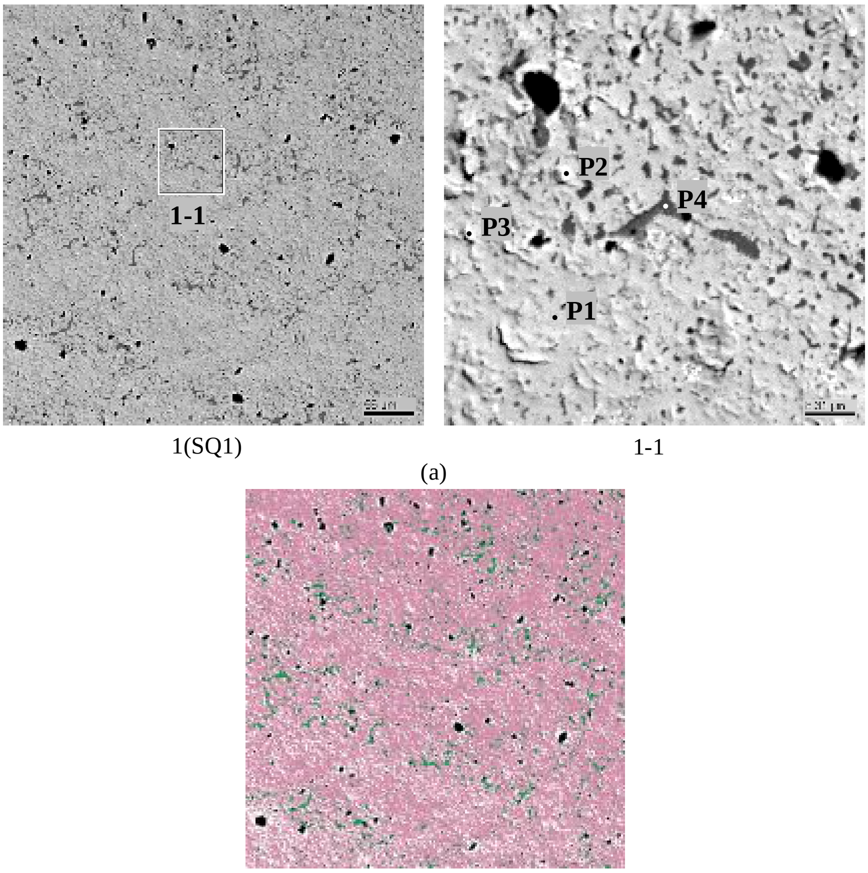

1(SQ1)

1-1

(a)

(b)

Fig. 3.16. Microphotographs (a) and microstructure of zone 1 (b), specimen CORD-29 presented in four contrasting colors

Table 3.15. EDX--analysis data and calculations of CORD-29 average compositions

#		U	Zr	O
SQ1	mass.%	64.63	20.27	15.1
	mol.%	18.89	15.46	65.65
	mol.% MeO_x	55.00	45.00	
SQ1^{calc}	mass.%	62.01	22.87	15.12
	mol.%	17.89	17.22	64.9
	mol.% MeO_x	50.95	49.05	
P1	mass.%	62.75	21.33	15.92
	mol.%	17.66	15.67	66.67
	mol.% MeO_x	52.99	47.01	
P2	mass.%	70.84	14.54	14.63
	mol.%	21.7	11.62	66.67
	mol.% MeO_x	65.12	34.88	
P3	mass.%	71.36	14.10	14.54
	mol.%	21.99	11.34	66.67
	mol.% MeO_x	65.98	34.02	
P4	mass.%	10.32	81.60	8.08
	mol.%	3.01	61.99	35.00
	mol.% MeO_x	4.62	95.38	

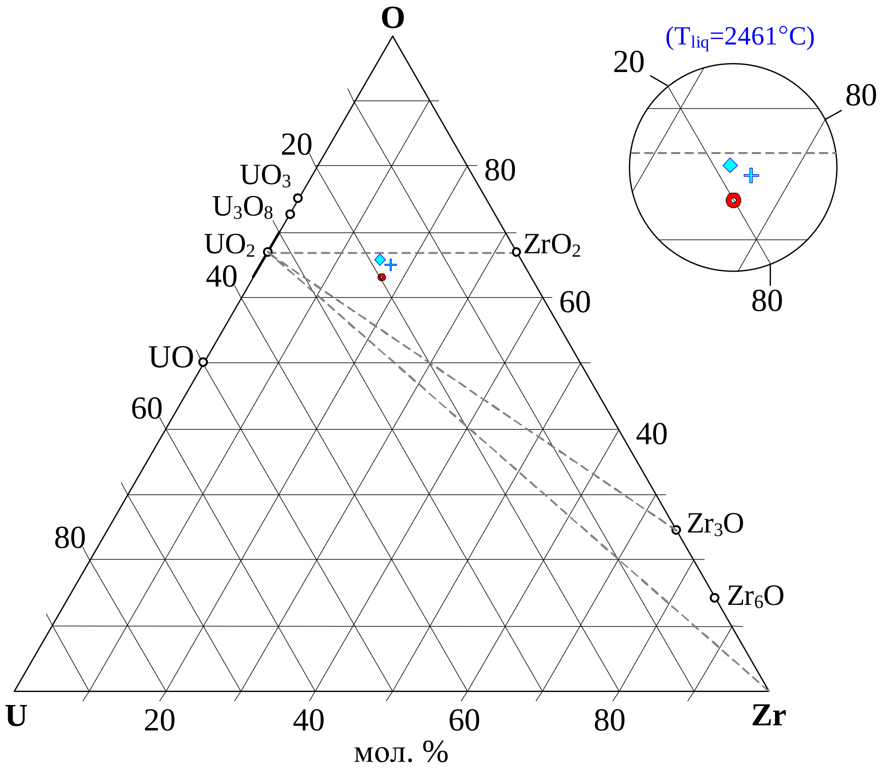

Fig. 3.17. Results of experiment CORD29: ◎ - initial composition, ◇ - SEM/EDX, + - SEM/density

Experiment CORD34

As noted before, CORD34 was performed to compare the experimental data provided by the COLOSS programme carried out in the ITU. Templates were prepared from melt samples, which were subjected to the SEM/EDX analysis (Fig. 3.18-3.21). Crystallized ingot was cut along the axis to prepare a template (Fig. 3.12).

Comparison of the melt sample (Fig. 3.18) and ingot microstructure (Fig. 3.23, 3.24), showed the fine-grain dendrite character of rod samples, which indicates crystallization in quenching conditions. These samples also have small porosity. No indications of the melt stratification were found.

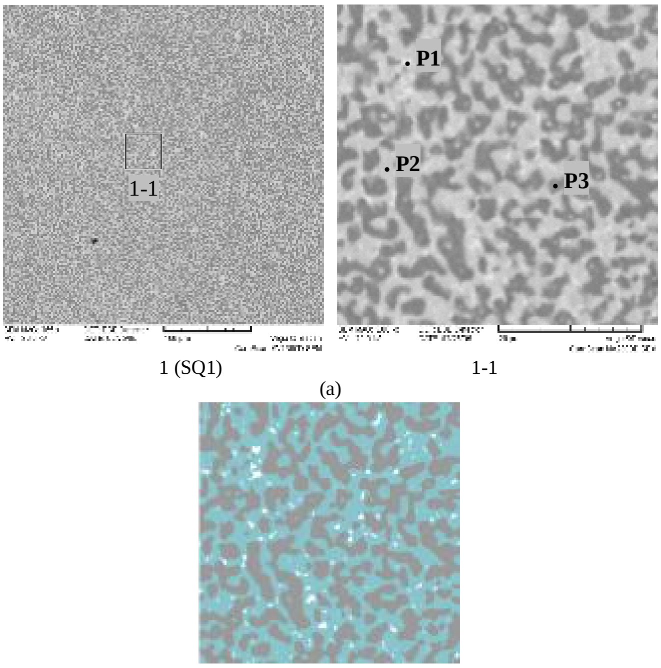

1 (SQ1) 1-1

(a)

(b)

Fig. 3.18. Microphotographs (a) and microstructure of zone 1-1 (b), rod sample No1, CORD-34 presented in three contrasting colors

Table 3.16. EDX analysis of rod sample #1

#		U	Zr	O
SQ1	mass.%	54.06	33.28	12.67
	mol.%	16.41	26.36	57.22
	mol.% MeO_x	38.37	61.63	
$SQ1^{calc}$	mass.%	57.10	32.88	10.02
	mol.%	19.56	29.39	51.05
	mol.% MeO_x	39.96	60.04	
P1	mass.%	87.71	3.09	9.19
	mol.%	37.72	3.47	58.8
	mol.% MeO_x	91.57	8.43	
P2	mass.%	79.89	6.72	13.4
	mol.%	26.92	5.91	67.17
	mol.% MeO_x	82.02	17.98	
P3	mass.%	17.14	70.72	12.13
	mol.%	4.48	48.28	47.23
	mol.% MeO_x	8.50	91.50	

Analysis of the specimen microstructure enables to make a conclusion about the coexistence of at least three solid solution phases. One of them is likely to be the $(U,Zr)O_{2-x}$-based phase, most refractory and close in composition to UO_{2-x}, its volume fraction is small (Fig. 3.18a, Table 3.16, point P1). Two others - $(U,Zr)O_{2-x}$-based phase having a higher Zr content (Table 3.16, point P2), its oxygen:cation ratio is close to 2; and the α-Zr(O)-based phase(Table 3.16, point P3).

In accordance with EDX uranium solubility in the last-mentioned phase coexisting in equilibrium in the $U_{1-x}Zr_xO_{2-y}$ solid solution in relation to the temperature, from which specimen quenching started (2340°C), can be estimated as $Zr_{2.74}U_{0.26}O_{1+x}$.

SEM images of Zone 1-1 of the rod sample #1 (Fig. 3.18b) presented in three colors enabled to determine volume fractions of coexisting phases: α-Zr(O)-based phase – 47.28 vol. %, $(U, Zr)O_{2-x}$ solid solution–based phase having small content of Zr, – 2.22 vol. %, $(U, Zr)O_{2-x}$ solid solution–based phase having high content of Zr – 50.5 vol. %.

Table 3.16 shows only the calculated average composition of sample ($SQ1^{calc}$). Credible experimental evaluation of the average composition was not possible due to the insignificant contrast between crystallized phases, fine-grain structure (even cation composition was difficult to determine) and continuous solubility of U, Zr and their oxidic forms in each other at high temperatures.

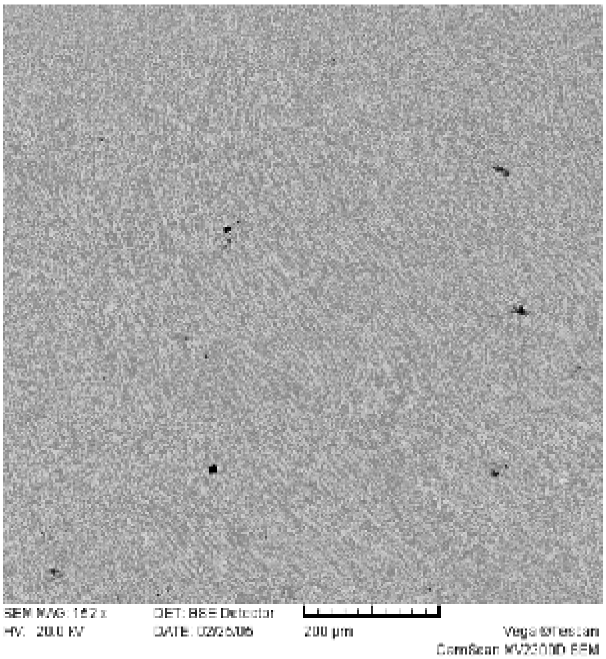

Fig. 3.19. Microphotograph of the specimen taken from rod sample #2, CORD34

Table 3.17. EDX analysis of rod sample #2

#		U	Zr	O
SQ	mass.%	53.37	35.10	11.53
	mol.%	16.87	28.94	54.19
	mol.% MeO_x	36.82	63.18	

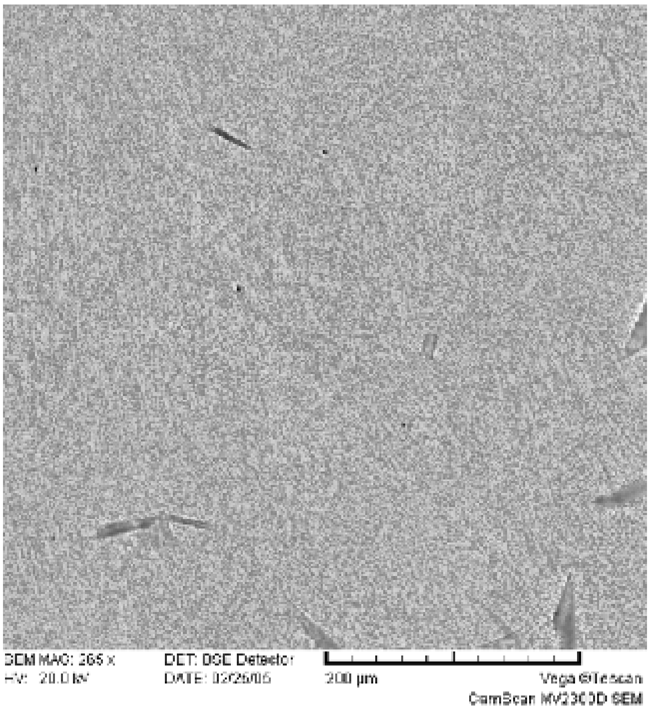

Fig. 3.20. Microphotograph of the specimen taken from rod sample #4, CORD34

Table 3.18. EDX analysis of rod sample #4

#		U	Zr	O
SQ	mass.%	55.70	31.86	12.44
	mol.%	17.20	25.67	57.13
	mol.% MeO_x	40.12	59.88	

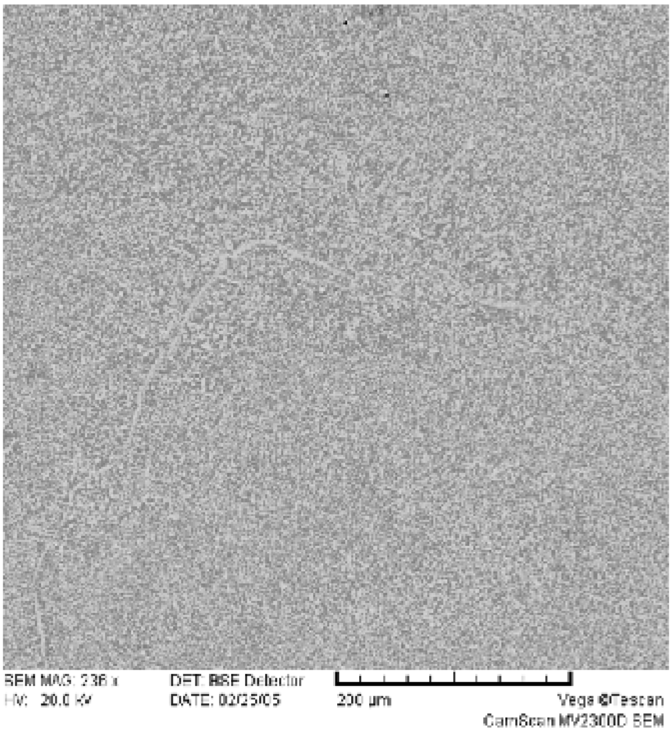

Fig. 3.21. Microphotograph of the specimen taken from rod sample #5, CORD34

Table 3.19. EDX analysis of rod sample #5

#		U	Zr	O
SQ	mass.%	55.41	32.09	12.49
	mol.%	17.05	25.77	57.18
	mol.% MeO_x	39.82	60.18	

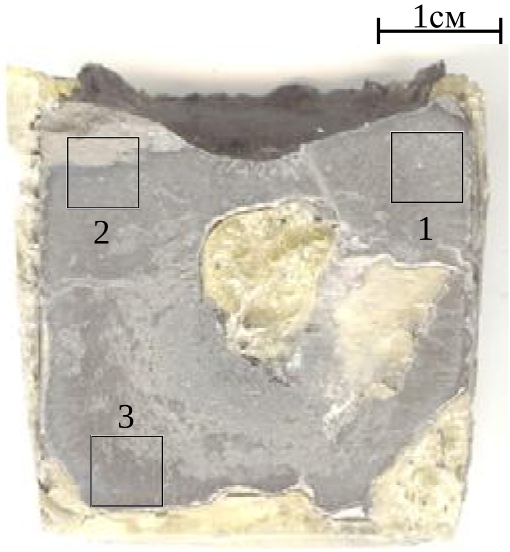

Fig. 3.22. Axial section of CORD34 ingot with marked locations chosen for SEM/EDX analysis

The considered phase (Fig. 3.23, region 1-1-2-1) has the following microstructural peculiarities: even distribution of heavier inclusions (light-colored grains in rounded dark formations). The light-grain formations are likely to testify to the decomposition of solid solution $Zr_{2.74}U_{0.26}O_{1+x}$ in the solid phase during cooling because of the lower uranium solubility limit (Table 3.20, metallized and oxidized solid solutions). This phenomenon can cause a lower than actual solubility during the phase analysis, because it was made for a point, not for the area (Table 3.20).

Similar analysis and calculations were performed for locations 1-1-1 and 1-1-2-1 (Fig. 3.23, Table 3.20). In their case a more accurate evaluation can be provided for ratio between α-Zr(O)-based grains and the matrix solid solution of UO_2-ZrO_2 (region 1-1-1, 46.35 vol.% to 52.27 vol.%, respectively, at the general porosity 1.38 vol.%), and for the phase ratio of the decomposed solid solutions (region 1-1-2-1 and Fig. 3.23b).

SEM composition of region 1-1-2-1 (Fig. 3.23b, metallized ss) can be made more accurate by evaluating the volume ratio of coexisting phases in the decomposed solid solution α-Zr(U)(O): oxidized phase based on solid solution $Zr_{3-x}U_xO$ – 88.43 vol. % (cation composition is taken from point P3, Table 3.20) and metallized phase assumably based on $U_{1-x}Zr_x$ solid solution – 11.57 vol.%. Such evaluation of the average composition of grains of decomposed solid solution is given in Table 3.20 (metallized ss). Molar ratio of decomposed phases $U_{1-x}Zr_x$:$Zr_{3-x}U_xO$ – 13.18:86.82 mol.% (recalculated for $Zr_{1-x}U_xO_{0.33}$).

The following can be concluded from the analysis of SEM images of regions 1-1-2 and 1-1-2-1: in spite of the weak contrast and vague boundaries the matrix phase from the UO_2-ZrO_2 side has at least three distinct phases: solid solution strongly enriched with UO_2 (Table 3.20, point P1 – 35.07 vol.% / 34.28 mol.%); solid solution less enriched with UO_2 (assumably, in composition it is close to point P2 from Table 3.16 – 59.31 vol.% / 59.33 mol.%); small amount of solid solution from ZrO_2 side (Table 3.20, point P2 – 5.63 vol.% / 6.39 mol.%). Calculated average composition of the grains in decomposed solid solution is given in Table 3.20 (oxidized ss).

Recalculation of the ratio between crystallized grains and solid solution matrix into the molar fractions taking these calculations into account (58.54 for 41.46 mol.%, respectively) enables to evaluate the average composition of the mixture as a whole (Table 3.20, $SQ1^{calc}$).

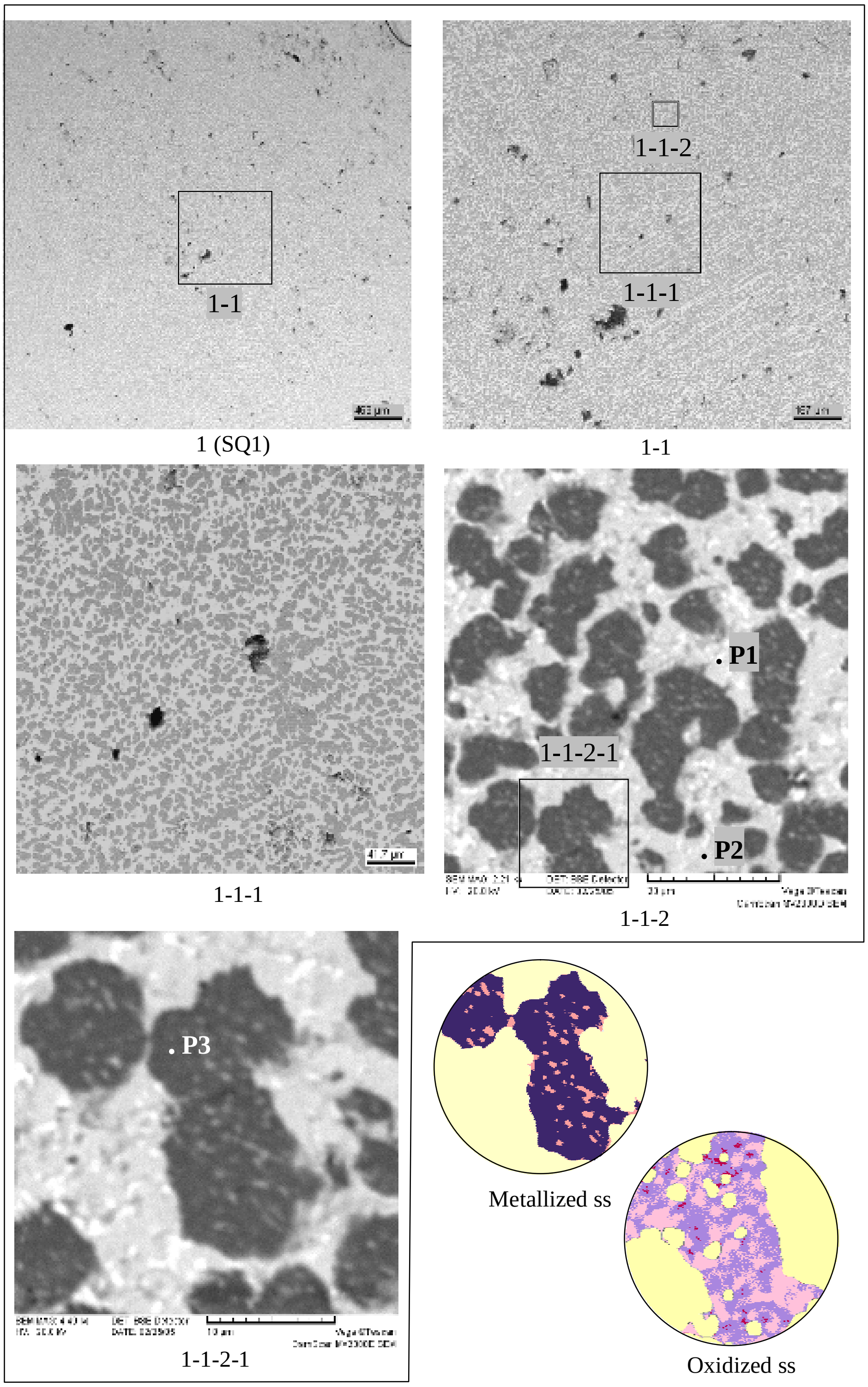

(a) (b)

Fig. 3.23. Microphotographs (a) and microstructure of zone 1-1 (b), region 1, ingot CORD34 presented in four colors

Table 3.20. EDX analysis of region 1

#		U	Zr	O
SQ1	mass.%	47.66	38.43	13.91
	mol.%	13.43	28.26	58.31
	mol.% MeO_x	32.22	67.78	
SQ1^{calc}	mass.%	47.03	45.32	7.65
	mol.%	16.85	42.37	40.78
	mol.% MeO_x	28.45	71.55	
P1	mass.%	84.53	2.38	13.09
	mol.%	29.62	2.17	68.21
	mol.% MeO_x	93.16	6.84	
P2	mass.%	40.13	46.02	13.86
	mol.%	10.95	32.78	56.27
	mol.% MeO_x	25.05	74.95	
P3	mass.%	16.22	72.31	11.46
	mol.%	4.32	50.26	45.42
	mol.% MeO_x	7.91	92.09	
Metallized ss	mass.%	25.34	70.58	4.08
	mol.%	9.38	68.17	22.45
	mol.% MeO_x	12.09	87.91	
Oxidized ss	mass.%	80.22	6.66	13.12
	mol.%	27.40	5.93	66.67
	mol.% MeO_x	82.20	17.80	
Metallized	mass.%	25.39	70.71	3.89
	mol.%	9.48	68.89	21.63
	mol.% MeO_x	12.10	87.90	
Oxidized	mass.%	82.18	6.82	11.01
	mol.%	31.16	6.74	62.09
	mol.% MeO_x	82.21	17.79	

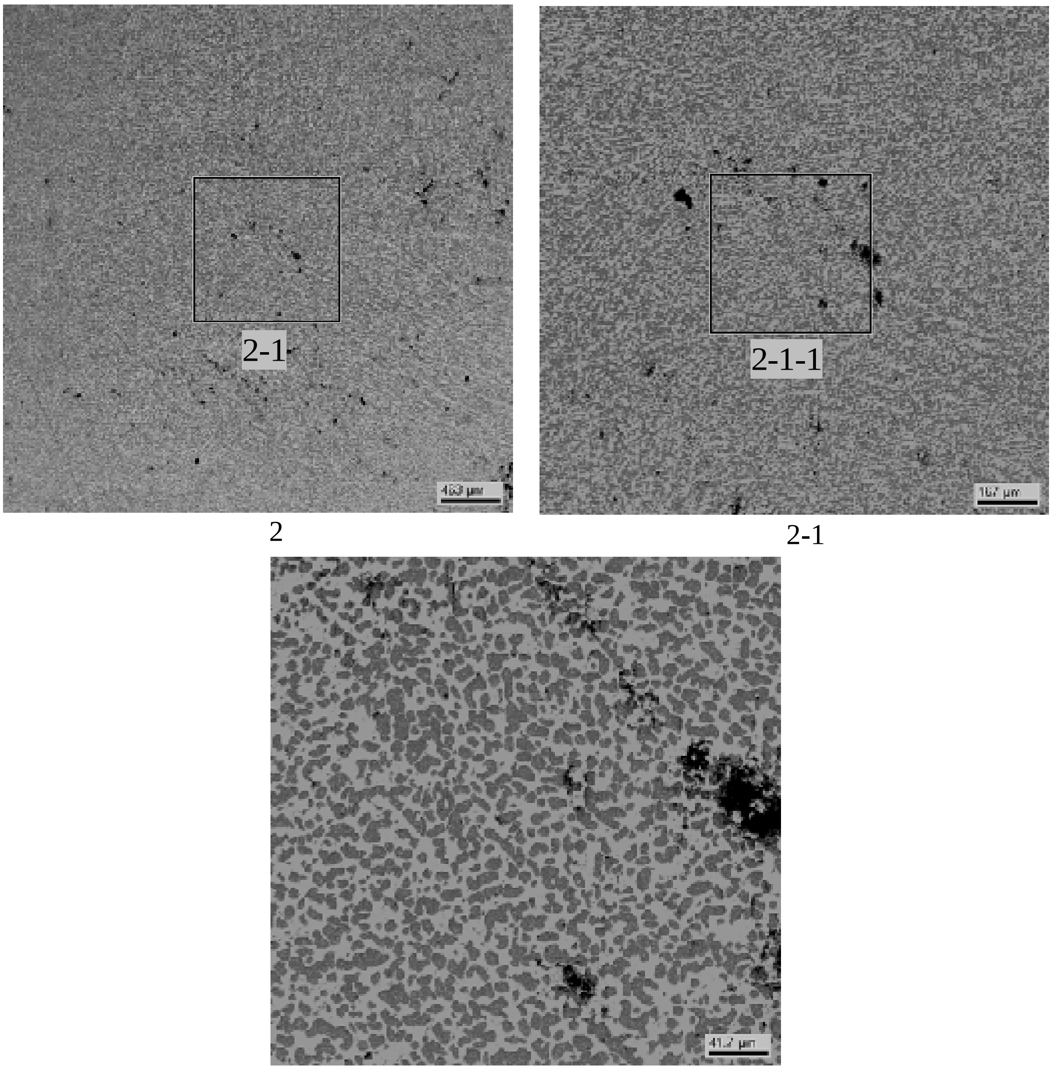

2 2-1

2-1-1

Fig. 3.24. Microphotographs of region 2, ingot CORD34

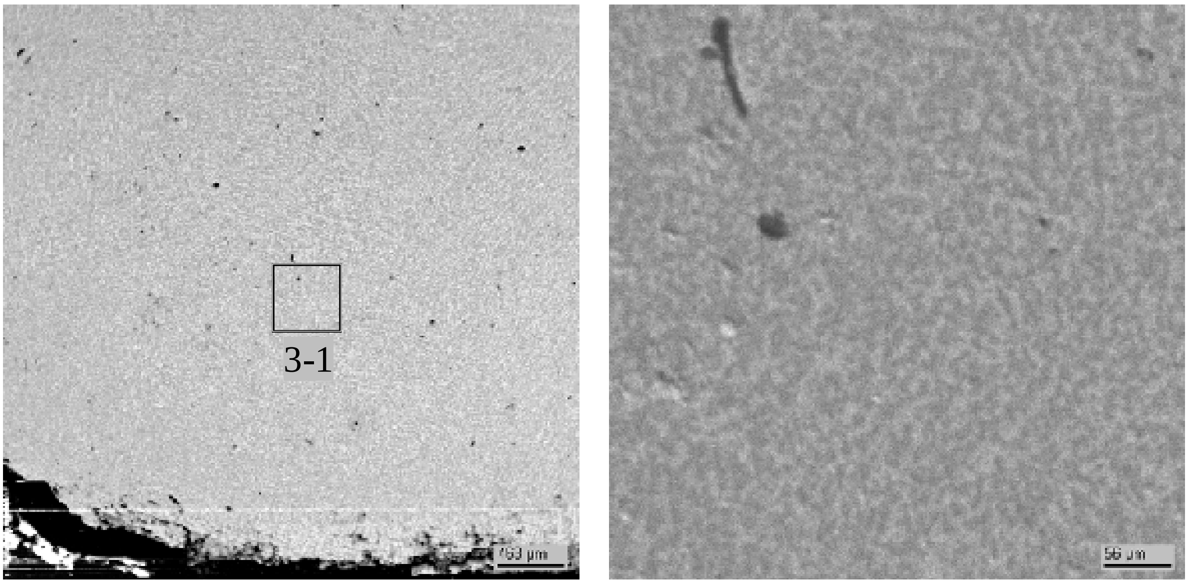

3 3-1 (SQ)

Fig. 3.25. Microphotographs of region 3, CORD34 ingot

Table 3.21. EDX analysis of region 3

#		U	Zr	O
SQ	mass.%	47.92	38.02	14.07
	mol.%	13.45	27.84	58.72
	mol.% MeO$_x$	32.58	67.42	

For the tie-line plotting it was assumed that the composition has a minimum deviation; the same methodology was used as in CORD28. The cation ratio calculated at the previous stage was used (metallized ss and oxidized ss). Oxygen solubility limits in phases were determined from the side of UO_2-ZrO_2 solid solution using /22/ and /26/ (61 mol. % from Zr side and 63 mol. % from U side at 2300°C). Calculation results and determined compositions of coexisting phases are presented on the concentration triangle (Fig. 3.16, metallized, oxidized).

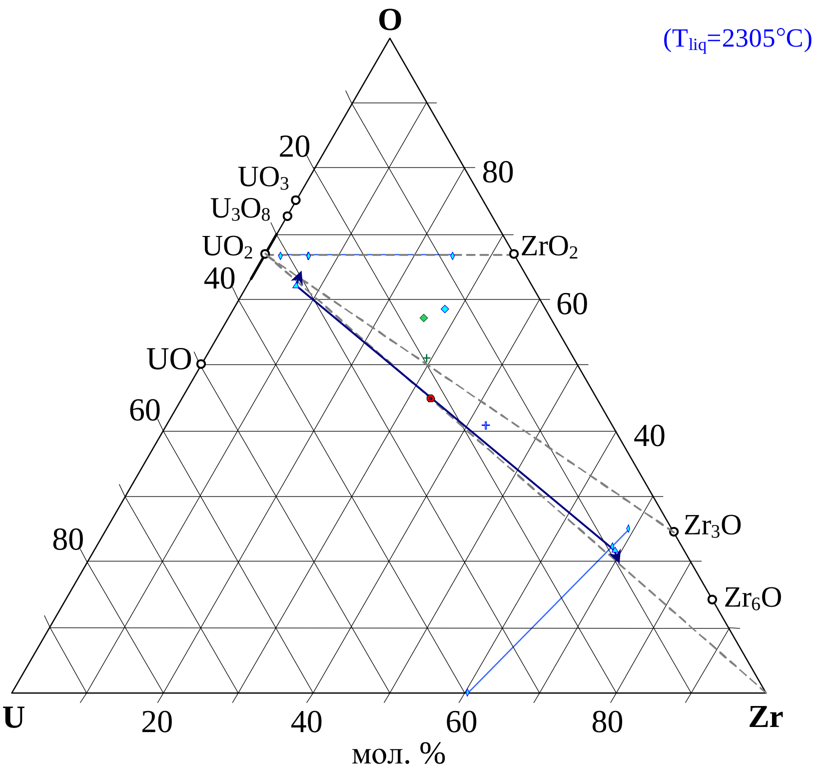

Fig. 3.26. Results of CORD34: ◍ - composition, ◇ - SEM/EDX, + - SEM/Density, ✧ - decomposition lines of solid solutions calculated by the SEM/density method, △ - ends of tie-lines calculated using the data of SEM/EDX/density, composition and oxygen solubility in U and Zr.
Blue – ingot analysis, green – melt sample analysis

SEM/EDX analysis of the crystallized ingot average composition (Fig. 3.23, 3.25) testifies to the difference between cation compositions of the proposed and actual compositions. This can be explained by the depletion of refractory component UO_{2-x} in the crystallized ingot, as the crystallization front was advancing from the crucible wall. This is confirmed by the evaluated average composition by the SEM/density (Table 3.20). Data of chemical analysis and XRF (Tables 3.5 and 3.9, respectively) are less shifted in the direction of Zr, because an average ingot sample was taken for analysis.

Therefore, in spite of considerable scattering of experimental data, it is possible to evaluate oxygen content in the coexisting phases using the available data on their cation composition and phase equilibria in the U-Zr-O system (see Section 1). As it was shown by the analysis of CORD34, the correctness of initial assumptions can be controlled (Fig. 3.26). In such calculations the issue of stratification of the studied composition is disregarded, because the character of the tie-line slope should be different in the region of two coexisting liquid phases.

Experiment CORD37

Templates were made from the melt sample and subjected to analysis (Fig. 3.27 and 3.28). Microstructure of samples is strongly dispersed (Fig. 3.27, region 1 or Fig. 3.28, region 3-1). Some samples contain rounded inhomogeneous inclusions - this testifies to the stratification of this composition at the temperature of quenching start (Fig. 3.27, region 4 and Fig. 3.28, regions 1 and 3). It is not possible to identify compositions of crystallized phases by SEM/EDX in such finely dispersed structure. Therefore, the evaluation of oxygen content by SEM/density is not possible too. Additionally to that weak contrast of the image (Fig. 3.29b) complicates the identification of volume fractions (light phase is solid solution-based from the side of UO_2 ~45.68 vol.%; grey phase is more enriched with ZrO_2 ~10.96 vol.%; dark phase is α-Zr(U)(O)-based ~43.37 vol.%). Due to the mentioned reasons the evaluation is rough.

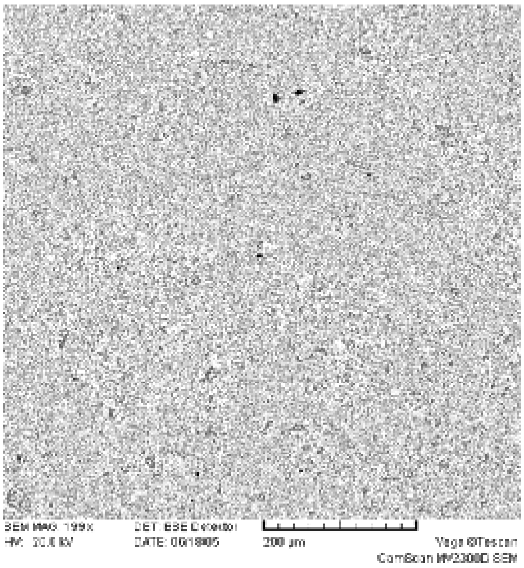

1 (SQ1)

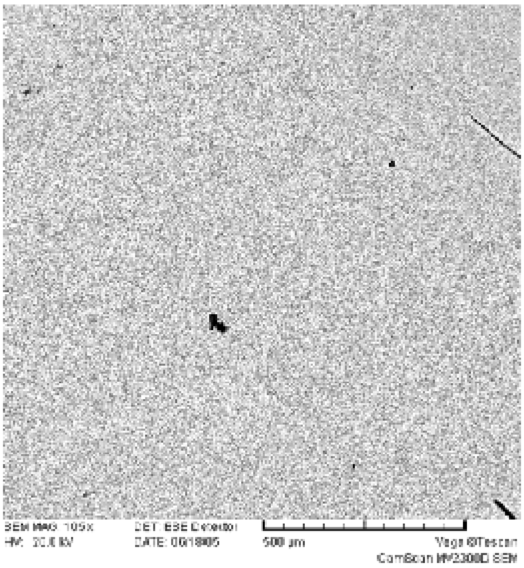

2 (SQ2)

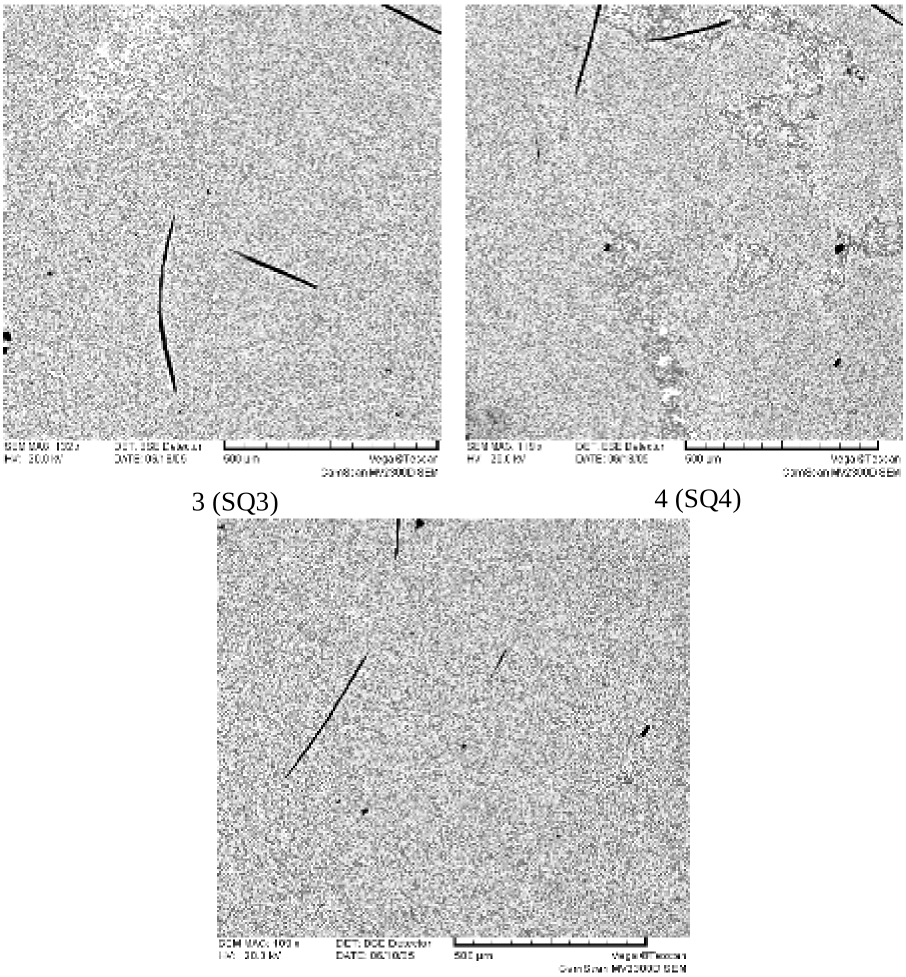

3 (SQ3) 4 (SQ4)

5 (SQ5)

Fig. 3.27. Microphotographs of specimens taken from Sample #1, CORD37

Table 3.21. EDX analysis of specimens taken from Sample #1

#		U	Zr	O
SQ1	mass.%	63.99	27.33	8.68
	mol.%	24.20	26.97	48.83
	mol.% MeO_x	47.30	52.70	
SQ2	mass.%	62.02	28.36	9.61
	mol.%	22.23	26.53	51.24
	mol.% MeO_x	45.59	54.41	
SQ3	mass.%	62.72	27.35	9.93
	mol.%	22.26	25.32	52.42
	mol.% MeO_x	46.78	53.22	
SQ4	mass.%	63.41	27.62	8.97
	mol.%	23.58	26.79	49.63
	mol.% MeO_x	46.81	53.19	
SQ5	mass.%	62.25	29.07	8.67
	mol.%	23.30	28.40	48.3
	mol.% MeO_x	45.07	54.93	

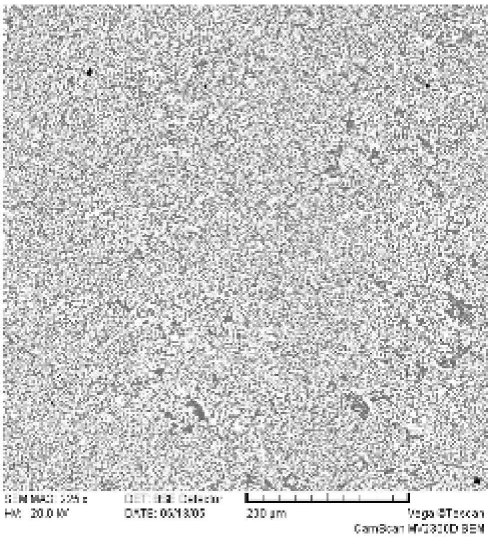

1 (SQ1)

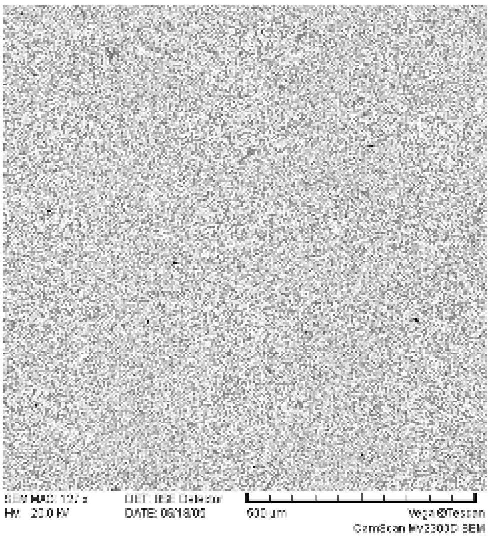

2 (SQ2)

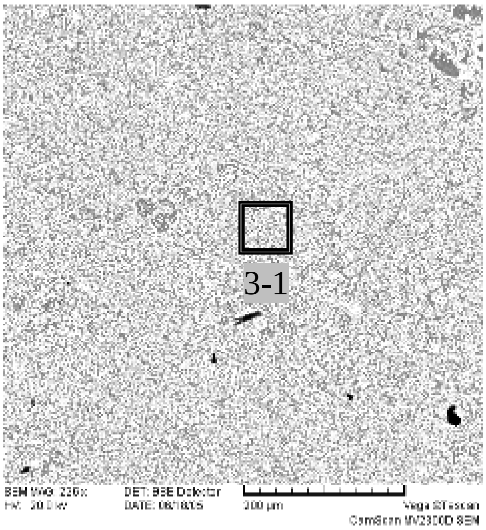

3 (SQ3)

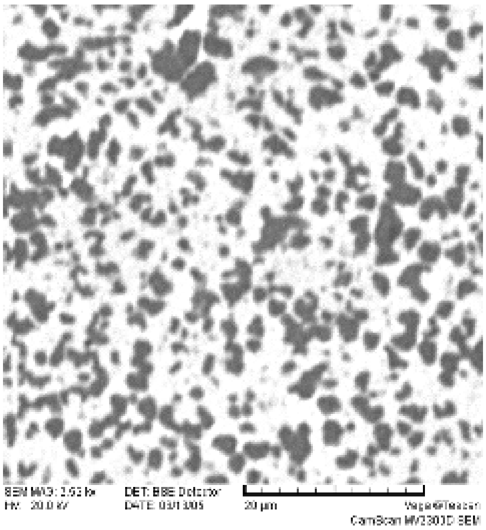

3-1

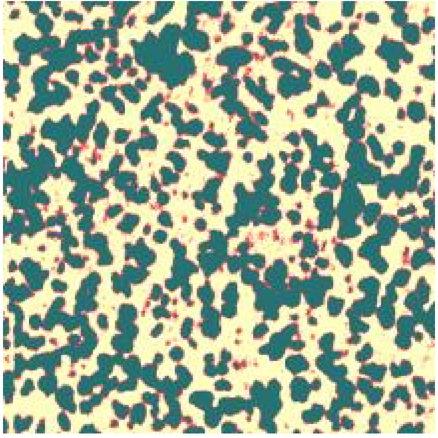

3-1 (b)

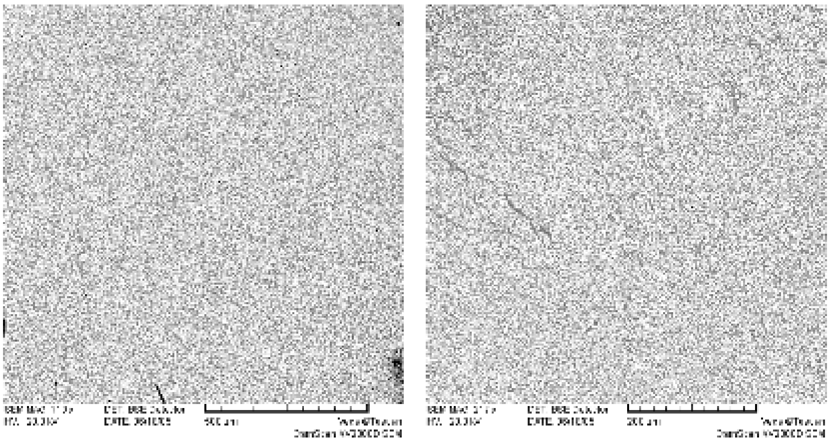

4 (SQ4) 5 (SQ5)

Fig. 3.28. Microphotographs of specimens taken from Sample #2, CORD37

Table 3.22. EDX analysis of specimens taken from Sample #2

#		U	Zr	O
SQ1	mass.%	60.09	30.36	9.55
	mol.%	21.35	28.15	50.49
	mol.%	43.14	56.86	
SQ2	mass.%	59.66	29.56	10.78
	mol.%	20.07	25.96	53.97
	mol.%	43.61	56.39	
SQ3	mass.%	58.83	29.97	11.20
	mol.%	19.37	25.75	54.88
	mol.%	42.93	57.07	
SQ4	mass.%	60.10	30.29	9.61
	mol.%	21.30	28.01	50.69
	mol.%	43.20	56.80	
SQ5	mass.%	58.47	31.09	10.44
	mol.%	19.83	27.51	52.66
	mol.%	41.89	58.11	

Fig. 3.29. Axial section of CORD37 ingot надписи на русском!

After crystallization the ingot separated into two parts – top having the mass of 198.8 g, and bottom having the mass of 253.7g.

Fig. 3.30 shows the top part of the axial ingot section with marked locations chosen for SEM/EDX studies; the bottom part is shown in Fig. 3.35.

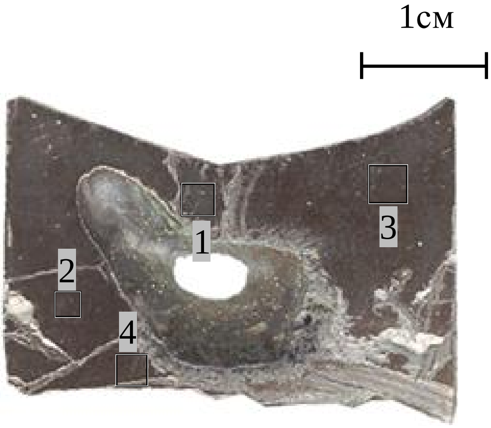

Fig.3.30. Top part (a) of the axial ingot section with marked locations of SEM/EDX studies, CORD37

Microstructure of the ingot top has a dendrite character in the whole studied surface of the cut section (Figs. 3.31-3.34), which indicates the quenching conditions of crystallization. A large pore in the central part should be noted – it takes about 1/3 of the top part volume. Its origin can be explained by shrinking and gas liberation during the melt crystallization. In terms of the phase formation the microstructure is similar to the microstructure observed in CORD-34 (compare 3.22 and 3.31). The dendrite-forming solid solution based on UO_2-ZrO_2 can be decomposed into, at least, two phases: UO_2-enriched phase (Fig. 3.31, point P1) and a phase with a lower content of UO_2 (Fig. 3.31, point P2). The phase undergoing a secondary crystallization in this layer is the α-Zr(U)(O)-based phase, which at cooling decomposes into two phases –α-Zr(U)(O)-based solid solution and, assumably, U-Zr-based solid solution (Fig. 3.31, region 1-1b, dark rounded phase with light-colored inclusions).

Volume ratios of coexisting phases (Fig. 3.31, 1-1b) were calculated separately for regions 1, 1-1 (Fig. 3.31) and region 3 (Fig. 3.33):

- total porosity – 0.31 vol. %,
- dendrite phase – 65.00 vol. % (solid solution enriched with UO_2 – 9.44 vol. %, matrix solid solution – 89.37 vol. %, α-Zr(O) grains– 1.19 vol. %),
- α-Zr(U)(O)-based solid solution – 34.69 vol. % (α-Zr(U)(O)-based solid solution – 96.99 vol. %, U-Zr – 3.01-based solid solution vol. %)

For region 2 (Fig. 3.32) having higher enrichment with refractory component in comparison with regions 1 and 3 (Fig. 3.31 and 3.33 respectively):

- total porosity – 0.10 vol. %,

- dendrite phase – 69.46 vol. % (solid solution enriched with UO_2 – 18.01 vol. %, matrix solid solution – 80.83 vol. %, α-Zr(O) grains– 1.16 vol. %),
- α-Zr(U)(O)-based solid solution – 30.44 vol. % (α-Zr(U)(O)-based solid solution – 97.22 vol. %, U-Zr-based solid solution – 2.78 vol. %).

For evaluating the credibility of calculations based on the proposed methodology all data were plotted on the diagram (Fig.3.42). The cation composition for the U-Zr-based solid solution was chosen like in CORD-34. It is reasonable to attribute fine grains of α-Zr(O) crystallized in the dendrite-forming phase to the secondary α-Zr(U)(O)-based phase, and, in this way, to correct the evaluated volume ratios of primary and secondary crystallization phases for regions 1, 1-1 and 3 (64.43 to 35.57 vol. %, respectively) and for region 2 (68.72 to 31.28 vol. %, respectively). Fig. 3.42 shows the compositions calculated using the SEM/density method. The shift of cation composition to the direction of uranium is probably explained by the 'capture' of UO_2-enriched phase during the SEM/EDX identification of the main matrix phase (point P2 Fig.3.31), or by the presence of a third phase from the ZrO_2-UO_2 side, which had a weak contrast with the matrix phase.

SEM/EDX study of the ingot bottom enables to conclude that it is very inhomogeneous in microstructure and composition. Its central part (Fig. 3.40) has the grains of ZrO_2-UO_2 solid solution. This explains a large scattering of data on cation ratio in the compositions determined by available methods (Fig. 3.42). For these reasons it is not possible to determine the composition of this experiment, differently from previous ones. The tie-line connecting the compositions of coexisting liquids can be constructed indirectly, using the data about the locally selected zones.

At this we should note certain peculiarities of the ingot bottom part crystallization, which provide a rough estimate of the ratio and composition of liquids coexisting in the system.

Analysis of the microstructure of the metallized component enables to conclude that $(U,Zr)O_{2-x}$ solid solution acts as the primary crystallization phase for this region; it co-crystallizes with the solid solution α-Zr(U)(O)-based phase, which, in its turn, at cooling decomposes into α-Zr(U)(O) and U-Zr solid solution (Fig. 3.36, regions 1-2-1, 1-2-1-1). It is very difficult to evaluate the amount of $(U,Zr)O_{2-x}$ solid solution using the SEM/EDX data because of the lack of contrast with drop-like inclusions (see Fig. 3.38, region 4). Only an expert estimate can be made - ~3 vol.% of this phase for the considered region. In relation to that it can be asserted that the composition shift is not considerable (Fig. 3.42).

Most fusible phase in this region is the U(Zr)-based solid solution (Fig. 3.36, points P1 and P2, Table3.26). Oxygen content measured by EDX in the last phase is doubtful, because it does not agree with available data on phase equilibria in the U-O system. Therefore, if we neglect dissolved Zr, which, in principle, can serve as the oxygen stabilizer in the considered phase, the oxygen content in it is likely to be minimal.

Analysis of zone 1-2-1 (Fig.3.36) was carried out for the evaluation of average composition in the metallized component of the melt. Phase ratio in it was determined as 42.14 vol.% of the U(Zr) solid solution-based phase and 57.86 vol.% α-Zr(U)(O)-based phase (which, in its turn, decomposes in the solid phase into the U-Zr solid solution – 4.38 vol.% and α-Zr(U)(O) – 95.62 vol. %). Table 3.26 (region $SQ^{metallized}$) presents the average composition of the metallized component calculated using the method of SEM/density for zone 1-2-1 without oxidic component. It is not possible to make a correct calculation of the average composition of the oxidized phase due to its small volume; but it is possible to make a similar analysis for the periphery zone of region 4 (Fig.3.38).

Image processing (Fig.3.38, 4b) enabled to get the ratio between the drop-like inclusions and metallized component of region 4, which was 25.06 to 74.9 vol. %. The metallized component has 60.46 vol. % of the U(Zr) solid solution-based phase and 39.54 vol. % of α-Zr(U)(O)-based phase (which, in its turn, decomposes into U-Zr solid solution – 6.08 vol. % and α-Zr(U)(O) – 93.92 vol. %, in the solid phase in accordance with region 4-1-1b processing results (Fig.3.38). Ratio between the α-Zr(U)(O) solid solution-based grains to the UO_2-ZrO_2 solid solutions, both for oxidized drops crystallized in region 4b (Fig.3.38), and for 4-1-1b drop gives a 0.5 vol.% difference, which can serve as the validity proof of determined volume ratios and enables to take an average value for evaluation – 32.22 to 67.78 vol. %, respectively. The UO_2-ZrO_2 solid solution ratio is 27.32 vol. % for the UO_2-enriched solid solution and 72.68 vol. % for the solid solution with a smaller UO_2 content. The average composition of metallized and oxidized components, as well as the total average composition of zone 4 (Fig.3.38), calculated by the SEM/density method, are presented in Table 3.28 (region $SQ^{metallized}$, $SQ^{oxidized}$, SQ^{calc}). The resulting evaluated data are plotted on the concentration triangle and a tie-line is constructed. The accuracy of its position is very much determined by the oxygen content and input data on the cation ratio in the coexisting phases, also by the densities attributed to the considered phases. The stratification effect in the periphery zone can be explained by the secondary stratification of the metallized phase during the melt cooling to the monotectic temperature. At this the average composition of region 4 (Fig.3.38) should be close to the metallized phase coexisting in equilibrium with the oxidized phase at the temperature of quenching start, which enables to determine the tie-line position at the quenching temperature. Consequently, the tie-line constructed using the data on the ingot top (SQ^{calc} Table3.23) and average composition of region 4 (Table3.28, SQ^{calc}) corresponds to the temperature, from which quenching was started. As mentioned before, it was not possible to make a reliable evaluation of the system composition. The secondary stratification is schematically explained in Fig. 3.43.

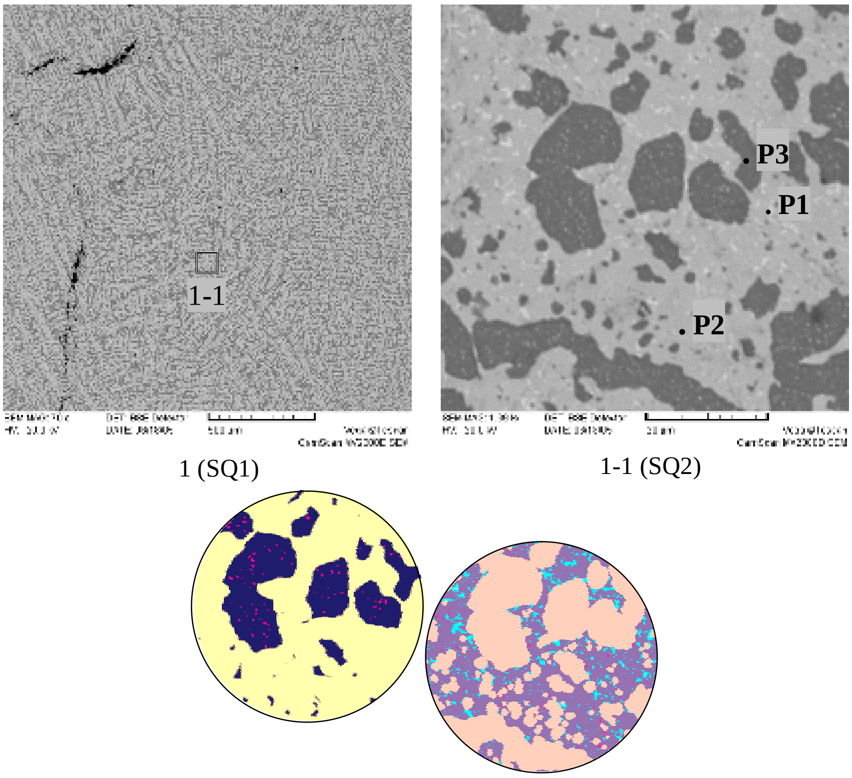

1 (SQ1)

1-1 (SQ2)

1-1 (b)

Fig. 3.31. Microphotographs of region 1, CORD37 ingot

Table 3.23. EDX analysis of region 1

#		U	Zr	O
SQ1	mass.%	58.16	30.49	11.35
	mol.%	18.97	25.94	55.09
	mol.%	42.23	57.77	
SQ1^{calc}	mass.%	64.95	24.61	10.45
	mol.%	22.82	22.56	54.62
	mol.%	50.29	49.71	
SQ2	mass.%	58.89	30.75	10.36
	mol.%	20.08	27.36	52.55
	mol.%	42.33	57.67	
P1	mass.%	89.26	1.32	9.42
	mol.%	38.33	1.48	60.2
	mol.%	96.29	3.71	
P2	mass.%	84.69	3.39	11.92
	mol.%	31.26	3.26	65.47
	mol.%	90.55	9.45	
P3	mass.%	9.00	84.19	6.81
	mol.%	2.73	66.58	30.69
	mol.%	3.94	96.06	

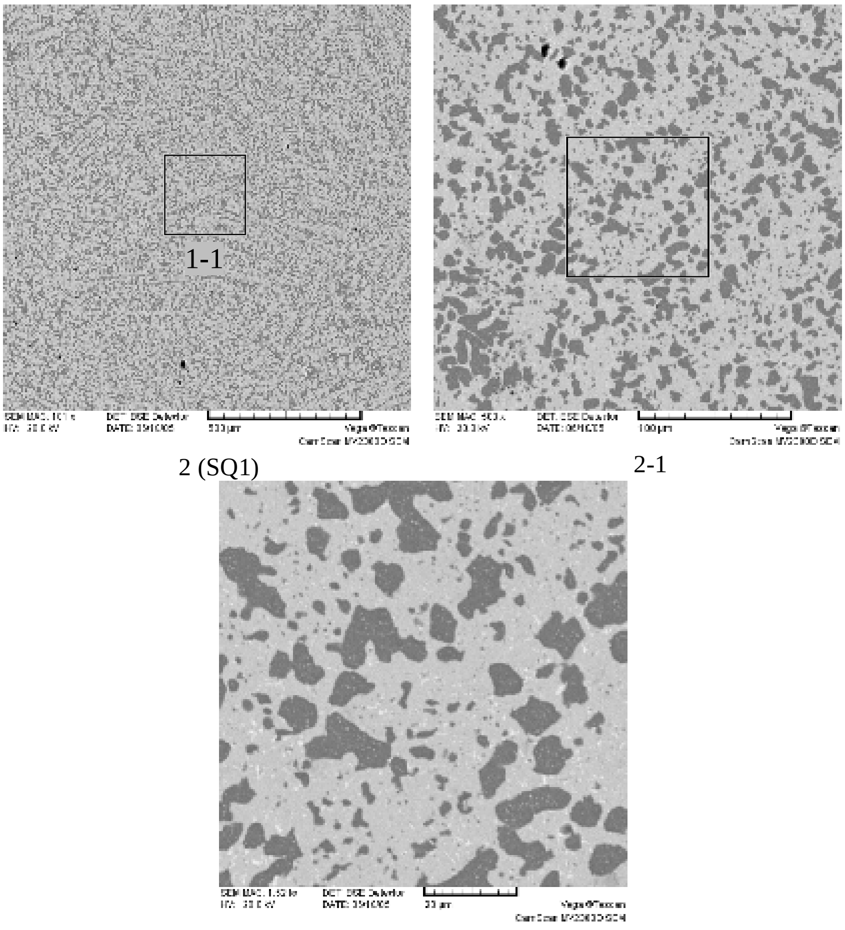

2 (SQ1)

2-1

2-1-1

Fig.3.32. Microphotographs of region 2, CORD37 ingot

Table 3.24. EDX analysis of region 2

#		U	Zr	O
SQ1	mass.%	60.12	28.34	11.54
	mol.%	19.67	24.19	56.14
	mol.% MeO_x	44.85	55.15	

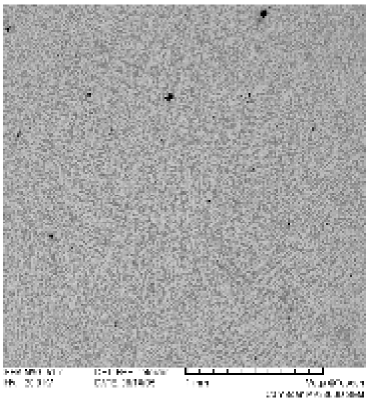

3 (SQ1)

Fig.3.33. Microphotographs of region 3, CORD37 ingot

Table 3.25. EDX analysis of region 3

#		U	Zr	O
SQ1	mass.%	58.23	30.26	11.5
	Mol.%	18.89	25.61	55.5
	Mol.%	42.44	57.56	

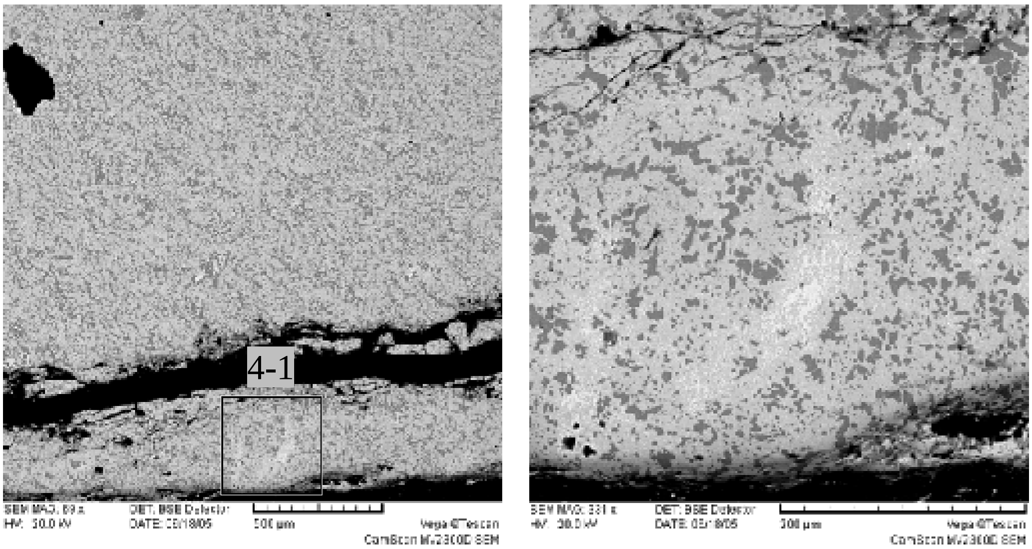

4

4-1

Fig. 3.34. Microphotographs of region 4, CORD37 ingot

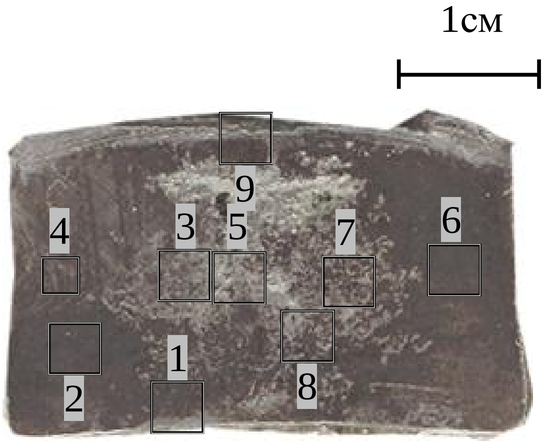

Fig.3.35. Bottom part of the ingot axial section with marked locations chosen for SEM/EDX studies, CORD37

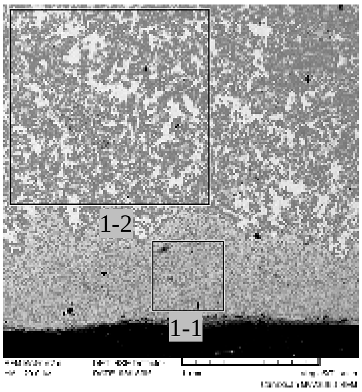

1

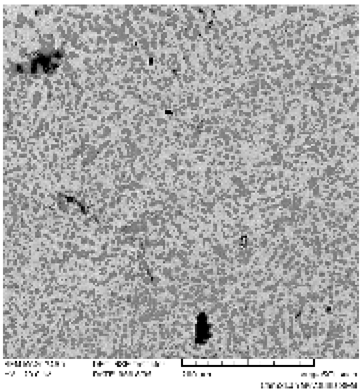

1-1 (SQ1)

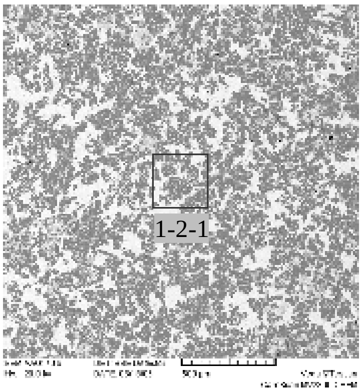

1-2 (SQ2)

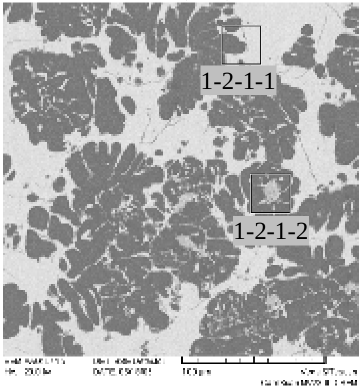

1-2-1

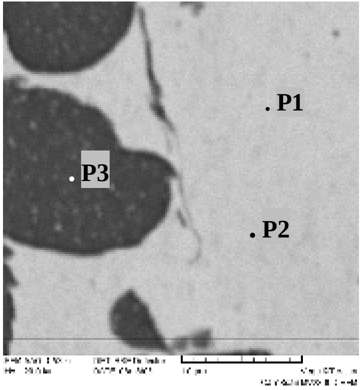

1-2-1-1

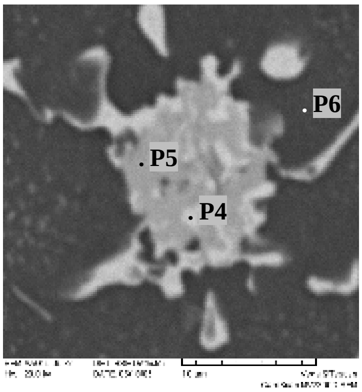

1-2-1-2

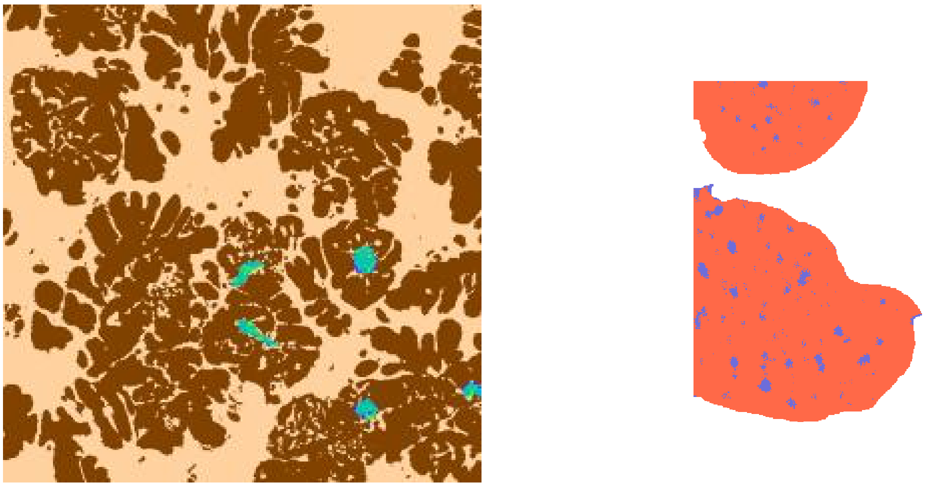

1-2-1 (b) 1-2-1-1 (b)

Fig. 3.36. Microphotographs of region 1, CORD37 ingot bottom

Table 3.26. EDX analysis of region 1

#		U	Zr	O
SQ1	mass.%	57.83	32.17	10.00
	mol.%	19.90	28.89	51.21
	mol.% MeO$_x$	40.79	59.21	
SQ2	mass.%	51.47	41.29	7.24
	mol.%	19.29	40.37	40.34
	mol.% MeO$_x$	32.33	67.67	
SQ^{metallized}	mass.%	66.35	31.91	1.74
	mol.%	37.80	47.43	14.77
	mol.% MeO$_x$	44.35	55.65	
P1	mass.%	89.84	2.85	7.31
	mol.%	43.6	3.61	52.8
	mol.% MeO$_x$	92.36	7.64	
P2	mass.%	90.35	2.76	6.90
	mol.%	45.14	3.59	51.27
	mol.% MeO$_x$	92.63	7.37	
P3	mass.%	5.53	88.36	6.11
	mol.%	1.69	70.51	27.79
	mol.% MeO$_x$	2.34	97.66	
P4	mass.%	90.68	1.00	8.32
	mol.%	41.77	1.20	57.03
	mol.% MeO$_x$	97.20	2.80	
P5	mass.%	87.74	2.38	9.88
	mol.%	36.42	2.58	61.00
	mol.% MeO$_x$	93.38	6.62	
P6	mass.%	6.03	86.91	7.06
	mol.%	1.78	67.12	31.09
	mol.% MeO$_x$	2.59	97.41	

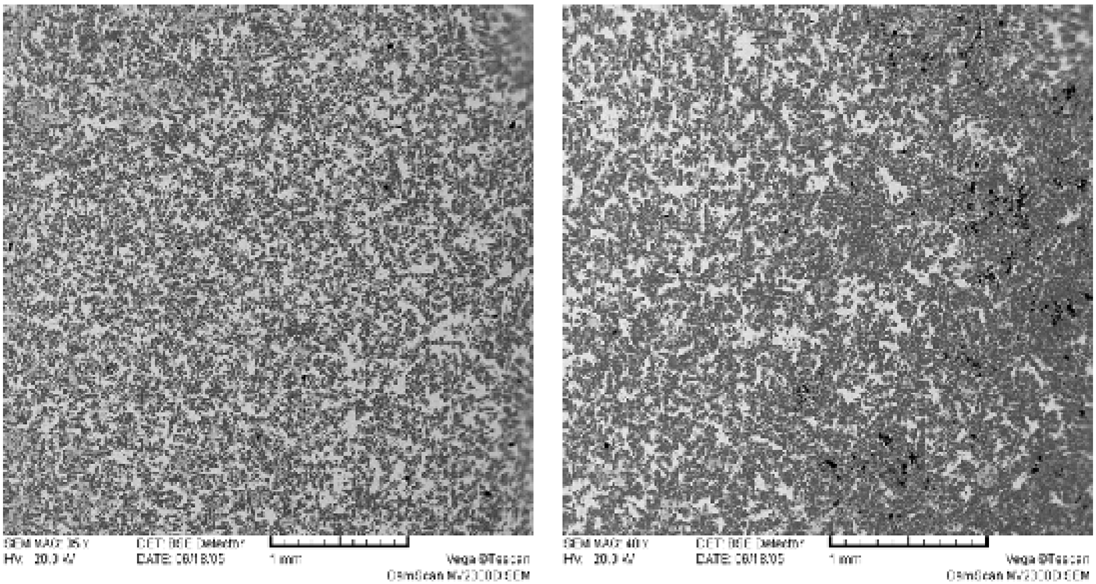

2 (SQ1)

3

Fig.3.37. Microphotographs of regions 2 and 3, CORD37 ingot bottom

Table 3.27. EDX analysis of region 2

#		U	Zr	O
SQ1	mass.%	56.01	36.49	7.5
	mol.%	21.31	36.22	42.47
	mol.% MeO_x	37.04	62.96	

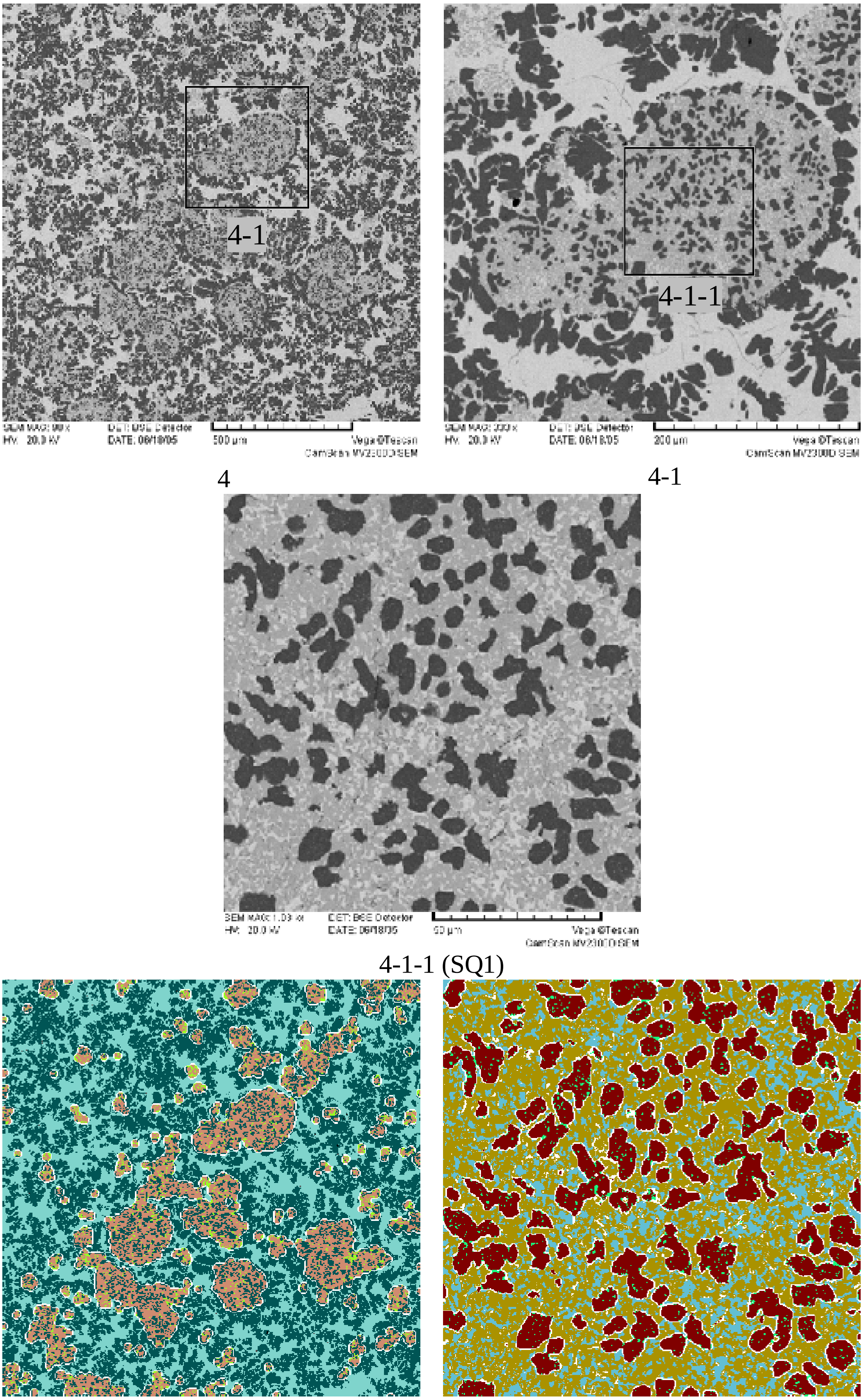

4

4-1

4-1-1 (SQ1)

4 (b) (SQ^{calc})

4-1-1 (b)

Fig.3.38. Microphotographs of region 4, CORD37 ingot bottom

Table 3.28. EDX analysis of region 4

#		U	Zr	O
SQ1	mass.%	64.08	26.41	9.50
	mol.%	23.35	25.12	51.53
	mol.%	48.18	51.82	
SQ^{metallized}	mass.%	64.53	33.65	1.83
	mol.%	35.95	48.91	15.13
	mol.%	42.36	57.64	
SQ^{oxidized}	mass.%	67.90	21.66	10.44
	mol.%	24.27	20.2	55.53
	mol.%	54.58	45.42	
SQ^{calc}	mass.%	65.27	31.01	3.71
	mol.%	32.40	40.17	27.43
	mol.%	44.65	55.35	

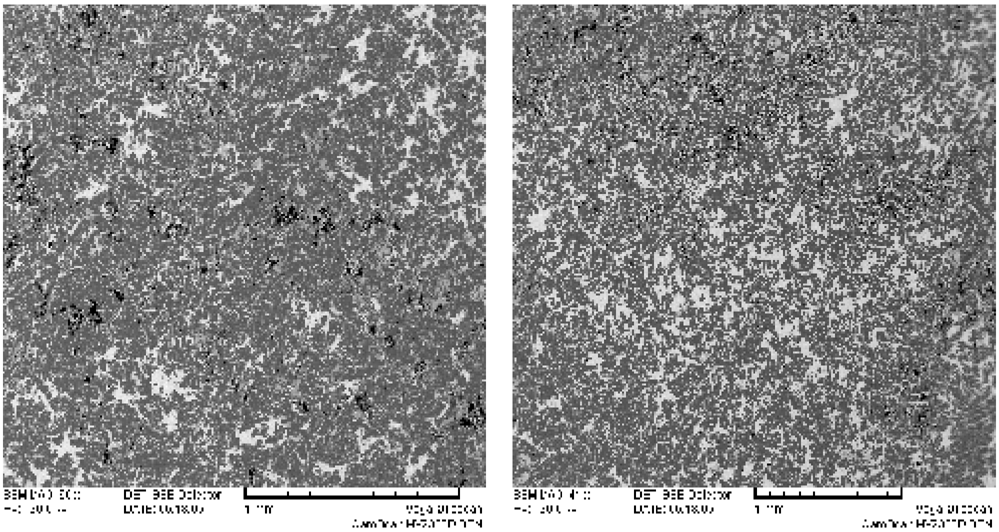

5 (SQ1) 6 (SQ2)

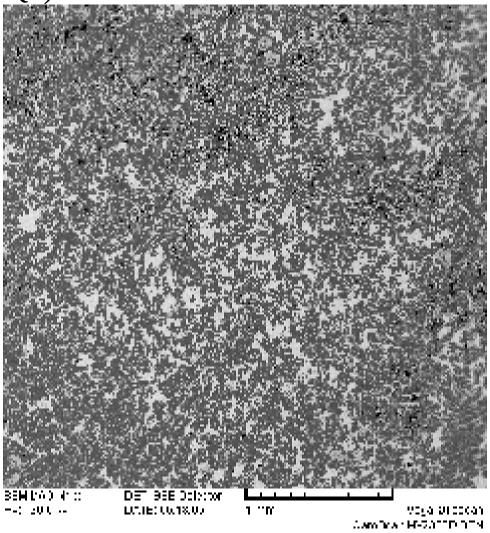

7 (SQ3)

Fig. 3.39. Microphotographs of regions 5-7, CORD37 ingot bottom

Table 3.29. EDX analysis of regions 5-7

#		U	Zr	O
SQ1	mass.%	40.44	52.34	7.23
	mol.%	14.21	48.00	37.79
	mol.% MeO_x	22.84	77.16	
SQ2	mass.%	50.97	42.11	6.92
	mol.%	19.33	41.66	39.01
	mol.% MeO_x	31.69	68.31	
SQ3	mass.%	45.56	47.64	6.80
	mol.%	16.81	45.86	37.33
	mol.% MeO_x	26.82	73.18	

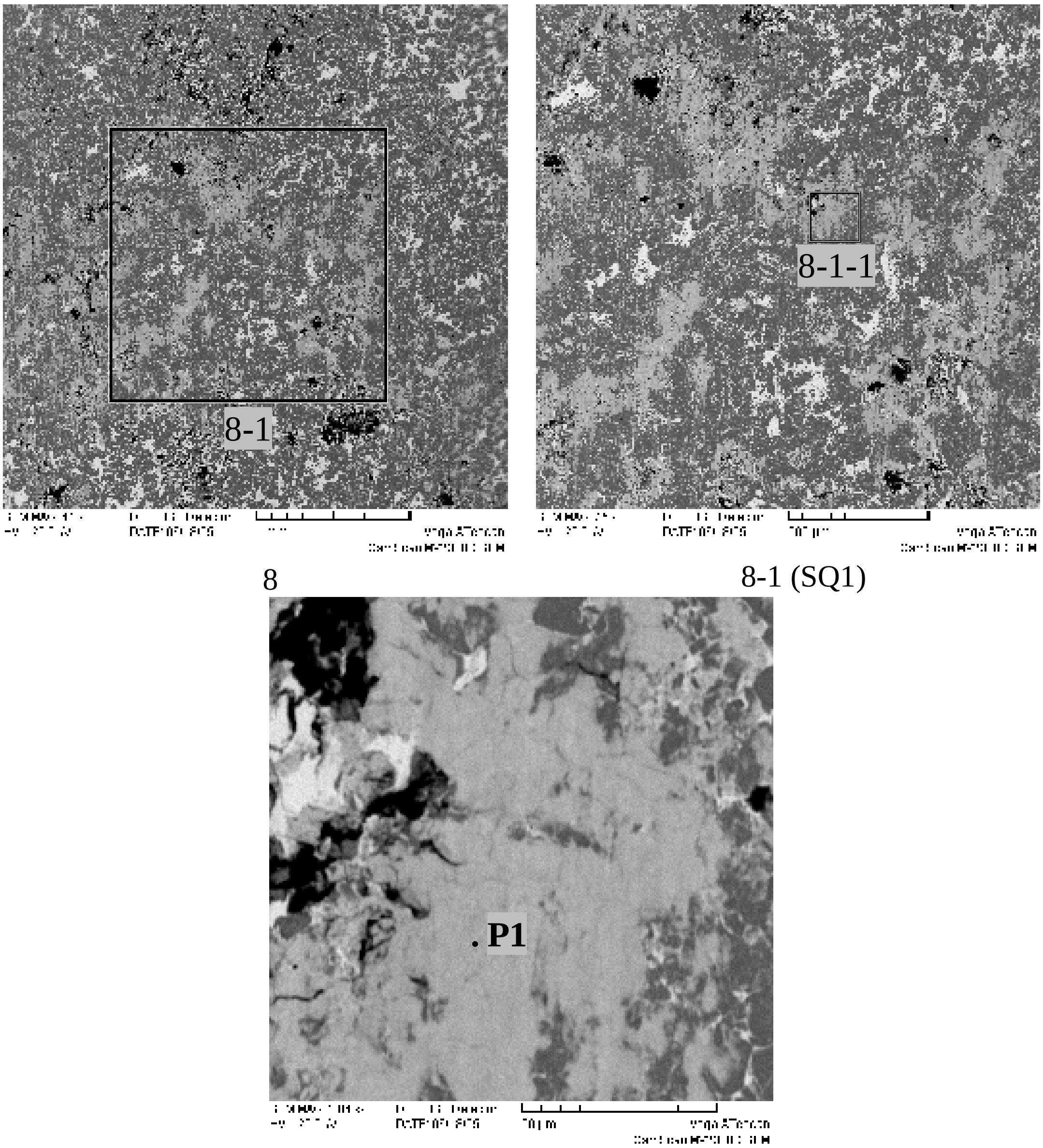

8

8-1 (SQ1)

8-1-1

Fig. 3.40. Microphotographs of region 8, CORD37 ingot bottom

Table 3.30. EDX analysis of region 8

#		U	Zr	O
SQ1	mass.%	43.38	48.96	7.67
	mol.%	15.21	44.79	40
	mol.% MeO_x	25.35	74.65	
P1	mass.%	74.24	13.72	12.05
	mol.%	25.66	12.37	61.97
	mol.% MeO_x	67.47	32.53	

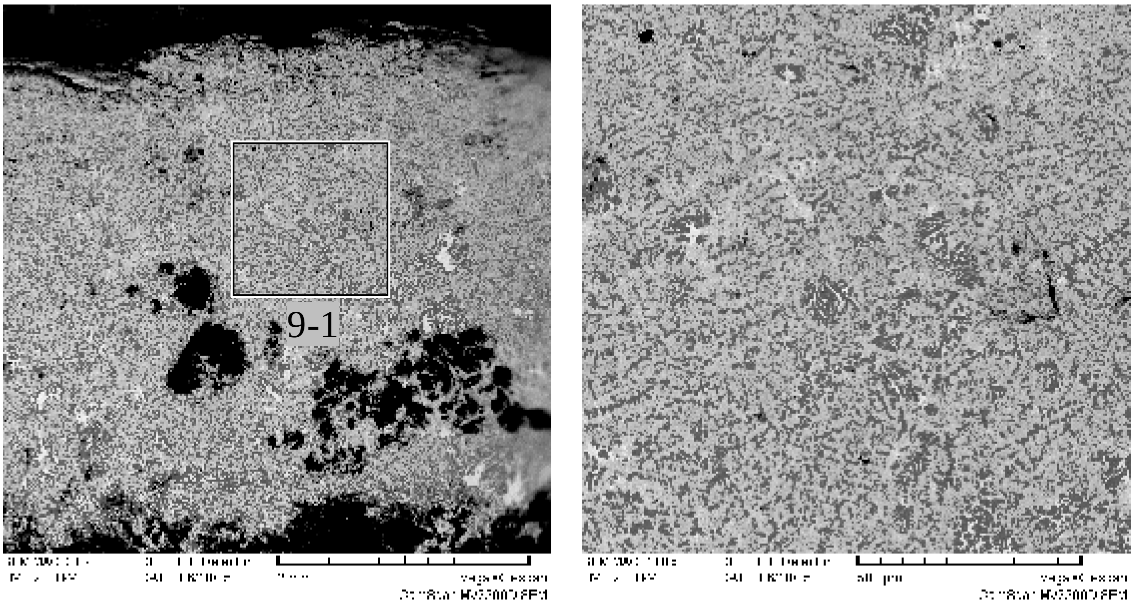

9 9-1 (SQ1)

Fig. 3.41. Microphotographs of region 9, CORD37 ingot bottom

Table 3.31. EDX analysis of region 9

#		U	Zr	O
SQ1	mass.%	62.21	27.24	10.55
	mol.%	21.43	24.48	54.09
	mol.% MeO_x	46.68	53.32	

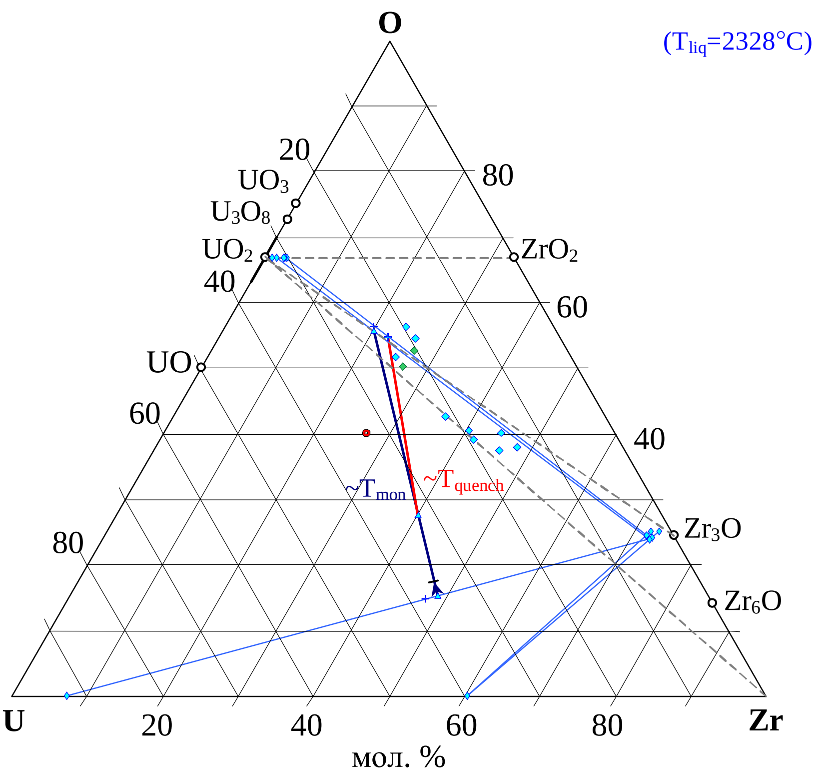

Fig. 3.42. Results of CORD37:◎ - composition, ◇ - SEM/EDX, + - SEM/density, ✧ - decomposition lines of solid solutions calculated by SEM/density, △ - ends of tie-lines calculated using the data of SEM/EDX/density and oxygen solubility in U and Zr in region 4.

Blue – ingot analysis, green – melt sample analysis.

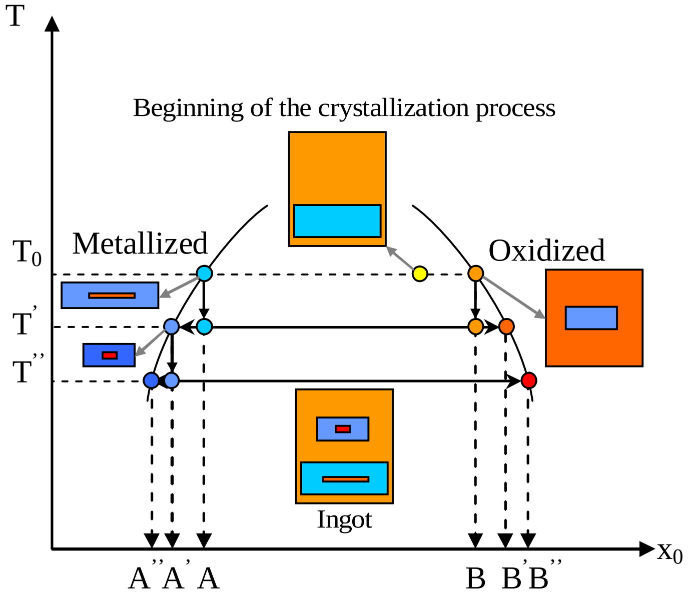

Fig. 3.43. Schematics of secondary stratification

T_0 – melt temperature, T' – melt temperature before the crystallization start; A and B – composition of metallic and oxidic melts during melting, respectively; A' and B' – composition of metallic and oxidic melts at temperature T', respectively, A'' и B'' – composition of metallic and oxidic melts at temperature T''

Experiment CORD41

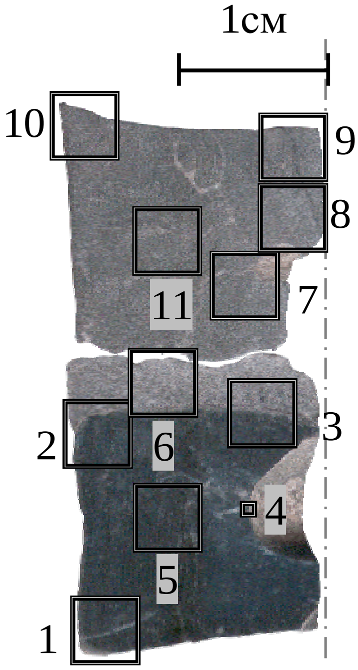

Fig. 3.44. Axial section of CORD41 ingot with locations of SEM/EDX studies

Two parts are clearly seen in the photograph of the CORD41 ingot axial section. The top part is opaque and homogeneous along the whole surface, and the bottom one has two layers – 3mm-wide opaque layer and the layer having metallic luster (Fig. 3.44).

Analysis of the cut section was made by the ABT-55 device equipped with a microprobe insensitive to light elements.

The analysis showed that the melt had two coexisting layers – top (light) oxidized layer and bottom (heavy) metallized one. Further one they will be referred to as oxidic and metallic layers.

During cooling and crystallization the phases formed a layered structure with a distinct boundary. At approx. 2 mm from the boundary both oxidic and metallic layers have metallic and oxidic drop-like inclusions. These droplets are likely to be secondary formations produced during the cooling of each layer heated to 160ºC above the monotectics temperature (in accordance with pyrometric measurements of the melt surface). The droplets are concentrated near the boundary due to a big difference of their and matrix liquid density. Effects of convective instability of the boundary also cannot be included due to the active convective mixing of the melt at the IMCC, and, as a consequence, penetration of droplets of one liquid into another.

Typical microstructure of the metallic bottom layer is shown in Figs. 3.45 and 3.49. Insignificant porosity is observed. The available data on phase equilibria in the U-O system (Fig. 1.14-1.16) enable to assert that U-based phase occupies most of the area (Table 3.32, P1; Table 3.35, P1; Table 3.36, P1). The rest two dendrite crystallized phases are UO_2-based solid solution having a small concentration of ZrO_2 (Table 3.32, P2) ZrO_2-based admixture (Table 3.32, P3-P5).

Analysis of 1-1b, 5b and 5-1b area images (Fig. 3.45 and 3.49) provides the average estimate of volume ratios of coexisting phases: porosity – 0.28 vol. %, ZrO_2-based admixture – 0.75 vol. %, UO_2-based phase of primary crystallization – 4.57 vol. %, U-based phase – 94.41 vol. %. Calculation of composition by the method of SEM/density for this composition is given in Table 3.35, $SQ1^{calc}$.

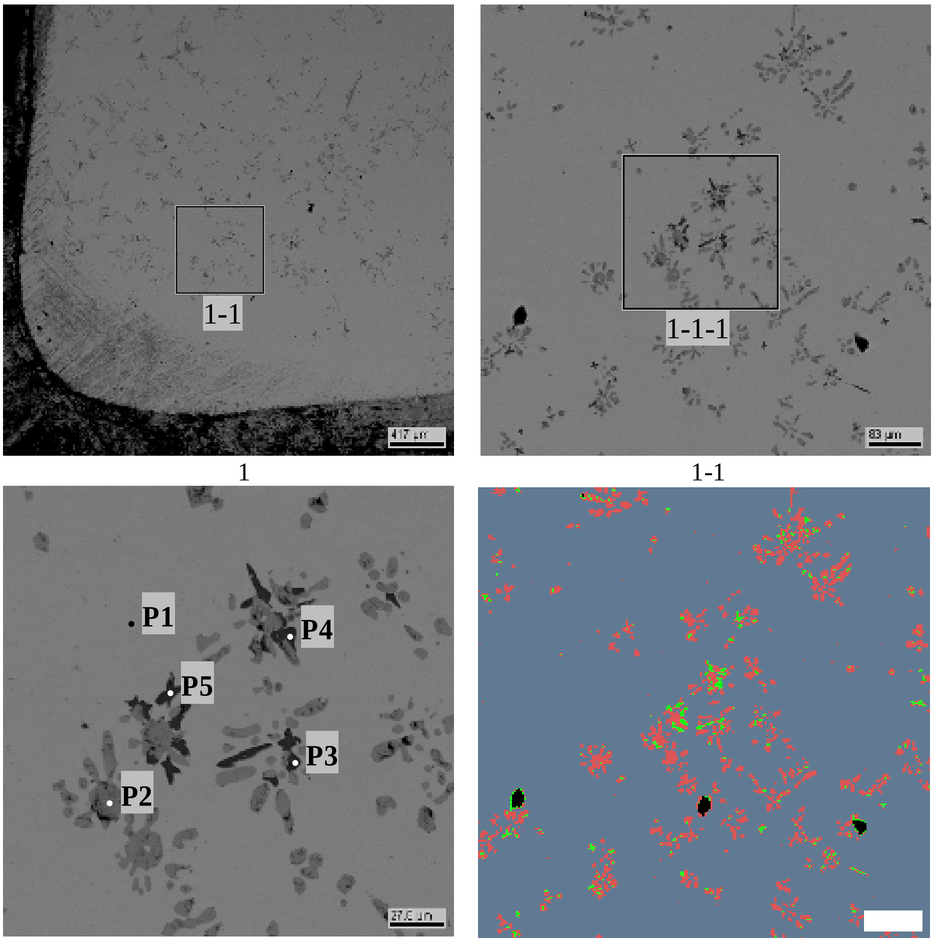

1 1-1

1-1-1 1-1 (b)

Fig. 3.45. Microphotographs of region 1, CORD41 ingot bottom

Table 3.32. EDX analysis of region 1

#		U	Zr	~O
P1	mass.%	96.86	-	3.14
	mol.%	67.49	-	32.51
	mol.% MeOx	100	-	
P2	mass.%	81.79	0.39	17.82
	mol.%	23.51	0.29	76.20
	mol.% MeOx	98.76	1.24	
P3	mass.%	24.97	50.68	24.35
	mol.%	4.81	25.46	69.74
	mol.% MeOx	15.88	84.12	
P4	mass.%	27.10	47.52	25.37
	mol.%	5.13	23.46	71.41
	mol.% MeOx	17.94	82.06	
P5	mass.%	24.69	51.62	23.69
	mol.%	4.82	26.32	68.86
	mol.% MeOx	15.49	84.51	

Microstructure of the metallic phase top is presented in Fig.3.46, 3.47 and 3.48 by regions 2-4 of the ingot. These regions are interesting for analysis, because of the presence of droplets belonging to the second (oxidic) liquid. For getting more comprehensive information about these regions the EDX analysis was complemented by the wave-dispersion analysis (WDX)carried out on the Camebax experimental facility (Ioffe Institute, head of research group – M.A. Zamorianskaya).

U-based phase was used for the calibration. Oxygen was determined from the mass deficit. The facility is equipped with the current stabilization system, which provides good convergence of results. The accuracy of element content determination is 2% rel. Optical microscope was used for positioning.

Matrix phase and phase inside the droplet inclusions observed through the optical microscope have blue color and typical metallic luster (U), oxidic droplets have yellow color. Noteworthy that UO_2-based dendrites have no optical difference from the matrix phase. The difference of optical properties between oxidic globules and dendrite crystallized phase of primary crystallization is explained by the presence of evenly distributed centers of another phase in the globules. U matrix phase also has whitish crystals of ZrO_2 admixture (Fig.3.46-3.48).

Table 3.34 shows statistically processed WDX data of region 2.

WDX analysis shows that the composition of metallic liquid (without oxidic globules) is close to the composition of the SQ1 region (Fig. 3.47a). Oxygen content in this region (after normalization for U and O)is about 13.51 at. %. The general error is difficult to evaluate, because the dendrites are not optically detectable and the accuracy of positioning is not high. It can only be assumed that it is definitely higher than the measurement error, which is 5 mol. %.

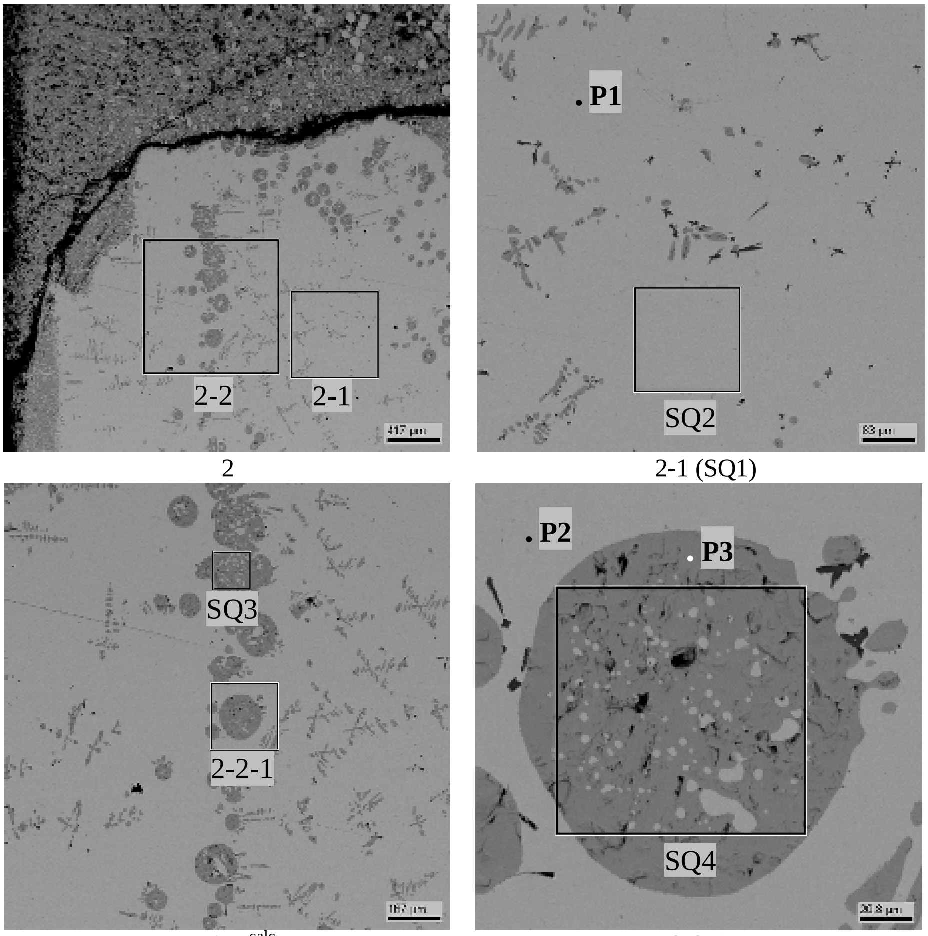

2

2-1 (SQ1)

2-2 (SQ^{calc})

2-2-1

Fig. 3.46. Microphotographs of region 2, CORD41 ingot bottom

Table 3.33. EDX analysis of region 2

#		U	Zr	~O
SQ1	mass.%	97.56	0.43	2.02
	mol.%	75.81	0.87	23.33
	mol.% MeOx	98.87	1.13	
SQ2	mass.%	98.96	-	1.04
	mol.%	86.47	-	13.53
	mol.% MeOx	100	-	
SQ3	mass.%	88.68	0.77	10.55
	mol.%	35.81	0.81	63.38
	mol.% MeOx	97.79	2.21	
SQ4	mass.%	86.10	0.76	13.14
	mol.%	30.35	0.70	68.95
	mol.% MeOx	97.75	2.25	
P1	mass.%	98.63	-	1.37
	mol.%	82.87	-	17.13
	mol.% MeOx	100	-	
P2	mass.%	99.04	-	0.96
	mol.%	87.44	-	12.56
	mol.% MeOx	100	-	
P3	mass.%	86.94	0.72	6.32
	mol.%	47.53	1.03	51.44
	mol.% MeOx	97.88	2.12	

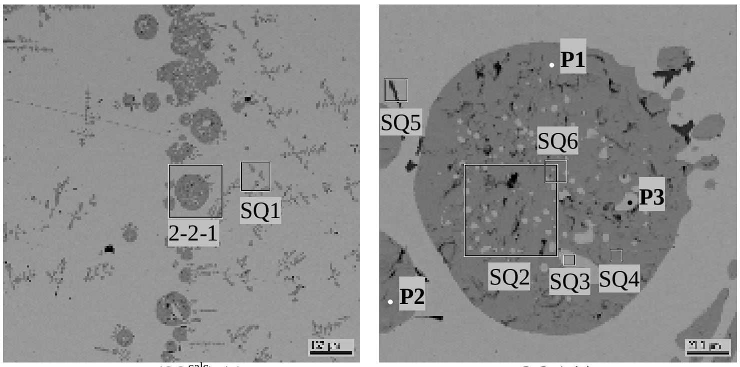

2-2 (SQ^{calc}) (a) 2-2-1 (a)

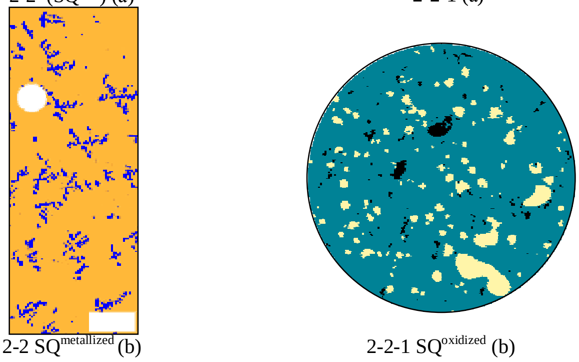

2-2 SQ^{metallized} (b) 2-2-1 SQ^{oxidized} (b)

Fig. 3.47. Microphotographs of region 2-2 with locations of WDX studies (a) presented in contrasting colors for SEM/Density analysis (b)

Table 3.34. WDX analysis of region 2-2 and SEM/density data of region 2

#		U	Zr	~O	Comment
SQ1	mass.%	97.94	0.72	1.34	5 measurements, measurement error for U 3.7 mass.% (about 5 mol.%) due to the dendrite invisibility
	mol.%	81.78	1.57	16.65	
	mol.% MeOx	98.12	1.88		
SQ2	mass.%	86.98	1.42	11.60	5 measurements, measurement error for U 0.06 mass.% is caused by high uniformly distributed porosity, deficit is partially compensated by U-based phase. These data cannot be used for calculations
	mol.%	33.04	1.41	65.55	
	mol.% MeOx	95.91	4.09		
SQ3	mass.%	98.99	1.01	-	2 measurements, measurement error for U 0.3 mass.%; difference with point P3 is explained by the unlimited solubility in U-Zr
	mol.%	97.41	2.59	-	
SQ4	mass.%	87.01	1.32	11.67	4 measurements, measurement error for U 0.6 mass.% is caused by the loose and porous structure
	mol.%	32.95	1.30	65.75	
	mol.% MeOx	96.19	3.81		
SQ5	mass.%	98.13	0.76	1.11	2 measurements, measurement error for U 0.7 mass.% – a little higher Zr content than in SQ1. Smaller content of oxygen can be explained by a smaller analyzed area -> smaller defects of the surface
	mol.%	84.14	1.70	14.16	
	mol.% MeOx	98.02	1.98		
SQ6	mass.%	87.19	1.34	11.47	4 measurements, measurement error for U 0.6 mass.%. Good agreement with SQ2, same problem.
	mol.%	33.36	1.34	65.30	
	mol.% MeOx	96.14	3.86		
SQ^{calc}	mass.%	99.26	-	0.74	Processing for areas 2 and 2-2
	mol.%	90.02	-	9.98	

#		U	Zr	~O	Comment
	mol.% MeOx	100	-		
SQ^{metallized}	mass.%	99.59	-	0.41	Processing for 3 areas 2, 2-2 and 2-2b
	mol.%	94.25	-	5.75	
	mol.% MeOx	100	-		
SQ^{oxidized}	mass.%	90.51	-	9.49	Processing for two areas 2-2 and 2-2-1b
	mol.%	39.05	-	60.95	
	mol.% MeOx		-		
P1	mass.%	88.45	1.14	10.41	6 measurements,
	mol.%	35.91	1.21	62.88	measurement error for U 0.94 mass.%
	mol.%	96.75	3.25		
P2	mass.%	88.59	0.78	10.63	5 measurements,
	mol.%	35.61	0.82	63.57	measurement error for U 0.34 mass.%
	mol.%	97.75	2.25		
P3	mass.%	99.23	0.77	-	3 measurements,
	mol.%	98.02	1.98	-	measurement error for U 0.38 mass.%

Note: average compositions are presented in the Table. Number of measurement is given in the comment.

Along with WDX studies calculation of metallic liquid composition was performed for region 2 using volume fractions of coexisting phase on the assumption that one phase is pure U, and another – UO_2. Total composition of metallized liquid (with oxidic globules) can be evaluated by analyzing images 2 and 2-2: U – 89.11 vol.%, UO_2 – 10.29 vol.%, porosity - 0.61 vol.%. calculated composition – SQ^{calc} is given in Table 3.34. Composition of the metallized liquid (without oxidic globules) was evaluated by analyzing images of regions 2, 2-2 and 2-2b: U – 93.93 vol.%, UO_2 – 5.82 vol.%, porosity - 0.25 vol.%. Calculated composition – SQ^{metallized} is also given in Table 3.34.

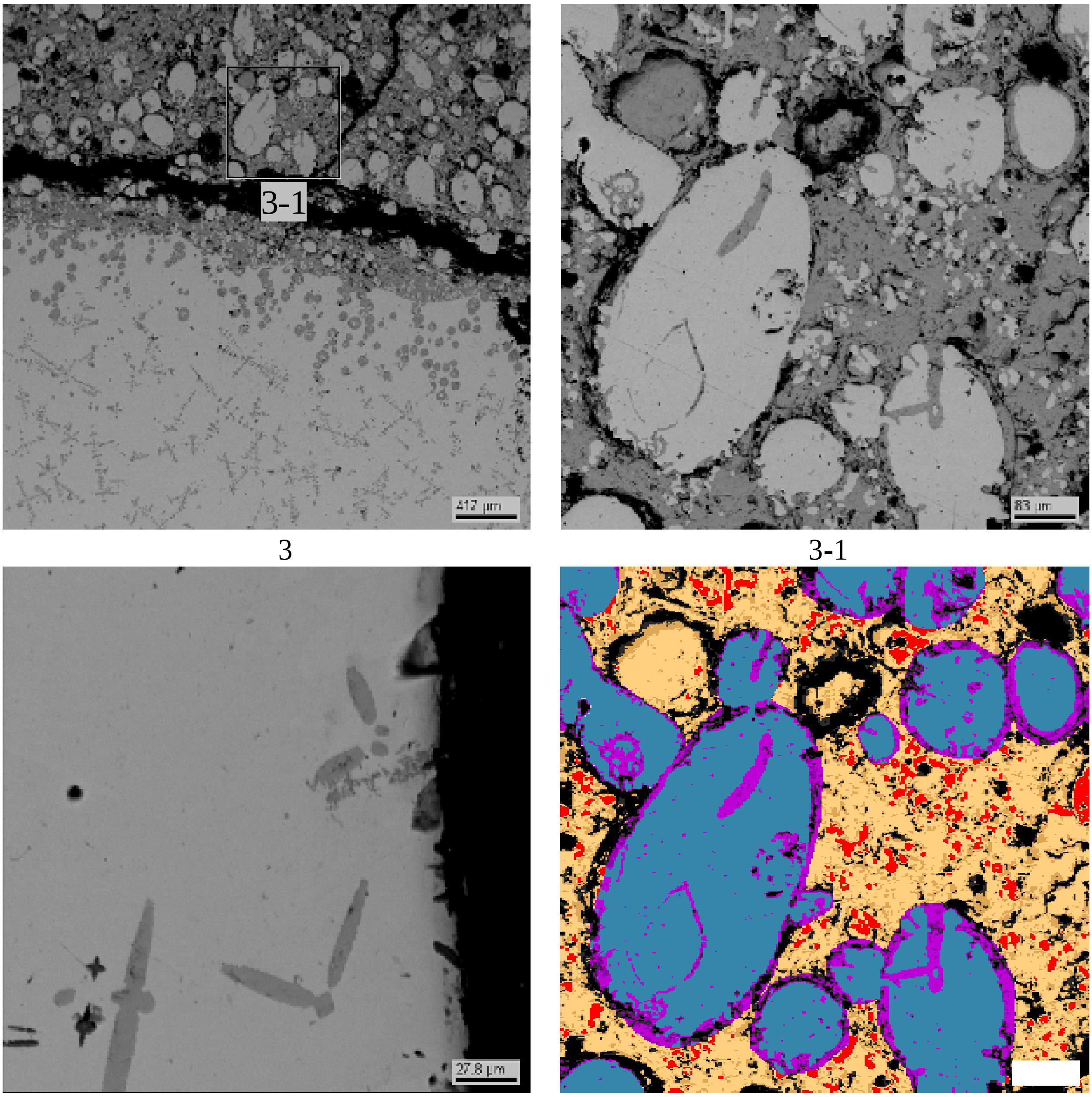

3 3-1

4 3-1 (b)

Fig. 3.48. Microphotographs of regions 3 and 4, CORD41 ingot bottom

Composition of metallized globules in the oxidic matrix was also evaluated by analyzing images of regions 3 and 6 (Fig. 3.48 и 3.50). Total composition of metallic globules is given in Table 3.36 $SQ^{metallized}$.

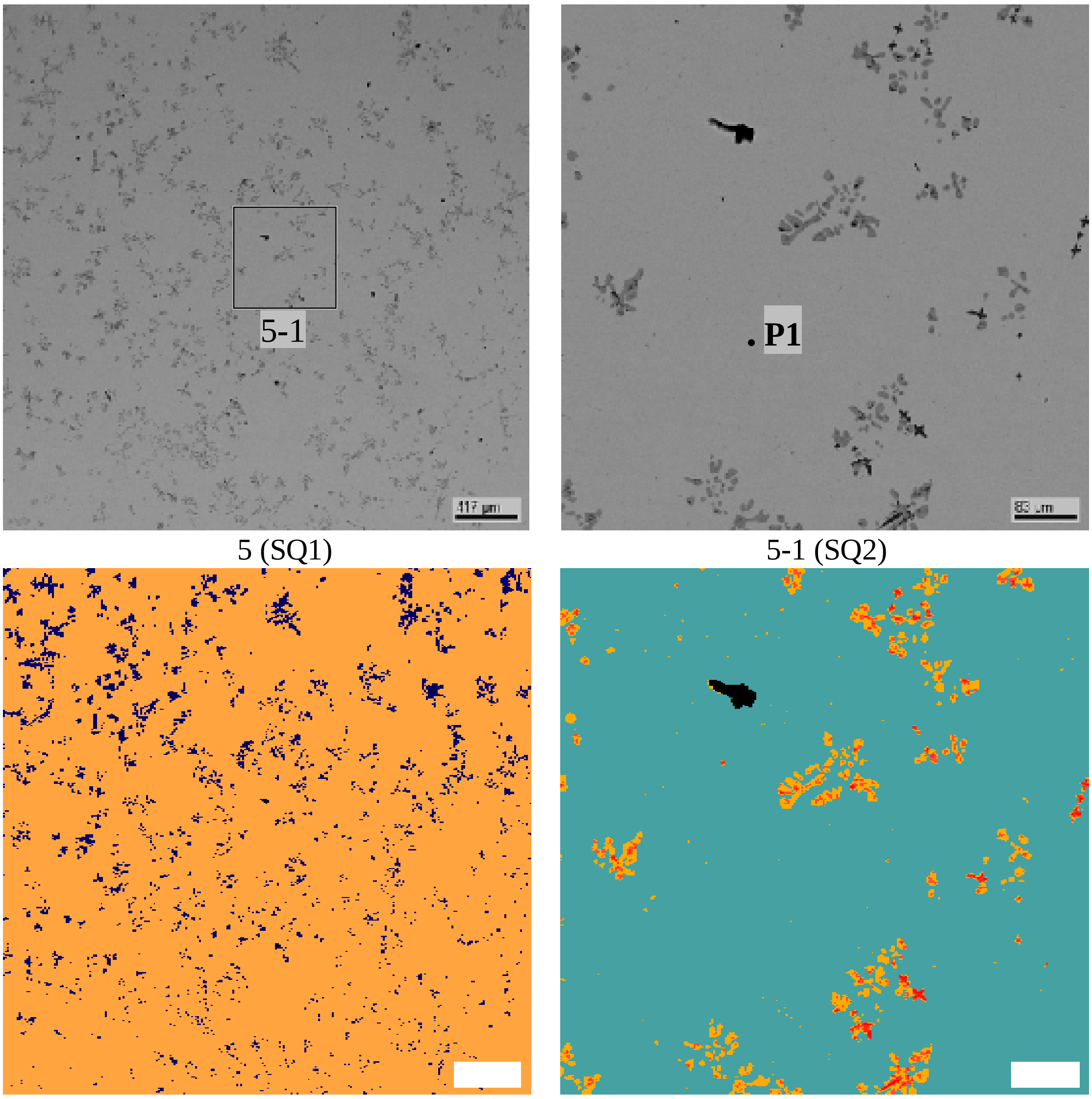

5 (SQ1)

5-1 (SQ2)

5 (b)

5-1 (b)

Fig. 3.49. Microphotographs of region 5, CORD41 ingot bottom

Table 3.35. EDX analysis of region 5

#		U	Zr	~O
SQ1	mass.%	88.84	0.28	10.87
	mol.%	35.34	0.29	64.36
	mol.% MeOx	99.17	0.83	
SQ1^{calc}	mass.%	99.68	-	0.32
	mol.%	95.42	-	4.58
	mol.% MeOx	100	-	
SQ2	mass.%	97.32	0.23	2.45
	mol.%	72.43	0.45	27.12
	mol.% MeOx	99.38	0.62	
P1	mass.%	98.28	-	1.72
	mol.%	79.29	-	20.71
	mol.% MeOx	100	-	

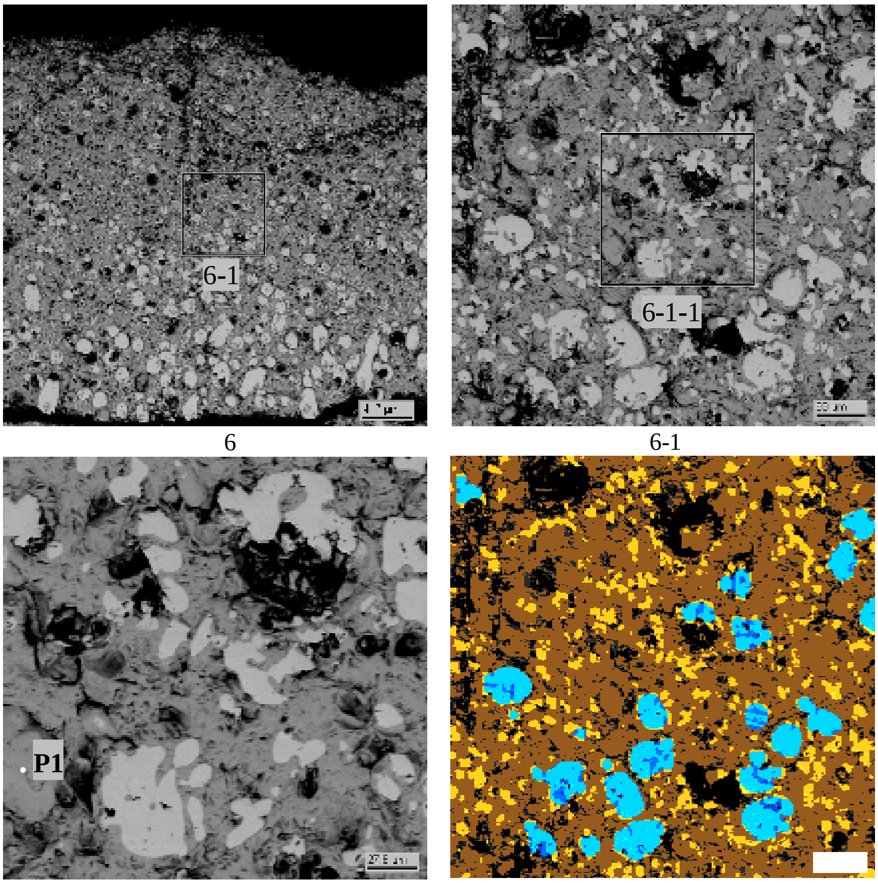

6 6-1

6-1-1 6-1 (b)

Fig. 3.50. Microphotographs of region 6, CORD41 ingot bottom

Table 3.36. EDX analysis of region 6 and SEM/density data of regions 3 and 6

#		U	Zr	~O
P1	mass.%	84.60	0.32	15.08
	mol.%	27.31	0.27	72.42
	mol.% MeOx	99.02	0.98	
SQ^{calc}	mass.%	92.32	-	7.68
	mol.%	44.69	-	55.31
$SQ^{metallized}$	mass.%	99.00	-	1.00
	mol.%	86.99	-	13.01
$SQ^{oxidized}$	mass.%	90.65	-	9.35
	mol.%	39.44	-	60.56

The microstructure of oxidic layer is shown in Fig. 3.48, 3.50, 3.51-3.55. In this system the oxidic liquid is more refractory. At reaching the monotectics temperature (quenching temperature is higher than monotectics) the monotectics reaction decomposes oxidic liquid into UO_2 and metallic liquid enriched with uranium (L_2=UO_{2-x} + L_1). UO_2 phase occupies the main area in the matrix having inclusions of metallic U, which is confirmed by the monotectic character of crystallization. A considerable porosity of this layer should be noted. Microstructure of oxidic globules located in the metallic matrix corresponds to the microstructure of oxidic layer.

The total composition of oxidized liquid can be evaluated by the analyzing images of regions 7-11. Analysis results are presented in Table 3.39 (SQ^{calc}). The boundary region between the oxide and metal was analyzed too. Table 3.36 presents the total composition of oxidized liquid with and without oxidic globules derived from the analysis of images of regions 3 and 6 (Fig. 3.48, 3.50) by SEM/Density (SQ^{calc}, и $SQ^{oxidized}$, respectively). The composition of oxidized liquid was also evaluated from the composition of globule 2-2-1b and globules 2-2 (Fig.3.47): U – 12.34 vol.%, UO_2 – 86.29 vol.%, porosity - 1.37 vol.%. calculated composition $SQ^{oxidized}$ is given in Table 3.34. In accordance with WDX in region 2 oxygen content in oxidic globule does not exceed 62.6 at.%, because the porosity of this region results in the increased mass deficit (Fig.3.47, Table3.34, SQ2 and SQ6).

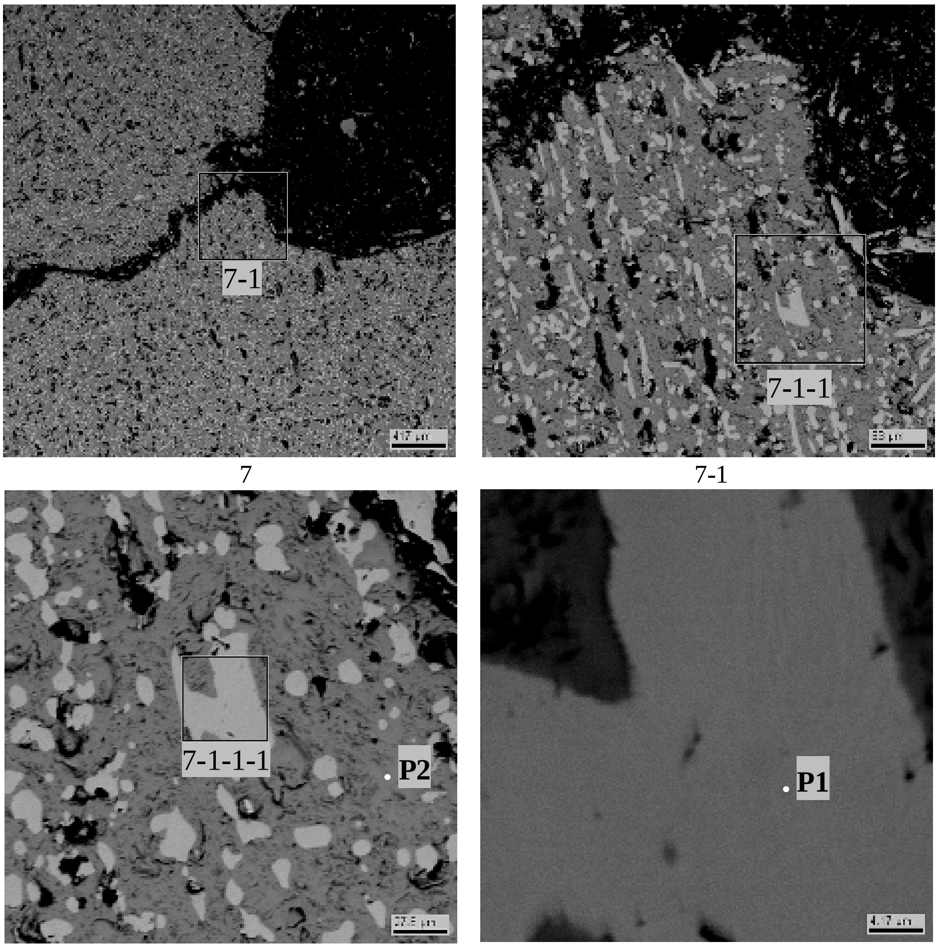

7 7-1

7-1-1 7-1-1-1

Fig. 3.51. Microphotographs of region 7, ingot CORD41

Table 3.37. EDX analysis of region 7

#		U	Zr	~O
P1	mass.%	98.26	0.70	1.05
	mol.%	84.97	1.57	13.46
	mol.% MeOx	98.18	1.82	
P2	mass.%	85.72	0.48	13.80
	mol.%	29.33	0.43	70.24
	mol.% MeOx	98.55	1.45	

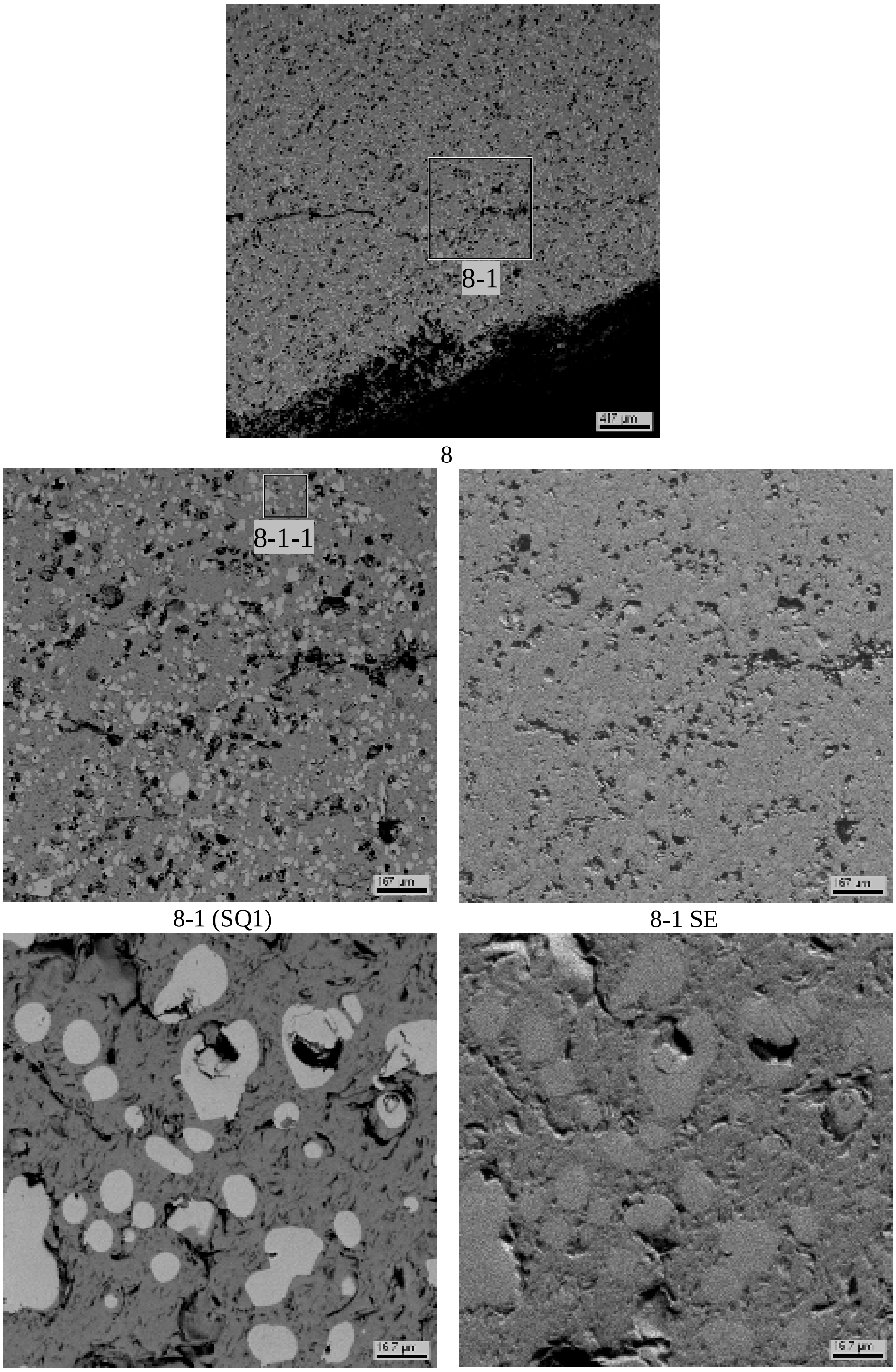

8

8-1 (SQ1) 8-1 SE

8-1-1 (SQ2) 8-1-1 SE

Fig. 3.52. Microphotographs of region 8, ingot CORD41

Table 3.38. EDX analysis of region 8

#		U	Zr	~O
SQ1	mass.%	77.98	0.80	21.23
	mol.%	19.70	0.53	79.78
	mol.% MeOx	97.40	2.60	
SQ2	mass.%	84.08	0.56	15.37
	mol.%	26.76	0.46	72.78
	mol.% MeOx	98.31	1.69	

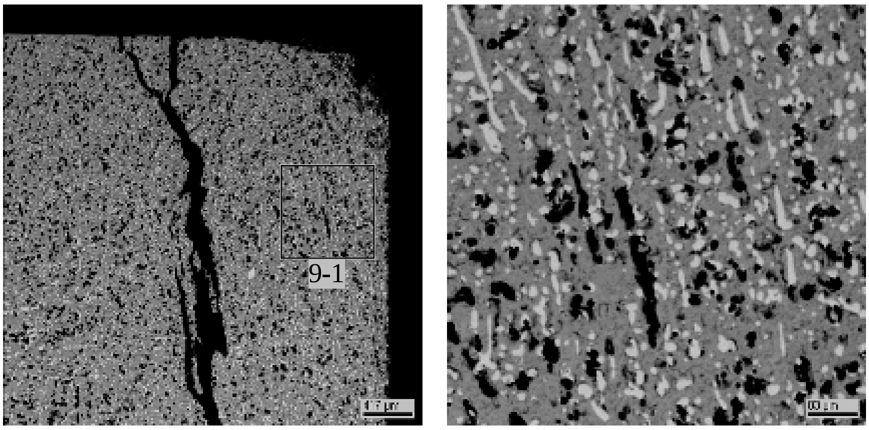

9 9-1

Fig. 3.53. Microphotographs of region 9, ingot CORD41

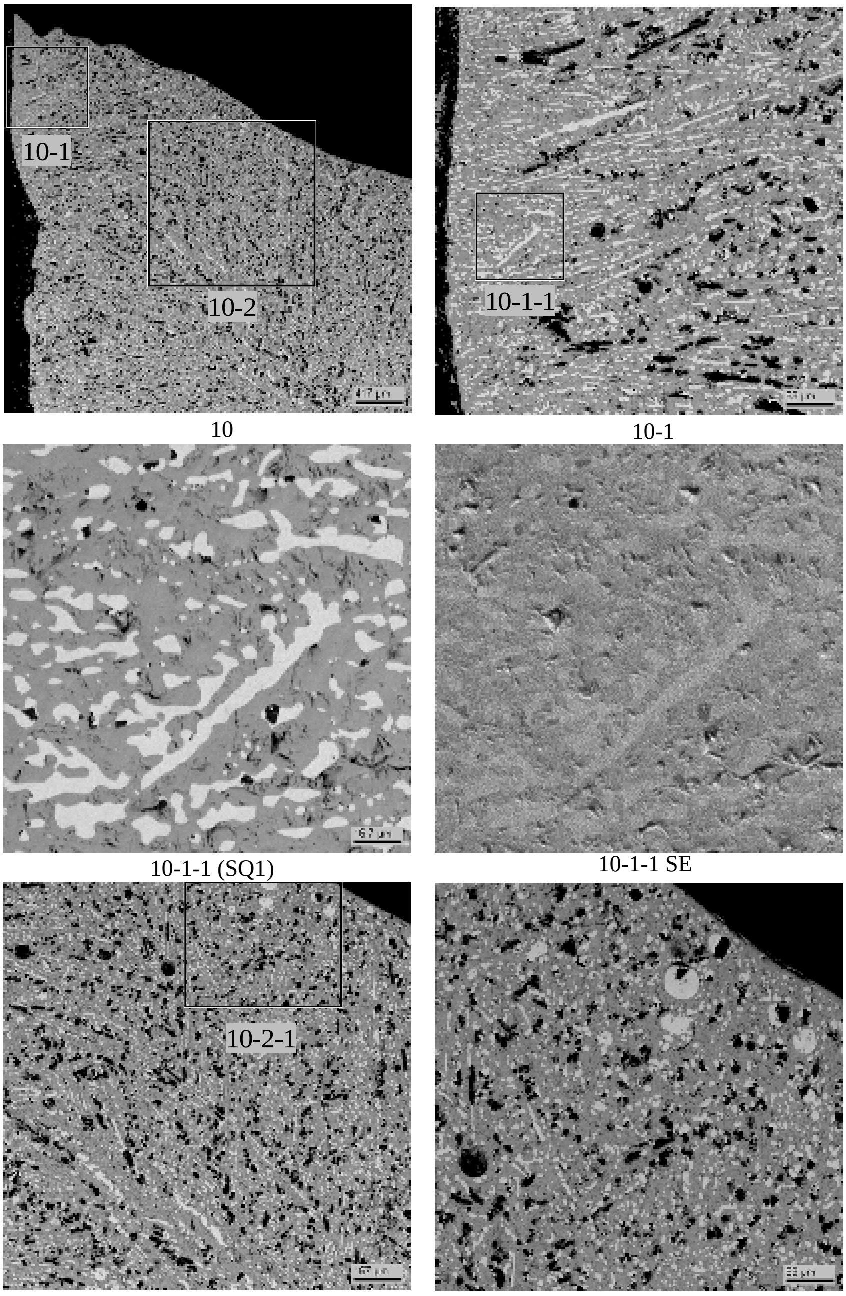

10 10-1

10-1-1 (SQ1) 10-1-1 SE

10-2 10-2-1

Fig. 3.54. Microphotographs of region 10, CORD41 ingot

Table 3.39. EDX analysis of region 10 and SEM/density data for regions 7-11 (SQ^{calc})

#		U	Zr	~O
SQ1	mass.%	86.98	0.72	12.30
	mol.%	31.99	0.69	67.32
	mol.% MeOx	97.88	2.12	
SQ^{calc}	mass.%	91.28	-	8.72
	mol.%	41.29	-	58.71

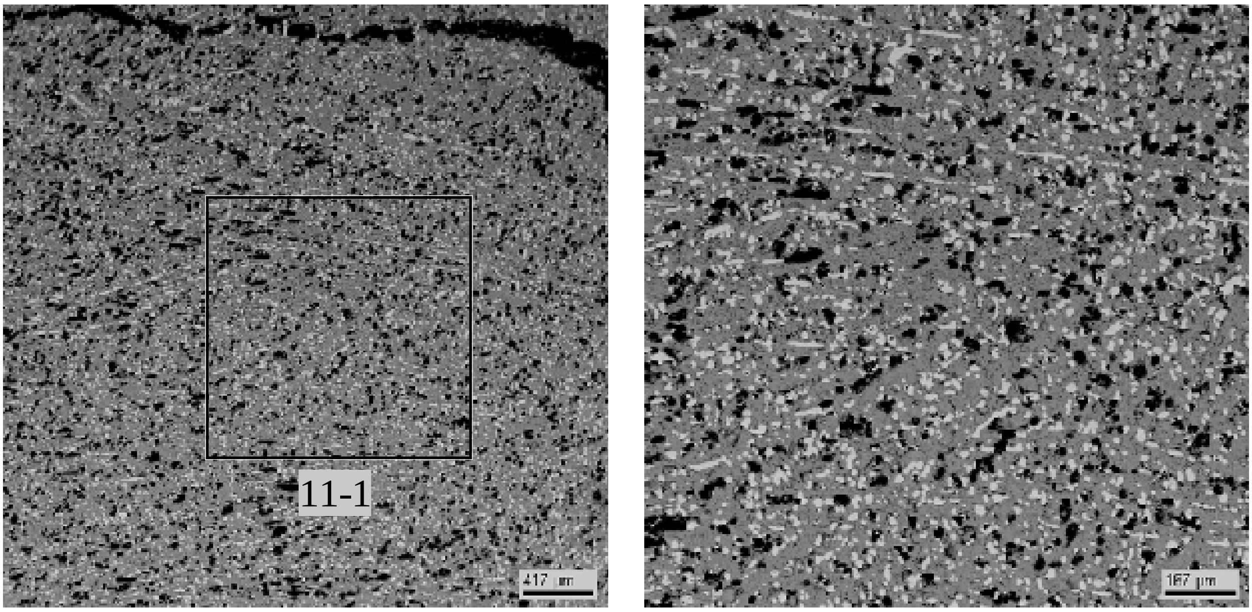

11 11-1

Fig. 3.55. Microphotographs of region 11, CORD41 ingot

The analysis of oxidic and metallic droplets’ shape and microstructure shows that during the melt cooling and crystallization the interaction between solid oxidic droplets (globules) with metallic liquid and metallic liquid droplets with solid oxidic matrix takes place. It is quite difficult to determine the location of boundary between globules and the matrix phase due to the bordering zone, which in case of metallic globules (Fig. 3.48 region 3-1) can be the primary crystallization phase of the matrix oxidic structure; and in case of oxidic globules (Fig.3.47 region 2-2, 2-2-1) it can be the primary crystallization phase of the matrix metallic melt. For this reason in our work the analysis of globule composition by the SEM/density method has additional uncertainty (in difference from work /2/).

If we take into account that the melt cooling and crystallization conditions were close to quenching, and the boundary surface between liquids was limited, it can be assumed that the mass exchange between the oxidic and metallic liquids at their cooling and crystallization was insignificant. If globules are considered as secondary formations, liquid compositions should be close to the average composition of the corresponding ingot part. SEM determination of the average composition of oxidic and metallic parts is complicated by the presence of layers with globules and necessary numerical averaging. Nevertheless, it can be asserted that the average compositions in question exist in the range between average compositions of layers with and without globules. These data are plotted on the diagram of the U–O (Fig.3.56) system. The figure demonstrates that our experimental results have a good agreement with data /2/ and confirm the elongated miscibility gap.

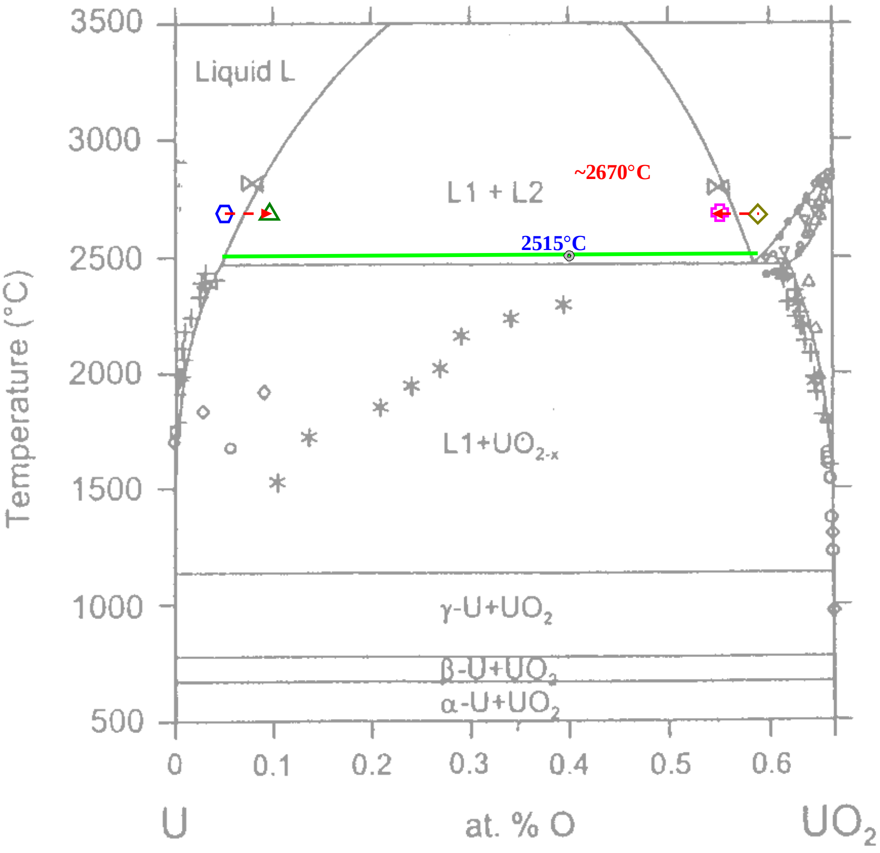

Fig. 3.56. Results of CORD41

metallic liquid: ⬡region without globules Table3.35 SQ^{calc} (95.42U-4.58O),
△ region with globules Table3.34 SQ^{calc} (90.02U-9.98O)

oxidic liquid: ◇ region without globules Table 3.39 SQ^{calc} (41.29U-58.71O),
✚region with globules Table3.36 SQ^{calc} (44.69U- 55.31O)

Experiment CORD42

As noted above, this experiment had a high content of metallic component. Photograph of the axial section shows that the volume of metallized layer is larger than in CORD37. Fig. 3.57 shows the axial section of the ingot with marked locations chosen for SEM/EDX studies.

Ingot has two layers: top, its microstructure is shown in Fig. 3.58-3.61, and bottom, its microstructure is shown in Fig. 3.65-3.69. Regions 5-7 represent the microstructure of boundary zone between the two layers (Fig. 3.62-3.64).

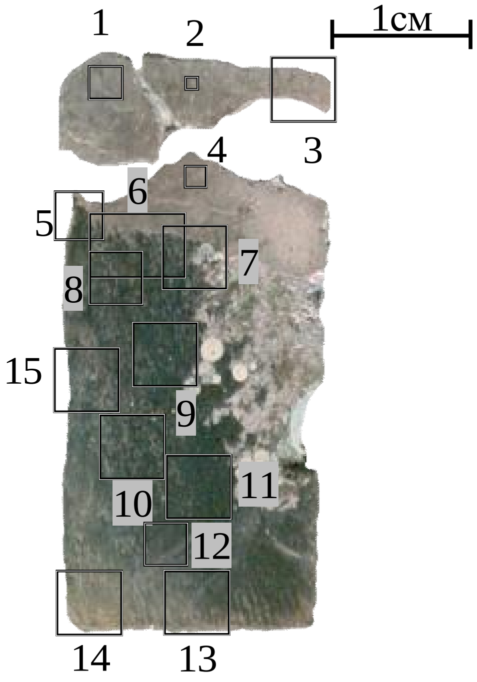

Fig. 3.57. Half of the CORD42 ingot axial section with marked locations chosen for studies

Similar to CORD34 and CORD37 the whole ingot top microstructure has a dendrite character (Fig. 3.58), which indicates quenching conditions of crystallization; the (U,Zr)O_{2-x} solid solution phase is definitely the phase of primary crystallization (Table 3.40, SQ6). Further cooling of the (U,Zr)O_{2-x} phase was accompanied by its decomposition into at least two phases – one enriched with UO_2 (Fig. 3.58, points P1, P2 and Table 3.40) and a phase with as lower content of UO_2 (Fig. 3.58, points P3-P5 and Table 3.40). The phase of secondary crystallization in this layer is the α-Zr(U)(O)-based phase (Fig. 3.58, SQ5 and Table 3.40), which at further cooling also decomposes into two phases: α-Zr(O)-based phase with a small content of uranium (Fig. 3.58, dark rounded phase, points P10-P12 and Table 3.40) and the U-Zr solid solution-based phase (Fig. 3.58, light inclusions in the dark rounded phase, points P6-P9 and Table 3.40).

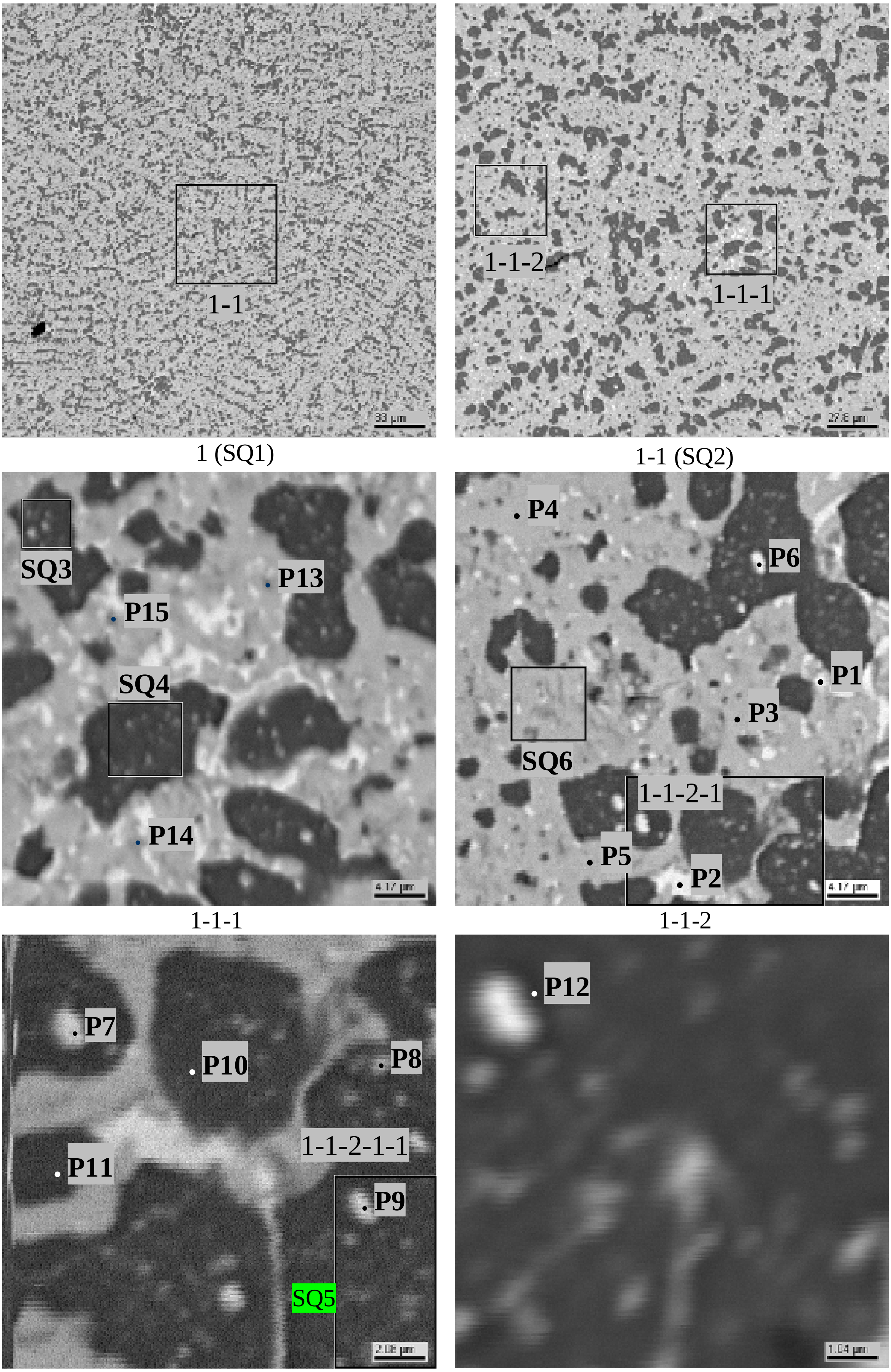

1 (SQ1) 1-1 (SQ2)

1-1-1 1-1-2

1-1-2-1 1-1-2-1-1 (SQ5)

Fig. 3.58. Microphotographs of Region 1, CORD42 ingot

Table 3.40. EDX analysis of region 1

#		U	Zr	~O
SQ1	mass.%	72.24	22.59	5.17
	mol.%	34.71	28.32	36.97
	mol.% MeO_x	55.06	44.94	
SQ2	mass.%	73.33	23.02	3.65
	mol.%	39.06	32.01	28.93
	mol.% MeO_x	54.96	45.04	
SQ3	mass.%	27.88	58.68	13.43
	mol.%	7.32	40.21	52.47
	mol.% MeO_x	15.40	84.60	
SQ4	mass.%	19.06	63.30	17.64
	mol.%	4.27	36.98	58.75
	mol.% MeO_x	10.34	89.66	
SQ5	mass.%	27.54	60.12	12.35
	mol.%	7.48	42.62	49.90
	mol.% MeO_x	14.93	85.07	
SQ6	mass.%	84.85	3.88	11.26
	mol.%	32.32	3.86	63.82
	mol.% MeO_x	89.34	10.66	
P1	mass.%	97.56	2.44	-
	mol.%	93.87	6.13	-
P2	mass.%	98.65	1.35	-
	mol.%	96.56	3.44	-
P3	mass.%	84.86	2.74	12.40
	mol.%	30.70	2.59	66.72
	mol.% MeO_x	92.22	7.78	
P4	mass.%	85.28	4.06	10.66
	mol.%	33.52	4.16	62.32
	mol.% MeO_x	88.96	11.04	
P5	mass.%	86.58	3.53	9.89
	mol.%	35.64	3.79	60.57
	mol.% MeO_x	90.39	9.61	
P6	mass.%	86.19	13.81	-
	mol.%	70.52	29.48	-
P7	mass.%	87.53	12.47	-
	mol.%	72.91	27.09	-
P8	mass.%	24.58	60.54	14.88
	mol.%	6.09	39.11	54.80
	mol.% MeO_x	13.47	86.53	
P9	mass.%	75.64	24.36	-
	mol.%	54.34	45.66	-
P10	mass.%	8.88	67.45	23.67
	mol.%	1.65	32.77	65.57
	mol.% MeO_x	4.80	95.20	
P11	mass.%	9.30	67.50	23.21
	mol.%	1.75	33.18	65.06
	mol.% MeO_x	5.01	94.99	
P12	mass.%	10.18	66.25	23.57
	mol.%	1.91	32.39	65.70

#		U	Zr	~O
	mol.% MeO$_x$	5.56	94.44	
P13	mass.%	14.64	61.38	23.97
	mol.%	2.76	30.14	67.11
	mol.% MeO$_x$	8.38	91.62	
P14	mass.%	9.69	66.05	24.26
	mol.%	1.78	31.74	66.48
	mol.% MeO$_x$	5.32	94.68	
P15	mass.%	26.54	56.76	16.70
	mol.%	6.27	35.00	58.72
	mol.% MeO$_x$	15.20	84.80	

Similar picture is observed in regions 2-4 (Fig. 3.59-3.61).

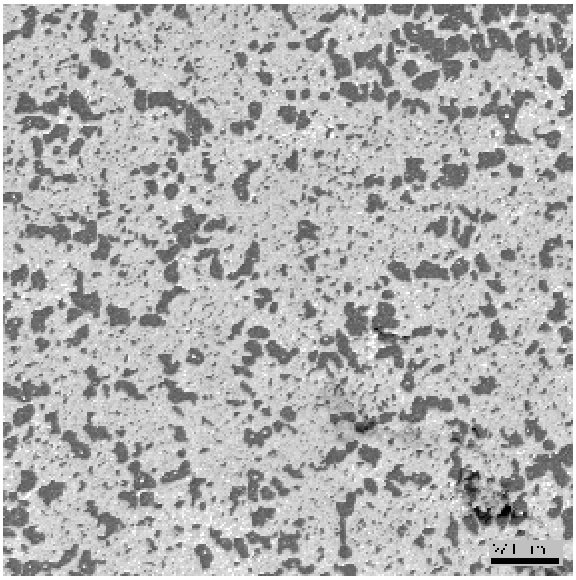

2 (SQ1)

Fig. 3.59. Microphotographs of region 2, CORD42 ingot

Table 3.41. EDX analysis of region 2

#		U	Zr	~O
SQ1	mass.%	68.42	21.61	9.96
	mol.%	25.06	20.66	54.28
	mol.% MeO$_x$	54.82	45.18	

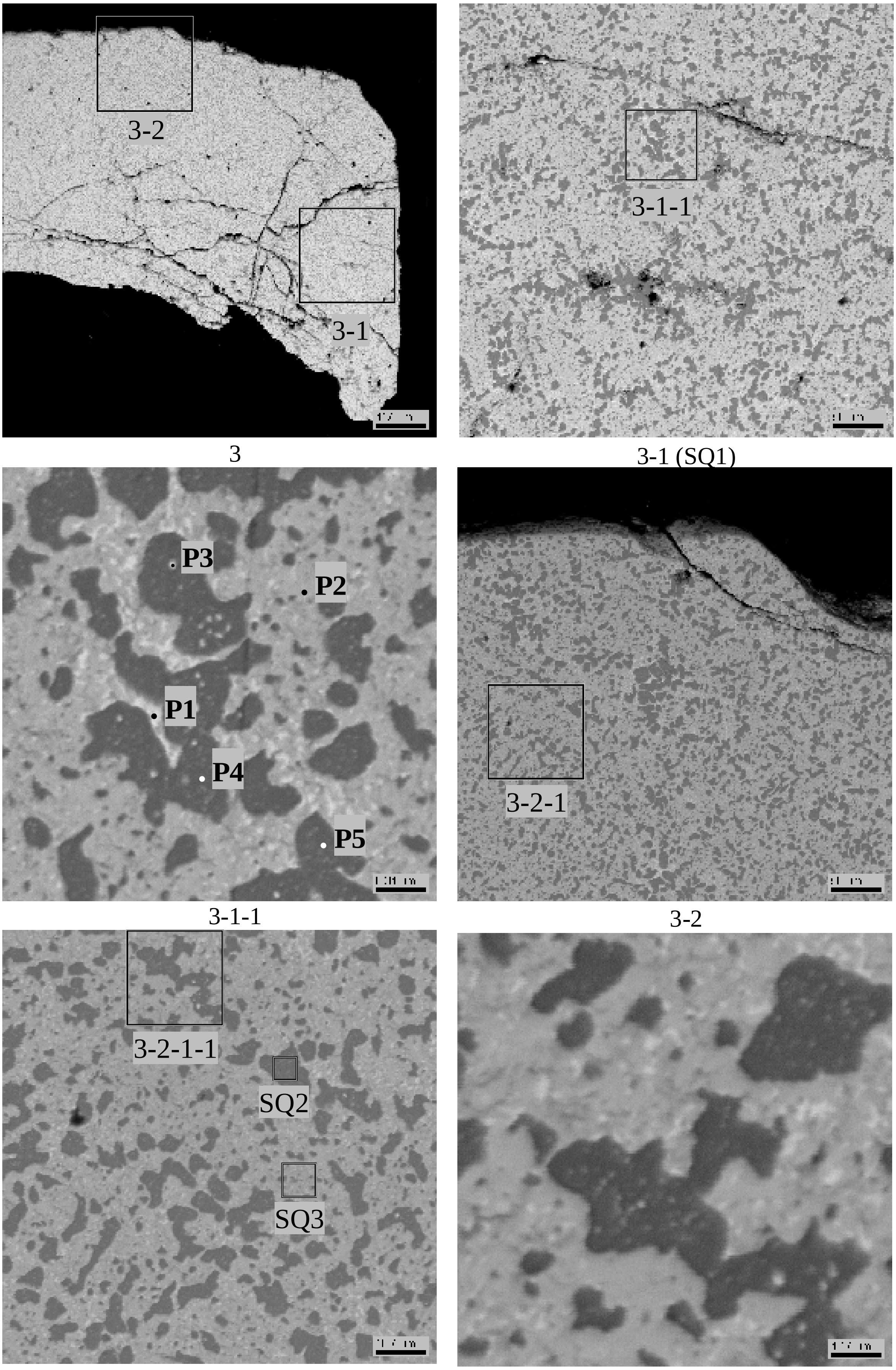

3 3-1 (SQ1)

3-1-1 3-2

3-2-1 3-2-1-1

Fig. 3.60. Microphotographs of region 3, CORD42 ingot

Table 3.42. EDX analysis of region 3

#		U	Zr	~O
SQ1	mass.%	70.99	22.96	6.05
	mol.%	32.13	27.11	40.76
	mol.% MeO_x	54.23	45.77	
SQ2	mass.%	12.14	65.90	21.96
	mol.%	2.38	33.67	63.96
	mol.% MeO_x	6.60	93.40	
SQ3	mass.%	81.56	7.47	10.97
	mol.%	30.86	7.37	61.77
	mol.% MeO_x	80.72	19.28	
P1	mass.%	97.25	2.75	-
	mol.%	93.14	6.86	-
P2	mass.%	85.24	2.48	12.28
	mol.%	31.07	2.36	66.57
	mol.% MeO_x	92.95	7.05	
P3	mass.%	38.89	55.49	5.62
	mol.%	14.55	54.18	31.27
	mol.% MeO_x	21.17	78.83	
P4	mass.%	18.43	64.14	17.44
	mol.%	4.14	37.59	58.27
	mol.% MeO_x	9.92	90.08	
P5	mass.%	7.22	69.17	23.61
	mol.%	1.34	33.48	65.18
	mol.% MeO_x	3.85	96.15	

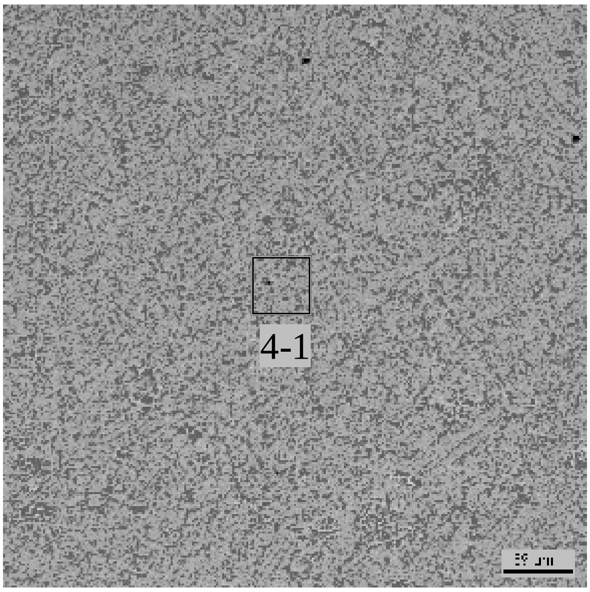

4 (SQ1)

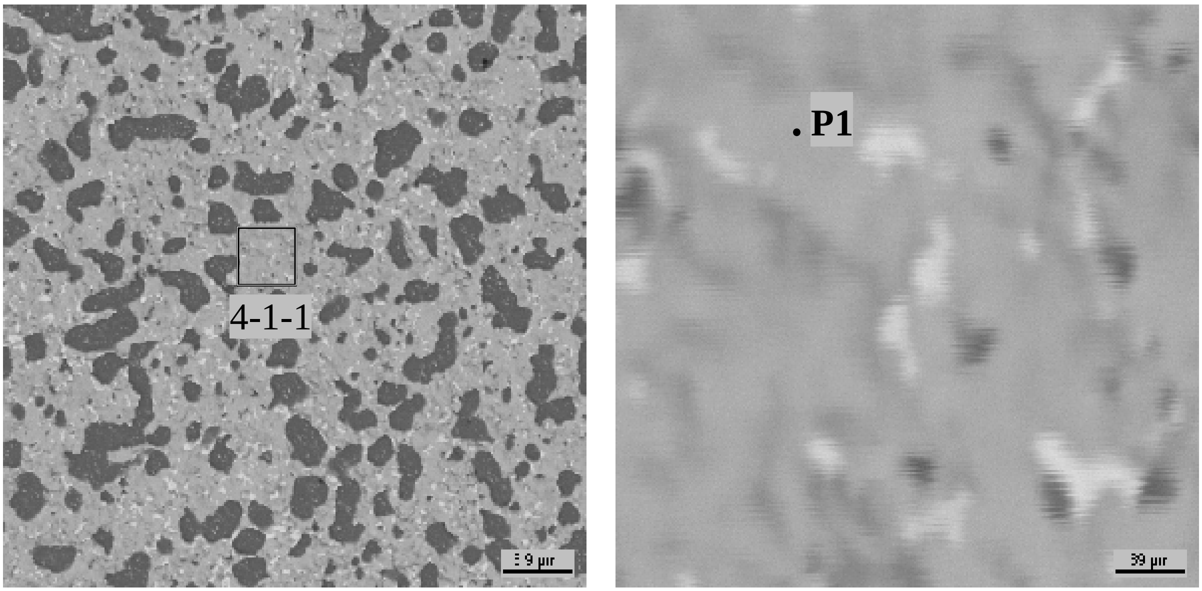

4-1 (SQ2) 4-1-1 (SQ3)

Fig. 3.61. Microphotographs of region 4, CORD42 ingot

Table 3.43. EDX analysis of region 4

#		U	Zr	~O
SQ1	mass.%	73.89	24.43	1.67
	mol.%	45.46	39.22	15.31
	mol.% MeO_x	53.68	46.32	
SQ2	mass.%	74.78	22.61	2.60
	mol.%	43.34	34.20	22.45
	mol.% MeO_x	55.89	44.11	
SQ3	mass.%	84.69	5.88	9.43
	mol.%	35.23	6.38	58.39
	mol.% MeO_x	84.66	15.34	
P1	mass.%	85.43	2.83	11.73
	mol.%	31.95	2.76	65.29
	mol.% MeO_x	92.04	7.96	

Region 5 represents the boundary between the two layers (Fig. 3.62).

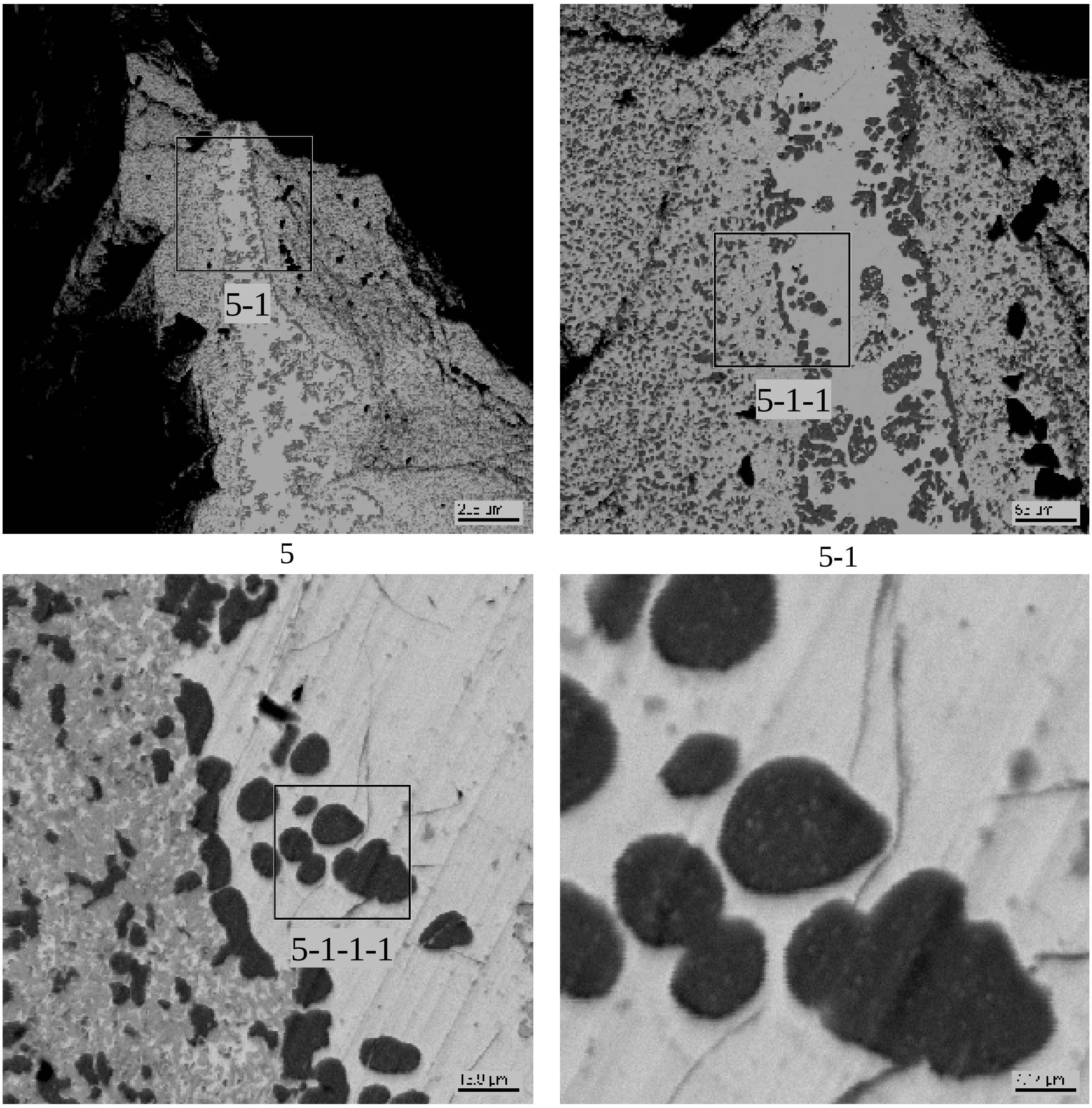

5

5-1

5-1-1

5-1-1-1

Fig. 3.62. Microphotographs of region 5, CORD42 ingot

Oxidic globules in the metallic matrix are especially distinct in the boundary region 6 of the ingot bottom (Fig. 3.63, region 6-1). Metallic globules observed in the oxidic component are smaller and have elongated shape (Fig. 3.63, region 6-4).

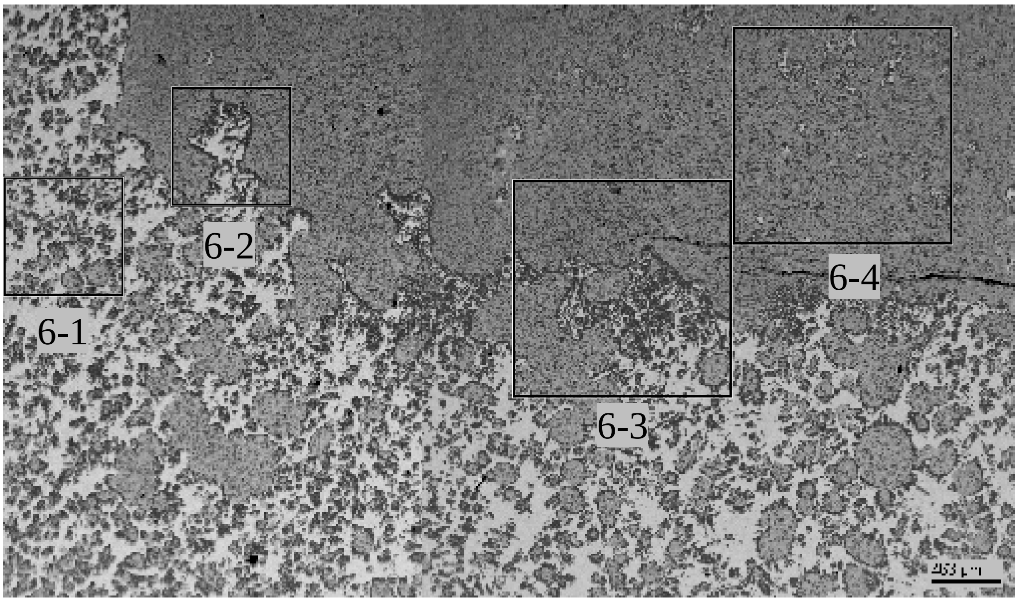

6

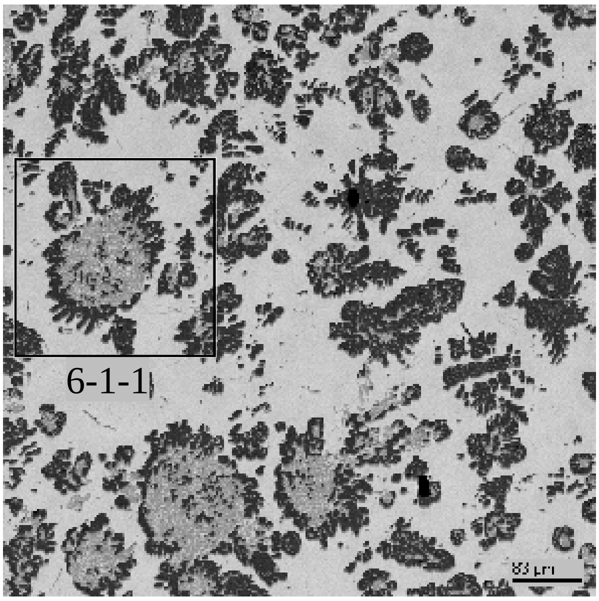

6-1

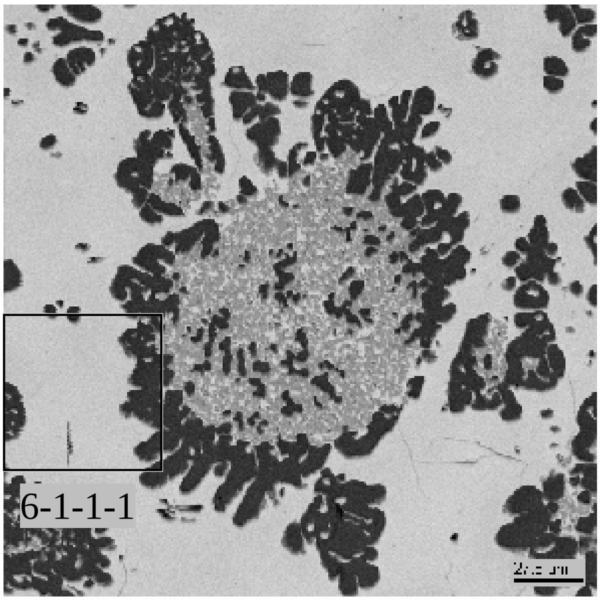

6-1-1

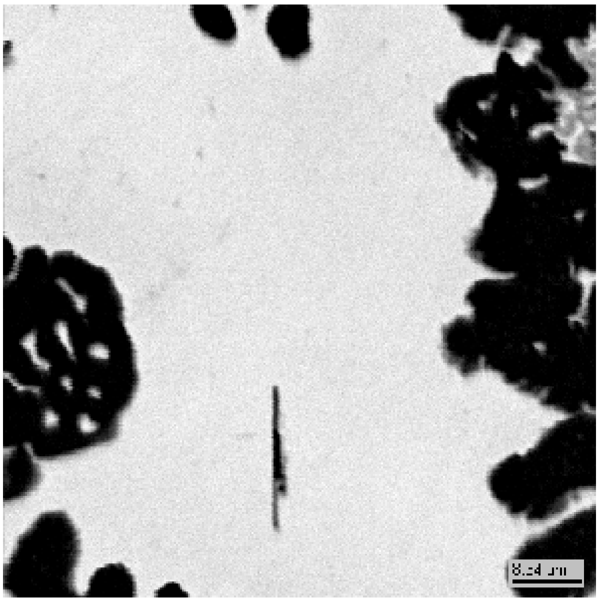

6-1-1-1

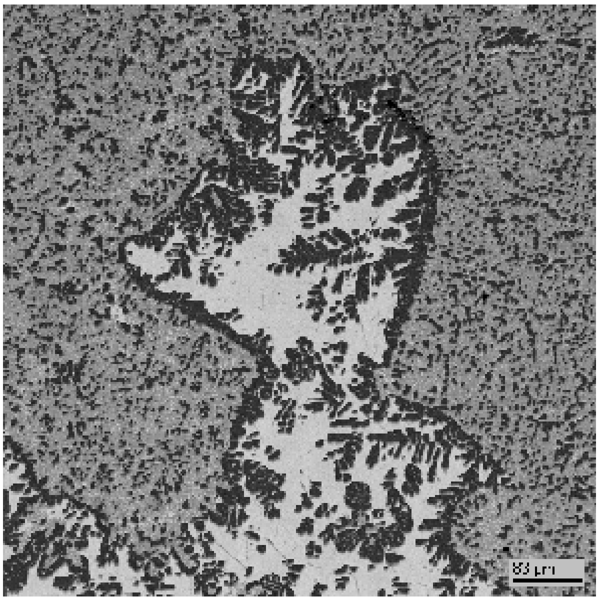

6-2

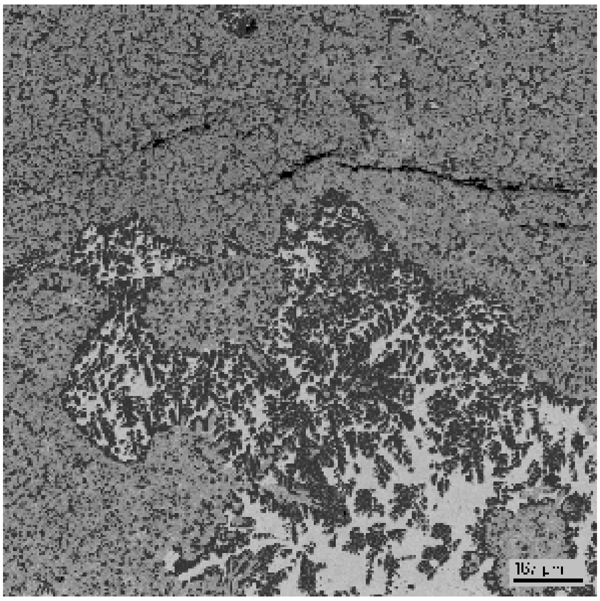

6-3

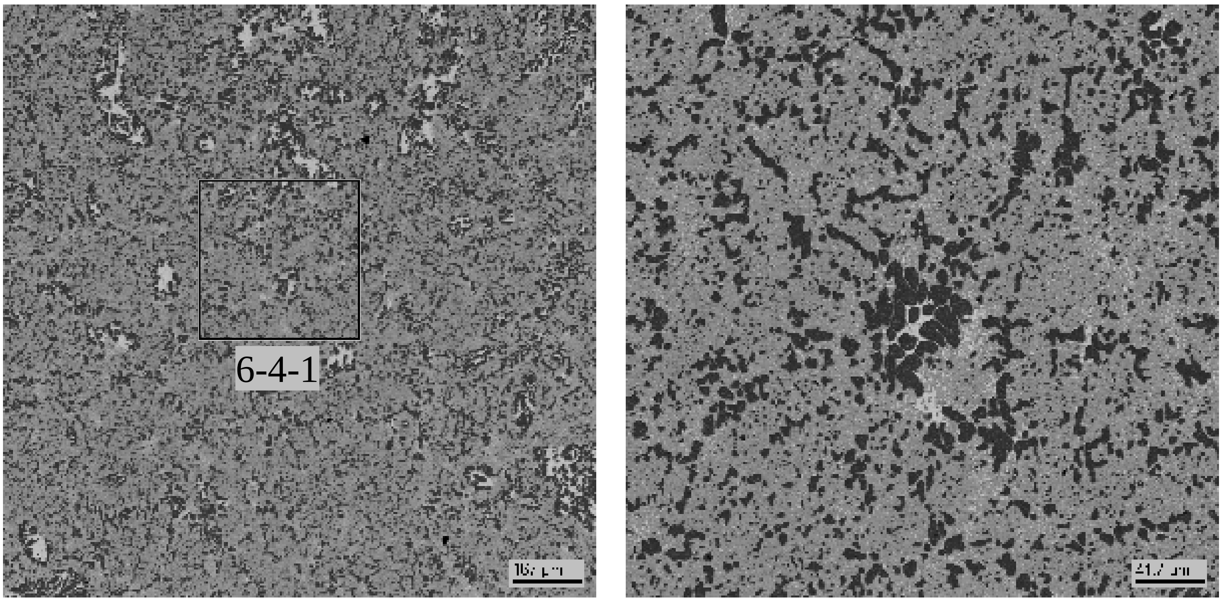

6-4 (SQ1) 6-4-1

Fig. 3.63. Microphotographs of region 6, CORD42 ingot

Table 3.44. EDX analysis of region 6

#		U	Zr	~O
SQ1	mass.%	74.35	21.69	3.95
	mol.%	39.18	29.83	31.00
	mol.% MeO_x	56.78	43.22	

Similar to region 6 the boundary region 7 has oxidic globules in the metallic matrix and metallic globules in the oxidic matrix (Fig. 3.64).

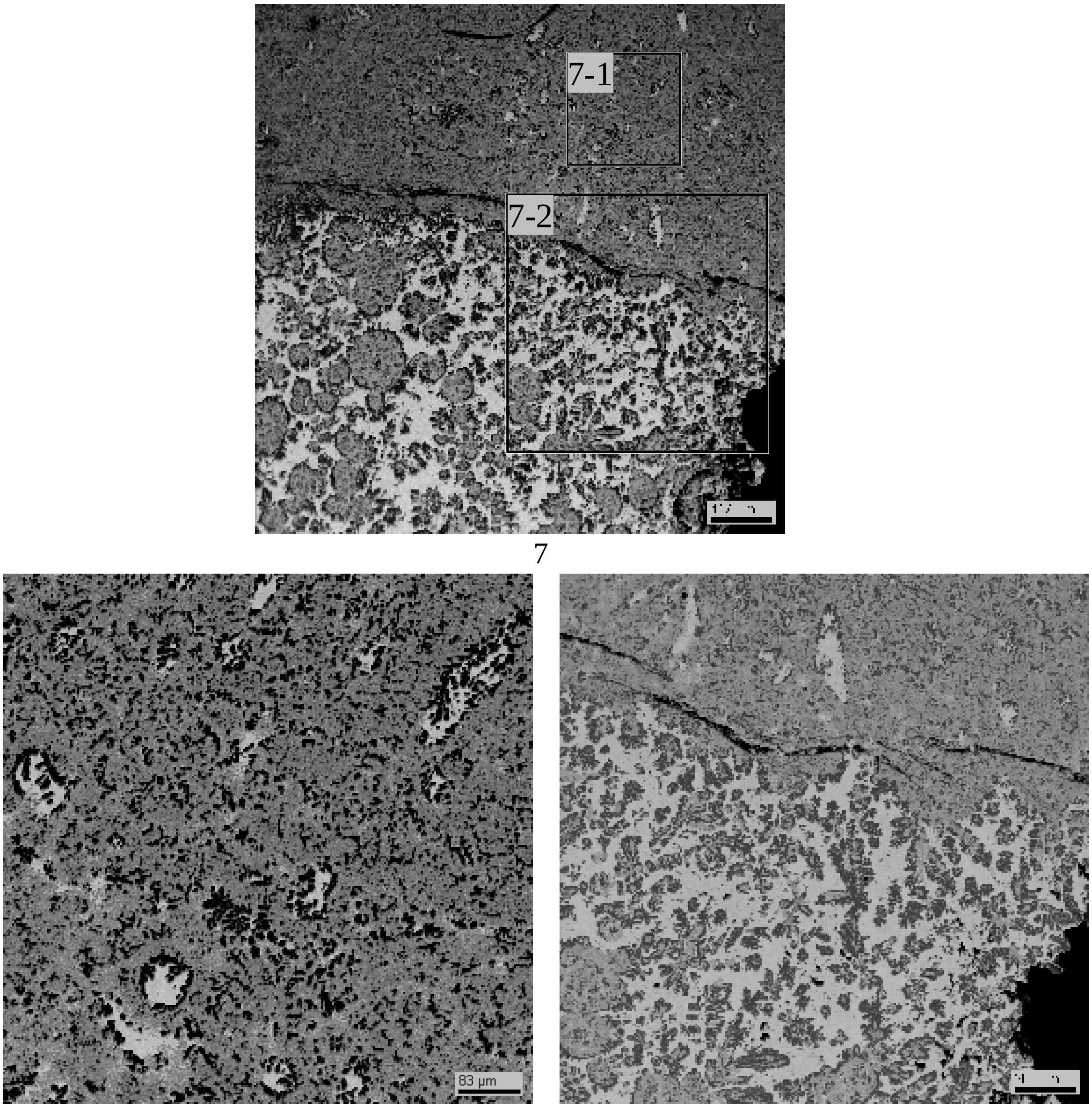

7

7-1

7-2

Fig. 3.64. Microphotographs of region 7

Regions 8-15 represent the microstructure of the metallized bottom layer of the ingot (Fig. 3.65-3.69). Practically all regions have spherical oxidic formations of the second liquid. Noteworthy is a considerable difference between the average composition of oxidic globules from the average composition of different regions of oxidic layer of the ingot, e.g. Fig.3.65, Table 3.45 regions SQ2, SQ3 and Fig.3.58, Table 3.40 region SQ1.

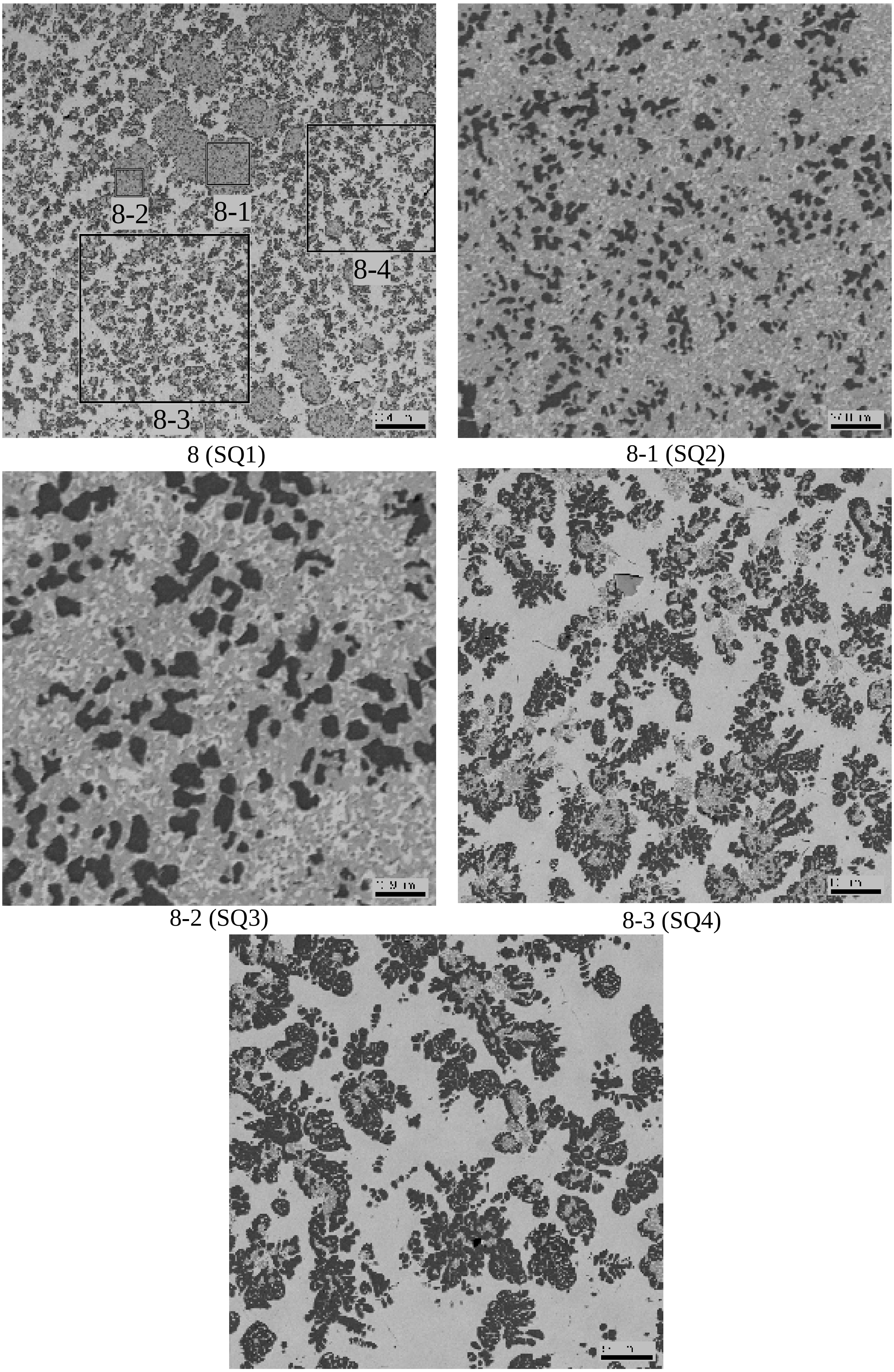

8 (SQ1)

8-1 (SQ2)

8-2 (SQ3)

8-3 (SQ4)

8-4 (SQ5)

Fig. 3.65. Microphotographs of region 8, CORD42 ingot

Table 3.45. EDX analysis of region 8, CORD42

#		U	Zr	~O
SQ1	mass.%	73.33	23.35	3.32
	mol.%	39.92	33.16	26.92
	mol.% MeO$_x$	54.62	45.38	
SQ2	mass.%	80.04	17.52	2.43
	mol.%	49.42	28.23	22.36
	mol.% MeO$_x$	63.64	36.36	
SQ3	mass.%	78.55	19.06	2.39
	mol.%	47.92	30.35	21.73
	mol.% MeO$_x$	61.23	38.77	
SQ4	mass.%	75.48	24.52	-
	mol.%	54.12	45.88	-
SQ5	mass.%	74.33	25.67	-
	mol.%	52.60	47.40	-

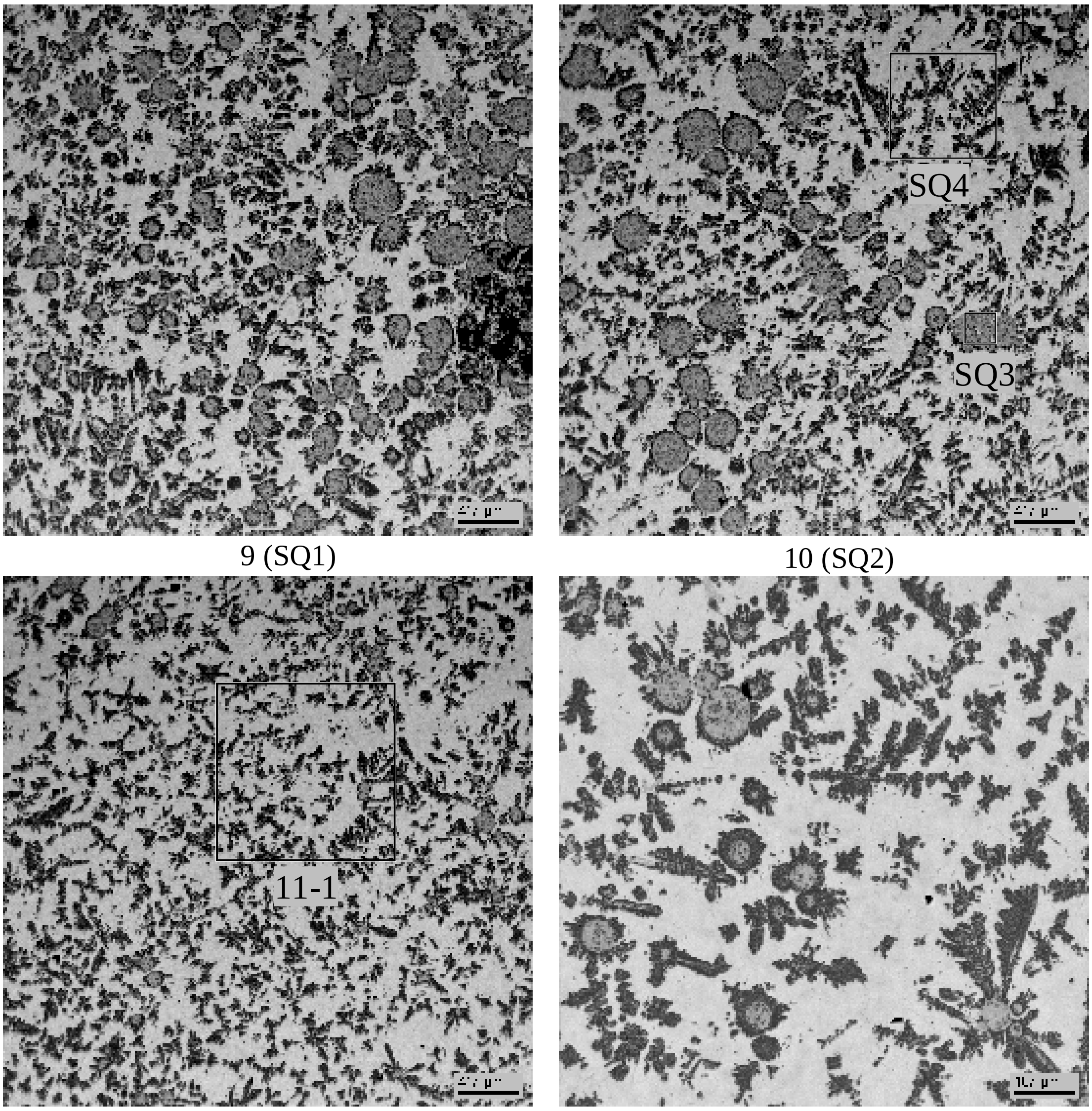

9 (SQ1)

10 (SQ2)

11 (SQ5)

11-1 (SQ6)

Fig. 3.66. Microphotographs of regions 9-11, CORD42 ingot

Table 3.46. EDX analysis of regions 9-11

#		U	Zr	~O
SQ1	mass.%	72.19	21.01	6.80
	mol.%	31.64	24.03	44.32
	mol.% MeO_x	56.84	43.16	
SQ2	mass.%	71.14	20.62	8.24
	mol.%	28.74	21.74	49.51
	mol.% MeO_x	56.93	43.07	
SQ3	mass.%	80.40	15.91	3.69
	mol.%	45.49	23.49	31.02
	mol.% MeO_x	65.95	34.05	
SQ4	mass.%	78.78	21.22	-
	mol.%	58.72	41.28	-
SQ5	mass.%	74.15	20.28	5.58
	mol.%	35.30	25.19	39.51
	mol.% MeO_x	58.36	41.64	
SQ6	mass.%	78.40	21.60	-
	mol.%	58.17	41.83	-

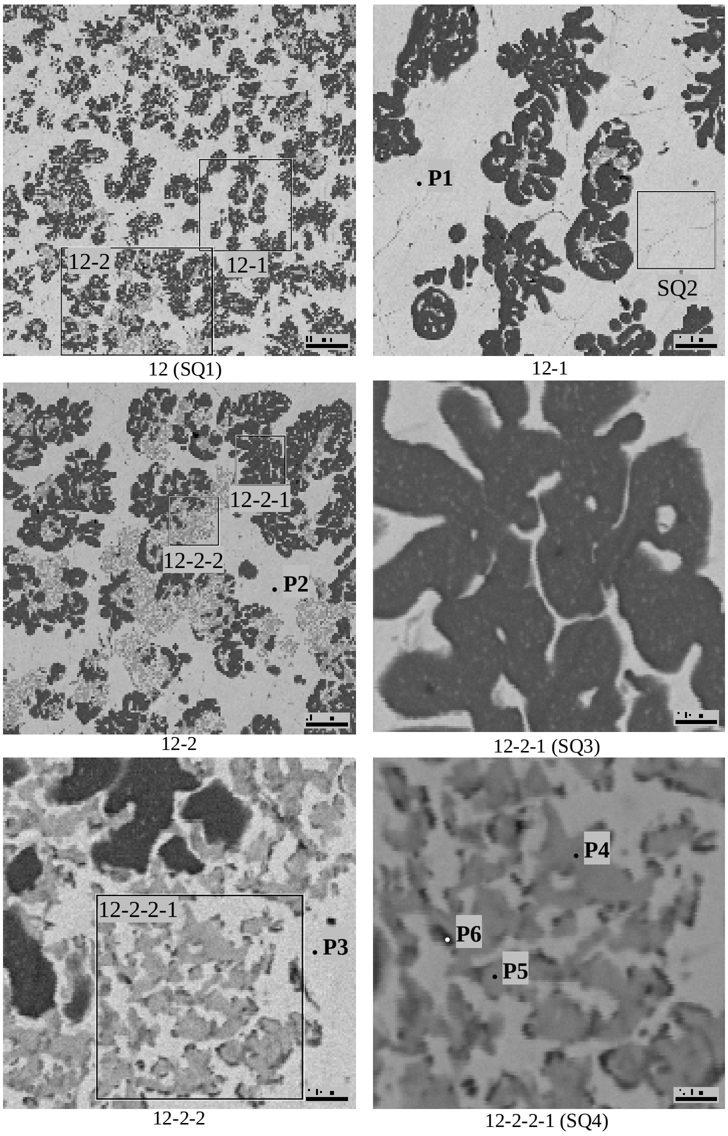

12 (SQ1) 12-1

12-2 12-2-1 (SQ3)

12-2-2 12-2-2-1 (SQ4)

Fig. 3.67. Microphotographs of region 12, CORD42 ingot

A rather even distribution of phases in the bottom layer should be noted (different from CORD37).

In the metallized layer the $(U,Zr)O_{2-x}$ solid solution is likely to be the phase of primary crystallization (Table 3.47, points P4, P5). The content of this phase in the metallic liquid is small. The α-Zr(U)(O)-based solid solution, which grows as a dendrite on crystallized $(U,Zr)O_{2-x}$ is the phase of secondary crystallization. The last to crystallize is U-enriched liquid with a small content of Zr (Table 3.47, points P1-P3)

Table 3.47. EDX analysis of region 12

#		U	Zr	~O
SQ1	mass.%	74.86	25.14	-
	mol.%	53.30	46.70	-
SQ2	mass.%	96.13	3.87	-
	mol.%	90.50	9.50	-
SQ3	mass.%	48.68	51.32	-
	mol.%	26.66	73.34	-
SQ4	mass.%	90.89	7.17	1.94
	mol.%	65.67	13.52	20.81
P1	mass.%	96.43	3.57	-
	mol.%	91.18	8.82	-
P2	mass.%	96.07	3.07	0.87
	mol.%	82.13	6.84	11.03
	mol.% MeO_x	92.31	7.69	
P3	mass.%	98.29	1.71	-
	mol.%	95.65	4.35	-
P4	mass.%	84.54	6.86	8.60
	mol.%	36.69	7.77	55.54
	mol.% MeO_x	82.53	17.47	
P5	mass.%	84.58	2.09	13.34
	mol.%	29.32	1.89	68.79
	mol.% MeO_x	93.95	6.05	
P6	mass.%	7.41	69.55	23.04
	mol.%	1.39	34.13	64.48
	mol.% MeO_x	3.92	96.08	

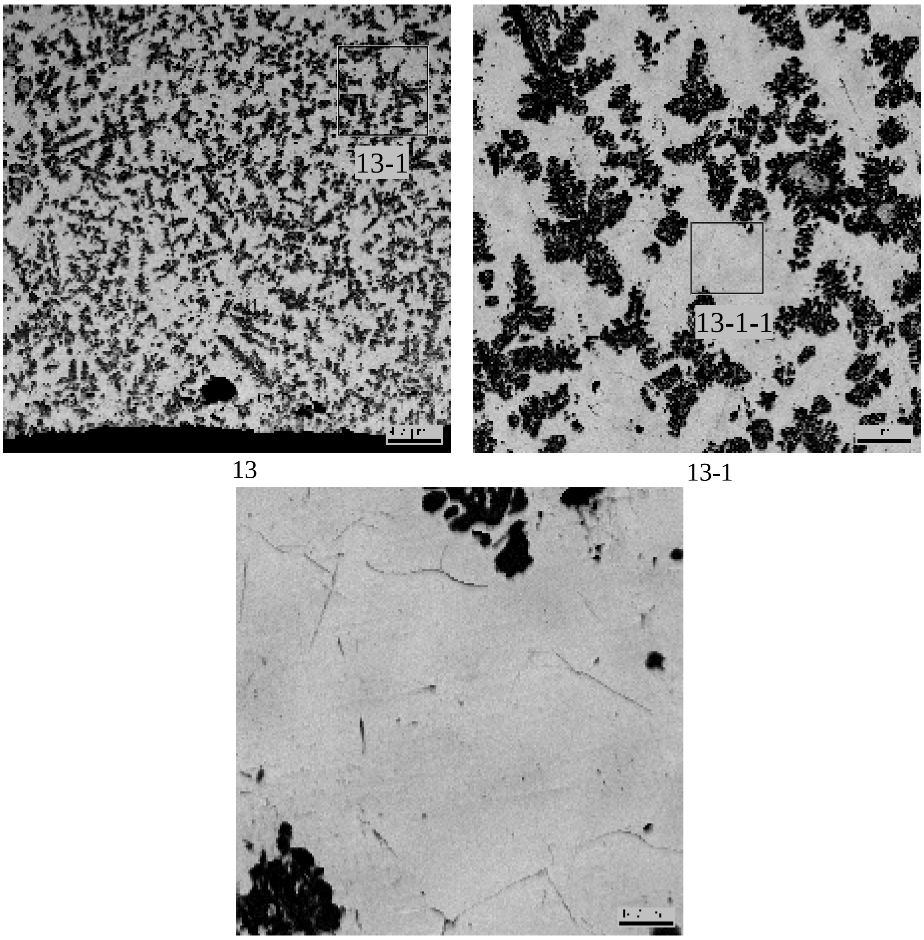

13 13-1

13-1-1

Fig. 3.68. Microphotographs of region 13 , CORD42 ingot

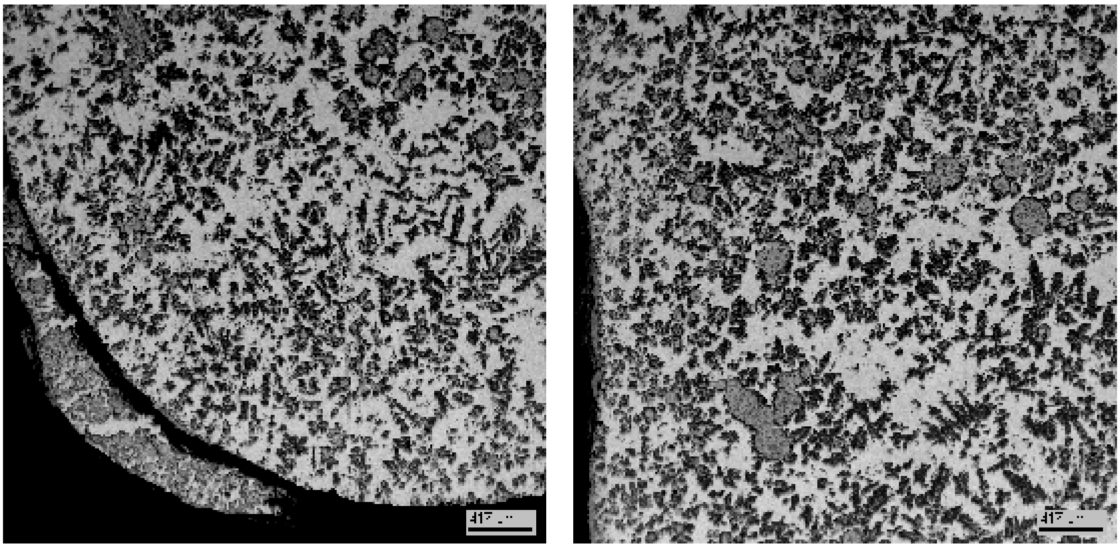

14 15

Fig. 3.69. Microphotographs of regions 14 and 15, CORD42 ingot

In difference to CORD37, practically all regions of CORD42 metallized layer have formations of the second liquid, which can be explained by high superheating of molten pool above the monotectic temperature.

3.4.6.2 SEM/EDX analysis of CD samples

In the CD series templates were prepared from samples, which were cut from ingots. Figs. 3.70-3.72 show the microstructure of the CD samples, the corresponding tables give their average compositions.

Experiment CD3

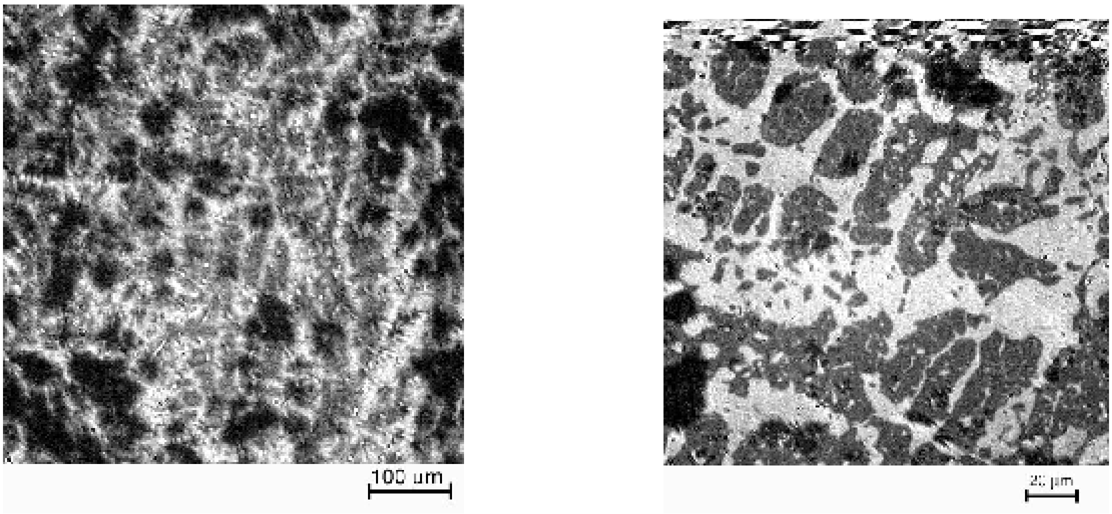

#		U	Zr	O	C	Nb	Hf
SQ	mol.%	11.25	39.81	47.00	1.57	0.32	0.05

Fig. 3.70. Microphotographs and EDX analysis of CD-3 sample

Experiment CD4

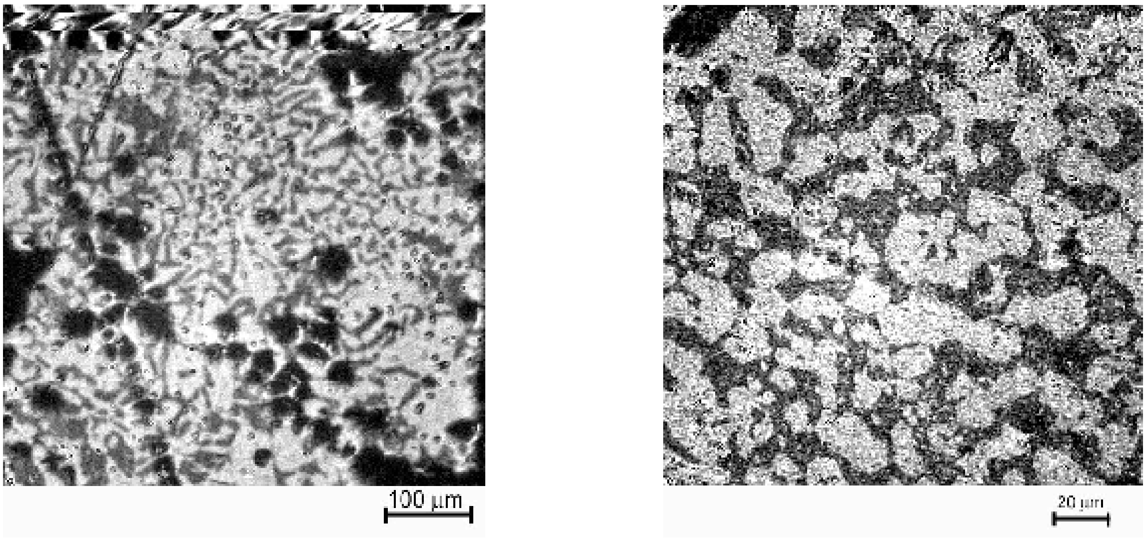

#		U	Zr	O	C	Nb	Hf
SQ	mol.%	4.69	50.74	42.30	1.75	0.36	0.07

Fig. 3.71. Microphotographs and EDX analysis of CD-4 sample

Experiment CD5

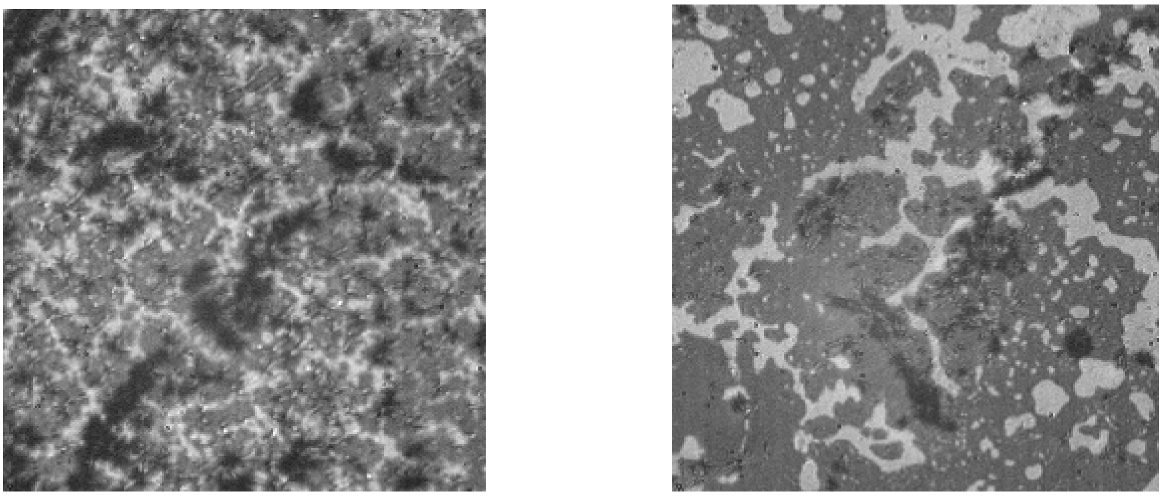

#		U	Zr	O	C	Nb	Hf
SQ	mol.%	16.27	25.22	56.95	0.89	0.63	0.04

Fig. 3.72. Microphotographs and EDX analysis of CD-5 sample

The content of carbon in the analyzed samples was 1-2 mol.%.

3.4.7. VPA IMCC liquidus measurements

Fig. 3.73-3.79 and Table 3.48 show the processing and summary of data from the CORD experimental series, which were provided by the VPA IMCC studies of the U-Zr-O system. The figures show thermograms with video frames of the molten pool surface during the liquidus temperature measurement.

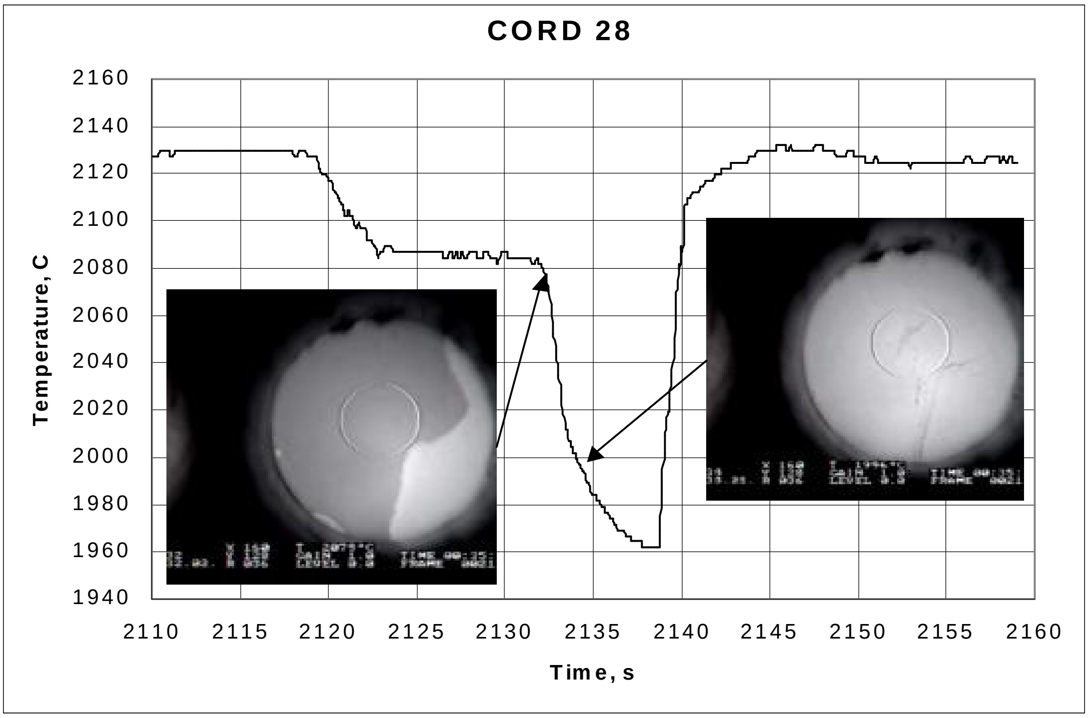

Fig. 3.73. CORD28-I thermogram with video frames of molten pool surface

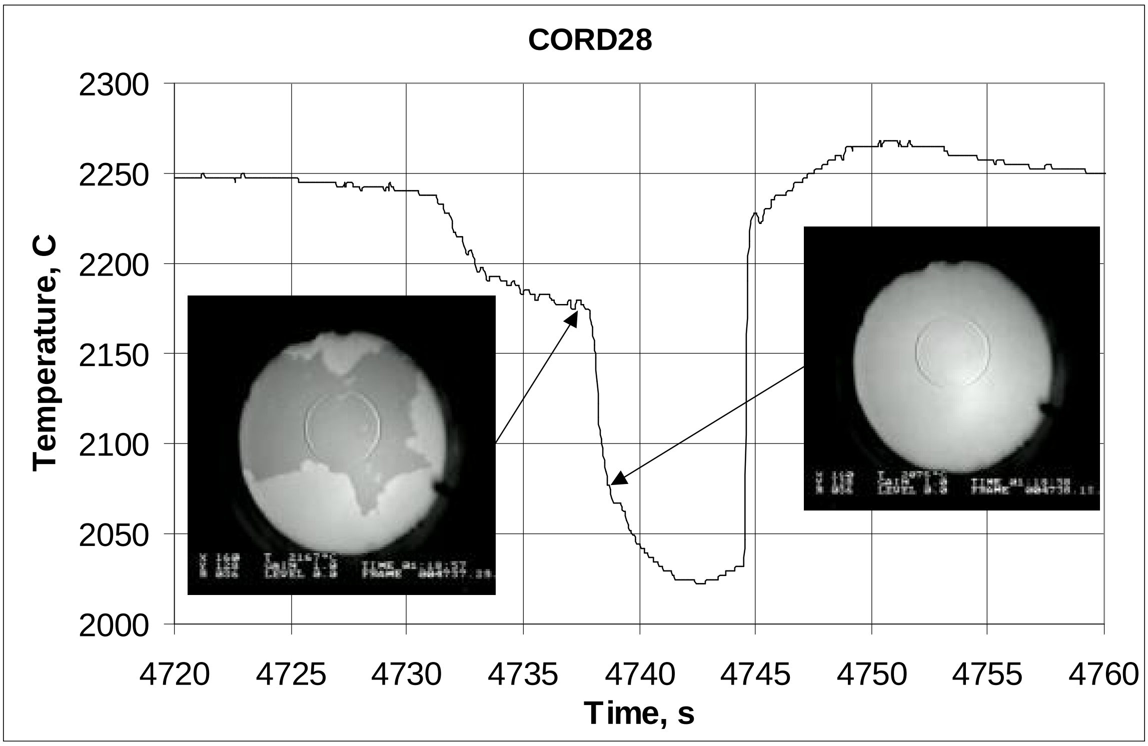

Fig. 3.74. CORD28-II thermogram with video frames of molten pool surface

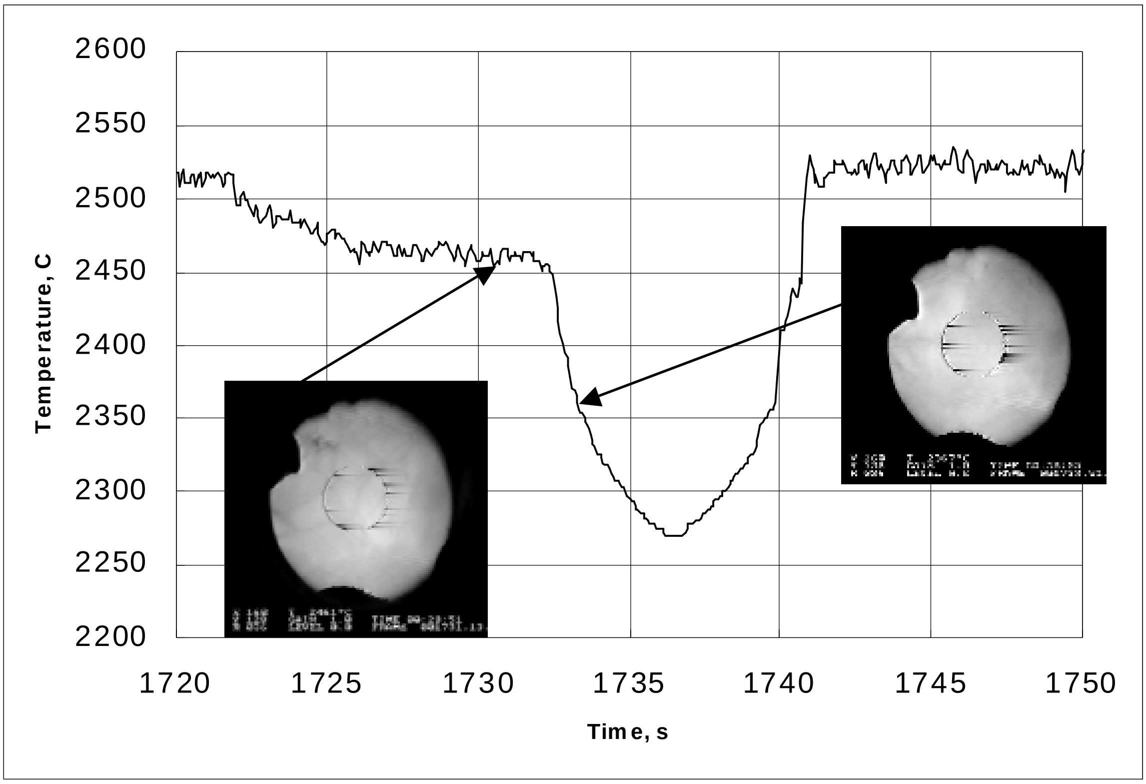

Fig. 3.75. CORD29 thermogram with video frames of molten pool surface

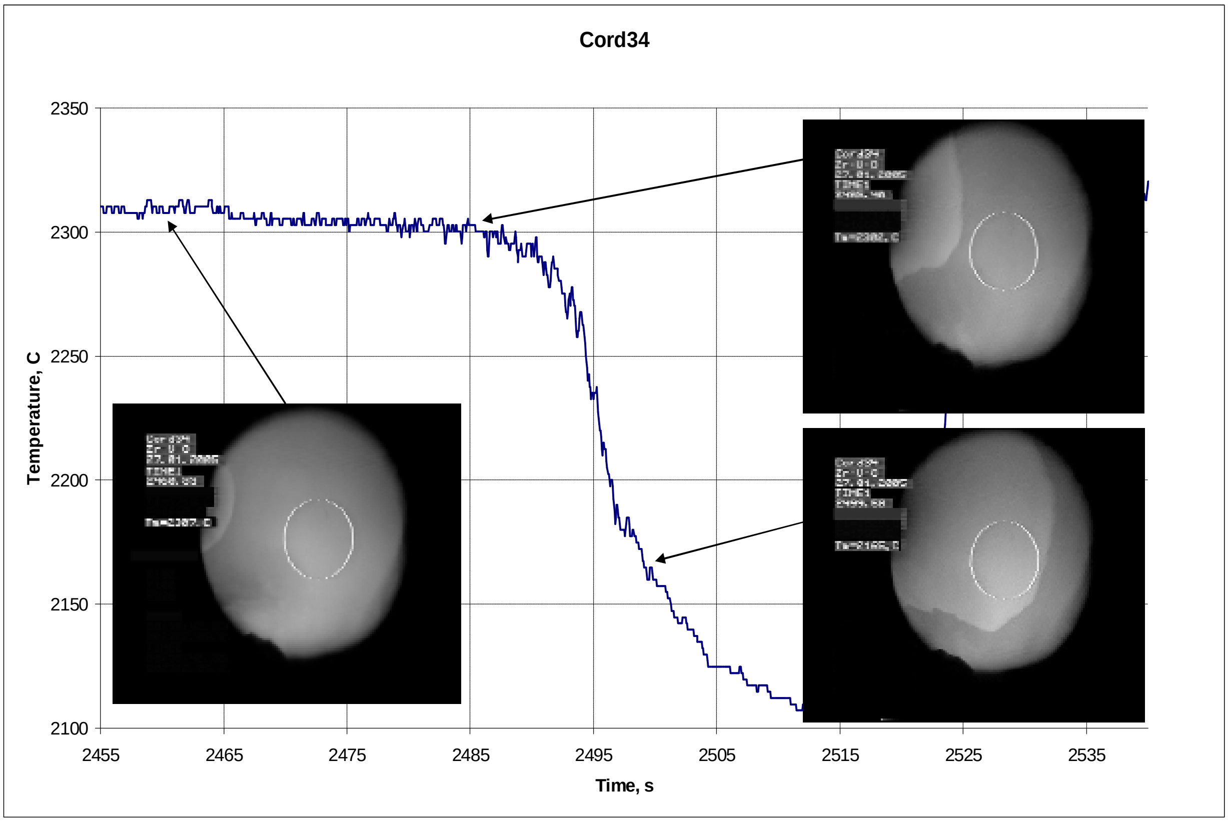

Fig. 3.76. CORD34 thermogram with video frames of molten pool surface

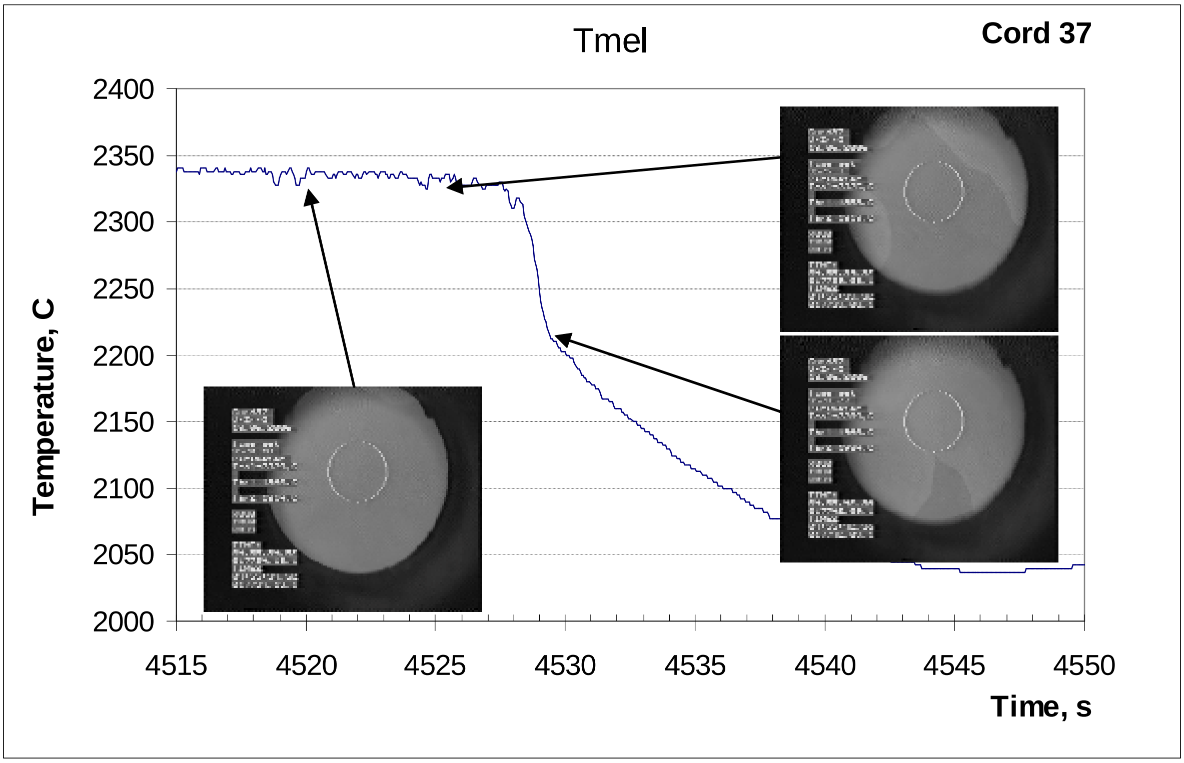

Fig. 3.77. CORD37 thermogram with video frames of molten pool surface

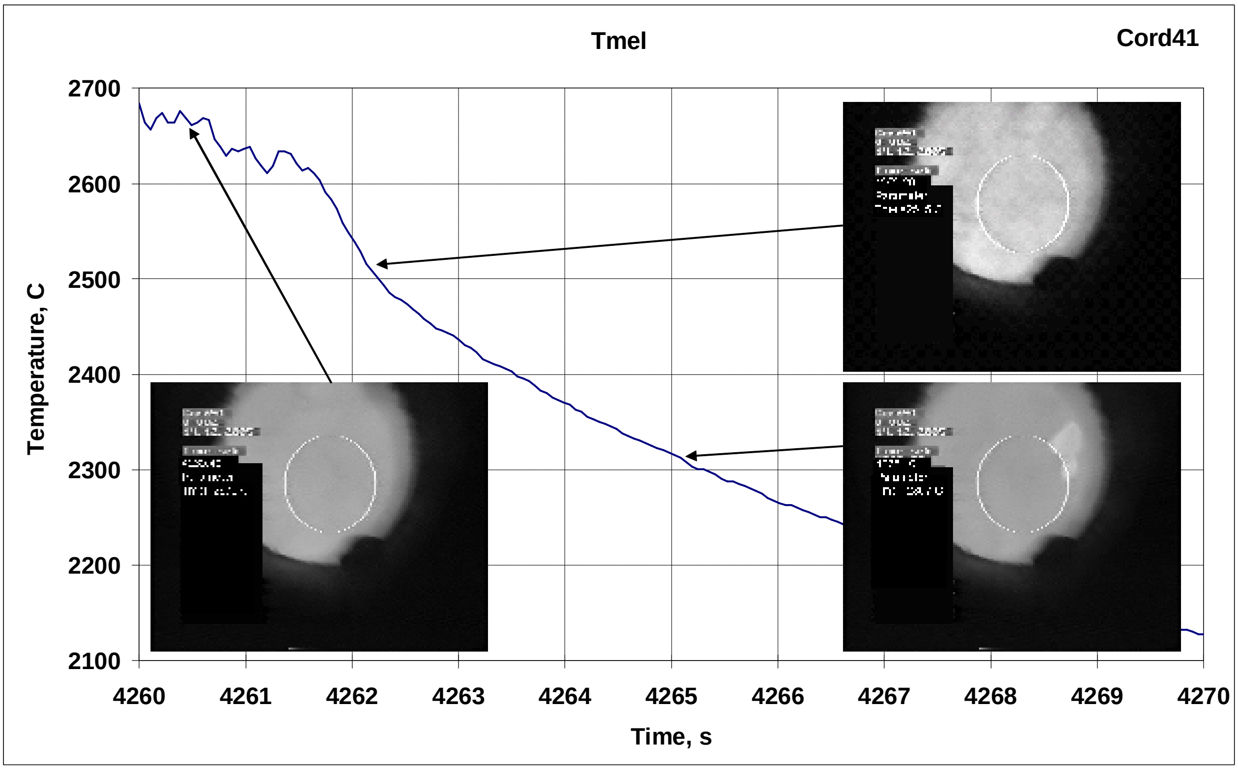

Fig. 3.78. CORD41 thermogram with video frames of molten pool surface

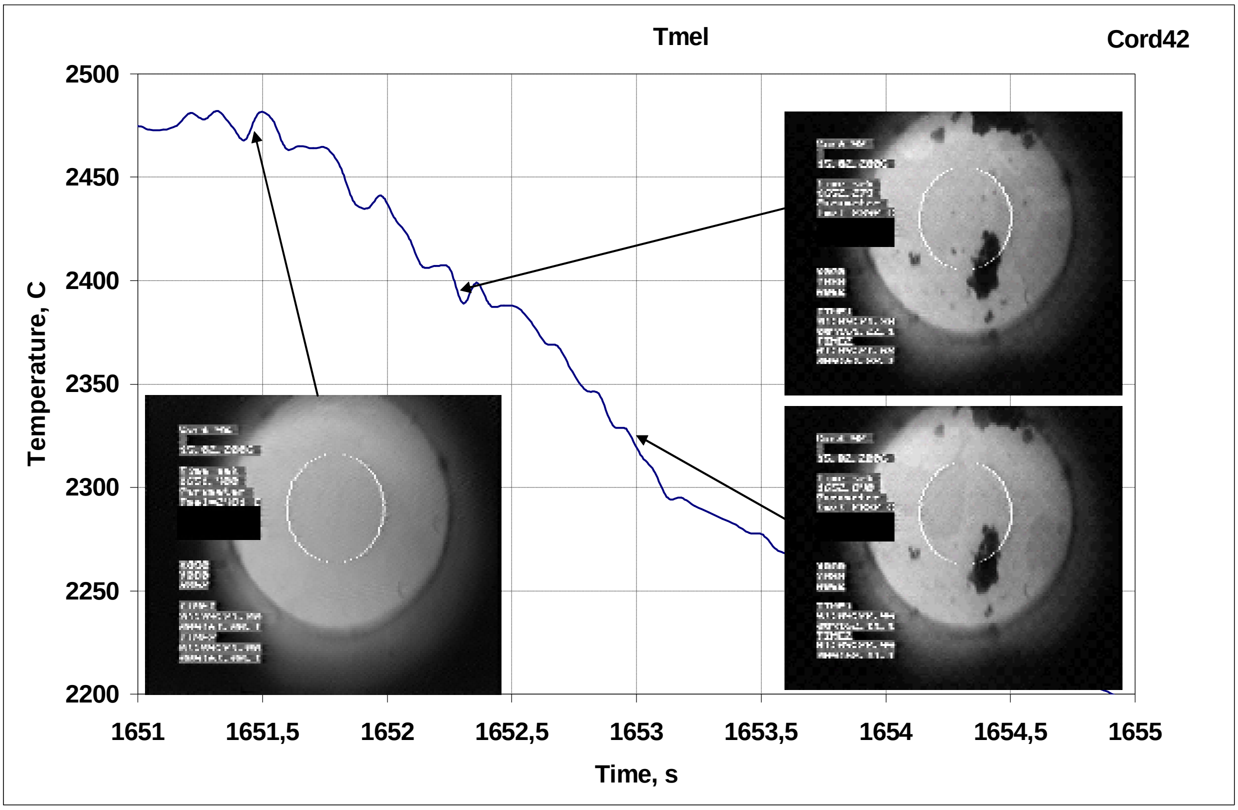

Fig. 3.79. CORD42 thermogram with video frames of molten pool surface

Table 3.48. Liquidus temperature of the U-Zr-O system measured by VPA IMCC

Test	Calculated initial melt composition including spillages and imbalance, at.%			Composition of melt samples in accordance with XRF, at.%			T_{liq}, °C
	U	Zr	O	U	Zr	O	
CORD28-I	7.7	53.6	38.7	7.7	53.7	38.6	2085
CORD28-II	13.0	43.9	43.2	12.9	43.9	43.2	2170
CORD29	20.0	17.1	63.0	19.8	17.2	63.0	2461
CORD34	22.1	33.8	44.1	21.5	34.7	43.8	2302 2307 2305
CORD37[2)]	32.5	29.2	38.3	-	-	-	2326 2330
CORD41[1),2)]	56.0	3.1	40.9	-	-	-	2515
CORD42[2)]	40.5	27.0	32.5	-	-	-	2390

[1)] 2.3g of aerosols were included into the calculated charge composition.

2) Due to the stratification the average melt composition cannot be determined from the sample of the top liquid.

3.4.8. Liquidus and solidus measurements on the “Tigel” facility

Fig. 3.80-3.92 and Table 3.49 show the processing and summary of the CD data on the U-Zr-O system provided by the thermogram differentiation method. The figures show thermograms, their fragments and temperature curves vs. time at liquidus and solidus measurements.

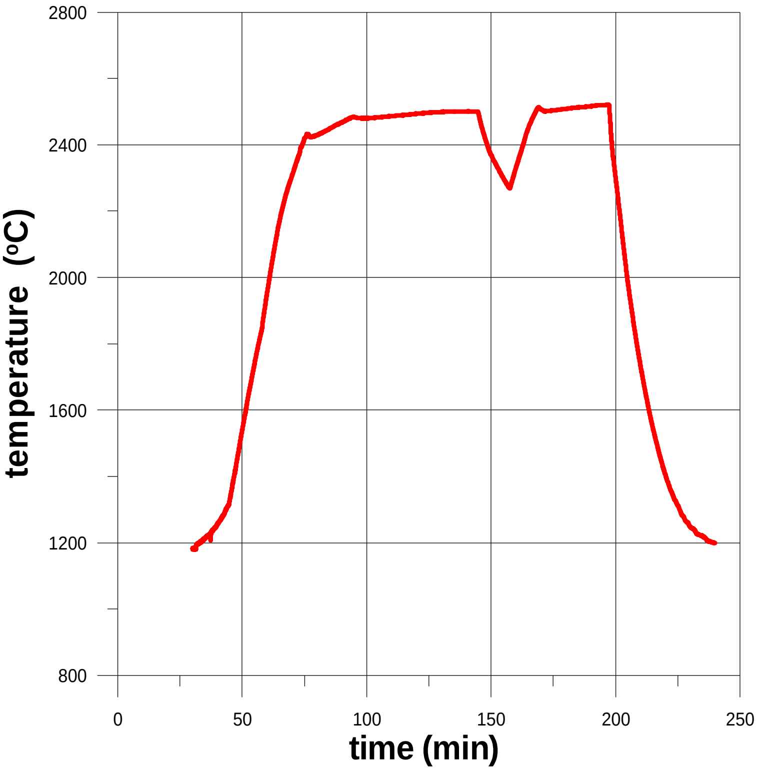

Fig. 3.80. CD1 thermogram

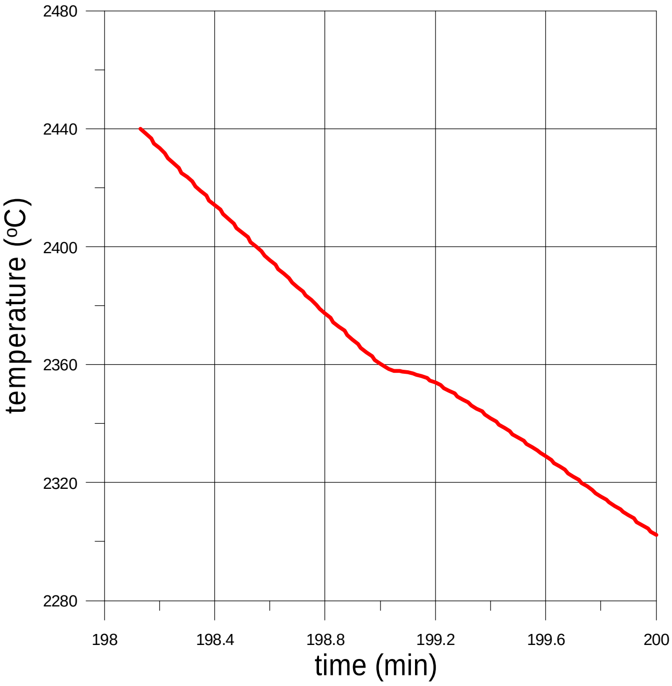

Fig. 3.81. CD1 thermogram fragment at melt cooling

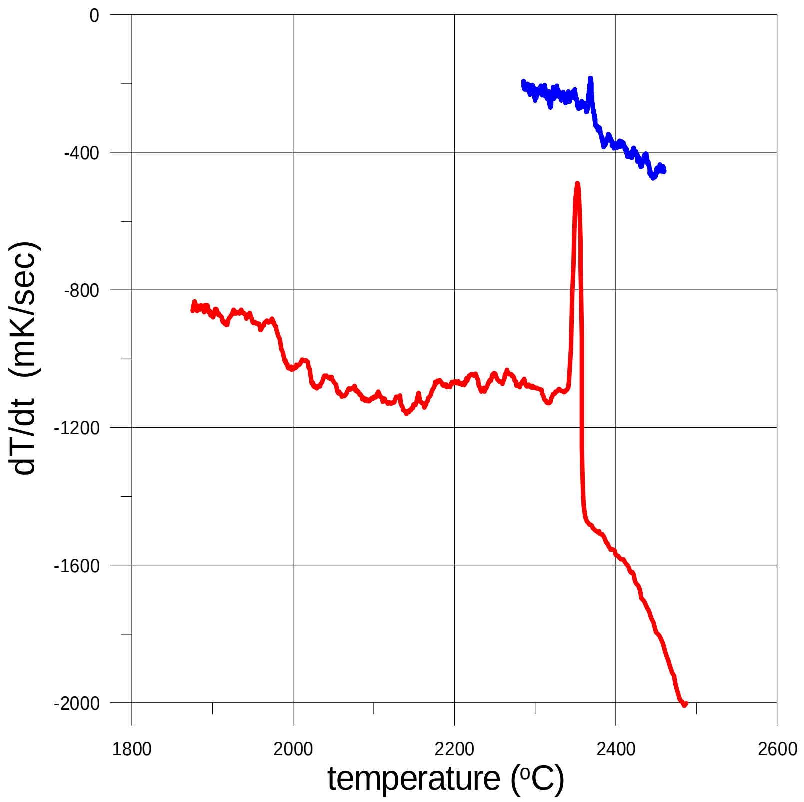

Fig. 3.82. Melt cooling rate vs. time in CD 1

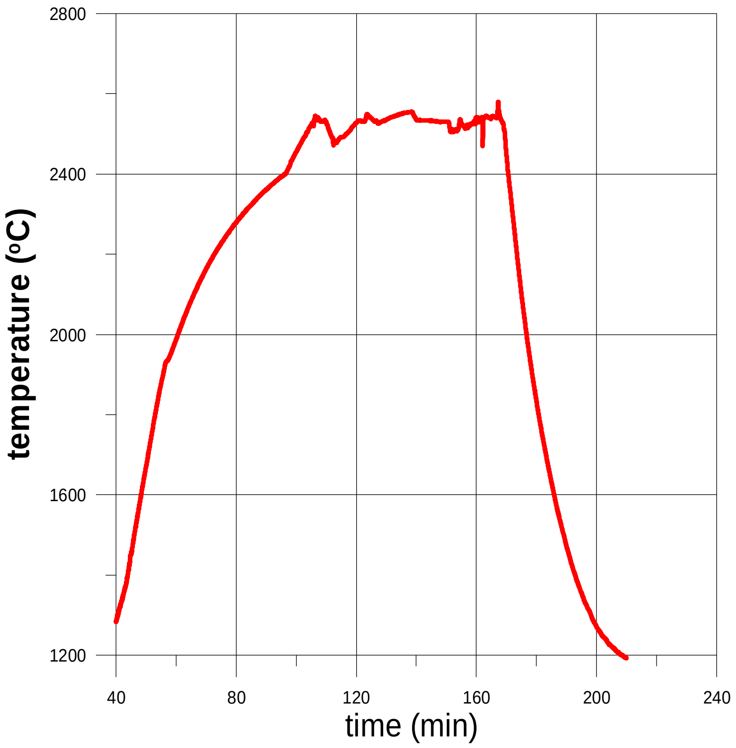

Fig. 3.83. CD2 thermogram

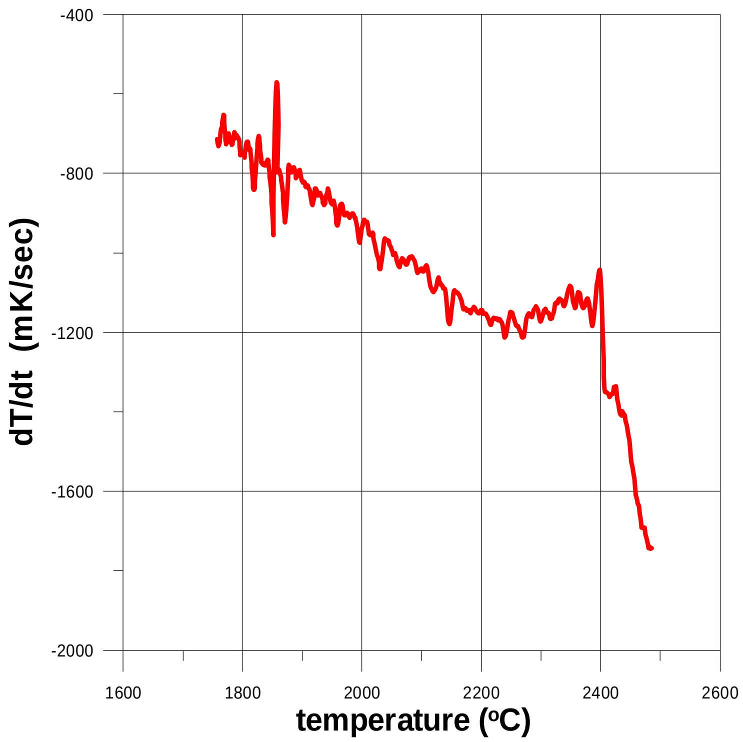

Fig. 3.84. Melt cooling rate vs. time in CD2

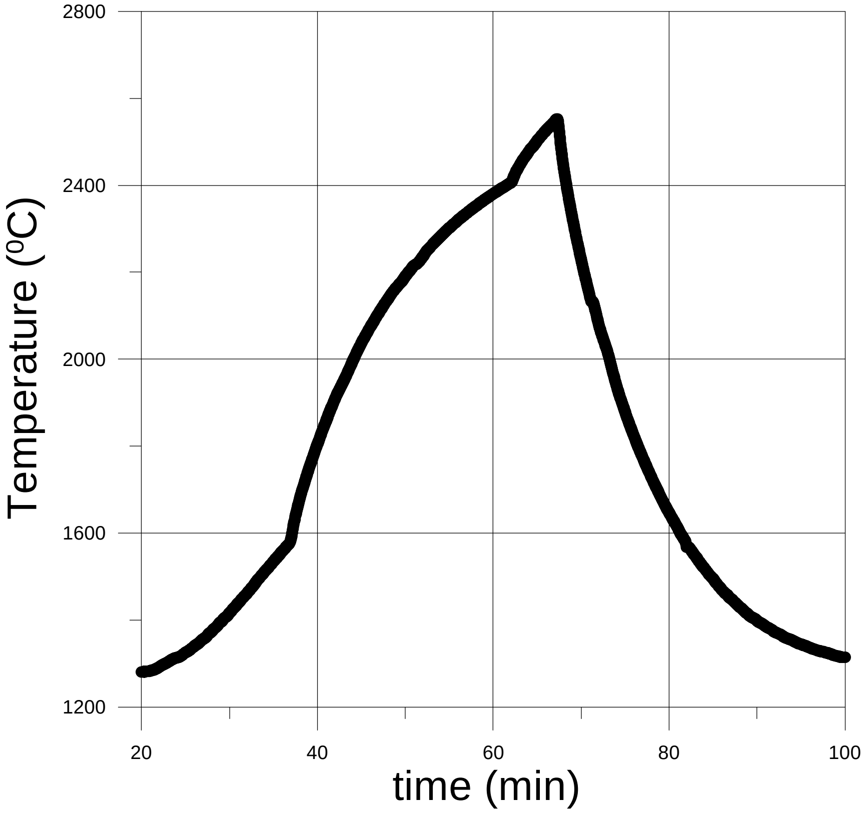

Fig. 3.85. CD3 thermogram

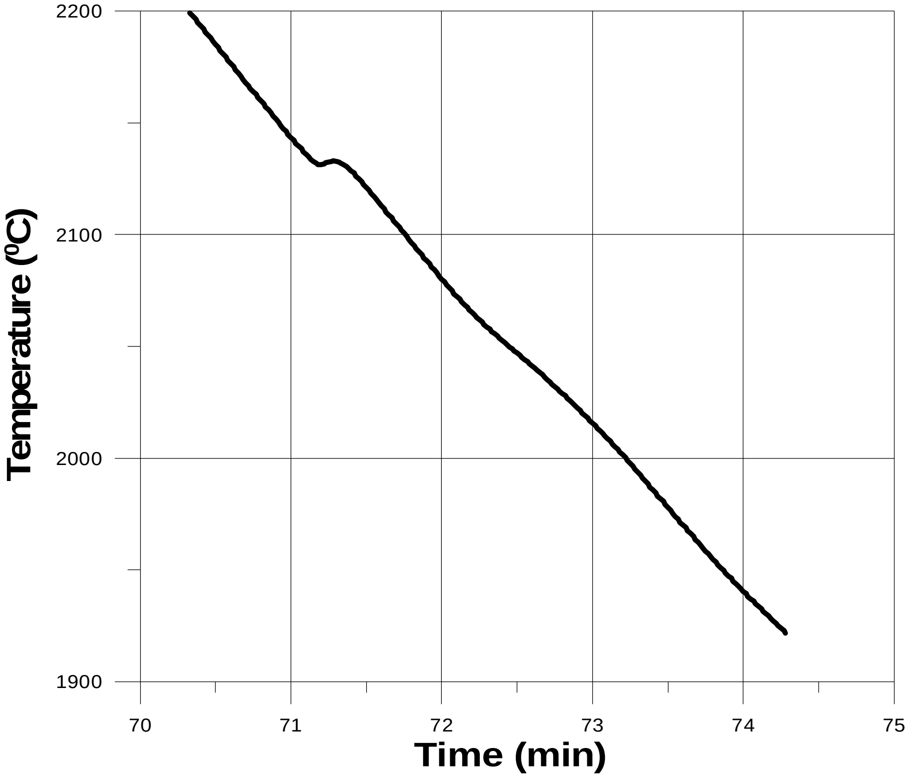

Fig. 3.86. CD3 thermogram fragment at melt cooling

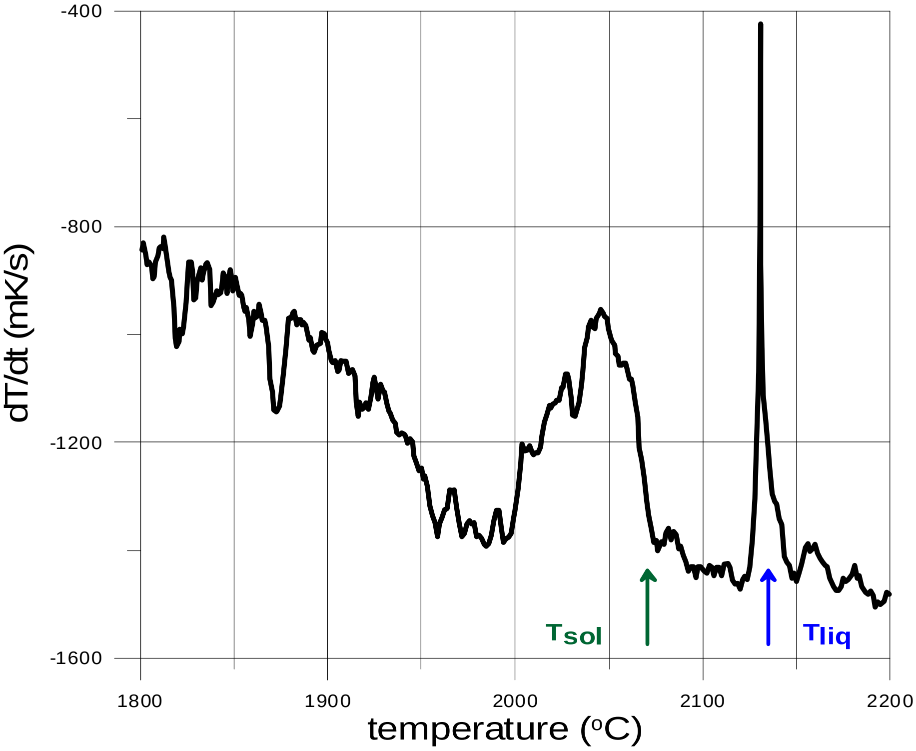

Fig. 3.87. Melt cooling rate vs. time in CD3

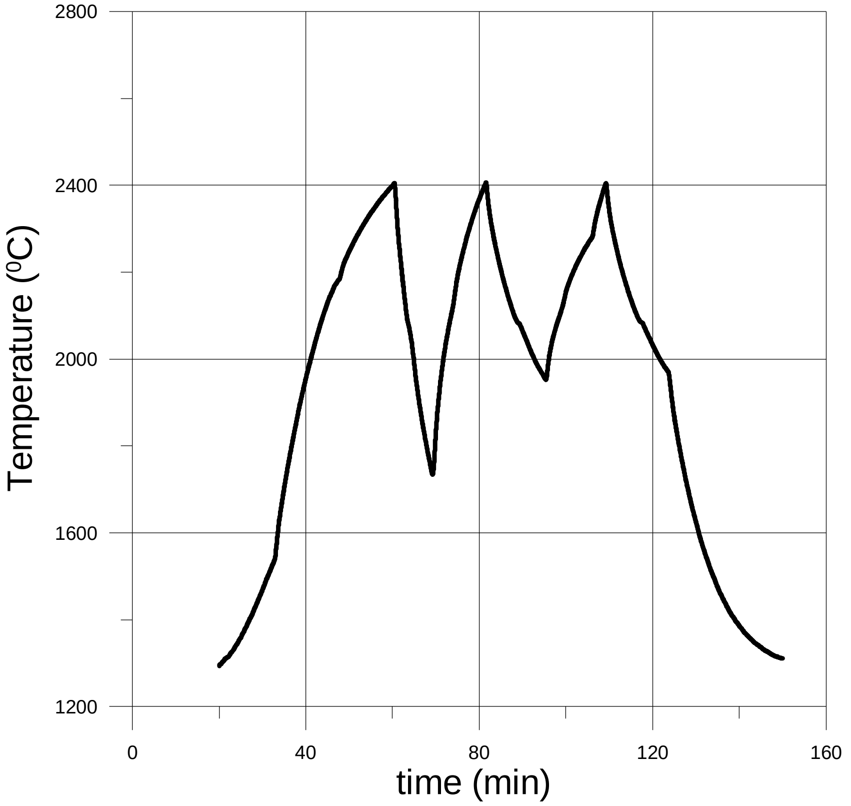

Fig. 3.88. CD4 thermogram

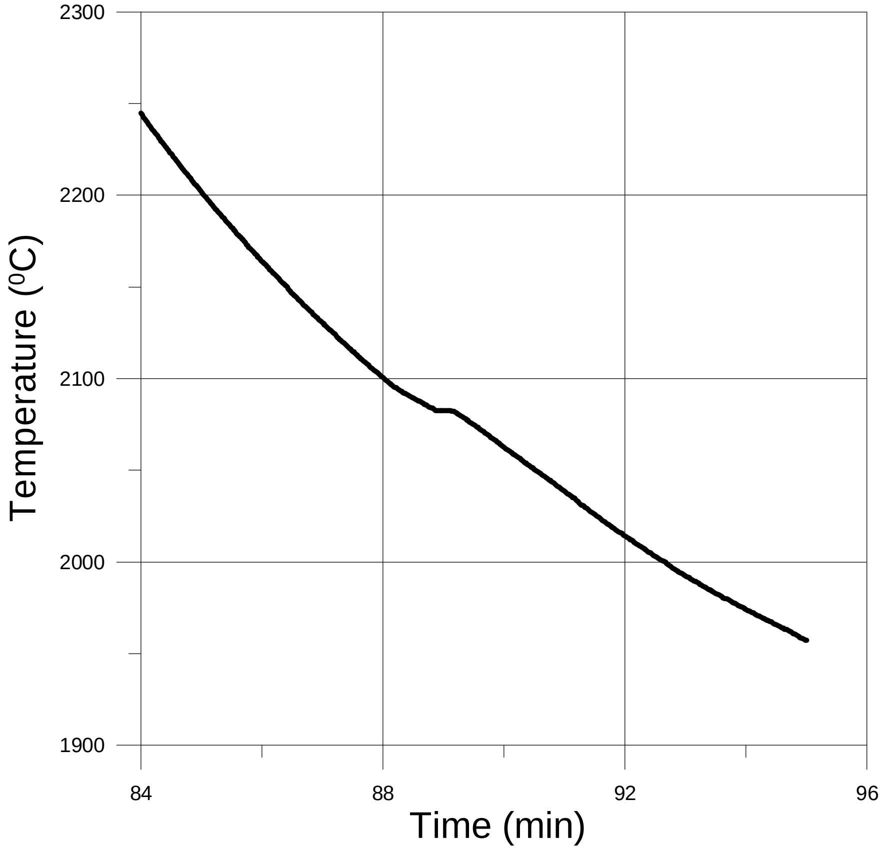

Fig. 3.89. CD4 thermogram fragment at melt cooling

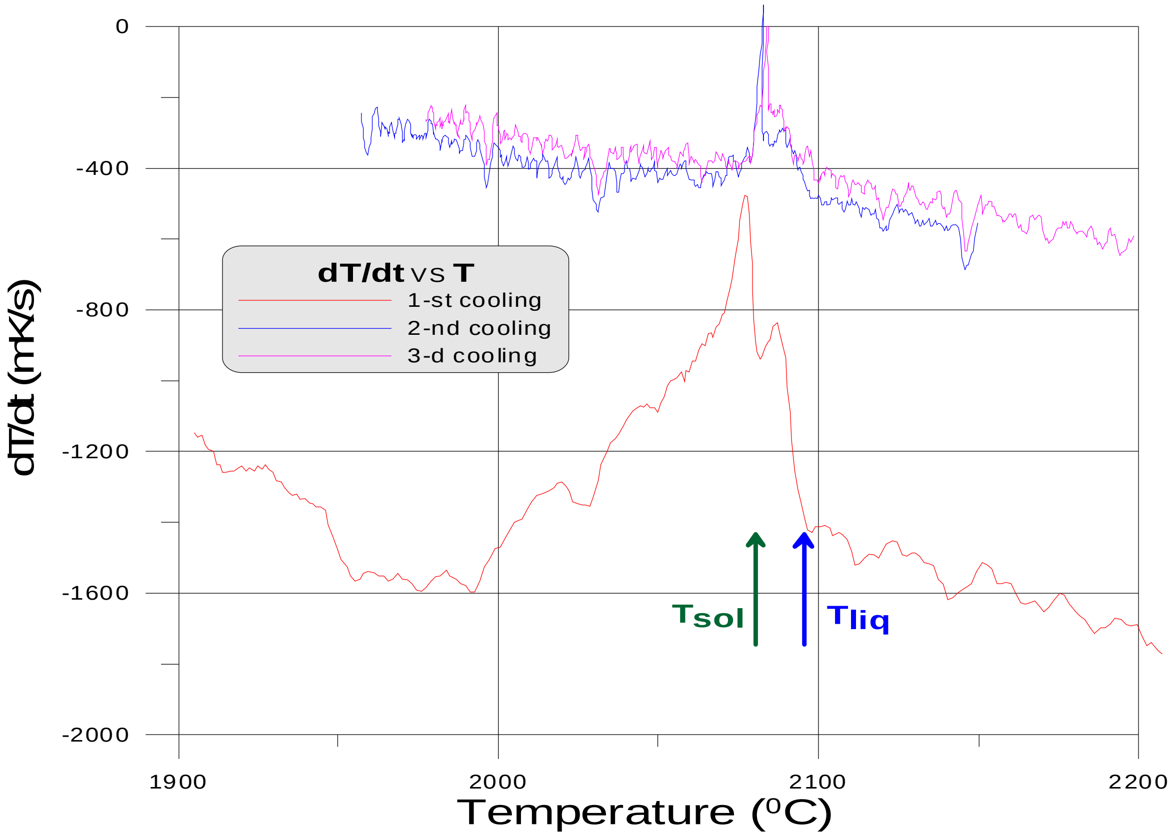

Fig. 3.90. Melt cooling rate vs. time in CD4

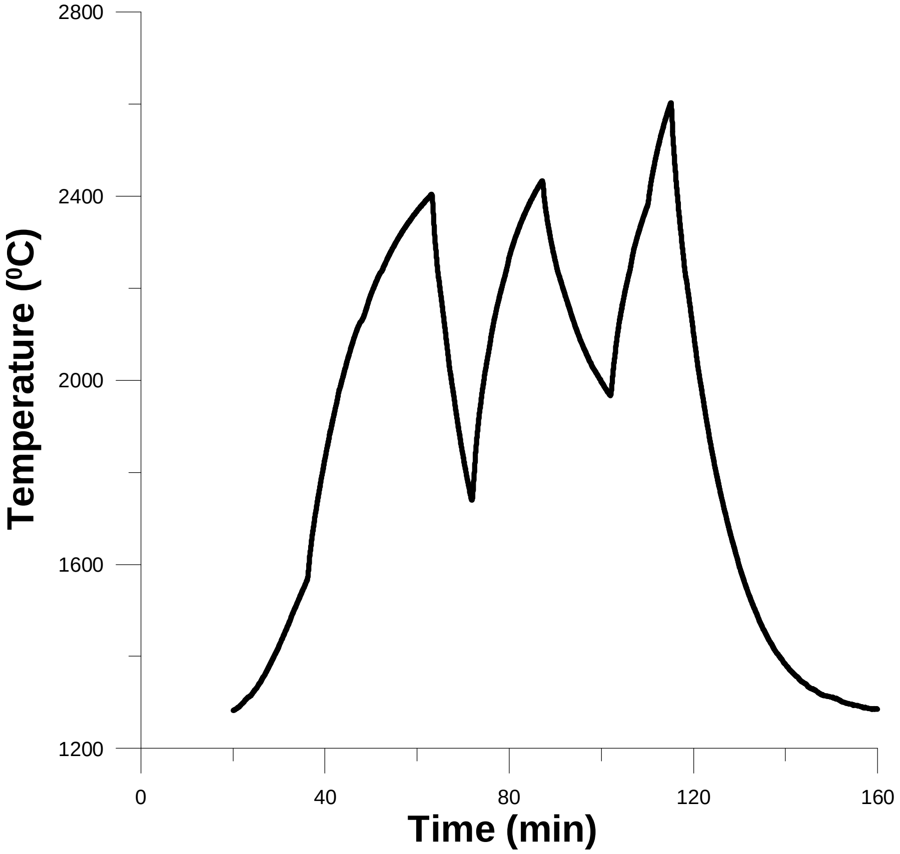

Fig. 3.91. CD5 thermogram

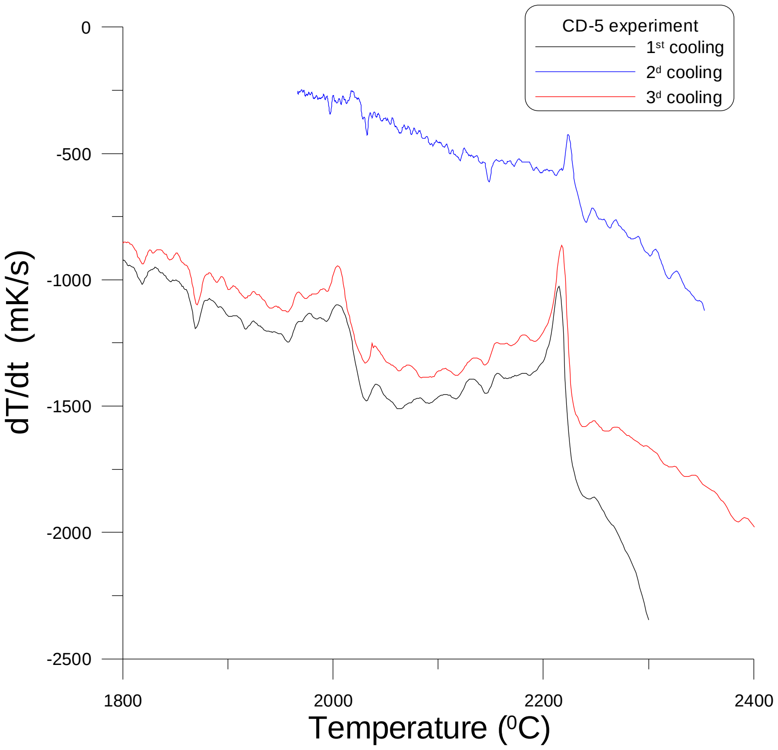

Fig. 3.92. Melt cooling rate vs. time in CD5

Table 3.49. Liquidus temperature of the U-Zr-O system determined by the thermogram differentiation

Test	Melt charge composition1), at.%			T_{sol}, °C	T_{liq}, °C
	U	Zr	O		
CD1	22.9	19.1	58.0	-	2370
CD2	25.7	15.8	58.5	-	2400
CD3	13.0	43.0	44.0	2072	2135
CD4	8.0	52.0	40.0	2085	2100
CD5	16.0	36.0	48.0	2025	2225

[1] –Charged materials in the hot crucible are molten completely, without losses..

As explained in Section 3.4.6.2, insignificant quantities of carbon in the melt (1-2 mol. %,) have practically no influence on the average composition; for this reason charge composition corresponds to the experimental point of the phase diagram.

3.4.9. Solidus measurements in the Galakhov microfurnace

As noted above, measurement of liquidus temperature of metal-oxidic systems in the Galakhov microfurnace is difficult due to the holder-sample interaction. Same circumstance influences solidus temperature measurements, especially in cases when the difference between solidus and liquidus temperatures is small. A significant error can result from the crystallization peculiarities, i.e. microstructure of the specimen used for determining solidus temperature (phase distribution in the specimen, presence of eutectic zones) and small liquid phase fraction near the solidus point of the specimen.

Experiment CORD28-II

Fig. 3.93 shows frames with specimen heating and melting in the Galakhov microfurnace, with the specimen deformation (melting) start - registered from the moment, when the corner of the analyzed sample melts (becomes rounded), and intensive melting when the melt spreads on the holder (Rod sample #2).

Solid sample

Sample corner deformation start

Melting start registered by the sample corner deformation

Sample intensive melting

Fig. 3.93. CORD28 sample during solidus temperature measurement by the visual polithermal analysis in the Galakhov microfurnace (Rod sample#1)

Experiment CORD34

Fig. 3.94 shows fragments of sample heating and melting with the deformation (shrinking) start and beginning of melting, which was determined by the observed lost sharpness of the sample corner (rod sample #4). Fig. 3.95 shows the sample and holder after analysis.

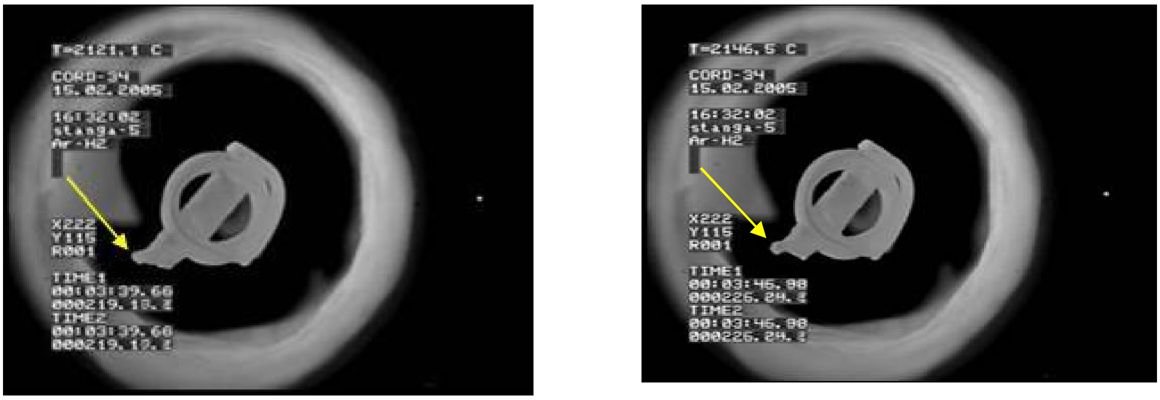

2121°C – sample corner deformation start

2146°C – observed melting start

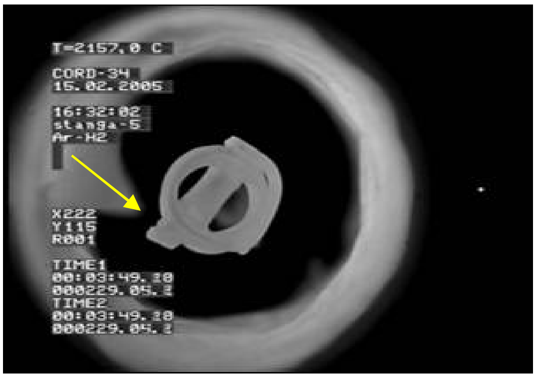

2157°C – complete corner deformation

Fig. 3.94. Samples during solidus temperature measurement by the visual polithermal analysis in the Galakhov microfurnace for CORD34 (Rod sample#4)

Fig. 3.95. Sample and holder after CORD34 analysis

Solidus temperature (melting start) for the CORD-34 rod sample determined by the visual-polythermal analysis in the Galakhov microfurnace was 2121-2157°C. Liquidus temperature was not determined due to the intensive sample-holder interaction.

Experiment CORD37

Fig. 3.96 shows images with the sample deformation and melting start registered from the moment of the sample corner reshaping (Rod sample #1).

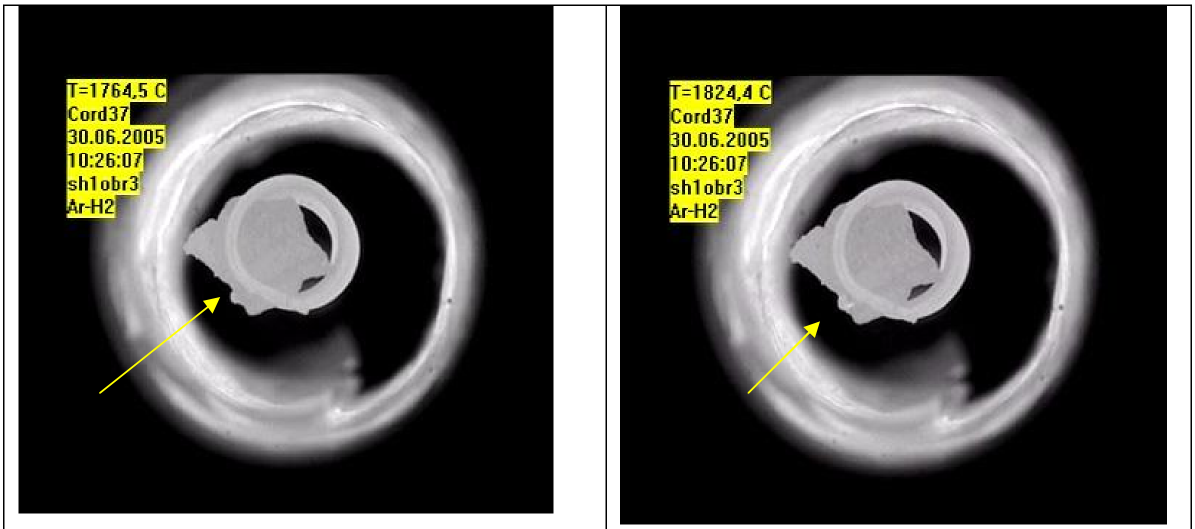

Solid sample

Corner deformation start

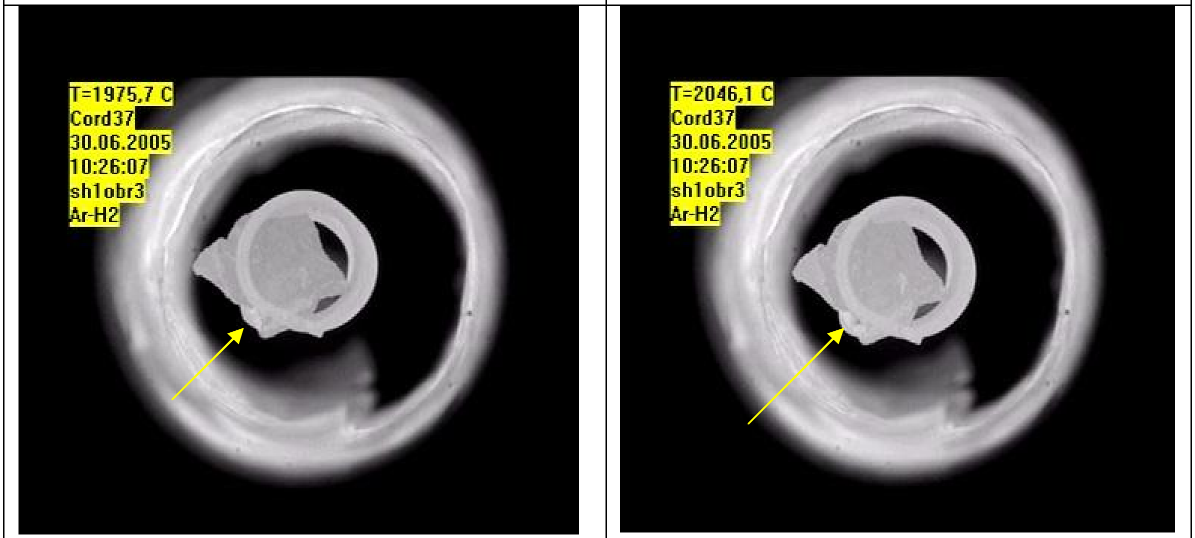

Corner melting

Corner spreading

Fig. 3.96. CORD37 sample during solidus temperature measurement by the visual polithermal analysis in the Galakhov microfurnace (Rod sample#1)

Solidus temperature (melting start) for the CORD37 rod sample determined by the visual-polythermal analysis in the Galakhov microfurnace was 1824-1860°C.

3.4.10. Oxygen measurement by the method of carbothermal reduction

The method of carbothermal reduction (CTR) was used for specifying oxygen content in the oxidic and metallic ingot parts. Initial mass of the samples subjected to analysis was ~ 500 mg, exposition time – 1 min. at 2300ºC in the inert atmosphere (argon).

In essence the method provides the separation of oxygen as CO - CO_2 from the molten sample at its reduction by carbon; this is followed by the gas phase analysis and measurement of the mass loss. Each sample is analyzed using a separate crucible made of porous graphite. A crucible containing one specimen, liquefier (nickel floater),and graphite powder is small (its diameter is 10 – 15 mm), so it does not need long-term degassation. Addition of the carbon powder and floater minimize CO_2 production and improve kinetic and thermodynamic conditions of gas liberation from specimens. During the analysis of certain systems it was found that introduction of the floater decreases the reduction, such systems were reduced in absence of the fusing agent. The analysis accuracy is quite high, if the crucible heating thermogram corresponds to the thermogram of the reference crucible. The general CTR flow-chart is shown in Fig. 3.97.

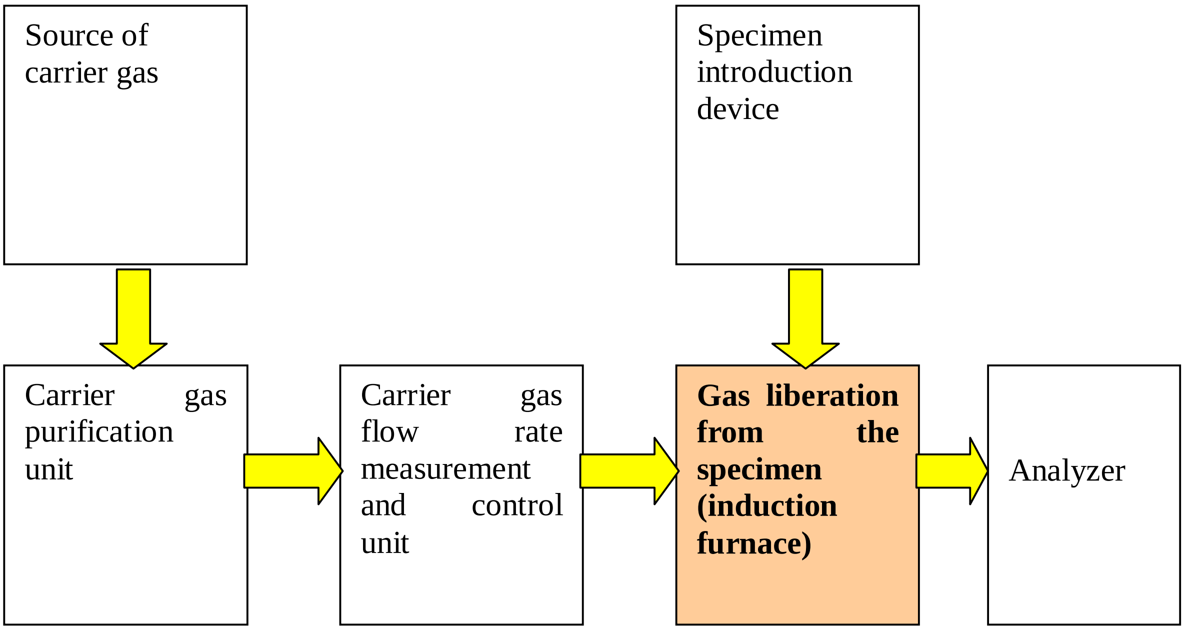

Fig. 3.97. Flow-chart of the CTR in the carrier gas flow

As it follows from the flow-chart, the setup consists of three parts:

- System for preparing carrier gas having purification and control units,

- Gas liberation unit from the specimen (furnace) having the specimen introduction device,

-Gas-analyzer.

An experimental induction furnace was manufactured, which had a coaxial water-cooled quartz tube, into which the graphite crucible with the sample was placed; and a gas line was assembled to supply the carrier gas and analyze off-gases. Fig. 3.98 shows the experimental cell and graphite crucible, and Fig. 3.99 – furnace schematics.

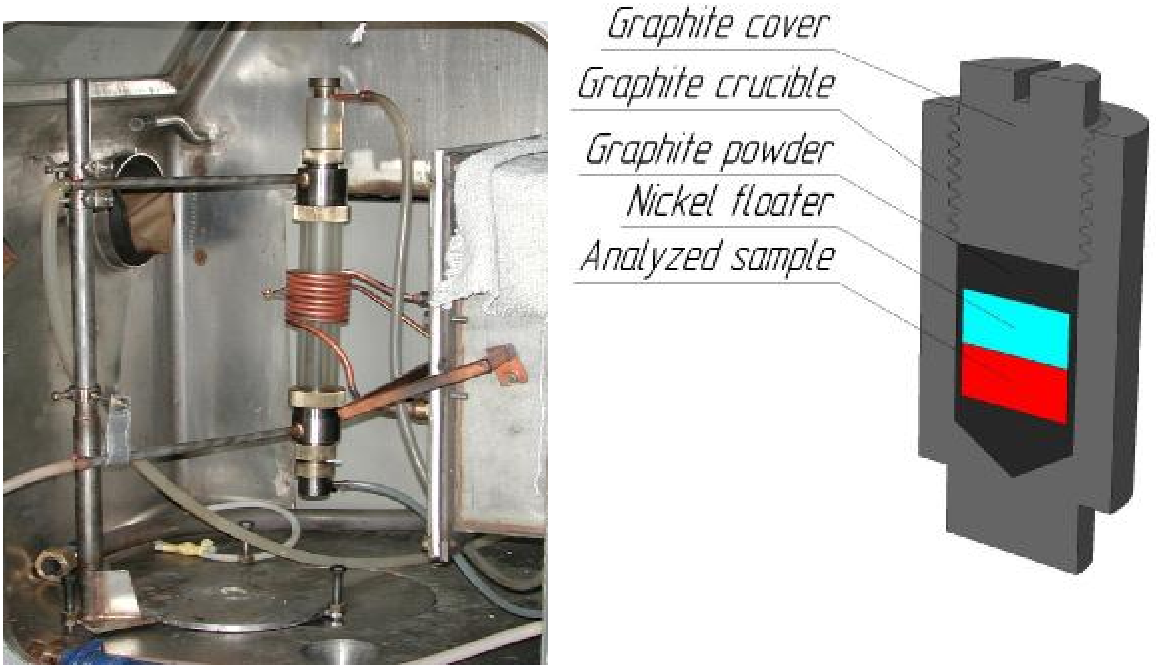

Fig. 3.98. CTR furnace and graphite crucible

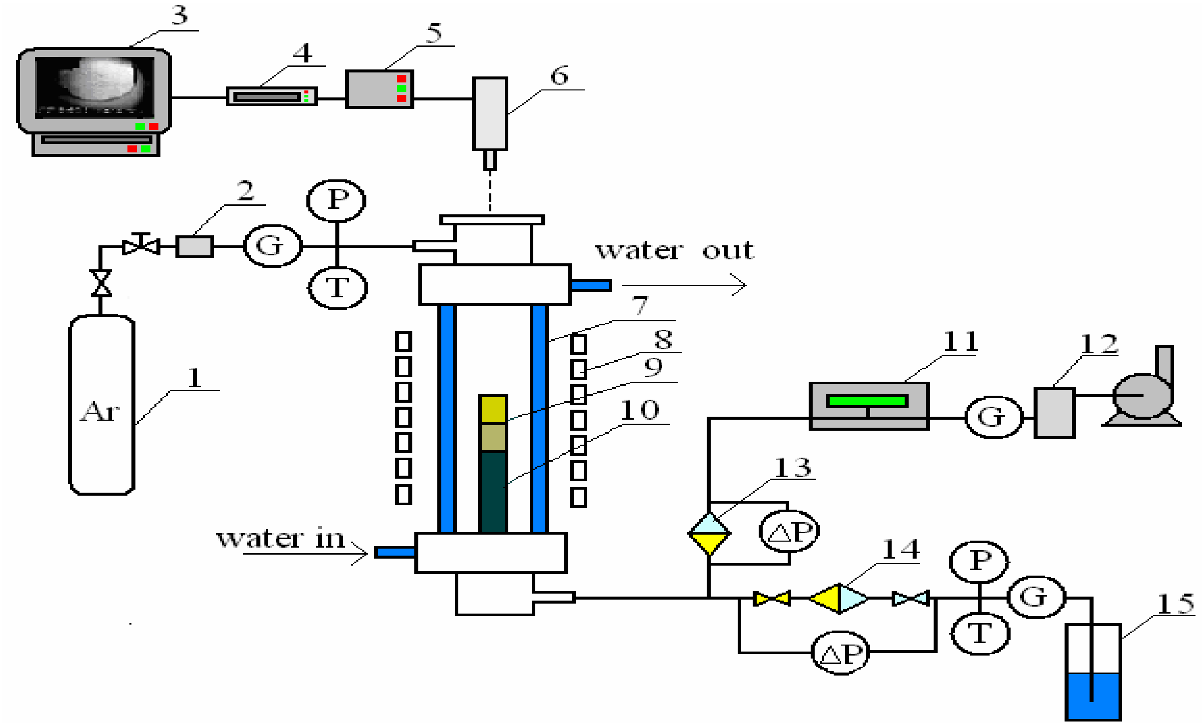

1- Ar tank; 2- Carrier gas purification unit; 3- Monitor/video recorder; 4-Video insert; 5- DAS; 6- Pyrometer combined with video camera; 7- Water-cooled quartz vessel of the furnace; 8- Inductor; 9- Crucibles (working and reference); 10- Crucible holder; 11- Mass-spectrometer; 12- Vacuum vessel (receiver); 13,14- Petrianov filters (A1); 15- Sparger with CO_2 absorbing solution.

Fig. 3.99. Schematics of the furnace for carbothermal reduction in the carrier gas flow

Analysis procedure included:

1. Recharging of drier for the carrier gas.
2. Sample weighing (approx. 0,5 g), mixing with carbon powder (about 30% from the sample mass), addition of the mixture into the graphite crucible, addition of the floater (Ni) amounting to 30-100% from the sample mass.
3. Weighing of the charged crucible.
4. Degassing of the crucible in a chamber at 1 mbar pressure.
5. Crucible placing into the furnace.
6. Sealing of the gas line and connection of the off-gas collection and analysis system.
7. Furnace flowing with carrier gas during 3 min. to remove air from the system;
8. Fast induction heating of the specimen to 1400°C;
9. Measurement of CO concentration in the off gas*;
10. Focusing of pyrometer and video camera on the crucible;
11. Gradual heating of the crucible to required temperature (2300 - 2550°C);
12. Crucible exposition at this temperature during 1÷5 min;
13. Heating disconnection and crucible cooling;
14. Calculation of oxygen content in the specimen from the mass deficit taking into account the blank test and CO volume.

*) In accordance with measurements CO2 concentration in gas did not exceed 2% for all samples.

Table 3.50 gives the main parameters of the analysis.

Table 3.50. Analysis parameters

Parameters	**Values**
Carrier gas	Ar
Carrier gas flow rate, ml/min	100÷3000
Final concentration if admixtures in the carrier gas, vol.%	below 10^{-3}
Temperature of the crucible, ^{0}C	2300÷3000
Time of specimen exposition at the working temperature, min	1÷5
Form of the sample	Powder or pieces
Floater (liquifier)	Compact nickel

Error of the oxygen measurement is below 3 % rel. Post-analysis mass deficit was calculated taking into account mass losses of the crucible and cover, also oxygen present in metallic nickel.

Table 3.51 gives measured oxygen concentrations in samples from CORD37, 41, 42 and their averaged values, which were used for specifying sample compositions and calculation of elemental material balances.

Table 3.51. Measured oxygen concentrations in samples from CORD37, 41, 42

CORD	**Sample**	**Content O, mass.%**	
		Experimental values	**Averaged values**
37[1]	Oxidic part of the ingot	8.49, 8.27	8.38 ± 0.11
	Metallic part of the ingot	3.4, 3.2	3.3± 0.1
	Sample #2	8.48	8.48± 0.1
42[2]	Oxidic part of the ingot	8.52, 8.08	8.3± 0.22
	Metallic part of the ingot	1.9, 1.7, 2.0, 1.5	1.775± 0.225
41[3]	Oxidic part of the ingot	7.61, 7.45	7.53± 0.08
	Metallic part of the ingot	0.37, 0.34, 0.38, 0.60	0.42± 0.17

[1] – Sampling location, Fig. 3.9;

[2] – Sampling location, Fig. 3.11;

[3] –Ssampling location, Fig. 3.10;

4. Discussion of results

Melt composition of CD tests was determined from the charge, because the hot crucible provides complete melting of the charged material, without losses. Insignificant volatilization of some components during the experiment also cannot cause a noticeable change in the melt composition having a large mass. Note minor pollution of the melt with carbon detected by the analysis. In our opinion small concentrations of refractory carbon-containing phase practically do not influence the results of thermal analysis, because thermal phenomena were determined from temperature changes in the crucible bottom. As it is known from /50/ (see Chapter 2.1 Carbon Induced Stratification), carbon-bearing phases present in the corium melt tend to have a density stratification, so they concentrate in the near-surface upper melt layers.

CORD tests also had melt compositions close to the charge composition. Some experiments showed insignificant depletion of melt composition in comparison with crucible charge caused by the crystallization of the refractory component (UO_2) on the cold crucible walls. Table 4.1 presents compositions of melt samples and ingots provided by different methods.

Table 4.1. Results of analyses CORD28, 29, 34, 37, 41, 42

Test	Sample	U, at.%			Zr, at.%			O, at.%		
		Chem.	XRF	EDX	Chem.	XRF	EDX	Chem.	XRF	EDX
28	Melt sample #1 (composition I)	6.9	7.7	8.2	55.3	53.7	54.3	37.8	38.6	37.5
	Melt sample #2 (composition II)	12.9	12.9	12.4	44.6	43.9	40.7	42.5	43.2	46.9
29	Melt sample	18.9	-	17.9	15.2	-	17.2	65.9		64.9
	Ingot average sample	19.3	19.8	-	15.7	17.2	-	65.0	63.0	-
34	Ingot average sample	25.0	21.5	16.9	39.6	34.7	42.4	35.4	43.8	40.8
	Rod sample#1	23.4	20.5	19.6	41.3	35.9	29.4	35.3	43.7	51.0
	Rod sample#2	-	20.2	16.9	-	36.2	29.0	-	43.5	54.1
	Rod sample#4	-	21.1	17.2	-	34.5	25.7	-	44.4	57.1
	Rod sample#5	-	21.3	17.0	-	35.0	25.8	-	43.7	57.2
37*	Melt sample #1	25.5	26.4	23.1	25.7	24.3	26.7	48.8	49.3	50.2
	Melt sample #2	26.0	27.5	20.4	25.0	22.5	27.1	49.0	49.8	52.5
	Ingot (Oxidic part)	25.7	24.6	24.3	25.8	27.5	20.5	48.5	47.9	55.5
	Ingot (Metallic part)	40.1	41.5	32.4	33.1	31.3	40.2	26.8	27.2	27.4

Test	Sample	U, at.%			Zr, at.%			O, at.%		
		Chem.	XRF	EDX	Chem.	XRF	EDX	Chem.	XRF	EDX
41	Ingot (Oxidic part)	43.7	-	41.3-44.7	1.4	-	-	54.9	-	55.3-58.7
	Ingot (Metallic part)	91.6	-	90.0-95.4	2.9	-	-	5.5	-	4.6-10.0
42**	Ingot (Oxidic part)	28.5	26.8	32	21.9	24.5	16.5	49.6	48.7	51.5
	Ingot (Metallic part)	52.9	53.4	47.4	29.5	29.0	35.9	17.5	17.6	16.7

*). Oxidic and metallic compositions of ingots where calculated by EDX for regions 4 Fig.3.38, Table 3.28

**). Oxidic and metallic compositions of ingots where calculated by EDX for region 10 Fig.3.66, Table 3.46

Data of chemical analysis and XRF include oxygen determined by the CTR. It is evident from the Table 4.1. that:

- Results of the EDX analysis are systematically different from the chemical analysis and XRF. Most distinct difference is in the data on oxygen content. As explained above, this can be attributed to the insensitivity of the XRF to oxygen and to the complexity of the data averaging explained by a significant micro- and macro-inhomogeneity of the ingot compositions.

- Comparison of data provided by chemical XRF analyses shows their good agreement within the acceptable error.

XRF and CTR results on oxygen were used as final data for melt composition corresponding to the measured liquidus temperatures. The measured liquidus and solidus temperatures were compared with the results of thermodynamical calculations provided by the GEMINI-2 program, NUCLEA-05 database was used (Table 4.2).

Table 4.2. Measured and calculated liquidus and solidus temperatures for compositions from experiments CORD28-I,II, 29, 34, 41, 42 and CD-3-5

Experiment	Composition, at.%			Experiment		Calculation	
	U	Zr	O	T_{liq}, K	T_{sol}, K	T_{liq}, K	T_{sol}, K
CORD28-I	7.7	53.7	38.6	2358	*	2238	2076
CD4	8.0	52.0	40.0	2373	2358	2231	2092
CORD28-II	12.9	43.9	43.2	2443	2249	2357	1917
CD3	13.0	43.0	44.0	2408	2345	2362	1985
CD5	16.0	36.0	48.0	2498	2298	2426	1988
CORD29	19.8	17.2	63.0	2734	*	2803	2103
CORD34	21.5	34.7	43.8	2578	2423	2470	1703
COLLOS (ITU test)	22.0	33.0	44.0	2550	2550	2486	1703
CORD37	32.5	29.2	38.3	2601	2115	2570	1710
CORD41	56.0	3.1	40.9	2788	*	2690	1440
CORD42	40.5	27.0	32.5	2663	*	2595	1705

*) – Not measured due to the interaction between melt and holder

Difference between measured and calculated liquidus temperatures is not large, it is about 100K, but it can be considerable for solidus temperature, in some cases it is as large as 700K. It can be explained by a very small fraction of fusible component in the specimen, this can result in a large error of all thermal analysis methods used.

As noted before, experiment CORD34 served as a benchmark for the cross-verification of reported results and ITU experiments /47/ within the EC COLLOS project using the method of laser pulse heating /48/, also for determining possible melt stratification, which was predicted for this composition by thermodynamic calculations using GEMINI-2 program. It follows from Table 4.2 and Fig. 4.1 that liquidus temperatures measured by different methods for one composition have a good agreement with each other and calculations.

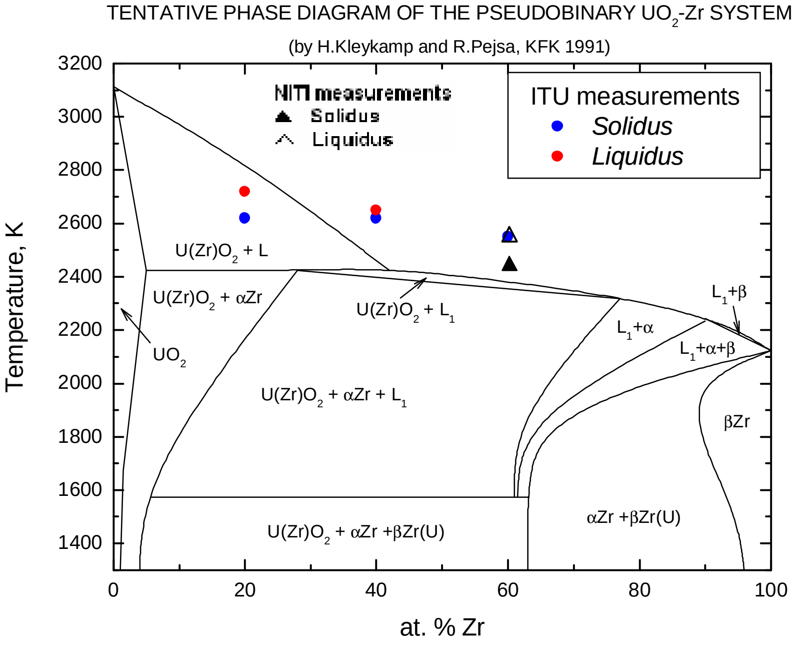

Fig. 4.1 Comparison of CORPHAD and COLOSS results with Kleykamp diagram /49/

Solidus temperatures measured in the Galakhov microfurnace for the CORD series have a substantial difference from values calculated using code GEMINI and database NUCLEA, also from the data of available pseudobinary diagrams /8/. We should remember that solidus temperatures determined in the current study can be lower than actual due to the sample-holder interaction or higher than actual due to the sample inhomogeneity.

CORD34 melt behavior after the complete charge melting and character of the melt crystallization indicatesingle liquid. CORD34 results along with the data of /14/ confirm a shorter miscibility gap in comparison with calculations using code GEMINI.

For the sake of comparison the CORD and CD results, together with results of other publications on the initial melt compositions near the UO_2-$ZrO_{0.53}$ section, are plotted on the pseudobinary section of UO_2-$ZrO_{0.53}$ (Fig. 4.2). It is evident from the figure that our data confirm the Hayward diagram of this section. Solidus temperature measured in CD3-5 has a good agreement with the solidus temperature from this diagram, and liquidus has a 30-100°C difference.

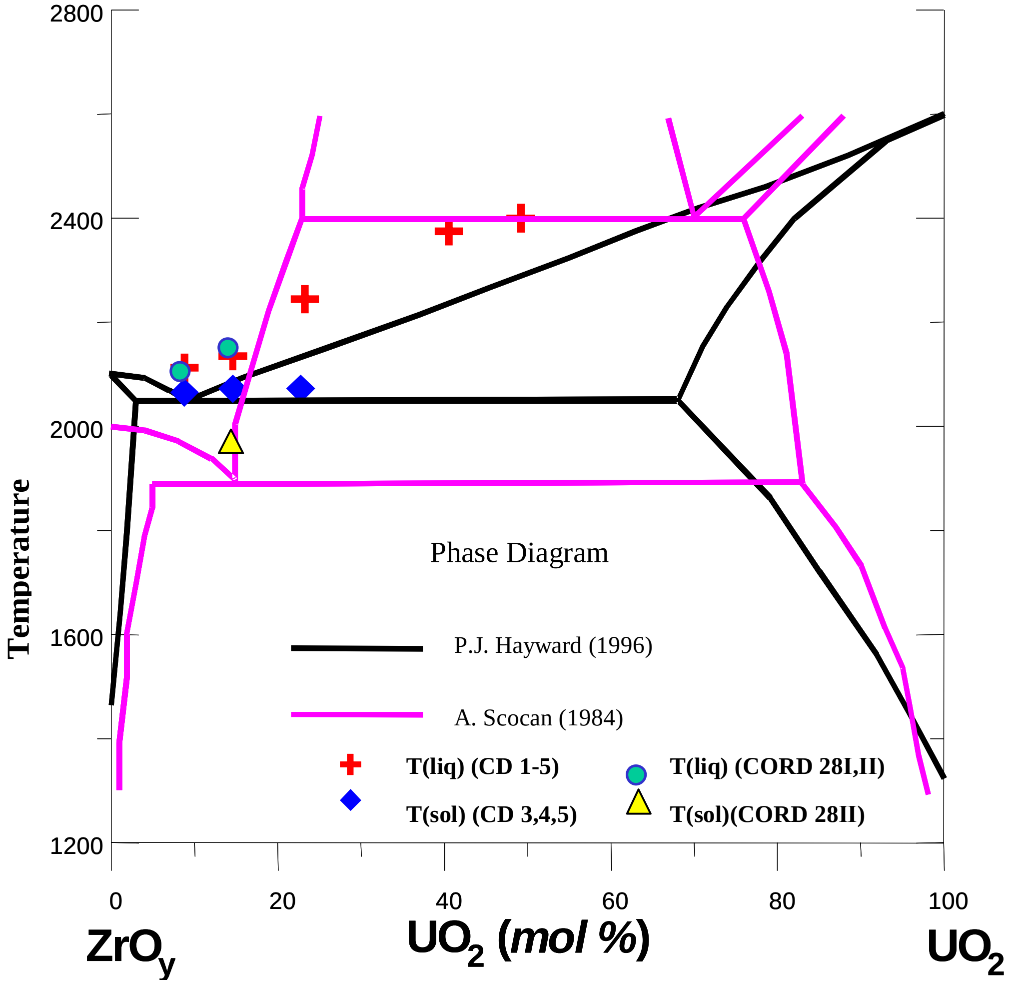

Fig. 4.2. Pseudobinary section UO$_2$-ZrO$_{0.53}$ of the U-Zr-O system in accordance with Hayward and Scocan /6, 7/ in comparison with reported results (Table 4.2)

CORD37 charge (Fig. 4.3) was chosen in order to have the melt composition closer to the central part of the predicted miscibility gap. During the experiment the second liquid was not observed on the pool surface. But the sample/ingot microstructure analysis showed the presence of crystallized oxidic droplets inside the metallic matrix and vice versa, which confirms that this melt decomposes into two liquids. Crystallized ingot easily separated into two parts almost equal in volume. Therefore, we can say that layering and gravitational stratification of liquids took place in the test; the top liquid contained more oxygen (further on - oxidic liquid), and the second, located in the melt bottom, had a much lower oxygen content (metallic liquid). In the close-to-quenching cooling conditions compositions of oxidic and metallic parts are likely to be very close to the compositions of corresponding stratified liquids. If that is the case, we can construct a tie-line using the determined average compositions of the ingot parts; and the tie-line will correspond to the temperature, from which the quenching was started.

It should noted, that each of the stratified layers (oxidic and metallic) has its own way of crystallization in accordance with its phase diagram. We have established that for both layers the primary crystallization phase is the (U,Zr)O$_{2-x}$ solid solution. In this case during the cooling of oxidic layer its composition changes along the solid solution line – the initial composition of oxidic liquid. Depending on the gap shape this ray can be tangent to it or cross it (Fig.4.3), probably from one side of the critical point. In the first case the monotectic process will not take place; in the second – the monotectic process at first will be accompanied by the increase of liberated liquid, which later will disappear completely (see Fig.4.3). Probably for this reason the oxidic layer does not have a classical monotectic microstructure, and different regions of the ingot can have a depleted primary crystallization phase. During the cooling of metallic layer, which is not a monotectic liquid, to the temperature of monotectics, a second liquid must be separated, after which the crystallization follows the standard scheme including the separation of the primary crystallization phase.

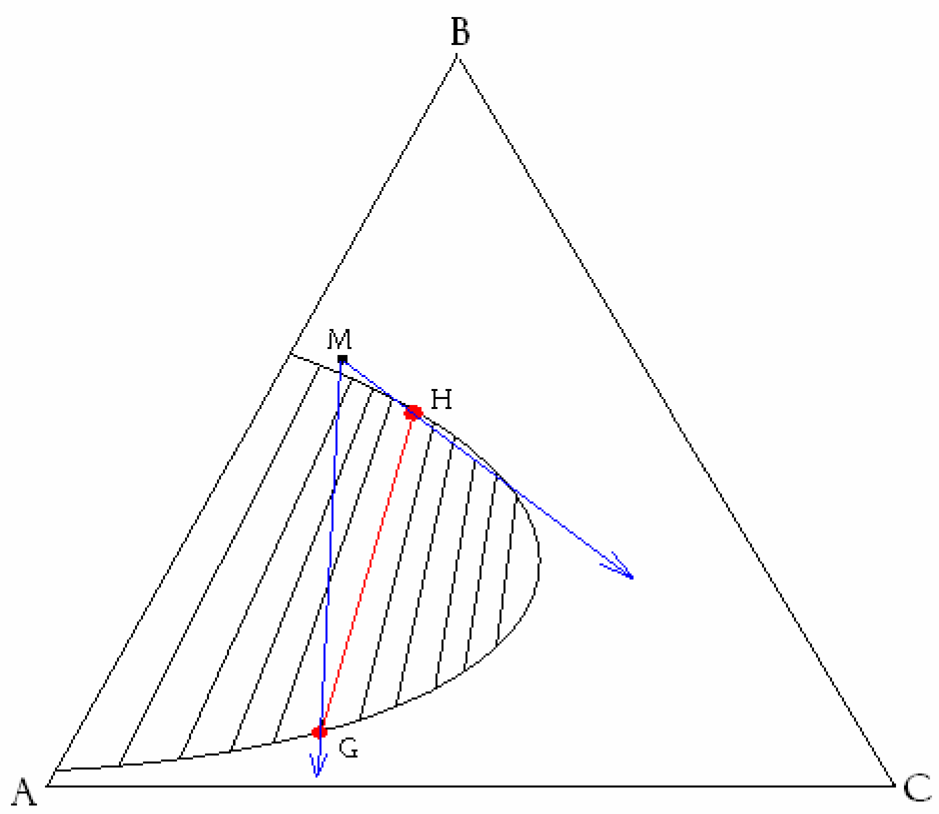

Fig.4.3 Crystallization ways of stratified liquids (M – primary crystallization liquid, H,G – corresponding compositions of oxidic and ,metallic liquids)

In the CORD37 ingot the top oxidic part has a homogeneous dendrite structure close to the CORD34 ingot, which is likely to indicate the absence of monotectic process in the oxidic liquid. $(U,Zr)O_{2-x}$ solid solution is the primary crystallization phase; α-Zr(U)(O) crystallizes after that. The bottom metallic part is also dendrite, where $(U,Zr)O_{2-x}$ solid solution is the primary crystallization phase, and αZr(U)(O) crystallizes around it; the last to crystallize is U-Zr solid solution enriched with U. The bottom metallic part has droplet inclusions of oxidic liquid, which were separated during melt cooling to the monotectic temperature. Fig. 4.4 shows compositions of coexisting liquids and tie-line directions determined by different methods of analysis.

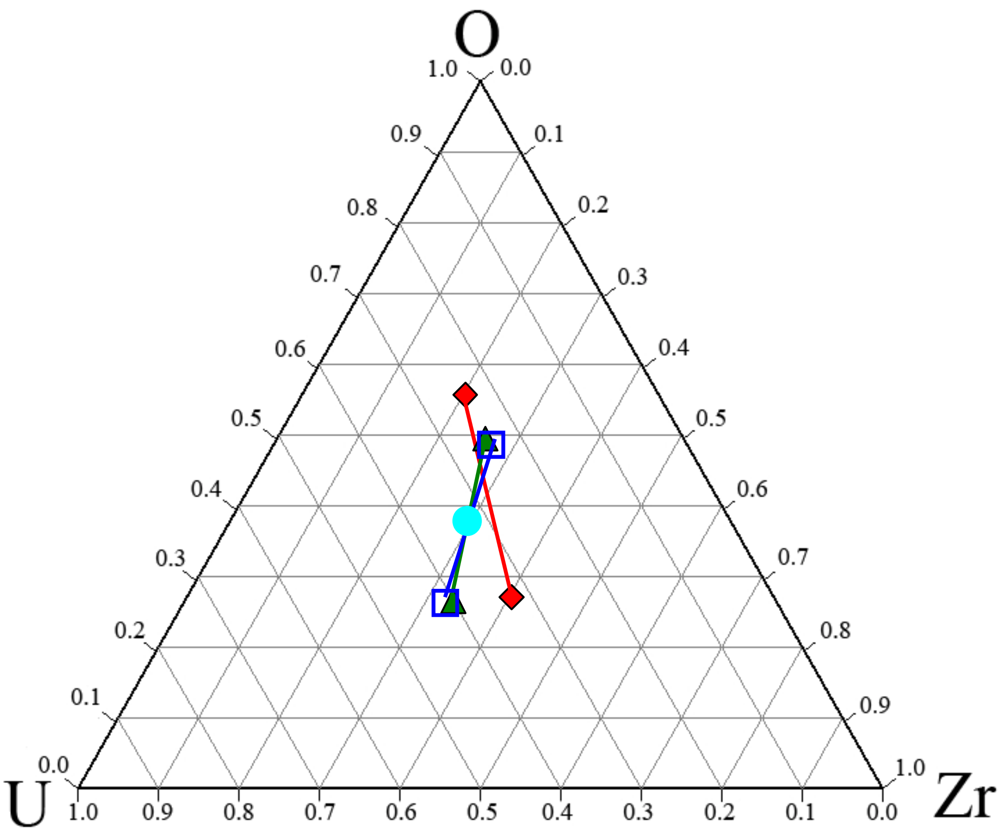

Fig.4.4 Compositions of coexisting liquids and tie-line directions ◆– in accordance with EDX, - XRF, - ChA вставить маркеры

In terms of cation ratio the compositions of oxidic liquid are practically the same in all analyses. In the EDX analysis the oxidic liquid composition was determined from the average composition of oxidic droplets in metallic matrix, because the droplet can most adequately represent the oxide coexisting with metal. The metallic part composition is inhomogeneous (see Fig. 3.32-3.37). EDX data on regions have a considerable difference. For this reason the EDX composition of metallic liquid can have a large error. Chemical and XRF data for most samples coincide; they probably correspond to the average composition of metallic liquid.. Compositions of the top (oxidic) and bottom (metallic) liquids quenched from 2370°C are given in Table 4.4.

Let us discuss the results of CORD 41, a reference experiment. Measured liquidus temperature does not contradict other published results. The ingot microanalysis showing the presence of crystallized droplets confirms the stratification of the studied melt composition. Ingot has two layers – oxidic and metallic, which shows that the density stratification of liquids took place in the experiment. Compositions of oxidic and metallic parts are inhomogeneous due to the concentration of liquid droplets near the boundary. Metallic droplets in the oxidic liquid and oxidic ones in the metallic matrix resulted from the secondary separation during cooling from 2675ºC to the monotectic temperature. In order to determine the composition of liquids corresponding to the quenching temperature (2675ºC), it is necessary to know the average compositions of each layer. As it was not possible to prepare representative average samples, a random analysis of ingot parts using alternative methods was made. In general the analysis results correspond to data from /2, 20, 21/ and confirm the presence of wide stratification region. It should be noted that metallic uranium used in the experiment contains 2.7 mass % of zirconium as admixture, it can influence the phase distribution of components. In accordance with chemical analysis Zr is distributed approximately evenly between oxidic and metallic phases. Resulting data are given in Table 4.3 and Fig.4.5 (Zr concentrations are added to uranium).

Table 4.3. CORD41 analysis of oxygen content

Sample	ChA	CTR	SEM/density
	O, at%		
Oxidic part of the ingot without globules	55.4	54.8	58.7
Oxidic part of the ingot without globules	-	-	55.3
Oxidic part of the ingot, average	55.8±0.5		
Metallic part of the ingot without globules	7.0*	5.9	4.6
Metallic part of the ingot with globules	11.9**	-	10.0
Metallic part of the ingot, average	8.4±2.6		

*) Average for zones IV and III Table3.5

**) Zone II Table3.5

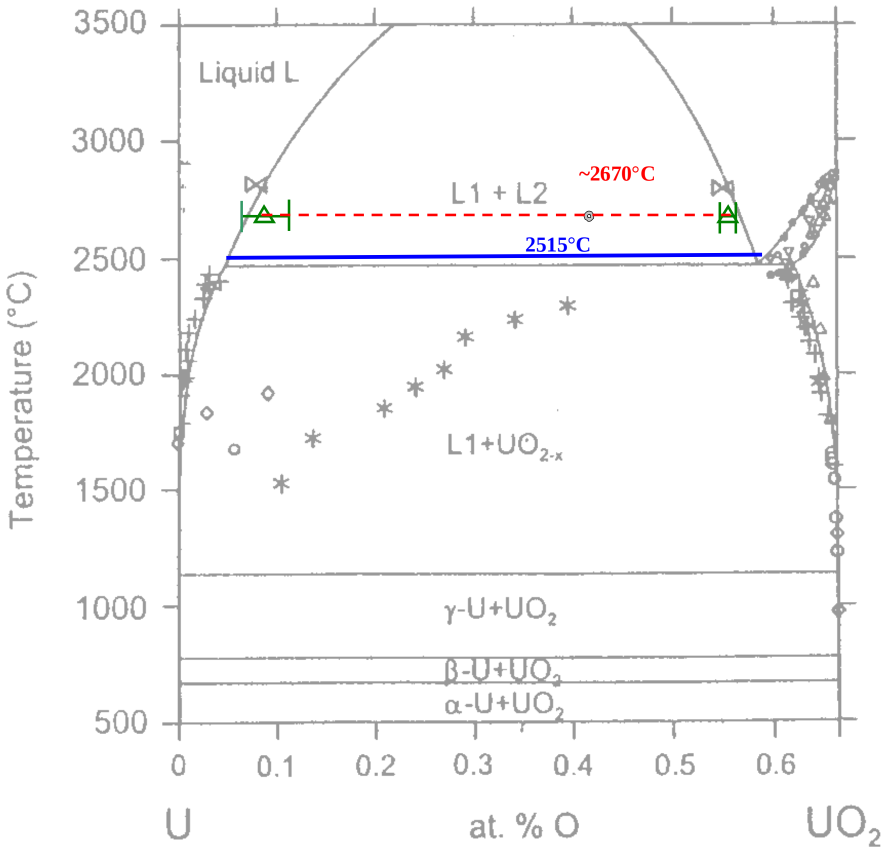

Fig. 4.5. Tie-line coordinates in the U-O system from CORD41 results

Just like in CORD37, in experiment CORD42 melt typical of the miscibility gap was produced. The studies showed that density stratification of oxidic and metallic layers took place in both experiments. Metallic and oxidic parts of CORD42 ingot correspond to phases identified in CORD37. Differently from CORD37 the microstructure of metallic part is even, and the separation of the second (oxidic) liquid is observed in the whole volume. It can be explained by the larger melt superheating above the monotectic temperature than in CORD37. Quenched metallic droplets in the oxidic part of the ingot were found near the layers' boundary. In accordance with microanalysis the composition of oxidic droplets in the metallic part is substantially different from the composition of oxidic part of the ingot. This can indicate the temperature difference of oxidic and metallic layers at quenching. If we assume that it is really so, the compositions of coexisting liquids can be determined from the average composition of metallic layer and compositions of crystallized oxidic droplets, and at the metallic liquid cooling the composition of oxidic droplets can change. Oxygen-insensitive probe was used for the EDX analysis. Results of the oxidic droplets and metallic layer analysis were recalculated (Table4.1) using the CTR of samples taken from the oxidic and metallic layers. Data of chemical analysis and XRF for the large inventory of samples from oxidic and metallic ingot layers coincide and have a considerable difference from EDX analysis. Fig. 4.5 shows compositions of coexisting liquids and tie-line directions determined by different methods of analysis.

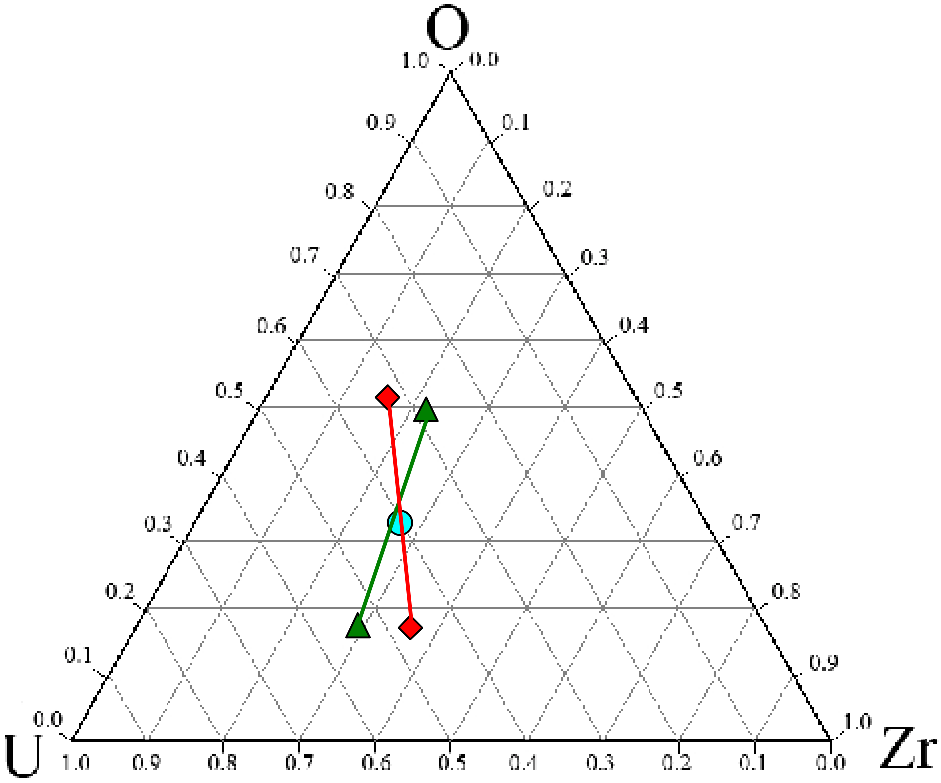

Fig. 4.6 Compositions of coexisting liquids and tie-line directions: ◆EDX data, ▲ XRF, ChA data

Liquidus temperature (monotectics) measured in the experiment agrees well with the calculations using the thermodynamical code GEMINI based on the NUCLEA database (Table 4.2), solidus temperature has an approx. 400K difference, which is caused by reasons explained above. The composition of top (oxidic) and bottom (metallic) liquids at quenching from 2480°C is given in Table 4.4.

The analyses of metallic and oxidic layers showed a good agreement (Table 4.4) in the cation composition and convergence with thermodynamical calculations using code GEMINI-2 and database NUCLEA-06.

Table 4.4 Analyses of metallic and oxidic layers of CORD37, 42 and thermodynamical calculation of coexisting phase compositions

CORD	**Method**	**Element**	**Experiment**		**Calculation**	
			Oxidic liquid	**Metallic liquid**	**Oxidic liquid**	**Metallic liquid**
			Composition, at.%			
37	**ChA**	**U**	25.7	40.1	24.4	44.6
	XRF		24.6	41.5		
	Average		***25.2±0.5***	***40.8±0.7***		
	CHA	**Zr**	25.8	33.1	21.1	41.4
	XRF		27.5	31.3		
	Average		***26.7±0.9***	***32.2±0.9***		
	ChA	**O**	47.4	27.2	54.5	14.1
	XRF		47.9	27.2		
	Average		***48.2±0.3***	***27.2***		
	Mass fraction		43.9	56.1	49.6	50.4
42	**ChA**	**U**	28.5	52.9	29.5	50.6
	XRF		26.8	53.4		
	Average		***27.7±0.9***	***53.2±0.3***		
	ChA	**Zr**	21.9	29.5	16.2	36.9
	XRF		24.5	29.0		
	Average		***23.2±1.3***	***29.3±0.3***		
	ChA	**O**	49.6	17.6	54.3	12.5
	XRF		48.7	17.6		
	Average		***49.2±0.4***	***17.6***		
	Mass fraction		34.7	65.3	35.7	64.3

In determining compositions of correlated points of the tie-line in the miscibility gap the main problem was in oxygen evaluation in the oxidic and, especially, metallic part of the ingot. In our opinion the XRF using additionally oxidized samples provided most accurate data (see section 3.4.4). The following factors can bring uncertainties into these data:

1. Composition changes, in particular, oxygen content at melt cooling, crystallization and ingot freezing. In spite of rather fast cooling of regions adjacent to the cold crucible after the formation of surface crust, which has low heat conductivity, the melt capsulates and cooling rate of bulk layers drops. In these conditions mass exchange can take place both between layers and between the melt and overlying atmosphere. But the comparison of oxygen in melt samples and in the oxidic ingot part in CORD37 (Table 4.1) shows that composition difference in accordance with XRF+CTR data is approx. 1-2 at %, that is, within the measurement error. A possible release of oxygen from the melt into the gas phase was checked by the analysis of the latter. None of the post-experimental ingot crystallized in argon showed an increased oxygen concentration.

2. Thermal gradient of the system, i.e. different temperatures of oxidic and metallic liquids could result from their different electric conductivities. The presence of thermal imbalance can influence the compositions of coexisting liquids. But the liquid having lower electric conductivity, in which lower power deposition can be expected – oxidic liquid – is above the metallic liquid. Taking into account a high speed of free convection melt mixing in the cold crucible we can be sure of intensive convective heat exchange between layers, which makes their temperatures even. Unfortunately the reported work did not provide the temperatures of coexisting liquids, because direct temperature measurements of chemically aggressive melt were not possible. Temperatures of layers can be calculated using the available code DYMELT, which has been verified for corium melt in the framework of the ISTC METCOR project.

Conclusions

Liquidus temperatures have been determined for compositions, which can be used for the NUCLEA database optimization. Different thermal analysis methods were used for the purpose. The recommended data are presented in Table 4.5.

Table4.5

Composition, at.%			**T_{liq}, K**	**Measurement method**
U	**Zr**	**O**		
7.7±0.2	53.7±1.6	38.6±1.2	2358±35	VPA IMCC
12.9±0.4	43.9±1.3	43.2±1.3	2443±36	
19.8±1.0	17.2±0.9	63.0±3.1	2734±41	
21.5±0.2	34.7±0.3	43.8±0.4	2578±38	
32.5±0.3	29.2±0.3	38.3±0.4	2601±39	
56.0±0.5	3.1±0.1	40.9±0.4	2788±42	
40.5±0.4	27.0±0.3	32.5±0.3	2663±40	
22.9±0.4	19.1±0.3	58.0±1.1	2643±39	Thermogram differentiation
25.7±0.5	15.8±0.3	58.5±1.1	2673±40	
13.0±0.2	43.0±0.8	44.0±0.8	2408±36	
8.0±0.1	52.0±1.0	40.0±0.8	2373±35	
16.0±0.3	36.0±0.7	48.0±0.9	2498±37	

Measured solidus temperatures were found to be systematically much higher than expected. This can probably be explained by the small amount of liquid phase during the sample melting.

The provided results confirm the adequacy of liquidus surface modelling in the system, but do not confirm or revise the calculated solidus temperature.

The IMCC technique proved to be an advantageous method for studying high-temperature melts in the miscibility gap. In the conditions of substantial difference between the liquids' densities the two-layer pool is established, which has oxidic layer on the surface. Melt quenching produces an ingot, which has oxidic and metallic parts. The completed studies of wide range of compositions have confirmed that the miscibility gap in the system occupies a smaller domain than predicted by thermodynamical calculations. More detailed study of the gap boundaries requires a much larger number of experiments.

Efficiency of the IMCC methodology for the tie-line studies in the miscibility gap has been demonstrated also for a more simple U-O system. The completed deficiency analysis of experimental methodologies and posttest analyses enables to recommend the following tie-line data as most credible:

		Composition, at%/quenching temperature, K		
		$U_{0.325}Zr_{0.292}O_{0.383}$ /2643	**$U_{0.405}Zr_{0.270}O_{0.325}$ /2753**	**$U_{0.560}Zr_{0.031}O_{0.409}$ /2948**
Composition of oxidic liquid, at%	**U**	**25.2±1.2**	**27.7±1.3**	**43.7±2.1**
	Zr	**26.7±1.3**	**23.2±1.1**	**1.4±0.07**
	O	**48.2±2.4**	**49.2±2.4**	**54.9±2.7**
Composition metallic liquid, at%	**U**	**40.8±2.0**	**53.2±2.6**	**88.8±4.4**
	Zr	**32.2±1.6**	**29.3±1.4**	**2.7±0.1**
	O	**27.2±1.3**	**17.6±0.8**	**8.5±2.5**

In conclusion it should be mentioned that the study provided a considerable amount of information on the crystallization pattern of different compositions in the studied system. This information can be used for specifying non-equilibrium melt solidification models. The updated models, in their turn, can be used for calculating compositions of liquids using the available data resulting from ingot analysis.

References

1. NUCLEA. Nuclear Thermodynamic Database. Version 2003-01 / Editor B.Cheynet. THERMODATA 2003, P. 17-19.
2. C. Gueneau, V. Dauvois, P. Perodeaud, C. Gonella, O. Dugne. “Liquid immiscibility in a (O,U,Zr) model corium” // J. Nuclear Materials 254 (1998), P. 158-174.
3. P.-Y. Chevalier, E. Fischer, B. Cheynet. “Progress in the thermodynamic modelling of the O-U-Zr ternary system.” // Computer Coupling of Phase Diagrams and Thermochemistry 28 (2004) P. 15-40
4. S.V. Bechta, E.V. Krushinov, V.I. Almjashev, S.A. Vitol, L.P. Mezentseva, Yu.B. Petrov, D.B. Lopukh, V.B. Khabensky, M. Barrachin, S. Hellmann, K. Froment, M. Fisher, W. Tromm, D. Bottomley, F. Defoort, V.V. Gusarov.. ”Phase diagram of the ZrO_2-FeO system.“ // J. Nucl. Mater. 348 (2006) P. 114-121.
5. S.V. Bechta, E.V. Krushinov, V.I. Almjashev, S.A. Vitol, L.P. Mezentseva, Yu.B. Petrov, D.B.Lopukh, V.B. Khabensky, M. Barrachin, S. Hellmann, K. Froment, M. Fisher, W. Tromm, D. Bottomley, F. Defoort, V.V. Gusarov. ”Phase diagram of the UO_2-FeO_{1+x} system“ // J. Nucl. Mater. in print (2006).
6. A. Scocan, 5th Meeting on Thermal Nuclear Reactor Safety, Karlsruhe, Spt. 9-13, 1984, P. 1035-1042.
7. P.J. Hayward, I.M. George, // J. Nucl. Mater. 232 (1996), P. 13-22
8. C. Politis, Report KFK 2167 (1975)
9. E.F. Juenke, J.F. White. Report GEMP-731 (1969).
10. W.A.Lambertson, M.H.Mueller Uranium Oxide Phase Equilibrium System: III, UO_2-ZrO_2 // J. Am. Ceram. Soc. 1953 Vol. 36, # 11. P. 365-368.
11. G.M.Wolten Solid Phase Transitions in the UO_2-ZrO_2 system // J. Am. Chem. Soc. 1958. Vol. 80, # 18. P. 4772-4775
12. P.E Evans. The System UO_2-ZrO_2 // J. Am. Ceram. Soc. 1960. Vol. 43, # 9. P. 443-447
13. N.M. Voronov, E.A., I.T.Voitekhova, Kovalev. Phase diagram of the system uranium dioxide – zirconium oxide / In the Alm.: Alloy composition of certain systems with uranium and thorium (Works of the Baykov Institute of metallurgy, the USSR ASc). Moscow Gosatomizdat. 1961. p. 467-481.
14. N.M. Voronov, R.M. Sofronova, I.T.Voitekhova. High-temperature chemistry of uranium oxides and their compounds/ M.: Atomizdat. 1971. 358 p.
15. Cohen J., Schaner B.E. A Metallographic and X-ray Study of the UO_2-ZrO_2 System // J. Nucl. Mater. 1963 Vol. 9, # 1. P. 18-52
16. Baes C.F., Shaffer J.H., McDuffie H.F. UO_2 and ZrO_2 behavior in molten fluorides // Trans. Am. Nucl. Soc. 1963. Vol. 6, # 2. P. 393.
17. P.D. Bottomley, M. Cooquerelle. // Nuclear Technology 87 (1989), P.120.
18. N.A. Toropov., V.P. Barzakovsky, I.A. Bondar et al. Phase diagrams of silicate systems. Reference book, issue 2. Metal-oxygen compounds of silicate systems / L.:Nauka. 1969. 372 p.
19. R.J. Ackermann / ANL-5482, Sept. 14, 1955.
20. A.E.Martin, R.K.Edwards. // J. Phys. Chem. 65 (1965), P. 1788.
21. R.K. Edwards, A.E. Martin. / In: Thermodynamics. IAEA, Vienna, 1966, V.2, P. 423.
22. P. Guinet, H. Vaugoyeau, P.L. Blum. // C. R. Acad. Sci. Paris 263 (1966), P. 17-20.
23. R.F. Domagala, D.J. McPherson. // Trans. AIME, 1954, V. 200, P. 238.
24. E. Gebhardt, H.D. Seghezzi, W. Dürrschnabel // J. of Nucl. Mater. 1961, V. 4, #3, P. 241

25. E.Gerhardt, G.Elssner // J. of Nucl. Mat. V.4. (1961), p.255
26. R.J. Ackermann, S.P. Garg, E.G. Rauh. High-temperature Phase Diagram for the System Zr-O // J. Am. Ceram. Soc. 1977. Vol. 60, # 7-8. P. 341-345.
27. J.P. Abriata, J. Barces, R. Versaci. The O-Zr (Oxygen-Zirconium) System // Bull. Alloy Phase Diagrams. 1986. V. 7. P. 116-123.
28. R. Arroyave, L. Kaufman, T.W. Eagar. Thermodynamic Modeling of the Zr-O system // CALPHAD. 2002. V.26. N.1. P. 95-118.
29. N.P Liakishev, O.A. Bannikh, N.N. Rokhlin et al. Phase diagrams of binary metallic systems. Reference Book, volume 3. Book 2 / M.: Mashinostroenie. 2001. 448 p.
30. B.W. Howlett, A.G. Knapton. / Proc. U.N.Intern. Conf. Peaceful Uses At. Energy, 2d Geneva. 1958. P. 104.
31. G.M. Butirin. High-density carbon materials. M. Chemistry, 1976.
32. O.S. Ivanov, G.N. Bagrov / Alloy composition of some systems with uranium and thorium. Alm. M.: Gosatomizdat, 1961. p. 5-19
33. T.A. Badaeva, R.I. Kuznetsova // Newsletter ASc USSR. Metals. 1970. N.2. C. 210-215.
34. Gibbs Energy Minimizer Software. THERMODATA-BP66-38402 Saint Martin D'Heres CEDEX- France.
35. V.G. Asmolov at al. On the existence of miscibility gap in the U-Zr-O system// High temperature thermal physics, 2004, V. 42, #2, C. 247-255.
36. F.Ya. Galakhov. High-temperature microfurnace for studying heterogeneous equilibria in the refractory oxide systems.- in.:Modern methods of silicate and construction material studies. M., 1961 p. 178-182.
37. V.B. Khabensky et al. Phase diagram studies of multicomponent systems of corium and products of its interaction with NPP materials. Phase 2. First year. Annual report # 1-1950.2-2004 (Attachment 1. Study of binary oxidic systems. System UO_2-FeO) // NITI
38. T.M. Florence. Analytical methods in the nuclear fuel cycle / Vienna: JAEA, 1972.
39. Methods for determining O/U ratio in the pre-stoichiometric UO_2. // Radiochemistry, 1994. V. 36, # .3. C.
40. GOST 12365-84. Alloy and high-alloy steels. Methods for zirconium detection.
41. S.V. Elinson, T.I. Nezhnova, … // Industrial laboratory, 1964. V. 30, #4.
42. V.G. Goriushina, E.V. Romanova, T.A. Archakova, … // Industrial laboratory, 1961, V. 27, #7.
43. D.I. Riabchikov., M.M. Seniavin. Analytical chemistry of uranium. M.: USSR ASc. 1962.
44. V.F. Lukianov, S.B. Savin, I.V. Nikolslaya. Photometric detection of uranium microquantities using arsenazo III. JACh., XV, issue.3. 1960.
45. N.F. Losev. Quantitative X-ray fluorescence analysis. M.: Nauka 1969.
46. PaulingFile project. Basic Database for Crystal Structures. http://crystdb.nims.go.jp
47. M. Sheindlin, W. Heinz, D. Bottomley, D. Knoche, B. Cremer, J. Somers, Further melting point measurements of the Zr-U-O system and their application: / Presentation to the 4th CORPHAD ISTC Project Meeting, RIAR, Dimitrovograd, Russia, September 14, 2004.
48. D. Manara et al. Melting of stoichiometric and hyperstoichiometric uranium dioxide// J. Nucl. Mater. 342 (2005), P. 148-163.
49. H. Kleykamp, R.Pejsa, Tentative phase diagram of the pseudobinary UO_2 – Zr system. KFK 1991
50. Integrated Report: Main Results of the MASCA1 and 2 Projects. Russian Research Centre “KURCHATOV INSTITUTE” OECD MASCA Project. November 2006